

# **MECHANICAL ENERGY HARVESTING USING REDUCED GRAPHENE OXIDE BASED NANOCOMPOSITES**

**Ph.D. Thesis**

By  
**MANOJIT PUSTY**



**DISCIPLINE OF METALLURGY ENGINEERING &  
MATERIALS SCIENCE  
INDIAN INSTITUTE OF TECHNOLOGY INDORE  
FEBRUARY 2020**





# **MECHANICAL ENERGY HARVESTING USING REDUCED GRAPHENE OXIDE BASED NANOCOMPOSITES**

**A THESIS**

*Submitted in partial fulfillment of the  
requirements for the award of the degree  
of*  
**DOCTOR OF PHILOSOPHY**

*by*  
**MANOJIT PUSTY**



**DISCIPLINE OF METALLURGY ENGINEERING &  
MATERIALS SCIENCE  
INDIAN INSTITUTE OF TECHNOLOGY INDORE  
FEBRUARY 2020**









# INDIAN INSTITUTE OF TECHNOLOGY INDORE

## CANDIDATE'S DECLARATION

I hereby certify that the work which is being presented in the thesis entitled **MECHANICAL ENERGY HARVESTING USING REDUCED GRAPHENE OXIDE BASED NANOCOMPOSITES** in the partial fulfillment of the requirements for the award of the degree of **DOCTOR OF PHILOSOPHY** and submitted in the **DISCIPLINE OF METALLURGY ENGINEERING AND MATERIALS SCIENCE, INDIAN INSTITUTE OF TECHNOLOGY INDORE**, is an authentic record of my own work carried out during the time period from December 2014 to February 2020 under the supervision of **Dr. Parasharam M. Shirage**, Associate Professor, Discipline of Metallurgy Engineering and Materials Science, Indian Institute of Technology Indore, and **Dr. Somaditya Sen**, Associate Professor, Discipline of Physics, Indian Institute of Technology Indore.

The matter presented in this thesis has not been submitted by me for the award of any other degree of this or any other institute.



Signature of the student with date  
(Manojit Pusty)

-----  
This is to certify that the above statement made by the candidate is correct to the best of my/our knowledge.



February 19, 2020

Signature of Thesis Supervisor #1 with date  
(Dr. Parasharam M. Shirage)



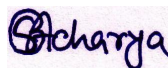
19.02.2020

Signature of Thesis Supervisor #2 with date  
(Dr. Somaditya Sen)

-----  
**Manojit Pusty** has successfully given his/her Ph.D. Oral Examination held on **June 30, 2020**



Signature of Chairperson (OEB)  
Date: 14.08.2020



Signature of External Examiner  
Date: 15.08.2020



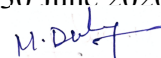
Signature(s) of Thesis Supervisor(s)  
Date: 30 June 2020



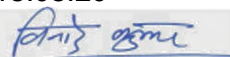
Signature of PSPC Member #1  
Date: 15.08.20



Signature of PSPC Member #2  
Date: 15/8/2020



Signature of Convener, DPGC  
Date: 17.08.2020



Signature of Head of Discipline  
Date: 18.08.2020



## ACKNOWLEDGEMENTS

First and foremost, I would like to express my sincere and deepest sense of gratitude to **Dr. Parasharam M. Shirage**, (Associate Professor, Discipline of Metallurgy Engineering and Materials Science, IIT Indore) for his guidance during my PhD tenure. I sincerely acknowledge him for providing me all the opportunities and motivations throughout my graduate studies. Special thanks to his encouragement at times of loss and despair. I acknowledge his assistance in helping me attend conferences, which has broadened my research horizon. I specially mention his encouragement to motivate me to pursue research and inspire me to develop an academic bent of mind.

I express my gratitude and thankfulness to my supervisor **Dr. Somaditya Sen** (Associate Professor, Discipline of Physics, IIT Indore) for his guidance and cooperation during my Ph.D.

I express deepest gratefulness to my PSPC members **Dr. I. A. Palani** (Associate Professor & Head of the Discipline, Discipline of Mechanical Engineering, IIT Indore) and **Dr. Md Aquil Khan** (Associate Professor & Head of the Discipline, Discipline of Mathematics, IIT Indore) for their valuable questions, insightful comments and motivation.

I acknowledge the support received in research from IIT Indore for providing the essential experimental facilities. I acknowledge the support provided by **Sophisticated Instrumentation Center (SIC)** at IIT Indore, for performing XRD, SEM, EDX, UV-Vis, FTIR, AFM, Rheometer measurements. I express my sincere gratitude and thankfulness to **Mr. Kinny Pandey, Mr. Ravinder, Mr. Nitin Upadhyay, Mr. Ghanashyam A. Bhavsar** for their help, support and cooperation in performing and planning various experiments.

I acknowledge **IIT Indore** for providing me fellowship under Teaching Assistant (TA) category and for providing expenses towards attending international conference during my PhD tenure.

I acknowledge **Council of Scientific and Industrial Research (CSIR), Govt. of India**, for providing me fellowship as **Senior Research Fellow (SRF-Direct)** under Fellowship Awardee (FA) category.

I acknowledge **International Travel Support (ITS)- Science and Engineering Research Board (SERB), Govt. of India** for providing financial assistance to attend international conference.

I would like to express my sincere thanks to **Dr. Sunil Kumar** (Assistant Professor, Discipline of Metallurgy Engineering and Materials Science, IIT Indore) for his help in discussing research topics. I thank **Dr. Rajneesh Mishra** (Associate Professor, Discipline of Chemistry, IIT Indore) for his help in performing UV-Visible Spectroscopy characterization. I sincerely thank **Dr. Amod C. Umarikar** (Associate Professor, Discipline of Electrical Engineering, IIT Indore) for providing me necessary facilities to perform research.

I also extend my sincere gratitude to, **Dr. Vasant Sathe** (Scientist-G), **Dr. Uday Deshpande** (Scientist-E), **Dr. V. Raghavendra Reddy** (Scientist-G), **Dr. A. M. Awasthi** (Scientist-H) UGC-DAE Consortium for Scientific Research, Indore for allowing me to use the research facilities.

I would like to express my gratitude to **Mr. Anand Petare**, **Mr. Pawan Chouhan**, **Mr. Satish Kaushal**, **Mr. Rishiraj Chouhan**, **Mr. Dipak Dhepte**, **Mr. Vinay Mishra** and **Mr. Deepak Rathore** for their help in planning, executing and helping me in experiments.

I would like to thank each one of my lab-mates **Dr. Yogendra Kumar**, **Dr. Prateek Bhojane**, **Mr. Kushal Mazumdar**, **Mr. Alfa Sharma**, **Ms. Lichchhavi** and **Mr. Subhash Chand Yadav** for being intelligent, amazing, kind and wonderful individuals who have helped me in every aspect of my research life. I sincerely express gratitude to my senior lab members **Dr. Mahesh Verma**, **Dr. Bhuvaneshwari Sakthivel** and **Dr. Darshna Potphode** for their kindness, guidance, help and support in performing research.

I am grateful to **Ms. Jasmine Fernandez** and **Dr. Jayant Kumar Mohanta** for helping me perform academic and experimental tasks during my PhD research span.

I am indebted to **Dr. Camellia Sarkar** for being a friend and a well-wisher.

I am grateful to my parents, family members, and all relatives for their patience, blessings and trust in me.

Date: 19/02/2020

Manojit Pusty

**Dedicated to**  
**My Parents, Teachers**  
**&**  
**All Well Wishers**





## LIST OF PUBLICATIONS

### (From the thesis work)

#### Journal Publications:

[1] **Manojit Pusty**, Lichchhavi Sinha, Parasharam M. Shirage, A flexible self-poled piezoelectric nanogenerator based on a *r*GO–Ag/PVDF nanocomposite, *New J. Chem.*, 43 (2019) 284-294. (**Impact Factor: 3.069**)

[2] **Manojit Pusty**, Alfa Sharma, Lichchhavi Sinha, Anjali Chaudhary, Parasharam Shirage, "Comparative Study with a Unique Arrangement to Tap Piezoelectric Output to Realize a Self-Poled PVDF Based Nanocomposite for Energy Harvesting Applications", *ChemistrySelect*, 2 (2017) 2774–2782. (**Impact Factor: 1.716**)

[3] **Manojit Pusty**, Amit Kumar Rana, Yogendra Kumar, Vasant Sathe, Somaditya Sen, Parasharam Shirage, "Synthesis of Partially Reduced Graphene Oxide/Silver Nanocomposite and Its Inhibitive Action on Pathogenic Fungi Grown Under Ambient Conditions", *ChemistrySelect*, 1 (2016) 4235–4245. (**Impact Factor: 1.716**)

[4] **Manojit Pusty**, Parasharam M. Shirage, “Gold Nanoparticle-Cellulose/PDMS Nanocomposite: A Flexible Dielectric Material for Harvesting Mechanical Energy” *RSC Adv.*, 10, (2020) 10097-10112. (**Impact Factor: 3.049**)



## LIST OF CONFERENCES

[1] **Oral presentation** at “**3<sup>rd</sup> International Conference on Advances in Functional Materials**” at University of California Los Angeles, Los Angeles, USA, during 14-17 August 2017.

[2] **Poster presentation** at “**National Conference on Study of Matter Using Intense Radiation Sources and Under Extreme Conditions**” at University Grants Commission-Department of Atomic Energy Consortium for Scientific Research Indore, India during 03-06 Nov 2016.

[3] **Poster presentation** at “**International Conference on Nanoscience and Technology**” at Indian Institute of Science Education and Research Pune, India during 29 Feb-02 March 2016.

[4] **Poster presentation** at “**Ramanujan Conclave**” at Indian Institute of Technology Indore, India during 22-23 Dec 2015.

### Courses

[1] Completed a Global Initiative of Academic Network (GIAN) course on “**Chemical Sensors: Principle, Technologies and Applications**” by Prof. Dr. Giovanni Neri, University of Messina, Italy and Associate Prof. Dr. Parasharam M. Shirage, IIT Indore, India during 01-09 July 2016.

[2] Completed a GIAN course on “**High-Pressure Synthesized Materials: A Chest of Treasure and Hints**” by Prof. Dr. Akira Aoy, Tsukuba, AIST, Japan and Associate Prof. Dr. Parasharam M. Shirage, IIT Indore, India during 11-19 July 2016.

[3] Completed an “**International Workshop on Advanced Nanoscience and Engineering**” organized by Discipline of Metallurgy Engineering and Materials Science, IIT Indore, India on 1 Dec 2017.

[4] Completed a TEQUIP sponsored Short Course on “**Advanced Surface Science and Engineering**” organized by Discipline of Metallurgy Engineering and Materials Science, IIT Indore, India during 26-28 March 2018.



# TABLE OF CONTENTS

<b>CANDIDATE’S DECLARATION</b>	<b>i</b>
<b>ACKNOWLEDGEMENTS</b>	<b>iii</b>
<b>LIST OF PUBLICATIONS</b>	<b>vii</b>
<b>LIST OF CONFERENCES/WORKSHOP</b>	<b>ix</b>
<b>TABLE OF CONTENTS</b>	<b>xi</b>
<b>LIST OF FIGURES</b>	<b>xvii</b>
<b>LIST OF TABLES</b>	<b>xxvii</b>
<b>ABBREVIATIONS</b>	<b>xxix</b>
<b>NOMENCLATURE</b>	<b>xxxiii</b>
 <b>CHAPTER 1: Introduction</b>	 <b>1</b>
1.1 Nanomaterials	1
1.2 Classification of Nanomaterials	2
1.2.1 Zero Dimensional Materials	2
1.2.2 One Dimensional Materials	3
1.2.3 Two Dimensional Materials	3
1.2.4 Three Dimensional Materials	3
1.3 Properties of Nanomaterials	4
1.3.1 Physical Properties	4
1.3.2 Magnetic Properties	4
1.3.3 Thermal Properties	5
1.3.4 Mechanical Properties	5
1.3.5 Chemical Properties	6
1.3.6 Optical Properties	7
1.3.7 Electronic Properties	7
1.4 Graphene and its Derivatives	8
1.5 Mechanical Energy Harvesting Applications of Nanomaterials	9
1.6 Nanogenerator	12

1.6.1 Piezoelectric Nanogenerators (PENGs)	13
1.6.2 Triboelectric Nanogenerators (TENG)	16
1.7 Anti-microbial Applications of Nanomaterials	18
1.7.1 Anti-microbial Materials	18
1.7.2 Anti-microbial Nanomaterials	18
1.7.3 Overcoming Antibiotic Resistance using Nanomaterials	19
1.7.4 Mechanisms of Antibacterial Activity of the NPs	20
1.7.4.1 Oxidative Stress	20
1.7.4.2 Dissolved Metal Ions	21
1.7.4.3 Non-oxidative Mechanisms	21
1.8 Objective and Scope of the Thesis	21
1.9 Chapter wise organization of the thesis:	26
References	27
<b>CHAPTER 2: Nanomaterial Synthesis and Characterizations</b>	<b>33</b>
2.1 Introduction	33
2.2 Synthesis of Nanomaterials	33
2.2.1 Bottom-up Synthesis	33
2.2.1.1 Colloidal Methods	34
2.2.1.2 Sol-Gel Synthesis	34
2.2.1.3 Emulsion Synthesis	34
2.2.1.4 Vapor Phase Deposition	34
2.2.1.5 Plasma-Assisted Deposition	34
2.2.1.6 Molecular Beam Epitaxy	34
2.2.1.7 Self-assembly Techniques	35
2.2.2 Top-Down Synthesis	35
2.3 Nano-Material Synthesized in this Dissertation	35
2.3.1 Graphene Oxide	35
2.3.2 Reduced graphene oxide-silver nanoparticle (rGO-Ag)	37
2.4 Nanomaterial-Polymer Nanocomposite Synthesized in this Dissertation	38
2.5 Material Characterization Techniques	41

2.5.1 X-Ray Diffraction Spectroscopy	41
2.5.2 Ultra Violet-Visible Spectrophotometry	44
2.5.3 Fourier Transform-Infrared Spectroscopy	46
2.5.3.1 Attenuated Total Reflection (ATR) Mode	48
2.5.4 Raman Spectroscopy	49
2.5.5 X-Ray Photoelectron Spectroscopy (XPS)	50
2.5.6 High Resolution Transmission Electron Microscopy (HR-TEM)	51
2.5.7 Scanning Electron Microscopy (SEM)	53
2.6 Summary	55
References	56
<b>CHAPTER 3: Synthesis and Study of Self-poled Polymer Based Nanocomposite for Energy Harvesting Applications with a Unique Arrangement to Tap Piezoelectric Output</b>	<b>59</b>
3.1 Overview	59
3.2 Results and Discussion	63
3.2.1 Material Synthesis	63
3.2.1.1 Synthesis of Graphene Oxide	63
3.2.1.2 Synthesis of Fe-reduced graphene oxide (Fe- <i>r</i> GO)	63
3.2.1.3 Synthesis of Fe- <i>r</i> GO/PVDF Nanocomposite film	64
3.2.1.4 Synthesis of CNT/PVDF nanocomposite film	64
3.2.2 Device fabrication	64
3.2.3 Material Characterizations	65
3.2.4 Electrical Conductivity Measurements	71
3.2.5 Electrical Characterizations	74
3.2.6 Electric Current Response Stability	79
3.3 Summary	80
References	81
<b>CHAPTER 4: Flexible Self-poled <i>r</i>GO-Ag/PVDF Nanocomposite Based Piezoelectric Nanogenerator</b>	<b>87</b>
4.1 Overview	87

4.2 Results and Discussion	90
4.2.1 Material Synthesis	90
4.2.2 Synthesis of Graphene Oxide	91
4.2.3 Synthesis of reduced graphene oxide-silver nanocomposite (rGO-Ag)	92
4.2.4 Fabrication of PENG	92
4.2.5 Material Characterizations of GO and rGO-Ag	93
4.2.6 Morphological and Structural Characterizations of rGO-Ag/PVDF nanocomposite	98
4.2.7 Electrical Characterizations	114
4.2.8 Energy Efficiency Calculation	121
4.3 Summary	130
References	131
<b>CHAPTER 5: Gold Nanoparticle-Cellulose/PDMS Nanocomposite Based Mechanical Energy Harvesting Application</b>	137
5.1 Overview	137
5.2 Results and Discussion	140
5.2.1 Synthesis of Au nanoparticle seeds	140
5.2.2 Synthesis of Au nanoparticles:	141
5.2.3 Fabrication of Piezoelectric Nanogenerator (PENG):	141
5.2.4 Material Characterizations	142
5.2.5 Electrical Characterizations	152
5.2.6 Piezoresponse Force Microscopy Characterizations	156
5.2.7 Efficiency Calculation	160
5.3 Summary	163
References	163
<b>CHAPTER 6: Inhibitive Action of Partially Reduced Graphene Oxide/Silver Nanocomposite on Pathogenic Fungi</b>	171
6.1 Overview	171
6.2 Results and Discussion	173
6.2.1 Synthesis of GO	173



6.2.2 Synthesis of <i>rGO</i> -Ag Nanocomposite	174
6.2.3 Instruments used for Material Characterizations and Electrical Characterizations	174
6.2.4 Material Characterizations	174
6.2.5 Silver Ion Release Test	182
6.2.6 Experimental Details of Silver Ion Release Test	183
6.3 Antifungal Application of <i>rGO</i> -Ag	184
6.3.1 Preparation of Agar Medium	184
6.3.2 FE-SEM Image of Fungal microbes	186
6.3.3 Plate Count Method to Ascertain Antifungal Activity	188
6.3.4 Synergistic effect of <i>rGO</i> -Ag	190
6.4 Summary	191
References	192
<b>CHAPTER 7: Conclusion and Future Scopes</b>	199
7.1 Thesis Summary	199
7.2 Future scope	202



# LIST OF FIGURES

## **Chapter 1**

<b>Figure No.</b>	<b>Figure Caption</b>	<b>Page No.</b>
<b>1.1</b>	Shows the classification of nanomaterials into three categories.	<b>2</b>
<b>1.2</b>	Shows the different chain conformations of PVDF.	<b>12</b>
<b>1.3</b>	Shows the schematic illustration of operation of PENG (a) at rest (b) under stress (c) when stress is removed.	<b>14</b>
<b>1.4</b>	Shows the $d_{31}$ and $d_{33}$ piezoelectric designs.	<b>16</b>
<b>1.5</b>	Shows the schematic illustration of TENG.	<b>17</b>

## **Chapter 2**

<b>Figure No.</b>	<b>Figure Caption</b>	<b>Page No.</b>
<b>2.1</b>	Shows the schematic illustration of working configuration of the XRD instrument.	<b>42</b>
<b>2.2</b>	Shows the schematic diagram of dual beam spectrophotometer under operation in transmittance mode.	<b>46</b>
<b>2.3</b>	Shows the schematic illustration of the working of the Fourier Transform Spectrometer.	<b>48</b>
<b>2.4</b>	Shows the schematic diagram of the ATR prism.	<b>49</b>
<b>2.5</b>	Shows the Photoelectron emission process.	<b>51</b>
<b>2.6</b>	Shows the schematic of the basic components of the HR-TEM.	<b>51</b>
<b>2.7</b>	Shows the schematic of the basic components of the SEM.	<b>55</b>
<b>2.8</b>	Shows the schematic of the different signals used by the SEM and the areas from which they originate.	<b>55</b>

### **Chapter 3**

<b>Figure No.</b>	<b>Figure Caption</b>	<b>Page No.</b>
<b>3.1</b>	Shows the diagram of the piezoelectric device under consideration that is used for energy harvesting.	<b>64</b>
<b>3.2</b>	Shows the SEM Image of (a) Fe- <i>r</i> GO (b) CNT.	<b>65</b>
<b>3.3</b>	Shows the FE-SEM Image of Fe- <i>r</i> GO.	<b>66</b>
<b>3.4</b>	Shows the EDS data which shows the compositional analysis in atomic percentage of Fe- <i>r</i> GO.	<b>67</b>
<b>3.5</b>	Shows the ATR-IR Spectra of (a) CNT/PVDF (b) Fe- <i>r</i> GO/PVDF (c) Neat PVDF, which is used to study the piezoelectric phases.	<b>68</b>
<b>3.6</b>	Shows the Raman Spectra of (a) Fe- <i>r</i> GO (b) CNT.	<b>69</b>
<b>3.7</b>	Shows the Raman Spectra of (a) Fe- <i>r</i> GO/PVDF nanocomposite (b) CNT/PVDF nanocomposite.	<b>69</b>
<b>3.8</b>	Shows the AC Electrical Conductivity vs frequency characteristics of (a) CNT/PVDF Nanocomposite (b) Fe- <i>r</i> GO/PVDF Nanocomposite (c) Pure PVDF.	<b>71</b>
<b>3.9</b>	Shows the rectified short circuit current generated due to finger tapplings from the (a) CNT/PVDF (b) Fe- <i>r</i> GO/PVDF (c) Neat PVDF based device.	<b>74</b>
<b>3.10</b>	Shows the open circuit voltage generated due to finger excitations from the (a) CNT/PVDF (b) Fe- <i>r</i> GO/PVDF (c) Neat PVDF based device.	<b>75</b>
<b>3.11</b>	Shows the open circuit rectified voltage generated due to finger excitations from the (a) CNT/PVDF (b) Fe- <i>r</i> GO/PVDF (c) Neat PVDF based device.	<b>77</b>
<b>3.12</b>	Shows the current response stability for CNT/PVDF nanocomposite film. Inset shows magnified current response.	<b>79</b>
<b>3.13</b>	Shows the current response stability for Fe- <i>r</i> GO/PVDF nanocomposite film. Inset shows magnified current response.	<b>80</b>

<b>3.14</b>	Shows the current response stability for pure PVDF nanocomposite film. Inset shows magnified current response.	<b>80</b>
-------------	--	-----------

#### **Chapter 4**

<b>Figure No.</b>	<b>Figure Caption</b>	<b>Page No.</b>
<b>4.1</b>	Shows the schematic of the step-wise fabrication of the PENG.	<b>91</b>
<b>4.2</b>	Shows the Raman Spectra of (a) GO and <i>r</i> GO-Ag (b) $I_D/I_G$ and $I_{2D}/I_G$ ratio of GO and <i>r</i> GO-Ag.	<b>93</b>
<b>4.3</b>	Shows the (a) SEM image (b) TEM image of <i>r</i> GO-Ag, where Ag nanoparticles are embedded in a thin layer of <i>r</i> GO matrix (c) SEM image of the surface morphology of 1.0 <i>r</i> GO-Ag/PVDF nanocomposite.	<b>94</b>
<b>4.4</b>	Shows the EDS results which shows the compositional details in atomic percentage of the <i>r</i> GO-Ag Nanocomposite.	<b>95</b>
<b>4.5</b>	Shows the XRD spectra of GO and <i>r</i> GO-Ag.	<b>96</b>
<b>4.6</b>	Shows the (a) XPS Survey Spectra of GO and <i>r</i> GO-Ag (b) C1s spectra of GO (c) C1s spectra of <i>r</i> GO-Ag.	<b>97</b>
<b>4.7</b>	Shows the X-ray diffraction patterns of (a) pure PVDF (b) 0.1 <i>r</i> GO-Ag/PVDF (c) 0.5 <i>r</i> GO-Ag/PVDF (d) 1.0 <i>r</i> GO-Ag/PVDF (e) 2.0 <i>r</i> GO-Ag/PVDF nanocomposite.	<b>100</b>
<b>4.8</b>	Shows the variation of total crystallinity, $\beta$ crystallinity, and $\gamma$ crystallinity in PVDF films with different <i>r</i> GO-Ag loadings.	<b>100</b>
<b>4.9</b>	Shows the FT-IR spectra of pure PVDF and <i>r</i> GO-Ag/PVDF nanocomposite in the region of 1600–600 $\text{cm}^{-1}$ .	<b>101</b>
<b>4.10</b>	Shows the (a) deconvoluted FT-IR spectra of 1.0 <i>r</i> GO-Ag/PVDF nanocomposite film in the region of 900-800 $\text{cm}^{-1}$ (b) FT-IR spectra of all the PVDF films in the region of 4000-2500 $\text{cm}^{-1}$ .	<b>102</b>

<b>4.11</b>	Shows the deconvoluted FT-IR spectra of (a) PVDF (b) 0.1 <i>r</i> GO-Ag/PVDF (c) 0.5 <i>r</i> GO-Ag/PVDF (d) 2.0 <i>r</i> GO-Ag/PVDF.	<b>104</b>
<b>4.12</b>	Shows the variation of relative proportion in percentage of combined electroactive polar $\beta$ and $\gamma$ -phases (in black) and only $\beta$ -phases (in red) of PVDF with different <i>r</i> GO-Ag loading by weight percentage.	<b>105</b>
<b>4.13</b>	Shows the variation of the damping coefficient with the increase in <i>r</i> GO-Ag concentration loading.	<b>106</b>
<b>4.14</b>	Shows the FT-IR spectra of all the <i>r</i> GO-Ag/PVDF based nanocomposites in the region of 3060-2940 $\text{cm}^{-1}$ .	<b>107</b>
<b>4.15</b>	Shows the dichroic ratio of the peak present at (a) 1274 $\text{cm}^{-1}$ belonging to $\beta$ -phase (b) 1232 $\text{cm}^{-1}$ belonging to $\gamma$ -phase (c) 832 $\text{cm}^{-1}$ belonging to $\gamma$ -phase.	<b>108</b>
<b>4.16</b>	Shows the Raman spectra of pure PVDF and <i>r</i> GO-Ag/PVDF nanocomposite in the region of 580–1800 $\text{cm}^{-1}$ .	<b>109</b>
<b>4.17</b>	Shows the schematic illustration of the intermediate steps in the formation of the $\beta$ -phase in <i>r</i> GO-Ag-PVDF.	<b>110</b>
<b>4.18</b>	Shows the schematic illustration of the <i>r</i> GO-Ag nano-sheets and PVDF molecules. The <i>r</i> GO-Ag nano-sheets, interacts with the PVDF chains to form the piezoelectric polar phases.	<b>111</b>
<b>4.19</b>	Shows the (a) <i>P-E</i> Loop test (b) variation of Energy Density (c) efficiency, of the various <i>r</i> GO-Ag/PVDF nanocomposite films.	<b>112</b>
<b>4.20</b>	Shows the <i>P-E</i> loop test curve where the shaded area (blue bars) shows the zone of Released Energy Density ( $U_R$ ), area inside the <i>P-E</i> loop shows the zone of Energy Loss ( $U_L$ ).	<b>114</b>
<b>4.21</b>	Shows the (a) generated open circuit output voltage that is measured by exciting the 2.0 <i>r</i> GO-Ag/PVDF, 1.0 <i>r</i> GO-Ag/PVDF, 0.5 <i>r</i> GO-Ag/PVDF, 0.1 <i>r</i> GO-Ag/PVDF, PVDF nanocomposite films by hand impulse imparting (b) magnified image of one cycle of voltage response from the nanocomposite after imparting and releasing the impulse (c) schematic diagram of the electrical connections that were used for the measurement of the electrical output using digital storage	<b>116</b>

	oscilloscope with hand impulse imparting and relaxation (d) photograph of the PENG that is encapsulated by PDMS (e) flexibility of PENG.	
<b>4.22</b>	Shows the (a) rectified output voltage that is measured by exciting the 2.0 rGO-Ag/PVDF, 1.0 rGO-Ag/PVDF, 0.5 rGO-Ag/PVDF, 0.1 rGO-Ag/PVDF, PVDF nanocomposite films by human hand impulse imparting (b) magnified image of one cycle of rectified voltage response of the nanocomposite after imparting and releasing the impulse (c) voltage that is accumulated in three capacitors having individual capacitance of 2.2, 4.7 and 10 $\mu$ f.	<b>117</b>
<b>4.23</b>	Shows the (a) short-circuit current that is measured by exciting the 2.0 rGO-Ag/PVDF, 1.0 rGO-Ag/PVDF, 0.5 rGO-Ag/PVDF, 0.1 rGO-Ag/PVDF, PVDF nanocomposite films by hand impulse imparting (b) magnified image of one cycle of current response due to human palm impulse imparting and releasing action.	<b>119</b>
<b>4.24</b>	Shows the (a) rectified short-circuit current that is measured by exciting the 2.0 rGO-Ag/PVDF, 1.0 rGO-Ag/PVDF, 0.5 rGO-Ag/PVDF, 0.1 rGO-Ag/PVDF, PVDF nanocomposite by hand impulse imparting (b) magnified image of one cycle of current response due to human palm impulse imparting and releasing action.	<b>120</b>
<b>4.25</b>	Shows the Stress vs Strain curve of the rGO-Ag/PVDF nanocomposite with different filler loadings.	<b>121</b>
<b>4.26</b>	Shows the (a) output voltage generated from 1.0 rGO-Ag/PVDF across the various resistance and the corresponding power density (b) average open circuit voltage and short circuit current generated by the various rGO-Ag/PVDF nanocomposite.	<b>123</b>
<b>4.27</b>	Shows the schematic illustration of the working mechanism of the PENG when excited by (a) human palm tappings (b) bendings.	<b>125</b>
<b>4.28</b>	Shows the (a) piezoelectric output voltage generated by the PENG when attached to human fingers under opening and closing motion, in the inset the PENG is shown attached to human fingers on the palm (b)	<b>126</b>

piezoelectric output voltage generated by the PENG when attached to a footwear under footstep excitation conditions, in the inset image of the PENG is shown which is attached to a footwear.

- 4.29** Shows the (a) LEDs that are connected in parallel connection on a bread board before lighting, inset schematic shows the circuit diagram of the arranged LEDs (b) lighting of the LEDs that are arranged to form the letters “IITI”, which is the abbreviation of Indian Institute of Technology Indore, after imparting continuous hand impulse. **127**
- 4.30** Shows the durability, where the PENG was tested with mechanically operated piezoelectric excitation source consecutively for three hours. **128**

## **Chapter 5**

- 5.1** Shows the schematic diagram of the step-wise fabrication process of the PENG. (a) Cellulose and PDMS were mixed in a beaker (b) Within the mixture of cellulose and PDMS varied quantity of Au NP colloid was added (c) The mixture was poured in a petri dish and was put in an electric furnace for curing (d) After curing the Au NP–Cellulose/PDMS nanocomposite was cut and Aluminium electrode was attached to the top and bottom of the composite (e) After that Polypropylene (PP) tapes were attached on the top to completely cover the Aluminium electrodes (f) Conducting wires were attached to both the surfaces (g) The nanocomposite was encapsulated by PDMS (h) Optical image of the as fabricated PENG (i) Optical image showing the flexibility of the PENG. **140**
- 5.2** Shows the XRD spectra of cellulose powder. **142**
- 5.3** Shows the FE-SEM image of (a) Cellulose microfibrils, the inset shows single microfibrils of cellulose (b) surface of the Au NP–Cellulose nanocomposite, indicating the complete encapsulation of cellulose microfibrils by PDMS. **143**



<b>5.4</b>	Shows the (a, b) HRTEM images of Au NPs at two different magnifications (c) lattice fringes (d) SAED pattern corresponding to <i>fcc</i> Au.	<b>144</b>
<b>5.5</b>	Shows the ATR-IR Spectra of Pure cellulose powder, 200 $\mu$ L Au NP-Cellulose, 20 $\mu$ L Au NP-Cellulose and 2 $\mu$ L Au NP-Cellulose.	<b>145</b>
<b>5.6</b>	Shows the UV-Visible spectra of Pure cellulose powder, 2 $\mu$ L Au NP-Cellulose, 20 $\mu$ L Au NP-Cellulose, 200 $\mu$ L Au NP-Cellulose and Au NP.	<b>147</b>
<b>5.7</b>	Shows the (a) Dielectric Constant vs Frequency (b) Dielectric Loss vs Frequency, characteristics of PDMS, Cellulose/PDMS, 2 $\mu$ L Au NP-Cellulose/PDMS, 20 $\mu$ L Au NP-Cellulose/PDMS, 200 $\mu$ L Au NP-Cellulose/PDMS, 20 $\mu$ L-Au/PDMS.	<b>147</b>
<b>5.8</b>	Shows the $\epsilon''$ vs $\epsilon'$ plot of (a) Cellulose/PDMS (b) 2 $\mu$ L Au NP-Cellulose/PDMS (c) 20 $\mu$ L Au NP-Cellulose/PDMS (d) 200 $\mu$ L Au NP-Cellulose/PDMS.	<b>151</b>
<b>5.9</b>	Shows the open circuit voltage of the (a) Pure PDMS (b) Cellulose/PDMS (c) 20 $\mu$ L Au NP-Cellulose/PDMS (d) 20 $\mu$ L-Au/PDMS.	<b>152</b>
<b>5.10</b>	Shows the short circuit current of the (a) Pure PDMS (b) Cellulose/PDMS (c) 20 $\mu$ L Au NP-Cellulose/PDMS (d) 20 $\mu$ L-Au/PDMS.	<b>155</b>
<b>5.11</b>	Shows the 3D PFM (a) height profile (b) amplitude response (c) phase response from the PDMS, Cellulose/PDMS and 20 $\mu$ L Au NP-Cellulose/PDMS nanocomposite samples respectively.	<b>156</b>
<b>5.12</b>	Shows the (a) stability of the PENG (b) charging of a 10 $\mu$ F capacitor by the PENG fabricated from 20 $\mu$ L Au NP-Cellulose/PDMS and Pure Cellulose/PDMS (c) LED in off condition when PENG is not excited (d) LED in on condition under human palm impact impartment (e) shows the touch sensor application of the Au NP-Cellulose/PDMS Nanogenerator. The LED is switched off when sensor/PENG is touched in the non-sensing area (f) the LED turns on when	<b>159</b>

sensor/PENG is touched in the sensing area (g) amplifier circuit diagram that is used to amplify the harvested current generated by the PENG, to ensure lighting the LED (h) the block diagram of the touch sensor application.

- 5.13** Shows the Stress vs Strain Curve of (a) Pure Cellulose/PDMS (b) 200 $\mu$ L Au NP-Cellulose/PDMS (c) 20 $\mu$ L Au NP-Cellulose/PDMS (d) 2 $\mu$ L Au NP-Cellulose/PDMS. **160**

## **Chapter 6**

- 6.1** Shows the SEM image of (a) GO which is wrinkled and crumbled and is prepared by modified Hummer's method; inset shows magnified image of the same (b) *r*GO-Ag Nanocomposite, where the Ag NPs are embedded on the surface of the wrinkled and crumbled *r*GO flakes; inset shows magnified image of Silver Nanoparticles. **175**
- 6.2** Shows the EDS results which indicate the compositional details in atomic percentage of the *r*GO-Ag Nanocomposite. **176**
- 6.3** Shows the (a) HRTEM image of *r*GO-Ag Nanocomposite (b) the lattice fringes of individual Ag Nanoparticle on *r*GO sheet. **176**
- 6.4** Shows the XRD Spectra of (a) Graphite (b) *r*GO (c) GO (d) *r*GO-Ag Nanocomposite. **177**
- 6.5** Shows the Raman Spectrum of (a) GO (b) *r*GO (c) *r*GO-Ag Nanocomposite. **178**
- 6.6** Shows the (a) XPS Survey Spectra which indicates the various elements present in GO and *r*GO-Ag NC (b) C1s Peak Deconvolution of GO (c) C1s peak Deconvolution of *r*GO-Ag Nanocomposite. **180**
- 6.7** Shows the FTIR Spectra of (a) GO (b) *r*GO (c) *r*GO-Ag Nanocomposite. **181**
- 6.8** Shows the UV-Vis Spectra of (a) GO (b) *r*GO-Ag Nanocomposite (c) *r*GO. **182**
- 6.9** Shows the (a) Silver ion release test results of *r*GO-Ag NC (b) standard curve of silver ions for calibration of the ion current. **184**

<b>6.10</b>	Shows the optical Images of Luria Bertani Agar Petri Plates just after exposure to fungus. Fungus incubated with (a) Water (b) Antibiotic Doxycycline (c) rGO-Ag Nanocomposite (d) GO (e) rGO (f) Ag Nanoparticles.	<b>185</b>
<b>6.11</b>	Shows the optical Images of Luria Bertani Agar Petri Plates, showing fungal growth profile after 3 days of incubation. Fungus incubated with (a) Water (b) Antibiotic Doxycycline (c) rGO-Ag Nanocomposite (d) GO (e) rGO (f) Ag Nanoparticles.	<b>185</b>
<b>6.12</b>	Shows the optical microscopy images of fungal colonies (a) indicating Hyphae like structures (b) Sporangiphore like structures.	<b>186</b>
<b>6.13</b>	Shows the SEM image of microbial cell culture where the fungal colonies are treated with (a) Water (b) Antibiotic Doxycycline (c) rGO-Ag Nanocomposite (d) GO (e) rGO (f) Ag NPs.	<b>187</b>
<b>6.14</b>	Shows the SEM image of microbial cell culture where it is found that (a), (c), (e) cell membrane intact before treatment, (b), (d), (f) cell membrane damaged after treatment with rGO-Ag Nanocomposite.	<b>188</b>
<b>6.15</b>	Shows LB Agar plate on which bacteria were grown by blowing air from mouth after 1 day of incubation.	<b>189</b>
<b>6.16</b>	Shows LB Agar plates containing bacteria grown by blowing air from mouth after 1 day of incubation, where the Agar Plates are treated with (a) Antibiotic Doxycycline (b) Silver Nanoparticles (c) rGO (d) GO (e) Water (f) rGO-Ag NC.	<b>189</b>



## LIST OF TABLES

<b>Table No.</b>	<b>Table Caption</b>	<b>Page No.</b>
<b>4.1</b>	Performance details of previously reported data on energy harvesting devices	<b>129</b>
<b>5.1</b>	Assignment of vibrational bands of cellulose I determined by IR Spectroscopy in ATR mode	<b>146</b>
<b>5.2</b>	Performance details of previously reported data on energy harvesting devices	<b>162</b>



## ABBREVIATIONS

AC	Alternating Current
AFM	Atomic Force Microscopy
ATR-IR	Attenuated Total Reflectance- Infra Red
BE	Binding Energy
BF	Bright Field
BSE	Back Scattered Electrons
BTO	Barium Titanate
CMP	Chemical Mechanical Polishing
CNF	Cellulose nanofibril
CNT	Carbon Nanotube
CVD	Chemical Vapour Deposition
DC	Direct Current
DF	Dark Field
DI	Deionized
DMF	Dimethyl Formamide
DNA	Deoxyribonucleic Acid
ECE	Electrode Composite Electrode
EMI	Electromagnetic Induction
F	Fluorine
Fe- <i>r</i> GO	Iron Nanoparticles Reduced Graphene oxide
FTIR	Fourier Transform Infrared
FWHM	Full Width at Half Maximum
GAg	Graphene -Silver
GIC	Graphite Intercalation Compound
GO	Graphene Oxide
GT	Graphene -TiO <sub>2</sub>

H	Hydrogen
HRTEM	High Resolution Transmission Microscopy
ICP	Inductively Coupled Plasma
IR	InfraRed
KE	Kinetic Energy
KNN	Sodium Potassium Niobate
LB	Luria Bertani
LED	Light Emitting Diodes
MWS	Millers Wagner Sillars
NP	Nanoparticle
PDMS	Polydimethylsiloxane
PFM	Piezoresponse Force Microscopy
PET	Polyethylene terephthalate
<i>P-E</i> Loop	Piezoelectric-Electric Field Loop
PENG	Piezoelectric Nanogenerator
PGO	Pristine Graphite oxide
PI	Polyimide
PLLA	Polylactic acid
PLGA	Poly (lactic-co-glycolic acid)
PMMA	Polymethyl methacrylate
PP	Polypropylene
PTFE	Polytetrafluoroethylene
PVD	Physical Vapor Deposition
PVDF	Polyvinylidene Fluoride
PVDF TrFE	Polyvinylidene Fluoride trifluoro ethylene
PZT	Lead Zirconate Titanate
<i>r</i> GO-Ag	Reduced graphene oxide -silver
ROS	Reactive oxygen species
SAED	Selected Area Electron



	Diffraction
SE	Scattered Electrons
SEM	Scanning Electron Microscope
SERS	Surface Enhanced Raman Scattering
SPR	Surface Plasmon Resonance
UV-Vis	Ultra Violet-Visible



## NOMENCLATURE

$\alpha$	Non-polar Piezoelectric Phase
$\beta$	Polar Piezoelectric phase
$\varepsilon'$	Dielectric constant
$\varepsilon''$	Dielectric loss
$\varepsilon_s$	Static permittivity
$\varepsilon_\infty$	Relative dielectric permittivity
$\gamma$	Polar Piezoelectric Phase
$A_\beta$	Area of the $\beta$ crystalline peaks
$A_\gamma$	Area of the $\gamma$ crystalline peaks
$A_{841}$	Absorption intensity at $841\text{ cm}^{-1}$
$A_{832}$	Absorption intensity at $832\text{ cm}^{-1}$
$a$	Absorption coefficient
$B$	Baseline Signal
$c$	Velocity of particle
$C$	Capacitance
$c_p$	Concentration
$C_s$	Specific heat per unit volume
$\Delta l$	Deformation in length
$\Delta t$	Average time duration between the two consecutive voltage peaks of the imparting pressure cycles
$d$ -spacing	Distance between atomic planes
$D$	Dark current of detector
$E_n$	Discrete Energy Level
$E_{in}$	Total Mechanical Energy
$E_{out}$	Electrical Energy Stored in Capacitor
$F$	Force

$F(\beta, \gamma)$	Relative proportion of both $\beta$ and $\gamma$ -phase crystallization
$F(\beta)$	Proportion of $\beta$ -crystallization phase in PVDF from FTIR analysis
$F(\gamma)$	Proportion of $\gamma$ -crystallization phase on PVDF from FTIR analysis
$f_c$	Critical frequency
$f_{min}$	Frequency of lowest dielectric constant
$g$	Acceleration of gravity
$h$	Distance
$\hbar$	Planck's Constant
$r_\beta$	Bohr radius
$l$	Path length of light
$L$	Orbital perimeter
$\mu$	micro
$m$	Mass
$M$	Mega
$n$	Dimensional coordinate
$\eta$	Overall Energy Efficiency
$\Omega$	ohms
$P$	Maximum Power Density
$P_0$	Incident power of light
$P_T$	Transmitted power of light
$I$	Current
$K_{841}$	Absorption coefficient at $841\text{ cm}^{-1}$
$K_{832}$	Absorption coefficient at $832\text{ cm}^{-1}$
$\sigma$	Imparted Pressure
$\sigma_s$	Stress
$S$	Surface Area

$v$	Speed of mobile carriers
$v_{as}$	Asymmetric FTIR vibrational band
$v_s$	Symmetric FTIR vibrational band
$v$	Velocity
$V$	Voltage
$W_{in}$	Input Energy
$l$	Free path
$l(f)$	Attenuation length related to frequency
$\lambda$	Wavelength
$r_{dc}$	Damping coefficient
$R$	Resistance
$R_L$	Load Resistance
$t$	Total Time
$\tau_{rel}$	Dielectric relaxation time
$T$	Absolute transmittance
$\phi_{spectrometer}$	Work function of the spectrometer
$\chi_{ct}$	Degree of crystallinity
$\sum A_{cr}$	Area under the crystalline region in the polymer
$\sum A_{amr}$	Area under the amorphous region in the polymer
$\chi_{c\beta}$	Total beta crystallinity
$\chi_{c\gamma}$	Total gamma crystallinity
$U_R$	Released energy density
$U_L$	Released energy loss
$Y$	Young's Modulus



# CHAPTER 1

---

## Introduction

---

### 1.1 Nanomaterials

Nanomaterials are usually considered with the materials with particle sizes varying from sub-nanometers to hundreds of nanometers. The scale of one nanometer(nm) can be compared to the length of an elemental atom. Materials in nanometer scale shows physical properties that are different from that of the bulk. The study of nanomaterials includes understanding the physical, chemical properties and their other phenomenon and processes. Synthesis of nanomaterials is an important process because this is what determines the dimensions as well as the properties of the nanomaterials. The synthesis of nanomaterials involves two processes, the “bottom-up” and the “top-down” approach. In the bottom-up approach elements or compounds are used for the synthesis of nanoparticles, nanotubes or layered sheets. This approach further requires following physical and chemical processes that may require costlier infrastructure. Nevertheless, it is essential to perform the study of nanomaterials as its importance revolves around solving practical life problems that cannot be addressed by bulk scale materials. In the top-down approach a 2-3 times larger object is synthesized than the desired nanostructure. Then to achieve the desired nanoscale features, nanopatterning techniques are utilized. This is a widely used method in the microelectronics industry. The advantages of the bottom-up approach are cost-effectiveness, scalability, uniformity of the nanomaterial. In comparison, the top-down approach provides better control towards the synthesis of nanomaterials.

## 1.2 Classification of Nanomaterials

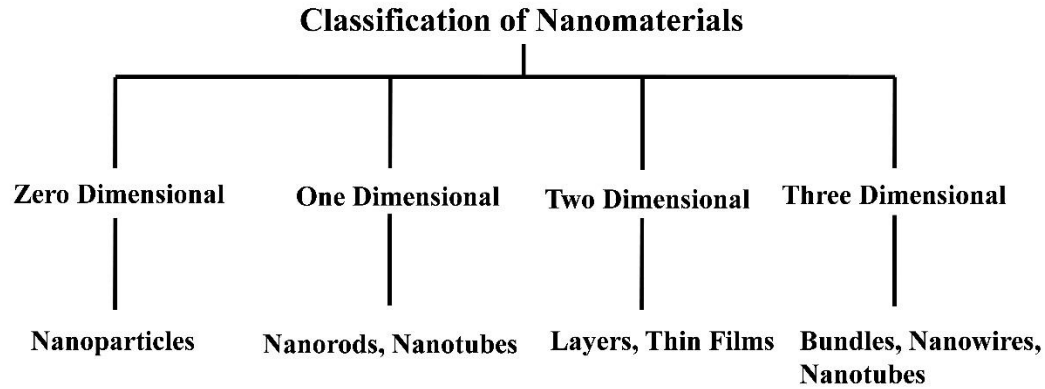


*Figure 1.1 Shows the classification of nanomaterials into three categories.*

Nanomaterials are classified into three categories as shown in Figure 1.1 viz. zero-dimensional (e.g. nanoparticles), one-dimensional (e.g. nanorods or nanotubes), two-dimensional (layers or thin films).

### 1.2.1 Zero Dimensional Materials

Zero-dimensional (0D) materials are materials that are sized in nanoscale level in all the three dimensions. In 0D materials all electrons are fully confined and cannot escape from the region of negative energies. Quantum confinement suggests that when an electron reaches from the valence band to the conduction band, an electron-hole pair is generated which is known as exciton. The exciton is created in the bulk lattice. The electron and the hole are separated by a distance known as exciton Bohr radius ( $r_\beta$ ). The  $r_\beta$  value depends on the composition of materials. In 0D materials the  $r_\beta$  value is same as magnitude of the diameter (L) of the nanocrystal, due to which the quantum confinement phenomenon arises. In extremely small dimensions the exciton quantum confinement generates discrete energy levels. The discrete energy ( $E_n$ ) for the various nanomaterials is given by the following equation:

For 0D:

$$E_n = \left[ \frac{\pi^2 \hbar^2}{2mL^2} \right] (n_x^2 + n_y^2 + n_z^2) \quad (1.1)$$



$\hbar$  is the Planck's constant,  $m$  is the mass of electron,  $L$  is orbital perimeter and  $n$  is dimensional coordinates.

Due to the confinement effect the bandgap increases effectively.

0D materials maybe amorphous, crystalline, single or poly-crystalline, maybe composed of single or multiple elements. They can have different shapes and forms and can exist in metallic, ceramic or polymeric forms.

### 1.2.2 One Dimensional Materials

One dimensional (1D) materials are nanoscale in size in two dimensions. Some example of 1D materials are nanotubes, nanofibers, nanorods and nanofilaments. The electrons are confined in two dimensions.

The discrete energy ( $E_n$ ) for 1D nanomaterials can be described by

For 1D:

$$E_n = \left[ \frac{\pi^2 \hbar^2}{2mL^2} \right] (n_x^2 + n_y^2) \quad (1.2)$$

### 1.2.3 Two Dimensional Materials

Two dimensional (2D) materials are sized in one nanoscale dimension. Some examples of 2D materials are sheets, layers, platelets.

Electrons are confined in only one dimension. 2D materials are made of various compositions. The discrete energy ( $E_n$ ) for 2D nanomaterials can be given by

For 2D:

$$E_n = \left[ \frac{\pi^2 \hbar^2}{2mL^2} \right] (n_x^2 + n_y^2) \quad (1.3)$$

### 1.2.4 Three Dimensional Materials

Three dimensional (3D) materials are bulk nanomaterials. These materials are not confined to nanoscale dimensions in all level. These materials may have dimensions beyond 100 nm. 3D materials are mainly comprised of nanoparticles, bundles, nanowires and nanotubes. The electrons are not confined in any dimension. In 3D materials ( $r_\beta$ ) is smaller than the overall size ( $L$ ) of the crystal. Consequently, the electron is free to migrate through the lattice, that indicates the detection of continuous energy

bands. The gap between the energy levels is infinitesimally small and hence the bandgap can be considered as a fixed value.

### 1.3 Properties of Nanomaterials

The properties of nanomaterials can be classified as

#### 1.3.1 Physical Properties

- *Ultrahigh surface effect*

With the reduction in the size of the nanomaterial to 1 nm the number of surface atoms are 99 % of the total number of atoms. These atoms have unsatisfied bonds due to lack of neighboring atoms and hence the nanomaterials show high chemical reactivity.

- *Ultrahigh volume effect*

The electrons become more mobile in nanoscale hence materials show low mass, porosity and density.

- *Quantum size effect*

This indicates the increase bandgap with the decrease in size.

#### 1.3.2 Magnetic Properties

Reduction in symmetry at the surface of a thin magnetic layer can lead to a very significant increase in magneto-crystalline anisotropy. If the electrostatic charges acting on the electrons in the magnetic shell of atom  $i$  are centered at the site of the nearest neighbor atoms  $j$  in its environment, a contribution to the anisotropy denoted by  $\omega_{ij}$  can be associated with each atom.

$$\omega_{ij} = k(\cos^2 \phi_j - 1/3) \quad (1.4)$$

where  $\phi_j$  is the angle between the direction of the magnetic moment of atom  $i$  and the vector joining this atom to atom  $j$ . The total surface anisotropy  $E_{SA}$  is given by

$$E_{SA} = \sum_j k \cos^2 \phi_j \quad (1.5)$$

In the nanoparticles of transition metal oxides, it is found that the average magnetization reduces. It is not possible to excite spin waves with wavelength greater than the diameter of the nanoparticles.

### 1.3.3 Thermal Properties

In solids heat is conducted by lattice waves. It is pertinent that lattice defects, grain boundaries will have impact on the thermal properties of nanoscale materials. The thermal conductivity by mobile carriers can be given by:

$$\kappa = \frac{1}{3} C v l \quad (1.6)$$

where  $\kappa$  is the thermal conductivity,  $C$  is the specific heat per unit volume,  $v$  is the speed of mobile carriers and  $l$  is the free path.

The carriers are generated from the electromagnetic or lattice waves with a wide spectrum of frequency. The relation for thermal conductivity and frequency can be expressed as

$$\kappa = \frac{1}{3} \int C(f) v l(f) d(f) v \quad (1.7)$$

where  $C(f)df$  is the contribution to specific heat per unit volume in the frequency interval  $df$ ,  $v$  is the group velocity of the waves,  $l(f)$  is the attenuation length related to frequency.

### 1.3.4 Mechanical Properties

In nanoscale materials owing to the small size the capability to strengthen the defects will increase. This happens in case of nanotubes, which possess extreme mechanical strength. Nanomaterials exhibit high interface to volume ratio, due to which plasticity, toughness and strain increases. The elastic limit of a material is related to the elastic constants of the material. The elastic constants are related to the density of structural defects.

Hardness is a commonly measured mechanical property of nanomaterials. Hardness (H) is the ratio between the load (F) applied to a hard ball and the residual indent (A) that is left on the material after the removal of the load.

$$H = \frac{F}{A} \quad (1.8)$$

The hardness can be related to the yield point ( $\sigma_y$ ) of a material by the following equation

$$H = 3\sigma_y \quad (1.9)$$

The yield point is the point beyond which plastic strain occurs. When stress is applied to a material two types of deformations occurs viz. elastic strain which is irreversible and plastic strain which can have permanent consequences.

Dislocation is another important term included in the mechanical properties of nanomaterials. Dislocation is the boundary in the alignment of two different sheared regions of the order of lattice parameters in the same material. Dislocation is a linear crystal defect.

### **1.3.5 Chemical Properties**

The electronic arrangement and hybridization determine the chemical properties of elements and compounds. Due to high surface to volume ratio in nanoscale materials the ability to form different crystallographic structures and symmetry changes. This alters the binding and catalytic properties of the materials. In nanoscale dimensions the pores can trap and hold or release other materials according to the requirement. In metal nanoparticles as the particle size increases structural changes occur to keep the system in the most favorable energy state. As the size of the particles change the ratio of the number of surface atoms to the total number atoms will change. This will result in the change of number of sites with specific positions on faces, edges and corners. Atoms with lower coordination number in case of monocrystals shows higher reactivity.

The melting point also changes in case of nanostructured materials. According to the Lindemann criterion, bulk material melts when fluctuations in interatomic distances reach 10 % of the lattice parameter.

### 1.3.6 Optical Properties

At the nanoscale the electronic band structure changes and thus the absorption, emission properties change accordingly. A plane electromagnetic wave can induce a polarization in a nanomaterial on which its optical response depends. The intensity transmitted by the nanomaterial with a thickness  $L$  is given by

$$I_t = I_0 \exp(-\alpha L), \text{ with } \alpha(\omega) = 2 \frac{\omega}{c} \kappa(\omega) \quad (1.10)$$

where the function for the complex refractive index can be expressed as

$$\tilde{n} = n + i\kappa = \epsilon^{1/2} \quad (1.11)$$

The surface plasmon resonance is a purely dielectric effect. The surface plasmon resonance originates due to the enhancement of the amplitude of the internal field  $E_i$  due to confinement effect arising in a nanoparticle, with respect to the incident field  $E$ . The incident field generates an oscillation in the electron cloud. The electron density of each cluster oscillates at the optical frequency relative to the lattice ions, creating an oscillating charge at its surface. This charge generates a restoring force and an electric dipole field, which reacts back on the electron motion and the amplitude of the electric field, which gets strengthened at resonance. This oscillation is related to the collective oscillation of an electron gas in a bulk system, the plasmon mode at frequency  $\omega_p$ , modified by the presence of interfaces.

### 1.3.7 Electronic Properties

The wave nature of electrons and lack of scattering electrons are related to the electronic properties of nanoparticles. The electronic properties change with the change in particle size or shape. When the particle size is comparable to the de Broglie wavelength,  $\lambda = h/mv$ , where  $h$  is Planck's constant,  $m$  is mass of the particle and  $v$  is the velocity, discrete

energy spectrum is observed, that leads to the three-dimensional confinement of electrons. Quantum tunneling of electrons takes place where the electrons move through adjacent electrons as the energy barrier is reduced. This leads to increase in the tunneling current.

In 0D materials the electrons are highly confined, as a result the conduction is dependent on other charge carriers. This carrier sensitivity of the charged state is known as "Coulomb blockade effects".

Also, in 0D materials there is no continuous distribution of states which affect the optical and electronic properties of such materials.

In solids the energy levels are grouped in bands which become discrete in confined systems. Due to this reason small metallic clusters exhibit a finite gap between highest occupied molecular orbital (HOMO) and the lowest unoccupied molecular orbital (LUMO).

## **1.4 Graphene and its Derivatives**

In this dissertation the nanomaterial used is graphene oxide, which is a derivative of graphene. Graphene is a single layer of graphite, that consists of hexagonally arranged  $sp^2$  hybridized Carbon atoms in two dimensional (2D) honeycomb structure which attracts a huge attention recently owing to its exceptional mechanical, electronic, thermal properties.[1, 2] Graphene has extraordinary optical and electrochemical properties. It also can adsorb a diversity of aromatic biomolecules through either  $\pi$ - $\pi$  stacking interaction or electrostatic interaction, which makes them a prime material for its applications in the assembly of biosensors and drugs delivery. However, it is difficult to obtain Graphene in pure form that meets all the above-mentioned criteria. It also involves cost factor. But the preparation of graphene oxide (GO) a derivative of Graphene is affordable in the laboratory. GO is an intermediate product which comprises of an abundance of oxygen in the form of hydroxyl, carboxyl, epoxide, carbonyl functional groups attached to the surface of the honeycomb like six-atom carbon rings. The functional groups present in graphene oxide can be readily altered with targeting ligands to realize targeted imaging and drug

delivery.[3, 4] The first application for drug delivery was reported by Liu *et al.*[5, 6] Graphene based materials have been intensively examined in the area of biomedicine and show favorable prospects in this field.[7–9] Three Dimensional Graphene scaffolds have shown the way for regeneration or transplantation of the human tissues as well as of the nervous system, which can lead to effective treatment of neurological disorders like Alzheimer's and Parkinson's diseases.[10]

### **1.5 Mechanical Energy Harvesting Applications of Nanomaterials**

Self-powered devices pose several advantages over traditional battery-operated systems as battery requires replacement or charge replenishment. The miniaturization of portable electronics is a trend in modern days, because miniaturization makes the components easy to carry and hide. However, the miniaturization of batteries is not realized in the same pace as the pace of technological advancements of modern electronics. This leaves a technological space to be occupied for which the nanogenerator seems to be a suitable contender. The concept of nanogenerator was realized by straining a single zinc oxide nanowire (ZnO NW) with the conducting tip of an atomic force microscope (AFM).[11] It was found that the stretched side of the NW developed a positive potential and the compressed side negative potential. This electric potential difference could be used for running low power electronic devices. The nanogenerator suits aptly towards fulfilling the requirement of sustainable, self-sufficient and eco-friendly source of alternative power. Although there are several sources of renewable energy like solar, wind, thermal but most of them are underutilized as they require huge infrastructure and human resource to operate. But there are certain forms of energy that remains in the environment that we live in but goes unnoticed. Mechanical vibrations are present everywhere in the surroundings that we live in. In fact, the human body generates mechanical vibrations from different bodily

processes for e.g. limb movement, blood flow in the vessels, heartbeat, *etc.* It is noteworthy that by tapping these sources of energy implantable medical devices can be realized. Example of some of the implantable medical devices are heartbeat monitors,[12] pacemakers,[13] cochlear implants, implantable sensors to measure heart rate, blood pressure, *etc.*[14] Biomechanical energy harvesting from the human body due to the muscle movements for conversion into electricity is an attractive prospect. The energy conversion can take place by many different mechanisms for *e.g.* piezoelectric effect, triboelectric effect, pyroelectric effect, *etc.* For the efficient conversion of the energy it is expected that the harvesters are flexible and lightweight. Plastic materials are ideal for the fabrication of flexible energy harvesters. Example of some of the plastics that can be used for the fabrication of flexible energy harvesters are polyethylene terephthalate (PET), polyimide (PI) and polydimethylsiloxane (PDMS). It needs to be mentioned that the plastics are only means to suspend the piezoelectric nanomaterials. Recent researchers have reported several piezoelectric material some of them apart from the before mentioned ZnO are BaTiO<sub>3</sub>(BTO),[15] Pb(Zr<sub>x</sub>Ti<sub>1-x</sub>)O<sub>3</sub> (PZT),[16] (1-x) Pb(Mg<sub>1/3</sub>Nb<sub>2/3</sub>)O<sub>3</sub>-xPbTiO<sub>3</sub> (PMN-PT),[17] BiFeO<sub>3</sub>,[18] ZnSnO<sub>3</sub>,[19] GaN.[20] It is noteworthy here that current research trends are based on lead free piezoelectric materials. But these materials are solids and are not stretchable. Some alternatives to make them flexible is through Chemical Mechanical Polishing (CMP) technology and by depositing thin films on flexible substrates.[21] Another approach is to use polydimethylsiloxane (PDMS) which is an elastomer. In this approach the inorganic piezoelectric materials are dispersed homogeneously to make a flexible composite. It is advantageous to use PDMS for body implantable or wearable applications because PDMS is flexible, easily moldable and is bio-compatible, as PDMS is flexible and biocompatible. PDMS based sensor devices can be used for extrinsic applications like measurement of muscle fatigue and intrinsic



applications like measurement of vital parameters including body temperature measurement.[22]

All of the above-mentioned compounds are piezoelectric in nature; however it is interesting to note that non-piezoelectric nanomaterials were not much in trend for use in piezoelectric energy harvesting. Although theoretically it is proved that non-piezoelectric materials can exhibit electrical polarization owing to flexoelectric effect originating due to strain gradient within the crystal, non-piezoelectric nanomaterials found limited usage in energy harvesting applications.[23] It was demonstrated by Karan *et al.* that by incorporating Iron nanoparticle-reduced graphene oxide (Fe-rGO) in polyvinylidene fluoride (PVDF) polymer flexible and efficient piezoelectric energy harvesting can be achieved.[24] PVDF is a synthetic polymer which shows the highest piezoelectricity among synthetic polymers like Nylon-11, polylactic acid (PLLA), poly(lactic-co-glycolic acid) (PLGA). Apart from the advantage of flexibility PVDF shows advantages in terms of thermal stability, chemical resistance, high elasticity, transparency and biocompatibility and easy processability, *etc.* Also, PVDF is light and expensive. The thickness of PVDF film can be varied between 6  $\mu\text{m}$  to 2 mm. PVDF is semi-crystalline polymer. The density of amorphous PVDF is  $1.68\text{ g cm}^{-3}$ . The density of PVDF in melt phase is  $1.45\text{--}1.48\text{ g cm}^{-3}$  at  $230\text{ }^{\circ}\text{C}$  and 1 bar. There are several polymorphs of PVDF that includes five chain conformation. The  $\alpha$ -phase is the most commonly occurring crystalline phase in PVDF that forms while the cooling of PVDF from the melt phase. The density of the  $\alpha$ -phase is  $1.92\text{ g cm}^{-3}$ . The  $\alpha$ -phase shows trans-gauche-trans-gauche (TGTG) chain conformation. This conformation is a combination of helical and planar zigzag structure. The rest of the four phases of PVDF are crystalline phases viz.  $\beta$ ,  $\gamma$ ,  $\delta$ ,  $\epsilon$ . The  $\beta$ -phase is the most desirable phase due to its high  $d_{33}$  coefficient value of  $34\text{ pC N}^{-1}$ . The density exhibited by the  $\beta$ -phase is  $1.97\text{ g cm}^{-3}$ . The  $\beta$ -phase exhibits all trans (TTT) planar zigzag. The  $\gamma$  and  $\epsilon$  phase exhibits  $\text{T}_3\text{GT}_3\text{G}$  chain conformation. The  $\delta$ -phase exhibits TGTG (trans–

gauche–trans–gauche) chain conformation. In the conventional process the  $\beta$ -phase can be induced in PVDF by  $\gamma$  solvent-casting, mechanical stretching of the  $\alpha$ -phase PVDF, and polarization under high electric fields. However, these processes induce micro-scale defects in PVDF and it is also unviable towards industrial manufacture. Such techniques have become outdated and hence there is a shift towards newer approach. Newer approaches include the addition of fillers like BaTiO<sub>3</sub>, clays, hydrated ionic salts, PMMA, TiO<sub>2</sub> and nanostructures (ferrite, palladium, gold and carbon nanotubes) into the polymer in the melt phase, so that films can be made. The mechanism behind the onset of the piezoelectric phases is the electrostatic interaction between positive and negative charge centres with the F and H atoms of PVDF, respectively.[25]

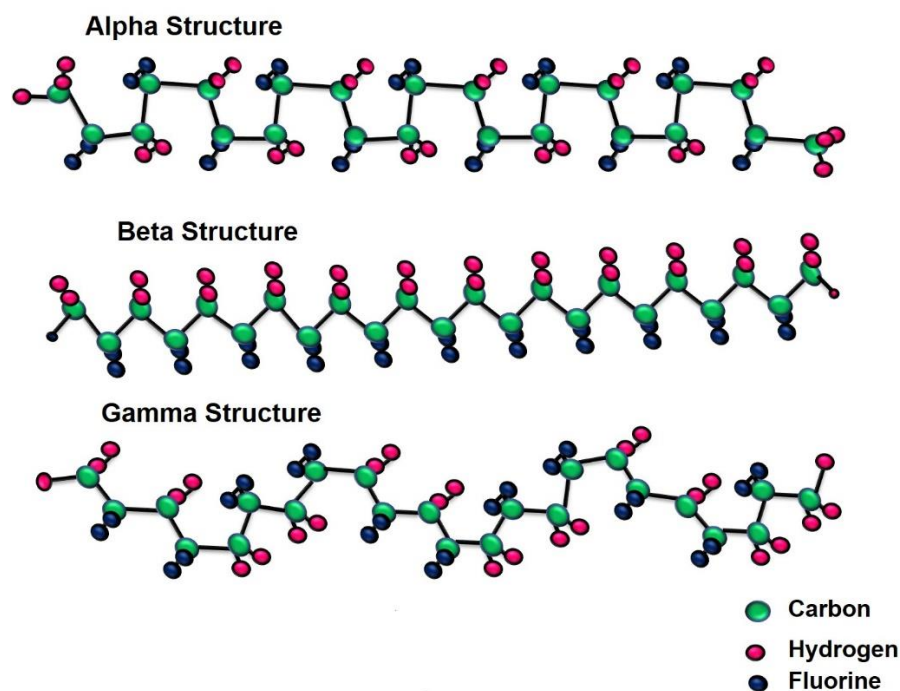


**Figure 1.2** Shows the different chain conformations of PVDF.

## 1.6 Nanogenerator

Nanogenerators mainly use three types of approaches including triboelectric, piezoelectric and pyroelectric. Nanogenerators have added a new dimension to the principles of converting mechanical energy into electrical energy using piezoelectric and triboelectric effects. Additionally,

some devices convert thermal energy into electricity with pyroelectric effect. It was reported that the piezoelectric systems perform better than triboelectric ones.[26] The common trend in nanogenerator research is to realize flexibility in devices. The role of a nanogenerator is to harvest mechanical energy that is present in the environment that gets wasted. The human body is an ideal source of harvesting mechanical energy. Movements originating from limb joints, finger movements, stretching and compressing movements of muscles can be used to harness mechanical energy. Flexibility in the energy harvesting devices is a key issue to efficiently derive mechanical vibrations from these sources owing to their uneven shape dynamics. Polymers, due to their stretchable characteristic and mechanical stability are preferred to produce nanogenerators. Polymers are used by two ways on nanogenerators. In the first way polymers have been used as matrix in nanocomposite generators. In the second way piezoelectric polymers have been used to produce polymeric flexible nanogenerators.[27] Highest output values are approximately 500 V and 5.3 mA for triboelectric nanogenerators;[28] 200 V and 1.5  $\mu$ A for piezoelectric nanogenerators.[29]

#### **1.6.1 Piezoelectric Nanogenerators (PENGs)**

A piezoelectric material when deformed mechanically generates net positive and negative charges across opposite surfaces. In a similar way when a voltage difference is applied across two different surfaces of a piezoelectric material a mechanical deformation takes place.[30] The piezoelectric effect arises due to non-centrosymmetric crystal structure, by which the atoms of the crystals are arranged. In polymers the piezoelectric effect arises due to the presence of opposite poles present in the amorphous regions.[31] The charge difference due to the presence of atoms of different elements in the polymer chains leads to the piezoelectric effect. According to the observation of Fukuda in 1974, the piezoelectric effect in biopolymers arises due to the presence of  $\alpha$  and  $\beta$ -helix arrangement of polymer chains. In bio-polymers the atomic composition is such that that the polymer

backbone is composed of chiral carbon which leads to the formation of electrical gradient.[32] The biggest advantage of the piezoelectric effect is that the electrical energy that is produced can be tapped to run external electrical appliances. The production and operation of the piezoelectric method is possible in both macro and micro dimensions.[33] Unimorph and bimorph type cantilevered beams are some of the simplest forms that are incorporated as piezoelectric nanogenerators. Cantilevered beam type piezoelectric nanogenerators can produce electricity in  $d_{33}$  and  $d_{31}$  piezoelectric production modes where, " $d$ " represents the piezoelectric constant of the material, and "31" or "33" represents the method of polarizing the material. The electrodes are perpendicular to the polarization direction in  $d_{31}$  mode whereas in the  $d_{33}$  mode the electrodes are arranged in the same direction of polarization.

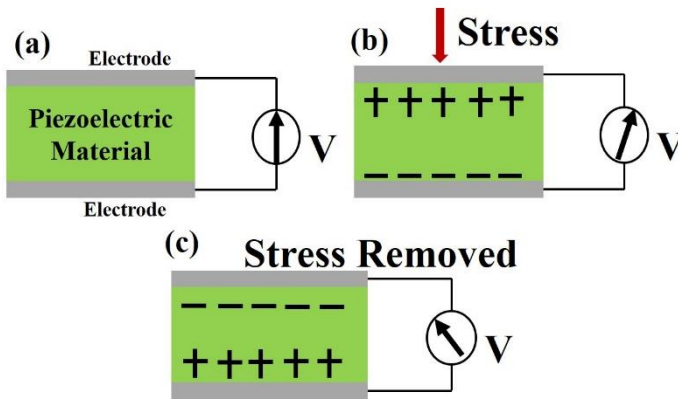


**Figure 1.3** Shows the schematic illustration of operation of PENG (a) at rest (b) under stress (c) when stress is removed.

The output voltage that is generated by the nanogenerator is alternating in nature and hence it must be rectified and stored for future use. To do this an AC-to-DC conversion is necessary. Apart from this, device modeling is also another factor that is related to the device performance. The device modeling is important because the output is dependent on two parameters, first the piezoelectric behavior of the layer and second that the electrical resistance are parallel to the external components.[34] In a nanogenerator piezoelectric nanowires are placed vertically on a conductive

surface. The vertical growth of the nanowires is done by chemical vapor deposition (CVD), inductively coupled plasma (ICP) deposition, and chemical solution methods. In the CVD method before the piezoelectric materials grows on the initiators that are attached to the surface. After that by using high heat the base material of the nanowire is atomized and sent to the surface. The initiators hold the particles on the surface and the nanowires are grown at that point. In the ICP method, like CVD, the piezoelectric material is brought to the vapor phase after that it is passed through an induction coil with a high voltage applied and sent to the surface where nanostructures are grown. In recent studies perovskite-type materials are also reported to be incorporated for nanogenerator application. Perovskites are compounds that have  $ABO_3$  formula. Perovskite shows good dielectric properties hence are preferred for studying nanogenerators.  $BaTiO_3$ ,  $Pb(Zr,Ti)O_3$  and  $(K, Na)NbO_3$  nanocrystals like nanorods, nanowires, nanobelts, *etc.* are most commonly used perovskite piezoelectric materials.[35, 36] These nanostructures were usually synthesized by hydrothermal method and molten salt method. The nanostructure-based nanogenerators have some advantages like mechanical flexibility with minimal defects in their structures, however most of the materials used are expensive because of their difficult and complicated manufacturing conditions. Also, they are brittle and are not efficient in case of large-scale applications due to low power output. In such circumstances polymers having piezoelectric property are good alternatives to the inorganic counterpart. The greatest advantage of piezoelectric polymers is that they bring in flexibility and also, they are suitable for low weight applications. Some of the piezoelectric polymers include PVDF, co-polymers of PVDF, Parylene-C and Amorphous polyimide. The most widely used piezoelectric polymer is PVDF as it has the largest piezoelectric coefficient, which is in the range of  $20\text{-}28\text{ pC N}^{-1}$ . The importance behind the research on piezoelectric nanogenerators is the fact that that it can tap the mechanical energy that gets wasted in the environment, which remains completely

untapped. Apart from that nanogenerators also promise implications on biological detections, environmental monitoring, personal electronics in miniaturized forms. Flexible and collapsible nanogenerators can be used to harvest biomechanical energy by attaching them to muscles or joints and as implanted biosensors. Recently some studies were reported to be based on electrospun PVDF nanofibres/nanofibre mats. However, they have certain disadvantages which are related to low output power due to phase content of PVDF, high electrical resistance and lower surface charge density in and over the nanofibres, respectively.[37, 38]

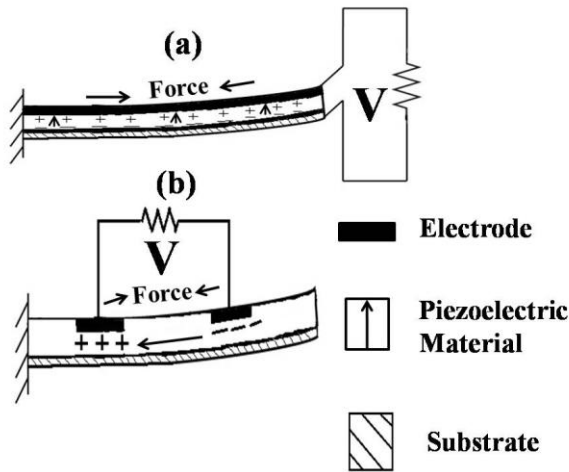


**Figure 1.4** Shows the  $d_{31}$  and  $d_{33}$  piezoelectric designs.

### 1.6.2 Triboelectric Nanogenerators (TENG)

Triboelectric nanogenerators are another kind of nanogenerators where the electricity generation mechanism is based upon the coupling between triboelectric effect and electrostatic induction. The triboelectric effect generates static polarized charges on the material surfaces that are under contact whereas, the electrostatic induction helps the generation of electrical potential from mechanical energy that results from mechanically agitated separation. Some of the advantages of TENG are broad availability of material, light in weight, cost-effectiveness, and high efficiency even at low operation frequency. A TENG can be constructed with any material with distinct charge affinity. Materials existing at the opposite ends of the triboelectric series is preferred for the fabrication of TENG. For example,

polytetrafluoroethylene (PTFE) and silicone are commonly used materials for attaining net negative triboelectric charges while nylon and metal are used for attaining net positive charges. The first TENG device that was demonstrated consisted of a polyester (PET) film and Kapton film with electrodes coated at their back. Figure 1.4 shows the schematic illustration of working of the TENG.[39] The device was operated by changing the contact status between the two films. The device underwent cyclic bending and pressing motion and in this process the device generated AC electrical signal. It is explained that when the two films come into contact under pressing and bending, triboelectric charges are induced on the surfaces. At the instant when the external force is released the charged surfaces are separated from each other due to which an electric potential difference will be built on the two electrodes attached to the films. Now if the electrodes are connected to an external load, charges will flow to counter the generation of the electric field. If the two films come close to each other due to mechanical force the potential difference on the electrodes will change and the current will flow back in the opposite direction. Through this way a continuous AC output can be obtained.[40]

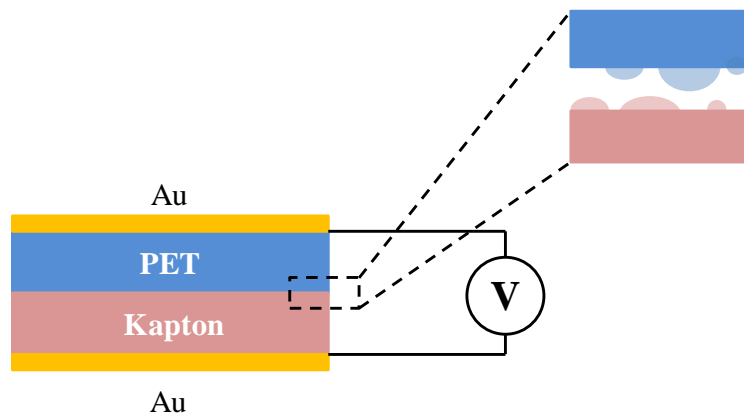


**Figure 1.5** Shows the schematic illustration of TENG.

## **1.7 Anti-microbial Applications of Nanomaterials**

### **1.7.1 Anti-microbial Materials**

Anti-microbial materials are those materials that inhibits the growth of micro-organisms like bacteria, fungi or algae. Anti-microbial agents are classified according to the type of micro-organisms they target. For example, the anti-microbial agents that kills bacteria are known as antibiotics, whereas the anti-microbial agents that kills fungi are known as antifungal agents. The location of existence of the micro-organisms are also of importance. Micro-organisms that live on non-living objects are treated by that class of anti-microbial agents that are known as disinfectants. Antiseptics are those class of anti-microbial agent that are applied to a living tissue to prevent infection in open wounds. Anti-biotics are applied to cure diseases that are caused by micro-organisms that live within a living body. Penicillin was the first antibiotic that was discovered accidentally by Alexander Fleming in 1928. Typically, antibiotics are used when the immune system of the body fails to fight the rapid growth of micro-organisms within it.

### **1.7.2 Anti-microbial Nanomaterials**

Antibiotics are the preferred medicines that are used to treat bacterial infections because they are highly effective and are affordable. Antibiotics target micro-organisms by damaging cell wall formation, or by disrupting translational mechanism and DNA replication mechanism. But micro-organisms can develop resistance against antibiotics. Micro-organisms does this by forming enzymes that counter the effect of antibiotics, by varying the composition of the cell. The advantages that nanoparticles have over antibiotics are that nanoparticles come in direct contact with the micro-organisms and hence micro-organisms have less chance of developing antibiotic resistance. Nanomaterials show anti-microbial effect mainly by three effects viz. oxidative stress, metal ion release, and non-oxidative mechanism.



### 1.7.3 Overcoming Antibiotic Resistance using Nanomaterials

The antibiotic resistance in micro-organisms can be due to two reasons i.e. internal and external. The internal resistance arises due to the spontaneous mutations of the genes within the micro-organisms i.e. micro-organisms develops drug resistant genes. The external reasons behind the antibiotic resistance are related with the biochemistry that is associated with the micro-organism cells and the surface with which they are exposed. Some of the biochemistry related mechanisms of antibiotic resistances are alteration of targets, generation of inactivated enzymes, use of active efflux pump systems, formation of biofilms, presence or absence of certain proteins.

Bacterial biofilms are also breeding grounds for development of mutant species of resistant bacteria. Research has shown that many nanoparticles can destroy the biofilms. Au-based NPs,[41] Ag-based NPs,[42] Mg-based NPs,[43] NO NP,[44] ZnO NPs,[45] CuO NPs,[46] Fe<sub>3</sub>O<sub>4</sub> NPs,[47] are reported to have damaging effect to bacterial biofilms. The destruction of biofilms is achieved by a smaller size and higher surface area-to-mass ratio, and the particle shape of NPs.

The treatment of infections caused by microbial strains with drug resistance is difficult using antibiotics because the antibiotics have poor membrane transport. Drugs of average size thus cannot create any effect on intracellular microbes. Delivering through modified NPs is a solution to this problem. NPs that are loaded with drugs and are used for drug delivery. The small size of the NPs allows them to enter the cell membrane and deliver the drug. NPs have advantages in carrying drugs e.g., the walls of liposomal NPs are composed of one or more lipid bilayers surrounding sphere-shaped NPs.[48] Also the NPs can help to increase the potency of the drugs. Targeted NP-based drug delivery consists of passive targeting or active targeting. Passive targeting is done by enhanced permeation and retention at the infection site, whereas active targeting is done by surface modification of NPs that allows the NP-based drug delivery system to selectively

recognize specific ligands on the cells at the infection site. Some examples of active targeting are receptor targeting, magnetic targeting, and temperature targeting.

#### **1.7.4 Mechanisms of Antibacterial Activity of the NPs**

The NPs need to be in contact with the bacterial cell to show antibacterial activity. The contact of the bacteria with the NPs are based on van der Waal's forces, receptor-ligand and hydrophobic interactions. The NPs then cross the cell membrane and enters the metabolic pathways. After that the NPs interact with the cell components like DNA, lysosomes, ribosomes and enzymes. The changes that are introduced are heterogenous alterations, change in cell membrane permeability, electrolyte balance disorders, enzyme inhibition, protein deactivation and changes in gene expression. The mechanisms by which NPs show anti-bacterial activity are oxidative stress, metal ion release and non-oxidative mechanisms.

##### **1.7.4.1 Oxidative Stress**

Oxidative stress is generated by Reacting Oxygen Species (ROS). The term ROS is used for molecules and reactive intermediates that have strong positive redox potential. The type of ROS varies with by different NPS. Some of the types of ROS are superoxide radical ( $O_2^-$ ), the hydroxyl radical ( $\cdot OH$ ), hydrogen peroxide ( $H_2O_2$ ), and singlet oxygen ( $O_2$ ). The different ROS exhibit different levels of dynamics and activity. The ROS are produced due to restructuring, defect sites, and oxygen vacancies in the crystal.[49] The unbalanced redox states produces oxidative stress in the cells, which damages the individual components of microbial cells.[50] ROS can directly damage the cell membrane, can interact with DNA, can attack proteins and depress the activity of certain periplasmic enzymes that are essential to maintaining normal morphology and physiological processes in bacterial cells.

#### **1.7.4.2 Dissolved Metal Ions**

The metal oxide is the ideal source for metal ions that are released slowly and are absorbed through the cell membrane. Inside the cell the metal ions interact directly with the functional groups of proteins and nucleic acids, such as mercapto ( $-SH$ ), amino ( $-NH$ ), and carboxyl ( $-COOH$ ) groups. This interaction damages the enzyme activity, changes the cell structure, affects the normal physiological processes, and ultimately inhibits the microorganism. Dissolved metal ions have weak antibacterial activity.[51]

#### **1.7.4.3 Non-oxidative Mechanisms**

The non-oxidative antibacterial mechanisms include broken cell membrane and visible pores, no damage to the Lipopolysaccharide (LPS) and Phosphatidylethanolamine (PE). It is found that ROS does not increase but many metabolic processes like amino acid metabolism, carbohydrate metabolism, energy metabolism, nucleotide metabolism are reduced.[52]

### **1.8 Objective and Scope of the Thesis**

The primary objective of the dissertation is based on the synthesis, characterization and application of *rGO*, metal/metal oxide and polymer nanocomposites. Nanomaterials have unique properties due to their extremely small structures. Fe-*rGO* and *rGO*-Ag were synthesized and were incorporated in PVDF to realize piezoelectric application of nanomaterials. PVDF is a piezoelectric polymer, whereby the addition of nanomaterials it was found that its piezoelectricity is enhanced. Also, the energy harvesting application of Au NP-Cellulose/PDMS based nanocomposite is realized. Also, in this work, the anti-fungal application of *rGO*-Ag nanocomposite is shown. According to the available literature, it is known that nanomaterials have various biological applications. It includes fluorescent biological labels, drug and gene delivery, bio-detection of pathogens, detection of proteins, probing of DNA structure, tissue engineering, tumor destruction

via heating (hyperthermia), separation and purification of biological molecules and cells, MRI contrast enhancement, phagokinetic studies.[53] The anti-microbial property of *r*GO-Ag opens the possibility for the development of microbial growth free human body wearable energy harvesting devices.

**The precise objective of the research studies undertaken in this dissertation are as follows:**

1. To synthesize and characterize graphene oxide. To synthesize graphene oxide based on modified Hummer's method.
2. To synthesize and characterize reduced graphene oxide-metal oxide nanocomposite. To develop a suitable technique.
3. To fabricate mechanical energy harvesting devices or nanogenerator by incorporating *r*GO based nanomaterials in PVDF. *r*GO based nanomaterials induce polar piezoelectric phases in PVDF that promises enhanced piezoelectric output voltages.
4. To find out the effect of addition of Au NPs in Au NP-Cellulose/PDMS based nanocomposite. To demonstrate the lighting LEDs and charging capacitors using the nanocomposite-based energy harvesting device.
5. To find out the antifungal application of *r*GO-Ag nanocomposite.

The primary objective of the thesis is to provide solutions to the problem of energy crisis and anti-biotic resistance using nanomaterials. This thesis aims at approaching towards a solution to the above-mentioned modern-day problems by the synthesis, characterization and application of GO-metal oxide nanocomposite-based nanomaterials. While looking to provide solutions to the modern-day problems using nanomaterials some issues that are important to look for are cost effectiveness, safety and efficiency. However, it needs to be mentioned here that the solutions that nanotechnology can provide are not limited to the ones mentioned in this work. Nanotechnology can provide solutions in the fields of disease diagnosis, water purification and desalination, food security etc. In the

Chapter 1 the importance of nanomaterials is introduced along with a brief discussion on the various synthesis techniques and properties of nanomaterials.

GO is a two-dimensional material, that has a layered structure. GO is a precursor to graphene. Graphene has extraordinary properties like high current density, ballistic transport, chemical inertness, high thermal conductivity, optical transmittance, and superficial hydrophobicity on a nanometer scale. These properties make graphene a nanomaterial to be widely studied and explored in the field of novel applications. The layered structure of the nanomaterials contributes to a large surface area, which can be an advantage. The large surface area makes it an ideal candidate to load metal nanoparticles on it. This opens the possibility for the formation of a new compound that shows new properties through mutual interactions. The study of the different properties of the nanomaterials are done using different material characterization techniques which is discussed in Chapter 2.

The objective of the thesis is to develop flexible, PENG device. Although TENGs have many advantages, like high energy conversion efficiency and large output voltage, some of their drawbacks are low durability and large package size. Also, the input impedance of TENG is very high, hence a large proportion of potentially usable power may be wasted due to impedance mismatch.[54] Hence to counter these problems associated with TENG, PENG is a suitable option which not only offers almost equally high performance but are ultra-sensitive, flexible, and sustainable.

Polyvinylidene fluoride (PVDF) which is a piezoelectric polymer is used in this work. PVDF used in this work comes in powder form. It is dissolved in polar organic solvent and casted into a film. The casting is done by pouring the solvent in a petri dish and keeping it in an electric furnace at 110 °C. However, the casting temperature was optimized by preparing PVDF films at different temperatures ranging from 90 °C to 120 °C. After

casting, the films were characterized with Fourier Transform Infrared Spectroscopy (FT-IR). The peaks obtained were compared together as well as with literature. In this way the casting temperature was optimized. PVDF shows several polar piezoelectric phases after they are externally poled. But in this work two different nanomaterials were incorporated viz. Iron-reduced graphene oxide (Fe-rGO) and Carbon nanotubes (CNT) were added to PVDF to induce the self-poling process and to compare the role of the nanomaterial filler that are added. Further, to realize mechanical energy harvesting, a unique device structure was employed in this work. The curved structure of the PVDF film ensured that the finger tapping would cause maximum deformation to the PVDF film thereby ensuring maximum electrical output from the mechanical energy harvesting process. This type of structure is not reported elsewhere.

Chapter 4 is a continuation of the work that is done in Chapter 3. In this chapter the development of a robust mechanical energy harvesting device is attempted that has an enhanced power output. Reduced graphene oxide-silver nanoparticle was incorporated in PVDF to induce the polar electroactive phases in PVDF, eliminating the poling process altogether. The curved structure of the PVDF film was not incorporated as was done in Chapter 3, instead the PVDF film was completely encapsulated by Polydimethylsiloxane (PDMS) which provides mechanical robustness. The PDMS encapsulation ensured that the energy harvesting device can withstand greater mechanical shocks thereby being able to generate greater electrical outputs. The mechanical energy harvester was attached to the hand and electrical voltage is recorded by exciting it with hand movements. It was also attached to a footwear and was excited by footsteps after wearing it. The experimental details and the results that are shown in this thesis can pave way for the development of piezoelectric nanogenerator with greater output power. This could be a step towards providing a suitable solution to the crisis of energy harvesting.

In Chapter 5 Gold nanoparticle (Au NP)-Cellulose/PDMS based nanogenerator is shown. In this work it is found that the presence of Au NPs enhances the piezoelectric output of cellulose. It is found that compared to pure PDMS, the dielectric constant of cellulose/PDMS nanocomposite is higher in magnitude. The nanogenerator could light LEDs and charge capacitors. A touch sensor application of the Au NP-Cellulose/PDMS based nanogenerator is also shown.

In Chapter 6 it is discussed how the synergistic effect of reduced graphene oxide and silver nanoparticle is successful in preventing the growth of pathogenic fungi. It is found that equal weights of graphene oxide and silver nanoparticles individually are not as much effective against the pathogenic fungi as is same quantity of *rGO-Ag*. Several parameters were adjusted to find out the effectiveness of the antifungal activity of the *rGO-Ag* nanocomposite. Fungus belonging to phylum *Zygomycota* were grown on Luria Bertani (LB) Agar plate and were transferred to the plates that were exposed to the nanomaterials. Material characterizations were performed to determine if the *rGO-Ag* nanocomposite that is under consideration is pure in form. This thesis work comprises the results of all the material characterizations that were performed along with other experimental details. The results were studied, compared and are discussed. The characterization results validate the synthesis methods used in this dissertation. The novelty of this thesis work is that although the antibacterial activity of *rGO-Ag* was known, the anti-fungal activity of *rGO-Ag* was not well known until the work that is reported in Chapter 6 of this dissertation. The importance of this finding lies in the fact that human body wearable mechanical energy harvesting devices can be developed that would inherently have anti-microbial properties. The footwear attachable mechanical energy harvesting device as described in Chapter 4 would also have the added advantage of being an anti-microbial growth proof material. Generally, a footwear must withstand sweat from the human skin that may lead to the build-up of microbial colonies around them. The *rGO-Ag*

nanocomposite is the common link between the mechanical energy harvesting application as well as anti-microbial application.

## **1.9 Chapter wise organization of the thesis:**

**Chapter 1: “Introduction”:** This chapter briefly introduces nanomaterials. Further, the classifications and properties of nanomaterials are discussed in this chapter. The anti-microbial applications of nanomaterials are discussed further. The mechanical energy harvesting application of nanomaterials is discussed.

**Chapter 2: “Nanomaterial Synthesis and Characterizations”:** In this chapter the different nanomaterial synthesis methods are discussed. Synthesis methods of various graphene oxide-based nanomaterials are discussed in this chapter, which is followed by a discussion on the synthesis of polymer nanocomposites of graphene oxide and its derivatives. Subsequently this chapter deals with different material characterization techniques.

**Chapter 3: “Synthesis and Study of Self-poled PVDF Polymer Based Nanocomposites for Energy Harvesting Applications with a Unique Arrangement to Tap Piezoelectric Output”:** In this chapter the mechanical energy harvesting performance of PVDF polymer-based nanocomposites are discussed. A unique arch shaped device structure is implemented to compare the energy harvesting performance of Iron reduced Graphene Oxide/PVDF and Carbon Nanotube/PVDF nanocomposites.

**Chapter 4: “Flexible Self-poled rGO-Ag/PVDF Nanocomposite based Piezoelectric Nanogenerator”:** In this chapter the synthesis, characterization and fabrication of Reduced Graphene Oxide-Silver nanoparticle is discussed. The mechanical energy harvesting performance of the fabricated piezoelectric nanogenerator is tested. The nanogenerator showed good efficiency and could charge capacitors, turn on light-emitting diodes.

**Chapter 5: “Piezoelectric-Plasmonic Hybrid Nanogenerator Based on Au NP-Cellulose/PDMS Nanocomposite”:** In this chapter Gold



nanoparticles are synthesized. To fabricate a nanogenerator the Gold nanoparticles are incorporated in Cellulose/PDMS matrix. The mechanical energy harvesting performance of the fabricated nanogenerator is tested. The nanogenerator showed enhanced output voltage and current. The enhancement in the electrical output is attributed to enhancement of the dielectric properties of the nanocomposite. The nanogenerator showed good efficiency and could charge capacitors, turn on light-emitting diodes. A touch sensor application is also demonstrated.

**Chapter 6: “Inhibitive Action of Partially Reduced Graphene Oxide/Silver Nanocomposite on Pathogenic Fungi”:** This chapter deals with the synthesis and characterizations of Graphene Oxide, Reduced Graphene Oxide-Silver nanoparticle nanocomposite. Also, the anti-fungal application of Reduced Graphene Oxide-Silver nanoparticle nanocomposite is shown.

**Chapter 7: “Conclusion and Future Scopes”:** In this chapter the main findings of the previous chapters are described. Also, the probable future scope of the research work that can be done is also discussed.

## References

1. Geim, A.K. *et al.*, (2007). The rise of graphene. *Nature materials*, 6(3), 183–191.
2. Geim, A.K. (2009). Graphene : Status and Prospects. *Science*, 324, 1530–1535.
3. Ostrikov, K. *et al.*, (2013). Plasma nanoscience: From nano-solids in plasmas to nano-plasmas in solids. *Advances in Physics*, 62(2), 113–224.
4. Choi, W. *et al.*, (2010). Synthesis of graphene and its applications: A review. *Critical Reviews in Solid State and Materials Sciences*, 35(1), 52–71.
5. Liu, Z. *et al.*, (2008). PEGylated Nano-Graphene Oxide for Delivery

- of Water Insoluble Cancer Drugs - Supplementary Information. *Journal of the American Chemical Society*, 130(33), 10876–10877.
6. Sun, X. *et al.*, (2008). Nano-graphene oxide for cellular imaging and drug delivery. *Nano Research*, 1(3), 203–212.
  7. Yang, K. *et al.*, (2013). Nano-graphene in biomedicine: Theranostic applications. *Chemical Society Reviews*, 42(2), 530–547.
  8. Zhang, Y. *et al.*, (2012). Graphene: A versatile nanoplatform for biomedical applications. *Nanoscale*, 4(13), 3833–3842.
  9. Shen, H. *et al.*, (2012). Biomedical applications of graphene. *Theranostics*, 2(3), 283–294.
  10. Akhavan, O. (2016). Graphene scaffolds in progressive nanotechnology/stem cell-based tissue engineering of the nervous system. *Journal of Materials Chemistry B*, 4(19), 3169–3190.
  11. Wang, Z.L. *et al.*, (2006). Piezoelectric Nanogenerators Based on ZnO nanowires arrays. *Science*, 312, 242–246.
  12. Zheng, Q. *et al.*, (2016). In Vivo Self-Powered Wireless Cardiac Monitoring via Implantable Triboelectric Nanogenerator. *ACS Nano*, 10(7), 6510–6518.
  13. Zheng, Q. *et al.*, (2014). In vivo powering of pacemaker by breathing-driven implanted triboelectric nanogenerator. *Advanced Materials*, 26(33), 5851–5856.
  14. Zheng, Q. *et al.*, (2017). Recent Progress on Piezoelectric and Triboelectric Energy Harvesters in Biomedical Systems. *Advanced Science*, 4(7), 1–23.
  15. Alluri, N.R. *et al.*, (2015). Flexible, hybrid piezoelectric film ( $\text{BaTi}_{(1-x)}\text{Zr}_x\text{O}_3$ )/PVDF nanogenerator as a self-powered fluid velocity sensor. *ACS Applied Materials and Interfaces*, 7(18), 9831–9840.
  16. Kwon, J. *et al.*, (2012). A high performance PZT ribbon-based nanogenerator using graphene transparent electrodes. *Energy and Environmental Science*, 5(10), 8970–8975.
  17. Hwang, G.T. *et al.*, (2014). Self-powered cardiac pacemaker enabled

- by flexible single crystalline PMN-PT piezoelectric energy harvester. *Advanced Materials*, 26(28), 4880–4887
18. Ren, X. *et al.*, (2016). Flexible Lead-Free BiFeO<sub>3</sub>/PDMS-Based Nanogenerator as Piezoelectric Energy Harvester. *ACS Applied Materials and Interfaces*, 8(39), 26190–26197.
  19. Alam, M.M. *et al.*, (2015). Lead-free ZnSnO<sub>3</sub>/MWCNTs-based self-poled flexible hybrid nanogenerator for piezoelectric power generation. *Nanotechnology*, 26(16) 165403-165408.
  20. Huang, C.Te, *et al.*, (2010). GaN nanowire arrays for high-output nanogenerators. *J. Am. Chem. Soc.* 2010, 132,13, 4766-4771.
  21. Niu, X. *et al.*, (2019). High-Performance PZT-Based Stretchable Piezoelectric Nanogenerator. *ACS Sustainable Chemistry and Engineering*, 7(1), 979–985.
  22. Kim, S. *et al.*, (2018). P(VDF-TrFE) Film on PDMS Substrate for Energy Harvesting Applications. *Appl. Sci.* 8, 213-223.
  23. Catalan, G. *et al.*, (2011). Flexoelectric rotation of polarization in ferroelectric thin films. *Nature Materials*, 10(12), 963–967.
  24. Karan, S.K. *et al.*, (2015). Self-powered flexible Fe-doped RGO/PVDF nanocomposite: An excellent material for a piezoelectric energy harvester. *Nanoscale*, 7(24), 10655–10666.
  25. Sebastian, M.S. *et al.*, (2016). Understanding nucleation of the electroactive  $\beta$ -phase of poly(vinylidene fluoride) by nanostructures. *RSC Advances*, 6(114), 113007–113015.
  26. Sankar Ganesh, R. *et al.*, (2017). Fabrication of the flexible nanogenerator from BTO nanopowders on graphene coated PMMA substrates by sol-gel method. *Materials Chemistry and Physics*, 192, 274–281.
  27. Park, K.I. *et al.*, (2016). Stretchable piezoelectric nanocomposite generator. *Nano Convergence*, 3(1), 1–12.
  28. Han, C. *et al.*, (2015). High power triboelectric nanogenerator based on printed circuit board (PCB) technology. *Nano Research*, 8(3),

- 722–730.
29. Park, K.II, *et al.* (2014). Highly-efficient, flexible piezoelectric PZT thin film nanogenerator on plastic substrates. *Advanced Materials*, 26(16), 2514–2520.
  30. Wang, Z.L. (2007). Nanopiezotronics. *Advanced Materials*, 19(6), 889–892.
  31. Fukada, E. (1968). Piezoelectricity in polymers and biological materials. *Ultrasonics*, 6(4), 229–234.
  32. Liu, Y. *et al.*, (2018). Ferroelectric polymers exhibiting behaviour reminiscent of a morphotropic phase boundary. *Nature*, 562(7725), 96–100.
  33. Wang, L. *et al.*, (2008). Vibration energy harvesting by magnetostrictive material. *Smart Materials and Structures*, 17(4), 045009-045022.
  34. Ottman, G.K. *et al.*, (2003). Optimized piezoelectric energy harvesting circuit using step-down converter in discontinuous conduction mode. *IEEE Transactions on Power Electronics*, 18(2), 696–703.
  35. Cheng, L.Q. *et al.*, (2016). A review on one dimensional perovskite nanocrystals for piezoelectric applications. *Journal of Materiomics*, 2(1), 25–36.
  36. Li, X. *et al.*, (2018). 1D Piezoelectric Material Based Nanogenerators: Methods, Materials and Property Optimization. *Nanomaterials*, 8(4), 188-214.
  37. Pu, J. *et al.*, (2010). Piezoelectric actuation of direct-write electrospun fibers. *Sensors and Actuators, A: Physical*, 164(1–2), 131–136.
  38. Chang, C. *at al.*, (2010). Direct-write piezoelectric polymeric nanogenerator with high energy conversion efficiency. *Nano Letters*, 10(2), 726–731.
  39. Fan, F.R. *et al.*, (2012). Flexible triboelectric generator. *Nano*

- Energy*, 1(2), 328–334.
40. Wu, C. (2019). Triboelectric Nanogenerator: A Foundation of the Energy for the New Era. *Advanced Energy Materials*, 9(1), 1–25.
  41. Yu, Q. *et al.*, (2016). Inhibition of gold nanoparticles (Au NPs) on pathogenic biofilm formation and invasion to host cells. *Scientific Reports*, 6, 26667–26680.
  42. Markowska, K. *et al.*, (2013). Silver nanoparticles as an alternative strategy against bacterial biofilms. *Acta biochimica Polonica*, 60(4), 523–30.
  43. Leung Y.H. *et al.*, (2014) Mechanisms of antibacterial activity of MgO: non-ROS mediated toxicity of MgO nanoparticles towards *Escherichia coli*. *Small*, 10(6), 1171–1183.
  44. Lellouche, J. *et al.*, (2012). Antibiofilm surface functionalization of catheters by magnesium fluoride nanoparticles. *International Journal of Nanomedicine*, 7, 1175–1188.
  45. Baak J.P., *et al.*, (2005). In endometrial hyperplasias, the molecular-genetics and morphometry-based EIN classification more accurately predicts cancer-progression than the WHO94. *Cancer*, 103(11), 2304–2312.
  46. Xu, W.P. *et al.*, (2011). Facile synthesis of silver@graphene oxide nanocomposites and their enhanced antibacterial properties. *Journal of Materials Chemistry*, 21(12), 4593–4597.
  47. Miao, L. *et al.*, (2016). Aggregation and removal of copper oxide (CuO) nanoparticles in wastewater environment and their effects on the microbial activities of wastewater biofilms. *Bioresource Technology*, 216, 537–544.
  48. Chifiriuc, C. *et al.*, (2012). Hybrid magnetite nanoparticles/rosmarinus officinalis essential oil nanobiosystem with antibiofilm activity. *Nanoscale Research Letters*, 7, 1–7.
  49. Qi, G. *et al.*, (2013). Vancomycin-modified mesoporous silica nanoparticles for selective recognition and killing of pathogenic

- gram-positive bacteria over macrophage-like cells. *ACS Applied Materials and Interfaces*, 5(21), 10874–10881.
50. Malka, E. *et al.*, (2013). Eradication of multi-drug resistant bacteria by a novel Zn-doped CuO nanocomposite. *Small*, 9(23), 4069–4076.
  51. Li, Y. *et al.*, (2012). Mechanism of photogenerated reactive oxygen species and correlation with the antibacterial properties of engineered metal-oxide nanoparticles. *ACS Nano*, 6(6), 5164–5173.
  52. Hussein, M.Z. *et al.*, (2014). Synthesis, characterization, and antimicrobial activity of an ampicillin-conjugated magnetic nanoantibiotic for medical applications. *International Journal of Nanomedicine*, 9, 3801–3814.
  53. Salata, O.V. (2004). Applications of nanoparticles in biology and medicine, *Journal of Nanobiotechnology*, 6, 1–6.
  54. Wu, M. *et al.*, (2018). High-performance piezoelectric-energy-harvester and self-powered mechanosensing using lead-free potassium-sodium niobate flexible piezoelectric composites. *Journal of Materials Chemistry A*, 6(34), 16439–16449.

# CHAPTER 2

---

## Nanomaterial Synthesis and Characterizations

---

### 2.1 Introduction

Nanomaterials are materials with particle sizes varying from sub-nanometers to hundreds of nanometers. The scale of one nanometer (nm) can be compared to the length of an elemental atom. Materials in nanometer scale show physical properties that are different from that of the bulk. The study of nanomaterials includes understanding the physical, chemical properties and their other phenomenon and processes. Synthesis of nanomaterials is an important process because this is what determines the dimensions as well as the properties of the nanomaterials. The synthesis of nanomaterials includes "bottom-up" approach. In the "bottom-up" approach, elements or compounds are used for the synthesis of nanoparticles, nanotubes or layered sheets. This approach requires following physical and chemical processes that may require costlier infrastructure. However, it is essential to perform the study of nanomaterials as its importance revolves around solving practical life problems that cannot be addressed by bulk scale materials.

### 2.2 Synthesis of Nanomaterials

The synthesis of nanomaterials can be classified in two ways

- Bottom-up Synthesis
- Top-down Synthesis

#### 2.2.1 Bottom-up Synthesis

The bottom-up synthesis method includes the aggregation and chemical reaction of precursor molecules to form nanostructures through controlled deposition. The methods under this synthesis can be further classified into the following categories.

#### **2.2.1.1 Colloidal Methods**

Here particles are synthesized in the size range from  $10^{-7}$  to  $10^{-9}$  m are suspended in colloidal sol. Thin films can be formed by spin casting or drop casting the colloids.

#### **2.2.1.2 Sol-Gel Synthesis**

Sol-gel method is a wet chemical method to fabricate nanomaterials from inorganic metal salts or metal organic compounds. The key steps in sol-gel synthesis process are hydrolysis, condensation, and gelation, *etc.*

#### **2.2.1.3 Emulsion Synthesis**

Microemulsions are a thermodynamically stable dispersion of two liquids of different phases. There are two types of microemulsions *water-in-oil* and *oil-in-water* emulsion. The nanoparticles are scattered in oil phase and are stabilized by surfactants in the *water-in-oil* microemulsion.

#### **2.2.1.4 Vapor Phase Deposition**

This technique can be classified into physical vapor deposition (PVD) and chemical vapor deposition (CVD). In PVD solid material is converted into gaseous phase by the means of a physical process. Later the gaseous material cools down and is deposited on a substrate. However, in CVD the gaseous species are thermally decomposed at high temperatures ranging from 500 to 1000 °C.

#### **2.2.1.5 Plasma-Assisted Deposition**

In this process the gas atoms are ionized by electrons emitted from heated filament and are deposited on a substrate.

#### **2.2.1.6 Molecular Beam Epitaxy**

Under ultrahigh vacuum thin films are grown epitaxially at a very slow rate.



### **2.2.1.7 Self-assembly Techniques**

Molecular units are organized in reverse process by non-covalent interactions.

### **2.2.2 Top-Down Synthesis**

In top down synthesis bulk particles are broken into smaller particles.

## **2.3 Nano-Material Synthesized in this Dissertation**

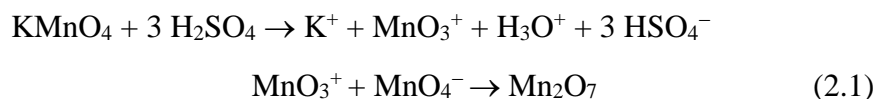
The following nanomaterials were synthesized

1. Graphene Oxide (GO)
2. Reduced graphene oxide (*r*GO)
3. Reduced graphene oxide-silver nanoparticle (*r*GO-Ag)
4. Iron-reduced graphene oxide (Fe-*r*GO)

### **2.3.1 Graphene Oxide**

In this work, graphene oxide was synthesized by modified Hummer's Method. The importance of GO is that it is the simplest precursor of graphene in terms of synthesis and cost. Graphene has extraordinary thermal, mechanical and optical properties which makes it a wonder material. Graphene is a two-dimensional (2-D) sheet of  $sp^2$ -hybridized carbon atoms which are arranged in honeycomb network structure. The amazing features of graphene makes it suitable for a varied range of applications in photonics, electronics, biomedical, and environmental applications. Graphene can play various roles like biosensor, drug carrier, energy storage material, adsorbent, polymer nanocomposite.[1] Graphene can be synthesized by CVD, which is a costly process. Also, graphene can be isolated by the scotch tape method which is not feasible for large scale production. In this regard synthesis of GO and then its reduction to *r*GO is a suitable solution. GO is a derivative of graphene which is also a 2D material and consists of oxygen containing functional groups. The oxygen containing functional groups are carboxylic, ketone, aldehyde groups. The first and foremost attempt to synthesize GO was attempted by B. C. Brodie.

In bulk form GO is also known as graphite oxide. The synthesis process involved chemicals like graphite,  $\text{KClO}_3$ ,  $\text{HNO}_3$ . The C:H:O ratio was 80.13:0.58: 19.29. Later L. Staudenmaier added chlorate and conc.  $\text{H}_2\text{SO}_4$  to the same formula used by Brodie. The advantage to the approach was increase in the C:O ratio to 2:1. Later Hummers and Offeman developed a method, where graphite,  $\text{KMnO}_4$ , conc.  $\text{H}_2\text{SO}_4$ , are reacted together. Permanganate decomposes to form diamanganese heptoxide,  $\text{Mn}_2\text{O}_7$  which is an active species in the synthesis of GO.



The conversion of graphite to GO occurs in three steps.[2]

Step1: Conversion of graphite to sulphuric acid-graphite intercalation compound ( $\text{H}_2\text{SO}_4$ -GIC). Stage 1 GIC forms within 3-5 mins.

Step2: Conversion of GIC to oxidized graphite called as "pristine graphite oxide" (PGO). Slower process may take hours.

Step3: Conversion of PGO to GO.

GO is  $sp^2$  hybridized arrangement of Carbon atoms and hence are electrically non-conductive. The reduction of graphene oxide brings back the original  $\pi$ -networks of the Carbon atoms. The reduction process is achieved through chemical, thermal or electrochemical means. The reduction of graphene oxide to graphene leads to graphene like material which is close to pristine graphene. In the chemical reduction method the direct addition of hydrazine hydrate or sodium borohydride.[3] The thermal reduction process involves heating of GO in furnace. The stacked structure of GO exfoliates at 1050 °C due to the generation of carbon dioxide.[4] In the thermal reduction process 30 % mass reduction of the GO takes place. Structural defects and voids are also generated. These structural defects and voids affect the bulk conductivity of the final product. In the electrochemical reduction method GO is coated on conducting electrodes and electrochemical sweep method is run.[5]

### 2.3.2 Reduced graphene oxide-silver nanoparticle (rGO-Ag)

Silver nanoparticles (Ag NPs) show unique optical, electrical, high electrical conductivity and biological properties. Ag NPs show several interesting biological properties, which includes anti-microbial action, anti-inflammatory, anti-cancer properties. Ag NPs can be synthesized by three methods viz. physical, chemical, biological methods. Spark discharge, pyrolysis, *etc.* are some of the physical methods of synthesis of Ag NPs. Chemical method includes the dissolution of Ag salts in water followed by the addition of capping agents and reducing agents. Biological methods use biological molecules like plant extract as reducing agents in the process of synthesis of Ag NPs.

The application of Ag NPs as antimicrobial agent is found to be safe in rats for therapeutic usage. The effectiveness of Silver against antibiotic resistant microbes is already reported. Ag in the form of Nanoparticles become more effective in this regard, because of the availability of higher number atoms on the surface of the NPs to interact with microbes and studies have confirmed that as size of the NPs increase, its effectiveness against microbes decrease. It is also reported that shape of the Ag NPs also impacts its antimicrobial property. The effectiveness of the Ag NPs was also found to be dose dependent. Ag NPs were also reported to be in application for water decontamination as a first step towards industrial application. However, it is necessary to disperse the NPs as solution to prevent their aggregation for bactericidal applications and for their separation to remove them after treatment. The Ag NPs needs mechanical support that can hold them in suspension for their effective action. Accordingly, previous works shows the immobilization of Ag NPs on SiO<sub>2</sub> matrix as well as onTiO<sub>2</sub> matrix, which are also biocompatible.

In another work it was reported that Ag was coated on carbon nanotubes (CNT) on pyrolytic carbon substrate and its bactericidal properties were studied. However, cost, ease of functionalization and cytotoxicity associated with human cells prohibit the usage of CNT as a

probable replacement for antibiotics. Graphene oxide is an ideal replacement of CNT in such circumstances. The layered structure of GO nanosheets provides enough surface area to load NPs on them. Also, it has good water dispersion property, can be functionalized with ease and shows bio-compatibility. Based on these results previously significant works were carried out to see the antimicrobial effect of GO/rGO-Ag Nanocomposite on species specific microbes.

## **2.4 Nanomaterial-Polymer Nanocomposite Synthesized in this Dissertation**

The development of polymer composites containing nanosized filler has been gaining popularity due to several advantages. One of the main advantages of using nanosized filler is the increased internal interfacial area. This results in maximized polymer-nanoparticles interactions. Addition of nanosized filler has the potential to dramatically improve polymer performances, including thermal and electrical conductivities, mechanical strength and stiffness, thermal stability, as well as flame retardancy. All these performance benefits are available without increasing the density of the base polymer. Factors such as type of nanofiller, size and shape of the nanofiller, volume of the nanofiller in the polymer, selection of polymer matrix and processing condition need to be fully understood because they might influence the properties of the polymer nanocomposites. Furthermore, hybrid nanofillers for polymer composites are gaining acceptance because they offer a range of properties that cannot be obtained with a single type of reinforcement.

By incorporating small volume fractions of electrically conducting fillers in polymer matrices exhibiting poor electrical, magnetic and dielectric magnetic properties. In this regard, nanocomposites represent a special case of composites consisting of dimension of filler in nanometer range in a matrix. Generally, polymer remains the most desirable matrix in these nanocomposites due to its simple processing conditions, corrosion resistance, mechanical flexibility and low density.

When the concentration of electrically conducting particles in a composite exceeds a certain level (percolation threshold), the particles meet each other and form a continuous path for electrons to travel, making it electrically conducting.

The percolation limit depends on the shape of the conducting particles. For example, carbon nanotubes with high aspect ratio can form a conducting network at much lower volume fractions and potentially lower costs than cheaper, traditional fillers such as carbon fibre and carbon black. In the past, a large number of conducting materials, such as graphite, carbon black, CNT, graphene and ICP, have been used as fillers in polymer matrix and investigated for EMI shielding.[6]

Plastic products are compounded with a material known as additives. Addition of additives transforms polymeric materials into more colourful, tougher, stiffer materials which are more resistant towards degradation. There are many types of additives such as filler, reinforcement, colorant, plasticizer, antioxidant and blowing agent. Each of these additives has its own function. The additives can be classified as a reinforcement, active filler and inactive filler depending on the aspect ratio (length/diameter) and compatibility with the polymer matrix. Reinforcement is mostly referred to as long and continuous fibres. It is commonly used in thermoset polymer in uni-directional, 2-dimensional and 3-dimensional fibre arrangements. The long and continuous fibre can be used up to 60 to 70 vol%, which subsequently increases its mechanical properties. Active and inactive fillers are referred to as fillers that are used to improve certain properties of the mixed materials and fillers that are used to lower the compound cost, respectively. These fillers are commonly used in the form of short and discontinuous fibre, flake, and particulate geometry. Depending on the fabrication method, the fillers are arranged in random orientation and produce a product with isotropic properties. Generally, 30 to 40 vol% of these fillers can be used to produce polymer composites. By the appropriate selection of these materials, not only the economics but also the other

properties, such as processing and mechanical behavior, can be improved. Adding fillers to the polymer affects the viscosity as compared to the neat polymer. Generally, by adding fillers, the dimensional stability and stiffness of the products can be improved. Depending on the required properties, types of fillers are normally the first thing to consider when it comes to the materials selection for the fabrication of polymer composite. They can be based on natural and synthetic fillers. Natural fillers are obtained from sources such as mineral, plant and animal. Synthetic filler can be further categorized into organic and inorganic fillers. Examples of synthetic inorganic fillers are synthetic diamond, carbon nanotubes, graphene nanoplatelets, silicon carbide, aluminium nitride and boron nitride. Synthetic organic fillers are commonly based on polymer type of fillers. Addition of organic fillers may affect the flammability and chemical resistance of the mixture. Hybrid fillers can be obtained by combining different filler and reinforcement sources. Addition of conductive fillers in polymer composites for electronic applications is mainly governed by price-performance relationships. Apart from reducing the price of the final material, conductive filler can also help to improve the thermal and electrical conductivities, shrinkage of the molding and stiffness, which are the principle limitations of bulk polymer. For example, to increase thermal conductivity of the composites, heat resistance at the filler-matrix interface needs to be minimized. This resistance results from phonon scattering process. Adding thermal conductive filler with a high aspect ratio, such as carbon nanotube, carbon nanofiber and nanowire, can easily form network structure and increase the thermal conductivity.[7]

**The following nanomaterial-polymer nanocomposite were synthesized**

1. Iron-reduced graphene oxide- polyvinylidene fluoride nanocomposite (Fe-*r*GO/PVDF)
2. Carbon nanotube-polyvinylidene fluoride nanocomposite (CNT/PVDF)
3. Reduced graphene oxide-silver nanoparticle- polyvinylidene fluoride nanocomposite (*r*GO-Ag/PVDF)

## 2.5 Material Characterization Techniques

### 2.5.1 X-Ray Diffraction Spectroscopy

When X-ray falls on a material, different types of interactions occur. Elastic or inelastic scattering of electrons takes place in a material when X-ray falls. Elastic scattering is responsible for the diffraction process (and also known as Thompson scattering) corresponds, where the energy of the incoming and outgoing photons are equal. Inelastic or Compton scattering refers to the case where the energy of the emitted photon is lower than the energy of the incoming photon. The energy difference is transferred to the scattering electron (which can recoil and be ejected from the atom). Elastic and inelastic scattering are used in analysis of materials.[8]

X-Ray Diffraction (XRD) is sensitive to crystalline phases as low as 0.1–1 wt %. Conventional XRD instruments use monochromatic X-ray radiation from Cu, Cr, Mo or Ag sources. Cu has a wavelength of 1.54 Å. When Cu radiation is used, the penetration depth in most of the materials will be several tens of microns (but it may be less for heavy materials such as Pb). The XRD process depends on the incident X-ray beam shape and collimation, and the angle of incidence. Conventional X-ray diffractometers have lateral resolution from 1 to 2 mm (high angle of incidence relative to the sample surface) to a few centimeters. The X-ray beam that is focused can have a diameter of typically 10 to 500 µm.

XRD analysis is dependent on Bragg's law and it is related to concepts of interspacing between atomic planes (“*d*-spacing”) and reciprocal lattice. Bragg’s law can be mathematically demonstrated using both concepts of waves interference in real space and wave vectors in reciprocal space. Bragg's law states that the interplanar spacing *d* can be determined by measuring the angle 2θ between the incident and diffracted directions of the radiation with wavelength λ in a material and *n* is the order of reflection

$$2d \sin\theta = n\lambda \quad (2.2)$$

The Bragg's equation helps to determine the atomic interplanar spacing by measuring the angle from the outgoing diffracted beam that has a fixed incident direction. From the measured angular  $2\theta$  position of the various diffraction peaks observed in a material, the corresponding  $d$  spacing can be determined. The specific set of values of  $d$  can be used to identify the chemistry of the material and its polymorphic phase.

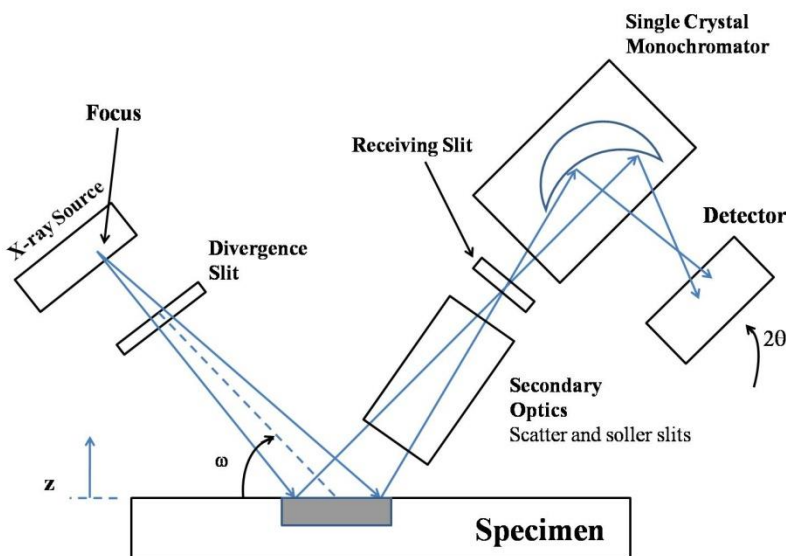


**Figure 2.1** Shows the schematic illustration of working configuration of the XRD instrument.

The X-ray is generated with a specific beam shape and focus by the X-ray source. The primary optics collimates and restricts the size and angular spread of the X-ray beam before reaching the sample to be analyzed). The sample stage is the place where the material which is to be analyzed is placed, which includes options of rotations and translations. The secondary optics collimates and restricts the size and angular distribution of the diffracted X-ray beam. And finally, there is a detector which has a specific sensitivity and resolution to the wavelength/energy being used in the experiment. Often to realize angular measurements, rotation of the detector is done which varies the diffraction angle,  $2\theta$ . Rotation of the sample and/or the X-ray tube to vary the angle of incidence  $\omega$  is also typically employed. The plane including the  $2\theta$  and  $\omega$  rotations corresponds



to the diffraction plane. Sealed ceramic tubes are typically employed as X-ray sources. X-rays are generated in a vacuum tube by electron emission from a Tungsten filament subjected to a high voltage potential relative to a grounded target (typically, a Cu anode). Typical high voltages in the range 20–50 kV and emission currents from 5 up to 50 mA are used. The X-ray beam is extracted from the tube through a Be window and it is then collimated by the primary optics in the instrument. Slits (Soller slits and divergence slits), are used as primary optics which reduces the angular beam divergence in directions perpendicular and parallel to the diffraction plane. Soller slits consist of a series of rectangular plates positioned perpendicular to the diffraction plane and are used to reduce the axial asymmetry of diffraction peaks (which would, otherwise, show shoulders at the low angle side). A divergence slit typically consists of a plate with a central, line-shaped orifice where the beam passes through. The opening of the slit is typically 1–2 mm and the size determines the area of the sample that is irradiated by the beam (smaller slits mean smaller sample irradiated surface area). The divergence slit must be small enough so that at small diffraction angles the X-ray beam still irradiates only the sample area (not outside, like parts of the sample holder). For sample stages in a conventional powder application, for the analysis of materials with fully random grain orientations, a simple sample stand can be used with no sample rotation or translation.

The basic information obtained from XRD Characteristics is summarized as mentioned below:

1. The presence of diffraction peaks indicates that crystalline grains are present. To determine if those peaks are from the same family of planes (parallel to each other), which indicate a highly-oriented material, or from various grain orientations (which is more typical in a powder or polycrystalline sample), indexing of the pattern needs to be performed. Specific software can be used to determine the crystalline structure of the material based on the angular  $2\theta$  position of the observed peaks. Therefore,

the angular position and relative intensity of the peaks are the key parameters used in this “fingerprinting” approach.

2. Peak positions are also used for unit cell determination and refinement, where  $a$ ,  $b$  and  $c$  are unit cell lengths and angles  $\alpha$ ,  $\beta$  and  $\gamma$  can be determined.

3. Relative comparison of peak areas (or in some cases, peak heights) can be used to provide quantitative determination between mixtures (or the various phases present in the sample) and to determine preferred orientation for a specific material.

4. The angular width of the diffraction peaks can be used for peak shape analysis where information about crystallite size, micro-strain and defects in the material can be extracted.

5. The shape of peak “tails” (that is, the shape of the diffraction peak curve at low intensity near the background) can also be used to model and identify diffuse scattering used for point defect quantification.

6. The presence of a broad diffraction feature indicates the presence of an amorphous material. Care must be taken here to ensure that this broad feature is not actually from the material used to hold the sample in the instrument (sample holder). In this example, that broad diffraction feature is from the sample since a low-background sample holder was used for the measurement.

### **2.5.2 Ultra Violet-Visible Spectrophotometry**

Optical spectroscopy is about investigating the properties of materials through their interaction with light. The idea is to measure how much light is reflected, transmitted or absorbed by that material. A material absorbs light when the incident photons create atomic or charge movements in the material. If we measure that absorption as a function of photon energy, we can get an insight into its electronic and atomic structure. The range of Ultra Violet-Visible (UV-Vis) spectrophotometry is 200 nm–3  $\mu$ m. Some of the common modes of its operation are transmittance, diffuse

transmittance, diffuse and specular reflectance, and variable angle specular reflectance.[9]

This is the simplest mode of experiment that one can perform with a UV-Vis spectrophotometer. It consists in measuring how much of a known incident light power ( $P_0$ ) shining on a sample passes through it, as a function of the light wavelength. It can be expressed as a percentage by

$$T = \frac{P_T}{P_0} \times 100 \quad (2.3)$$

where  $P_T$  is the power of the light that made through the sample and  $T$  its transmittance. The light sources do not emit equal intensities of light on all wavelengths. The detector response is a function of wavelength, mirrors, windows, gratings, and other optical components. It is necessary to know how all these factors affect the values read on the detector. These contributions to the spectrum are not originated from the sample and is known as baseline. Besides the contribution to the spectrum due to the baseline, another source of error towards the determination of the absolute transmission is the non-zero response of the detector under dark conditions which is known as the dark current. To quantify the system, baseline of a known sample is measured. To measure the dark current of the detectors, the light path is blocked by using an opaque sample. These quantities may vary slowly with usage of the instrument, so the best approach is to determine them at the time of each measurement. If the sample is in a bulk film form the baseline can be measured by carrying out the measurement without any sample. If the sample has a substrate or a solvent, the baseline measurement is done using a clean piece of substrate or the pure solvent. After measuring the spectrum from a sample, the dark current of the detectors ( $D$ ) is subtracted, then the raw spectrum obtained ( $T_0$ ) is divided by the baseline ( $B$ ), also corrected for the dark current, to determine the contribution solely due to the sample, the absolute transmittance ( $T$ ).

$$T = \frac{T_0 - D}{B - D} \quad (2.4)$$

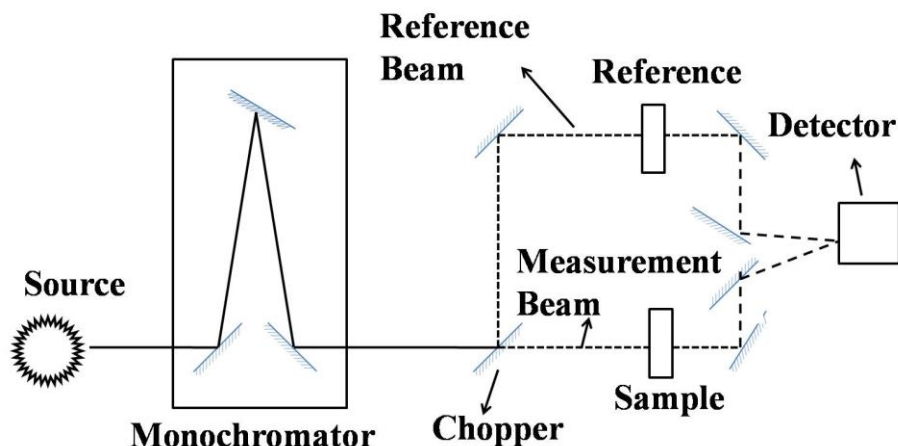


**Figure 2.2** Shows the schematic diagram of dual beam spectrophotometer under operation in transmittance mode.

The absorbance of a sample is calculated from either its transmittance or the reflectance spectra, if all the part of light that is not transmitted is absorbed. The absorbance calculated in this fashion is effectively the attenuation of the light due to the optical density of the sample.

One of the most common uses of spectrophotometry is to quantify the concentration of solutions from their absorbance spectra. The Beer-Lambert law states that the absorbance of a solution is linearly proportional to its concentration  $c$ , and the path length  $l$  of the light in the solution. The proportionality coefficient is the molar absorptivity  $K$ .

$$\text{Absorption} = Kl.c = al \quad (2.5)$$

where,  $a$  is the absorption coefficient

### 2.5.3 Fourier Transform-Infrared Spectroscopy

The photons with energies in the infra-red range of the spectrum interact mostly with phonons and molecular vibrations and rotations, which depend strongly on the material's atomic structure. Thus, Fourier Transform-Infrared Spectroscopy (FTIR) is a useful technique to probe the structural properties of matter. A certain vibration mode needs to create a change on the dipole moment of the material to be active for absorption

(infra-red active), *i.e.* to produce an absorption peak on that material's spectrum.[10]

The FT spectrometer design is based on light interference rather. The FT spectrometer uses a Michelson interferometer with a movable mirror moving at a fixed frequency and directs all wavelengths at once to the detector. The frequency of this mirror's movement is constantly monitored and calibrated using a reference laser. This laser serves also as a real-time wavelength reference which is acquired simultaneously to data collection.

The principle of operation of FT lies on the interference between the light travelling through the two different arms of the interferometer. A monochromatic light beam, with the path difference ( $\Delta$ ) between the two arms of the interferometer is an integer multiple of the wavelength, the beams will interfere constructively and when it is an integer multiple plus half of the wavelength they will interfere destructively and cancel each other. This will generate an oscillatory signal on the detector as a function of time. Different wavelengths interfere differently for given positions of the movable mirror. When monochromatic light passes through the interferometer, it creates an oscillating response on the detector. With polychromatic light, the presence of multiple wavelengths results in a superimposed signal oscillating in time with different frequencies. This combined signal is what we call an interferogram. To recover the frequency domain spectrum, we apply a Fourier transform to the interferogram.

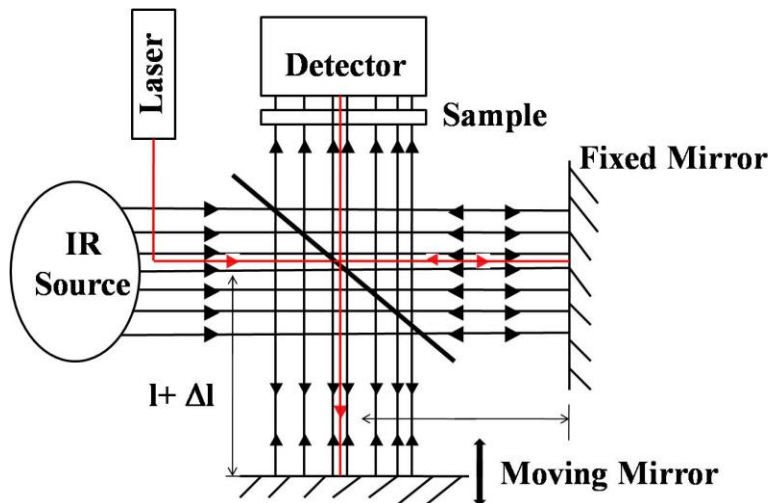


**Figure 2.3** Shows the schematic illustration of the working of the Fourier Transform Spectrometer.

### 2.5.3.1 Attenuated Total Reflection (ATR) Mode

The attenuated total reflection (ATR) mode depends on the total internal reflection in a prism that is in contact with the sample being measured. Total internal reflection takes place when light travelling in a high refractive index material impinges on the interface to a lower refraction index at an angle greater than the critical angle. If the light travels between two different media, it crosses the interface between the media, and it changes its speed and is deflected at an angle related to the angle of incidence according to Snell's law:

$$n_1 \sin \theta_1 = n_2 \sin \theta_2 \quad (2.6)$$

where,  $n_1$  and  $n_2$  are the indexes of refraction of the two media and  $\theta_1$  and  $\theta_2$  are the angles of incidence and refraction. If  $n_1 > n_2$  for a critical angle of incidence  $\theta_c = \arcsin \frac{n_2}{n_1}$ ,  $\theta_2 = \frac{\pi}{2}$  and the light will reflect completely and not cross the interface. The electric field of the light in the second medium decays exponentially. If within the decay distance  $d$  the light is absorbed, this will frustrate the total reflection. This is the principle of the ATR method.

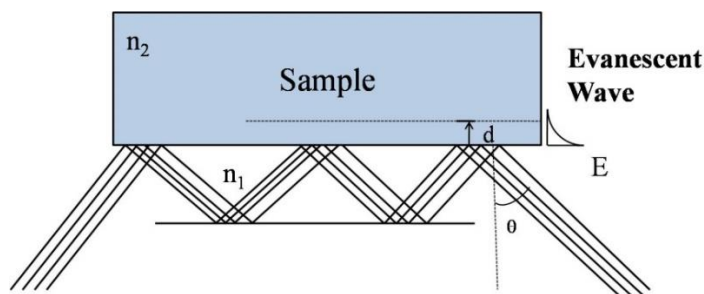


**Figure 2.4** Shows the schematic diagram of the ATR prism.

#### 2.5.4 Raman Spectroscopy

Raman spectroscopy is based upon the fact that when a material sample is illuminated with monochromatic light, in addition to the light scattered elastically (Rayleigh scattering), a small portion of the light is inelastically scattered where its energy is changed. The difference in the energy of the emerging photons with the incident photons correspond to the energy that is absorbed or released by collective vibrations of the atoms in the sample, phonons in solids, normal vibration modes in molecules, liquids or gases. This scattering is known as the Raman effect. Because the vibration levels of a sample are intrinsically dependent on its atomic structure, the Raman effect can be used as an effective tool for structural and chemical characterization, similarly to the IR spectroscopy. The Raman scattering is a very weak effect, that have an intensity 3–5 orders of magnitude weaker than the Rayleigh scattering, which is also about 3–4 orders of magnitude less intense than the incident excitation light beam. Raman scattered photons may present a higher or lower energy than the original incident photons, depending if it gains or loses energy to the vibration modes of the sample. Due to this fact, the Raman spectrum of a sample is composed typically by peaks symmetrically distributed around the central Rayleigh peak. The peaks with energy lower than the Rayleigh peak are termed Stokes peaks. The peaks at a higher energy than the Rayleigh peak are called anti-Stokes peaks.[11]

### 2.5.5 X-Ray Photoelectron Spectroscopy (XPS)

X-ray photoelectron spectroscopy (XPS) is based on photoelectric effect.[12] In the photoelectron emission process, an incident photon of energy  $h\nu$  is absorbed by an atom. With that energy, a photoelectron is emitted with a kinetic energy equal to:

$$KE = h\nu - BE - \phi_{\text{spectrometer}} \quad (2.7)$$

where BE is equal to the binding energy of the electron and  $\phi_{\text{spectrometer}}$  is the work function of the spectrometer. To produce photoelectrons having discrete binding energies, a monoenergetic source of X-rays is necessary. The kinetic energies of the photoelectrons are dependent on the X-ray source energy, hence the photoelectron spectra are presented on a binding energy scale.

$$KE = h\nu - BE - \phi_{\text{spectrometer}} \quad (2.8)$$

By following the process of photoelectron emission, an ion in the excited state is created. The excess energy of this ion is released through a relaxation process in which an electron from an upper shell fills the hole and then either an X-ray photon is released (X-ray fluorescence), or a second electron is emitted (Auger electron emission). In each case, energy is conserved in the relaxation and the X-ray photon or Auger electron is emitted with energy equal to the differences in energies of the orbitals. When plotted on a binding energy scale, the positions of Auger lines will depend on the X-ray source energy. For this reason, X-ray induced Auger spectra are typically presented on a kinetic energy scale. This allows for straightforward comparison with electron induced Auger spectra.

$$KE_{\text{Auger}} = BE_1 - BE_2 - BE_3 \quad (2.9)$$



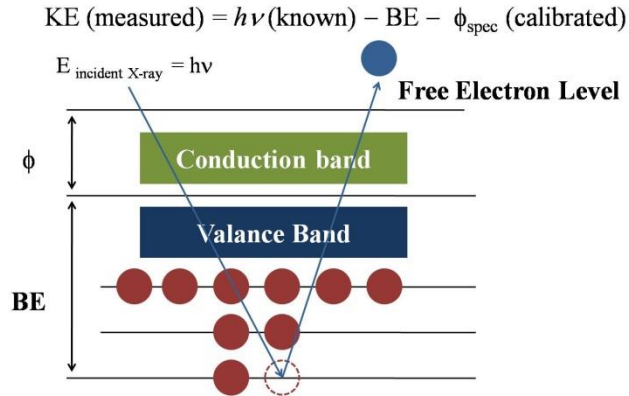


**Figure 2.5** Shows the Photoelectron emission process.

### 2.5.6 High Resolution Transmission Electron Microscopy (HR-TEM)

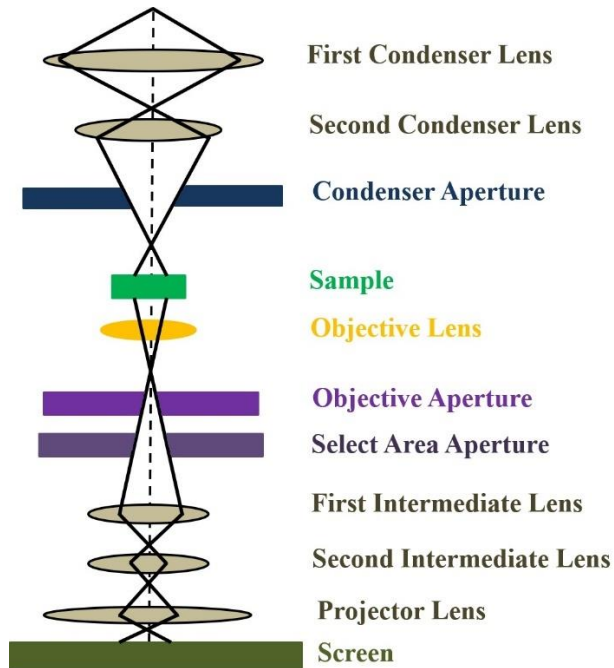


**Figure 2.6** Shows the schematic of the basic components of the HR-TEM.

The schematic of the basic components of the HR-TEM is shown in Figure 2.6. The TEM imaging system is divided into three different parts which are known as the illumination system, objective lens and stage, and imaging system. The illumination system is the part that exists from the top till the sample holder. In the illumination system the sample is illuminated with an incident electron beam. After that comes the objective lens and the

stage. Finally, the TEM imaging system comprises of the intermediate lens and the projector lens.

Unlike photos and neutrons, electrons are charged particles and thus have strong interaction with specimen (atoms) due to the strong Coulomb interaction. When high energy electrons enter a thin specimen, electrons can go through the specimen forming into a transmitted beam. They can also undergo elastic scattering and inelastic scattering. These interactions of high energy electrons with a specimen (atoms) generate signals such as secondary electrons, backscattered electrons, Auger electrons, Bremsstrahlung (continuous) X-rays, characteristic X-rays, visible lights, and electron-hole pairs in the specimen. Some of these signals are used for imaging and composition analysis in TEM. The incident electron beam can be treated as a wave with a certain wavelength determined by the acceleration voltage. When the electron wave travels inside a crystal, most electrons go forward and form the transmitted beam and scattered or diffracted (the Bragg diffraction) and form into diffracted beams. Both transmitted and diffracted beams are elastically scattered and are coherent. When the scattering angle is high, scattered electrons lose coherence.

Electrons travel inside crystal as a wave and the wave is scattered following the law of Bragg diffraction. Depending on crystal structure and orientation of the specimen, the diffraction results in an orientation dependent intensity distribution and thus it can be used to create contrast in TEM images. A diffraction pattern is formed on the back-focal-plane including transmitted beam and diffracted beams. A bright-field (BF) image is obtained by allowing the transmitted beam through an objective aperture to form a TEM image. A darkfield (DF) image is obtained by allowing a diffracted beam to go through.

High-resolution TEM (HRTEM) imaging is a phase contrast imaging technique. This phase contrast originates from the differences in the phase of the electron waves scattered through a thin specimen. In the

two-beam condition, if both transmitted and diffracted beams are selected by the objective aperture, the transmitted and diffracted beams interfere with each other and form a set of lattice fringes perpendicular to the diffraction vector. When the specimen is tilted to a low-index zone axis and multiple beams are selected, fringes corresponding to an array of spots are visible. The spacings of the spots are inversely related to the lattice spacings.[13]

Diffraction patterns provide substantial structural information of samples. There are several advantages of electron diffraction over X-ray crystallography. A small amount of material is good enough for TEM study. The specimen does not need to be a single phase or a single crystal. Multiphase or a polycrystalline powder can be studied by electron diffraction as well. In addition, TEM allows compositional study of phases using Energy Dispersive X-ray Spectroscopy (EDS). These advantages are very important to identify new phases since new phases are typically small amount, multiphase, and with unknown composition. Two famous examples that new structures are identified by TEM are quasicrystal and carbon nanotubes.

Selected-area electron diffraction (SAED) is a basic TEM technique to obtain diffraction information from a part of the specimen. A selected-area aperture is inserted below the sample holder and in the image plane of the objective lens. Only the area selected by the aperture on the screen contributes to the SAED pattern. In case of polycrystalline specimens, if more than one crystal contributes to the SAED pattern, it can be difficult or impossible to analyze. As such, it is useful to select a single crystalline region for analysis at a time. It may also be useful to select two crystals at a time, to examine the crystallographic orientation between them.

### **2.5.7 Scanning Electron Microscopy (SEM)**

A scanning electron microscope consists of an electron gun and a series of electromagnetic lenses and apertures which is shown in Figure 2.7. However, in SEM the electron beam emitted from an electron gun is

condensed to a fine probe for surface scanning. In SEM the electron gun for generating an electron beam is the same as in a TEM. Advanced SEM systems use a field emission gun because of its high beam brightness. Beam brightness plays an important role in imaging quality in SEM. The acceleration voltage for generating an electron beam is in the range 1–40 kV, which is about one order of magnitude less than that for a TEM. In SEM optical path goes through several electromagnetic lenses, including condenser lenses and one objective lens. The electromagnetic lenses in a SEM are for electron probe formation, not for image formation directly as in a TEM. The condenser lens reduces the crossover diameter of the electron beam; then, the objective lens focuses the electron beam as a probe with a diameter on the nanometer scale. The SEM lens system demagnifies the electron beam by about 10,000 $\times$  for a thermionic source and 10–100 $\times$  for a field emission source.

When high-energy electrons strike a specimen, the electrons are scattered by atoms of the specimen. Electron scattering results in a change of direction of travel of electrons under the specimen surface. The interaction between electrons and specimen atoms occurs within a certain volume under the specimen surface. Both scattered electrons (SE) and back scattered electrons (BSE) generated by scattering are used as signal sources for forming SEM images. However, SEs and BSEs, which are collected by a detector, escape from different locations in the specimen. The zone is usually described as pear-shaped, which is shown in Figure 2.8. The size of the zone increases with the energy of incident electrons in the probe. Besides SEs and BSEs, characteristic X-rays are also produced in the interaction zone, and these are useful for chemical analysis.[14]

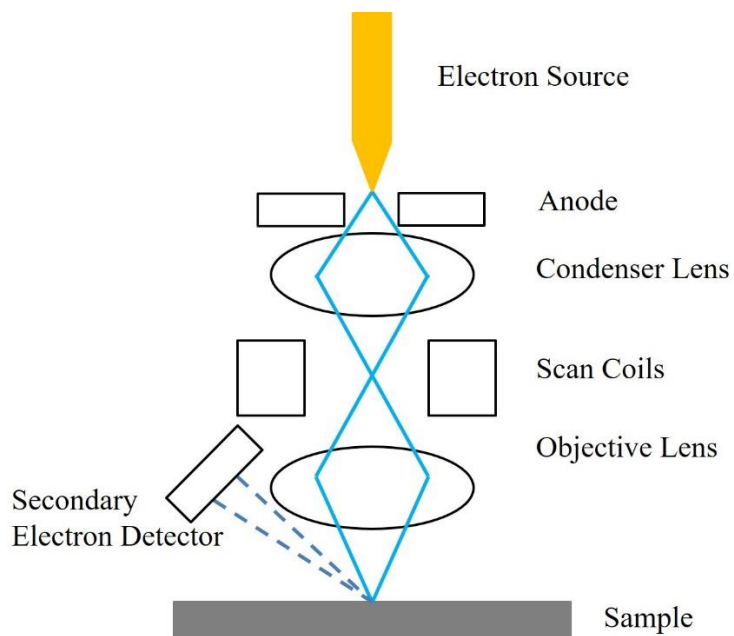


**Figure 2.7** Shows the schematic of the basic components of the SEM.

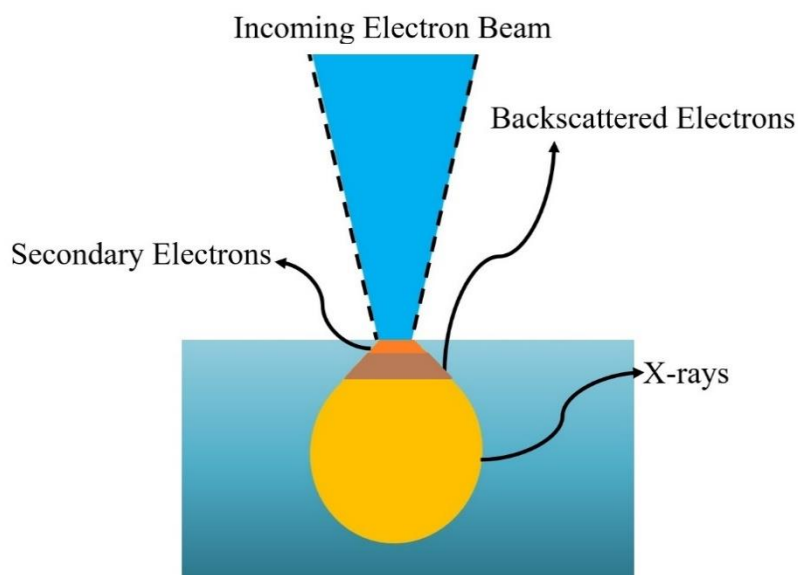


**Figure 2.8** Shows the schematic of the different signals used by the SEM and the areas from which they originate.

## 2.6 Summary

In this section we have discussed that the field of nanomaterial synthesis is broad and dynamic. The synthesis process is broadly characterized into two processes bottom-up process and top-down synthesis

process. The bottom-up process consists of Colloidal Methods, Sol-Gel Synthesis, Emulsion Synthesis, Vapor Phase Deposition, Plasma-Assisted Deposition, Molecular Beam Epitaxy, Self-assembly Techniques. In top-down synthesis process large particles are broken into finer pieces.

Characterization techniques are used in materials science by which material's structure and properties are probed and measured. Characterization techniques are necessary for the scientific understanding of materials. When a nanomaterial is synthesized it is necessary to inspect the quality of the material through characterizations techniques. Identification of the proper phase of the nanomaterial is done by comparing the present data with the data that is available in literature and database. Also, during nanomaterial synthesis identification of a new material is done when two or more entities in the form of elements or compounds are reacted together is also done by characterization techniques. Generally, characterization techniques inspect the physical and chemical properties of nanomaterials.

## References

1. Lee, X.J. *et al.*, (2019). Review on graphene and its derivatives: Synthesis methods and potential industrial implementation. *Journal of the Taiwan Institute of Chemical Engineers*, 98, 163–180.
2. Dimiev, A.M. *et al.*, (2014). Mechanism of graphene oxide formation. *ACS Nano*, 8(3), 3060–3068.
3. Guex, L.G. *et al.*, (2017). Experimental review: Chemical reduction of graphene oxide (GO) to reduced graphene oxide (rGO) by aqueous chemistry. *Nanoscale*, 9(27), 9562–9571.
4. Mcallister, M.J. *et al.*, (2007). Single Sheet Functionalized Graphene by Oxidation and Thermal Expansion of Graphite. *Chem. Mater.*, 19, 4396–4404.
5. Sundaram, R.S. *et al.*, (2008). Electrochemical modification of graphene. *Advanced Materials*, 20(16), 3050–3053.
6. Chung, D.D.L. (2001). Electromagnetic interference shielding

- effectiveness of carbon materials. *Carbon*, 39(2), 279–285.
7. Teng, C.C. *et al.*, (2011). Synergetic effect of hybrid boron nitride and multi-walled carbon nanotubes on the thermal conductivity of epoxy composites. *Materials Chemistry and Physics*, 126(3), 722–728.
  8. Kauffman, H.S. *et al.*, (1954). X-Ray Diffraction. *Anal. Chem.*, 26,1, 31-34.
  9. Bigio, I.J. *et al.*, (1997). Ultraviolet and visible spectroscopies for tissue diagnostics: fluorescence spectroscopy and elastic-scattering spectroscopy. *Phys. Med. Biol.*, 42, 803-814.
  10. Schmitt, J. *et al.*, (1998). FTIR-spectroscopy in microbial and material analysis. *International Biodeterioration & Biodegradation*, 41(1), 1-11.
  11. Malard, L.M. *et al.*, (2009). Raman spectroscopy in graphene. *Physics Reports*, 473, 51-87.
  12. Watts, J.F., Wolstenholme, J., (2003) An Introduction to Surface Analysis by XPS and AES, second ed. J. Wiley, New York, pp. 1-10 (0470847123).
  13. Williams, D.B., Carter, C.B., (2009) Transmission electron microscopy: a textbook for materials science, second ed. Springer, New York, pp. 216-235 (9780387765006).
  14. Goldstein, J., *et al.*, (2003) Scanning Electron Microscopy and X-ray Microanalysis, third ed. Springer, pp. 167-181 (0306472929).





## CHAPTER 3

---

### **Synthesis and Study of Self-poled PVDF Polymer Based Nanocomposite for Energy Harvesting Applications with a Unique Arrangement to Tap Piezoelectric Output**

---

#### **3.1 Overview**

In this chapter we discuss the mechanical energy harvesting application of metal oxide/graphene oxide nanocomposite. It is already discussed previously that nanomaterials show properties that are different from the bulk. Hence, the possibility of exploring the hidden potential of nanomaterials to solve the current problems that mankind faces today is a welcome proposition. With the miniaturization of portable electronics, electronic devices that used to come in large sizes have turned smaller and smaller. All electronic appliances that were popular twenty years back are available in much smaller sizes today for e.g. mobile phones, digital cameras. The above-mentioned miniaturization also requires existence of power sources that are small to run the electronic devices. But batteries require charge replenishment, maintenance and show size concerns. The world looks beyond to find convenient sources to power the batteries. Several attempts were made to find out alternatives to the batteries. The ideal alternative is to develop such a mechanism with the help of nanotechnology to generate power by itself.[1, 2] A piezoelectric material that accumulates charge on the application of mechanical energy can be a probable alternative to provide solution to such a challenge. Piezoelectric materials exist either in the natural (like berlinite, quartz, topaz) or synthetic form (like  $\text{BaTiO}_3$ ,  $\text{PbTiO}_3$ , lead zirconate titanate (PZT),  $\text{ZnO}$ , poly(vinylidene fluoride) (PVDF) etc.). Among all of them we have

selected PVDF as a host material to incorporate nanomaterial into it to harvest mechanical energy. PVDF is flexible, malleable, lightweight, stretchable as well as biocompatible. PVDF has found application in electrical energy harvesting from kinetic energy, to realize low power electronics.[3] The appearance of piezoelectricity in PVDF was shown by Heiji Kawai in 1969. PVDF films were stretched several times of their original length and the poling process was done by the application of a static electric field of 300 kV/cm.[4]

Graphene, which is a single layer of hexagonally arranged  $sp^2$  hybridized carbon atoms, has many fascinating properties like high electron mobility, high thermal conductivity, high thermal stability, large surface area as well as excellent mechanical strength.[5, 6] The work in this chapter revolves around enhancement of the various properties of PVDF. Also, it is well known that graphene has several important properties like high electron mobility, high thermal conductivity, high thermal stability, large surface area, excellent mechanical strength. Using these properties of graphene by incorporating them in the polymer matrix, desired properties of PVDF can be observed. However, a polymer composite of graphene-based material faces several other challenges. Graphene comprises of single layer of hexagonal carbon atoms with  $\pi$ - $\pi$  bonds, which leads to the stacking of the sheets among themselves. Interfacial slippage is another problem which arises due to externally applied stress occurring from poor interaction between the graphene sheets and polymer matrix. To prevent poor interaction between polymer and graphene, functionalization of graphene is a promising method. Functionalization of graphene sheets comprises of addition of functional groups to graphene basal plane. Oxidative functionalization of graphene to form graphene oxide is an easy way to functionalize graphene. In graphene oxide the oxygen containing functional groups are attached to the carbon atoms, which binds with the polymer atoms resulting in better graphene oxide and polymer interaction. But the addition of functional groups renders poor electrical conductivity within the

graphene sheets which arises due to  $sp^3$  hybridization in graphene oxide. To realize the excellent electrical and mechanical properties of graphene, graphene oxide is reduced to form reduced graphene oxide (rGO).[7] Previous reports have shown that the interaction between rGO and PVDF is homogeneous and strong.[8]

The addition of conductive filler changes the permittivity of the polymer matrix. It is previously shown that the addition of graphene-TiO<sub>2</sub> (GT) hybrid sheets enhances the permittivity and decreases the dielectric loss in a polymer nanocomposite.[9] Permittivity is the ability of the medium to permit electric field lines. The permittivity of polymer increases due to the addition of conductive fillers as it reaches the percolation threshold. The percolation threshold is the theory of formation of interconnected pathways within a random system. The permittivity increases due to the formation of microcapacitor networks within the polymer matrix. A microcapacitor is formed when conductive particles are covered by dielectric polymer layer. However, they are not perfect capacitors but are modeled as a resistor and a capacitance in parallel. Dielectric loss is the property of a material by which it loses energy e.g. heat. The dielectric loss occurs when a large leakage current flows through the conductive pathways within the polymer matrix. Addition of conductive filler within the polymer matrix enhances the number electrical contacts which in turn reduces the number of microcapacitors, consequently the permittivity also reduces. Microcapacitor in GT hybrid sheets are formed in this way, the graphene sheets act as electrodes whereas the TiO<sub>2</sub> nanorods behave as dielectric, that prevents the direct contact between the graphene sheets. It is reported recently that addition of graphene-silver (GAg) in PVDF enhances the dielectric permittivity.[10] The existence of an electrostatic component and tensile stress is reported previously between graphene oxide and polymer that resulted in enhanced piezoelectric output.[11, 12]

Piezoelectricity in PVDF originates due to the nucleation of specific

polar crystalline phases. The  $\alpha$ -phase is the dominant crystalline phase in PVDF, which is a non-polar phase. Whereas customarily  $\beta$  and  $\gamma$ -phases show piezoelectric effect. The piezoelectric effect originates in PVDF because of the strong dipole moment of the PVDF monomer unit. Among the two other phases  $\beta$  phase shows highest dipole moment per unit cell. In order to introduce  $\beta$  phase from parent  $\alpha$ -phase there are several techniques like mechanical stretching, high pressure, external electric field, ultra-fast cooling or by the addition of nucleating fillers like hydrated ionic salts, polymers or nanomaterials.[13] It was shown by Alamusi *et al.* that piezoelectric  $\beta$  phase is induced in PVDF due to the addition of reduced graphene oxide.[14] Layek *et al.* reported that addition of poly(methyl methacrylate)-functionalized graphene nanocomposite, resulted in the induction of crystalline  $\beta$  phase in PVDF.[15] It was reported recently by Karan *et al.* that by the addition of Iron-reduced graphene oxide (Fe-*r*GO) in PVDF the nucleation and stabilization of polar  $\gamma$ -phase takes place.[16] Apart from Fe-*r*GO it is also found that the addition of CNT nucleates the  $\beta$  phase in PVDF.[17] The large aspect ratio, low molecular weights, excellent mechanical strength, high electrical and thermal conductivity properties of CNTs makes it an ideal material to be incorporated in polymer. [18-20]

Due to the advantages of CNT and Fe-*r*GO as discussed earlier they are used as fillers in this work and CNT/PVDF nanocomposite and Fe-*r*GO/PVDF nanocomposite are synthesized. In this work the energy harvesting behavior of the nanocomposites are studied by constructing a unique device structure. The device was excited by finger tapping. Material characterizations showed the enhancement in the piezoelectric phases due to the addition of the fillers in PVDF. Electrical characterizations showed an enhancement in the output voltages as compared to previously reported work.[16]

## **3.2 Results and Discussion**

### **3.2.1 Material Synthesis**

All the chemicals were purchased from Merck, India.

#### **3.2.1.1 Synthesis of Graphene Oxide**

Graphene Oxide was synthesized by modified Hummer's Method. A 0.5 mg/ml of GO dispersion was prepared with De-ionized (DI) water.[21, 22] Initially, 1g of Graphite Powder, 1g of Sodium Nitrate and 50 mL of Sulphuric Acid were put in a round bottom flask and were stirred in an ice bath for 30 minutes. After some time 6g of Potassium Permanganate was slowly added to the flask at 0°C and stirred. After 30 minutes the round bottom flask was transferred to water bath maintained at 40°C and stirred for 1 hour. Later 100 mL of De-ionized (DI) water was added to the flask and the temperature of the water bath was slowly raised to 95°C. After 30 minutes the solution was diluted by 200 mL DI water. 1 hour later Hydrogen Peroxide was added. After the addition of Hydrogen Peroxide the colour of the solution changed from brown to yellow. The final solution was filtered. The filtrate was dispersed in water and subsequently the solution was centrifuged to separate out lighter GO particles. The lighter GO particles were again centrifuged. This time the supernatant was discarded, and the colloidal precipitate was collected and dispersed in DI water. Finally, this solution was sonicated to obtain completely exfoliated graphene oxide.

#### **3.2.1.2 Synthesis of Fe-reduced graphene oxide (Fe-rGO)**

100 ml of GO suspension was mixed with 1 g of Fe powder and after that 20 ml of HCl was added into it. Then the suspension was stirred for 1 hour, which was followed by sonication for 1 hour. After that the sample was washed by centrifugation method to obtain clean Fe-rGO, which was dried to obtain a powder form. After that, a dispersion of 1 mg/ml of Fe-rGO in DMF was prepared.[23]

### 3.2.1.3 Synthesis of Fe-rGO/PVDF Nanocomposite film

To dissolve PVDF in DMF 1 g of PVDF was added to 10 ml DMF. The mixture was stirred by keeping it at a temperature of 90 °C. After the PVDF dissolves completely in DMF a thick transparent suspension was formed. Then 20 ml of Fe-rGO/DMF suspension is added to it. The mixture was stirred for 1 hour at same conditions, followed by sonication for another 1 hour, to ensure complete mixing of Fe-rGO and PVDF. The mixture was transferred to a petri dish of 10 cm diameter and kept in a furnace at 110 °C for 24 hours for complete removal of DMF.[16]

### 3.2.1.4 Synthesis of CNT/PVDF nanocomposite film

To dissolve PVDF in DMF 1 g of PVDF was added to 10 ml DMF. The mixture was stirred by keeping it at a temperature of 90 °C. After the PVDF dissolves completely in DMF a thick transparent suspension was formed. Within it 20 ml of CNT/DMF suspension was added (1 mg/ml). Which was followed by similar treatment as is explained in the synthesis procedure of Fe-rGO/PVDF nanocomposite.

### 3.2.2 Device fabrication

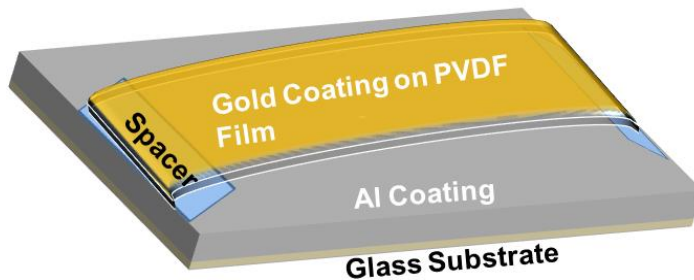


**Figure 3.1** Shows the diagram of the piezoelectric device under consideration that is used for energy harvesting.

Figure 3.1 shows the schematic diagram of the device used for energy harvesting. To realize the energy harvesting application harmonic finger tapping was applied on top of the arched PVDF film, which was coated with gold on the top. Finger excitation was previously reported to be used for energy harvesting applications.[16, 24-26] The arch was designed

and fabricated in such a way so that the film could revert back to its original position after the finger impact was removed. The arch shape of the device was maintained by connecting each end of the PVDF film to a double-sided tape which was connected to a glass slide. While the fabrication of the arch it was ensured that the arch does not touch the glass slide under any condition when the device is not excited. The glass substrate that were used had dimensions of  $75 \times 25 \text{ mm}^2$ . The dimensions of the piezoelectric film used were  $80 \times 25 \text{ mm}^2$ . An additional length of 5 mm was kept with the film so that the natural arch was formed with the double-sided tape. Similar type of arrangement for mechanical energy harvesting was reported previously.[27, 28] Gold was chosen as an electrode because it is not chemically reactive and it does not tend to penetrate inside the polymer surface, unlike Aluminium. The reason behind this was the fact that the atomic radius of Gold is more compared to Aluminium and due to this reason the penetration of Gold within PVDF will be less as compared to Aluminium.[29] Aluminum was sputtered on the glass slide, which was used as the bottom electrode. It is expected that the bottom electrode surface will be exposed to greater mechanical stress, hence to counter the problem the thickness of the Aluminium electrode was kept thick as compared to the top electrode. Under such circumstances keeping cost-effectiveness in the view, the idea to use Aluminium metal is a better proposition.

### 3.2.3 Material Characterizations

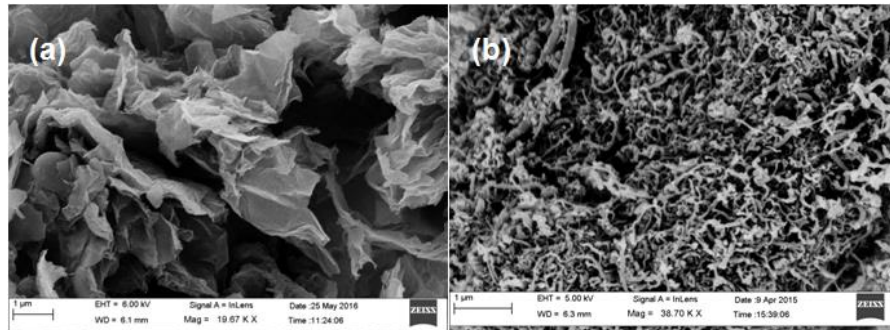
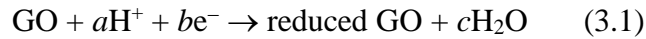


**Figure 3.2** Shows the SEM Image of (a) Fe-rGO (b) CNT.

As seen in Figure 3.2 (a) the SEM image exhibits wrinkled, crumbled and corrugated morphology of Fe-*r*GO. The corrugations in the two-dimensional graphene sheets are attributed to the bending of the two-dimensional graphene layers in the process of becoming thermodynamically stable.[30, 23] Figure 3.2 (b) shows the SEM image of CNTs with long tube-like structures.

In the synthesis process of Fe-*r*GO, Fe powder and HCl are used as mentioned before. The  $H^+$  ions react with Fe powder to produce  $Fe^{2+}$  with the addition of HCl. The  $Fe^{2+}$  ions adsorb the GO sheets. The reduction of GO becomes easy due to the fast electron transport from Fe/ $Fe^{2+}$  to the GO sheets, which happens while the GO sheets cover the surface of the Fe particles.[23] Fe (II) and Fe (III) valence forms of Fe ions remains trapped between the GO sheets in the Fe-*r*GO.[16]

The reduction process is expressed in the following equation:



The GO sheets after adsorbing on the surface of the positively charged Fe particles forms spherical structures, which is indicated by SEM image as shown in Figure 3.3.

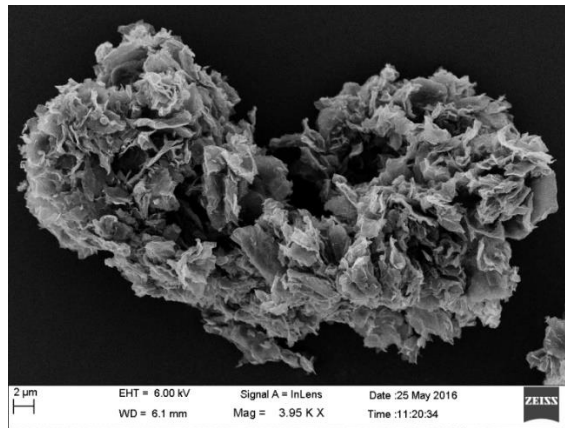


**Figure 3.3** Shows the FE-SEM Image of Fe-*r*GO.

The spherical structures can be identified from SEM images only with lower magnification. The 2-dimensional graphene layers form the spherical structures as shown in Figure 3.3 retaining their wrinkled, crumbled and corrugated morphology by staying closely adsorbed around



the Fe particles. Similar spherical structures of *r*GO were formed during the synthesis process of Fe-*r*GO as was reported by Fan *et al.*[23]

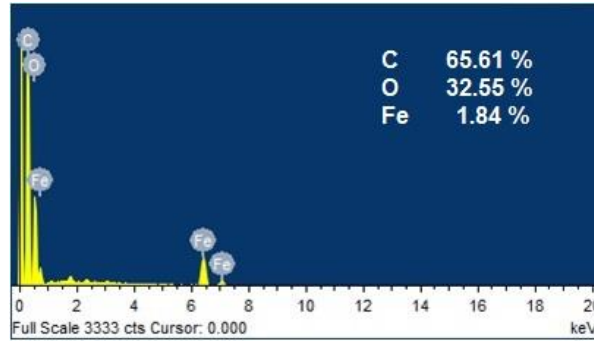


**Figure 3.4** Shows the EDS data which shows the compositional analysis in atomic percentage of Fe-*r*GO.

Energy Dispersive X-ray Spectroscopy (EDS) was used to find out the composition of Fe-*r*GO, which is shown in Figure 3.4. The presence of carbon, oxygen and iron are 65.61 %, 32.55 %, 1.84 % by atomic percentage in the Fe-*r*GO sample.

The presence of non-polar  $\alpha$ -phase and polar, both  $\beta$  and  $\gamma$ -phase of PVDF nanocomposite is confirmed by Attenuated total reflectance-Infrared Spectroscopy (ATR-IR). The ATR-IR spectra of the CNT/PVDF, Fe-*r*GO/PVDF and neat PVDF nanocomposite are shown in Figure 3.5. The peaks at 764, 796, 976, 1149, 1210  $\text{cm}^{-1}$  corresponds to the non-polar  $\alpha$  phase. The  $\alpha$ -phase peak at 764  $\text{cm}^{-1}$  is prominent in neat PVDF, whereas is less prominent in Fe-*r*GO/PVDF and almost disappears in CNT/PVDF. The 1274  $\text{cm}^{-1}$  peak that belongs to the  $\beta$ -phase is visible in both the nanocomposite films but is not present in neat PVDF. The presence of peaks at 832 and 1234  $\text{cm}^{-1}$  belongs to the  $\gamma$ -phase. The  $\alpha$ -phase peak that is present at 796  $\text{cm}^{-1}$  is properly visible in pure PVDF and gets reduced in Fe-*r*GO/PVDF nanocomposite and becomes completely invisible in CNT/PVDF nanocomposite. The peaks present at 976, 1149 and 1210  $\text{cm}^{-1}$  are considerably diminished in the PVDF nanocomposite films but are present in pure PVDF. The infrared spectroscopy data analysis indicates

that electrically active phases are present in Fe-*r*GO/PVDF as well as in CNT/PVDF nanocomposite films.[13, 16, 31, 32]

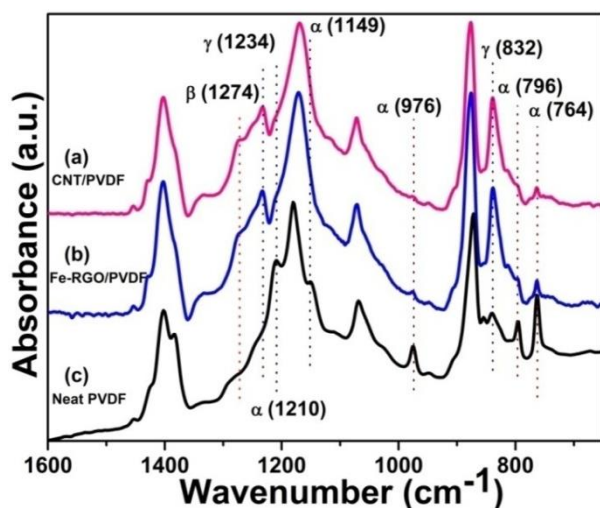


**Figure 3.5** Shows the ATR-IR Spectra of (a) CNT/PVDF (b) Fe-*r*GO/PVDF (c) Neat PVDF which is used to study the piezoelectric phases.

The FTIR characterizations indicated the presence of polar piezoelectric  $\beta$  and  $\gamma$ -phase in PVDF because of the addition of Fe-*r*GO and CNT in Fe-*r*GO. Electrical poling process was not followed during the synthesis of the polymers. The nucleation of piezoelectric polar phases even without following the electrical poling process indicates the self-alignment of the monomer units that consists of fluorine and hydrogen atoms attached to the carbon atoms. The self-alignment of the monomer units happens due to the electrostatic interaction of the fluorine and hydrogen atoms with  $\pi$  electrons present in *r*GO/CNT and Fe/iron oxide and functional groups present in *r*GO. Within the polymer matrix polymer chains are also formed in the process of the synthesis of the nanocomposite film in the melt phase. Initially the dipole moments present in the polymer are perpendicular to the direction of the polymer chains. Due to the addition of the nanofillers the monomer units get arranged in such a way that all the dipoles are packed in a parallel morphology which contribute to an overall dipole moment per unit cell. This indicates how the self-poling process takes place within the polymer matrix even without the application of external electrical or

mechanical energy.[33] The self-polarization of the dipoles occur in such a way that it supports a stress induced polarization, in the direction of the applied stress.[34] Such type of self-poled PVDF based polymer composites as explained in the previous section shows  $d_{33}$  piezoelectric charge coefficient.[35]

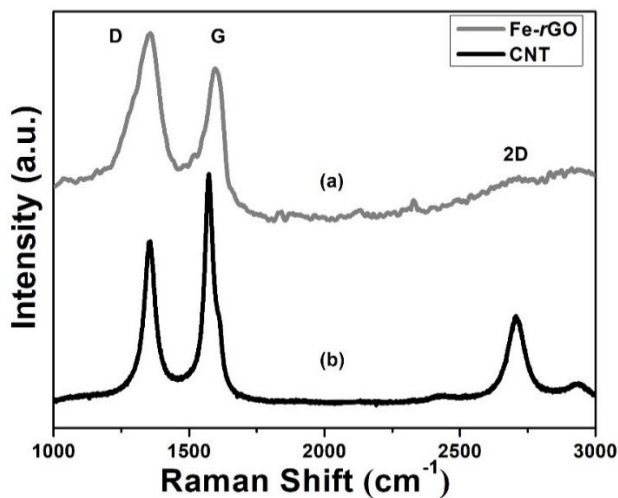


**Figure 3.6** Shows the Raman Spectra of (a) Fe-rGO (b) CNT.

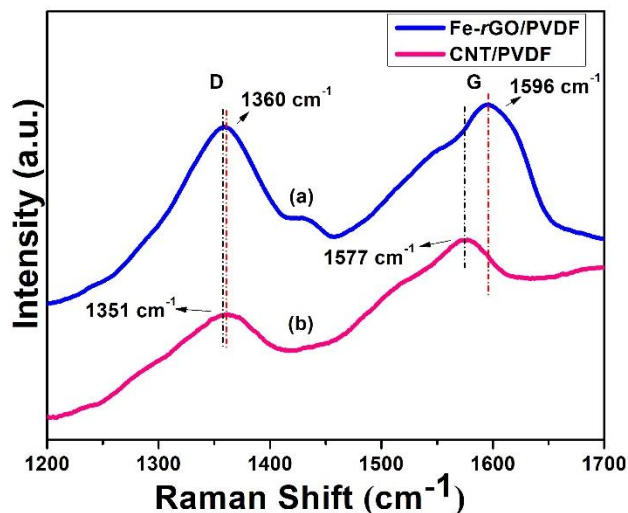


**Figure 3.7** Shows the Raman Spectra of (a) Fe-rGO/PVDF nanocomposite (b) CNT/PVDF nanocomposite.

The Raman Spectra of Fe-rGO and CNT are given in Figure 3.6 (a) and (b) respectively. The D band in Raman spectra of single layer graphene oxide is located near  $1350\text{ cm}^{-1}$  which originates by the breathing mode of  $\kappa$ -point phonons of  $A_{1g}$  symmetry of the defects involved in the  $sp^3$ -

hybridized carbon bonds such as hydroxyl and/or epoxide bonds. The intensity of the D band is related to the size of the in-plane  $sp^2$  domains. The G band of graphene oxide is located near  $1582\text{ cm}^{-1}$  which originates from the first order scattering of the  $E_{2g}$  phonons of the  $sp^2$ -hybridized carbon atoms. The 2D band originates at  $2679\text{ cm}^{-1}$  which is sensitive to the stacking of graphene sheets.

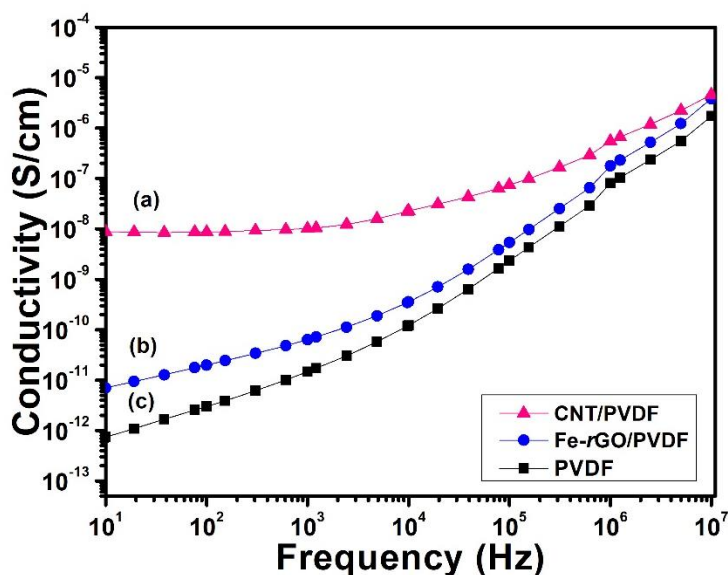
It is accepted in case of single layer graphene that the G and 2D bands are located at  $\sim 1585\text{ cm}^{-1}$  and  $\sim 2679\text{ cm}^{-1}$ . In case of multi-layer graphene (between 2-6 layers) the G and 2D bands shift to lower and higher wavenumber by  $6\text{ cm}^{-1}$  and  $19\text{ cm}^{-1}$  respectively. The D band of Fe-*r*GO is found at  $1358\text{ cm}^{-1}$  in this work, whereas the G and 2D bands are located at  $1596\text{ cm}^{-1}$  and  $2704\text{ cm}^{-1}$  respectively. It is established that the ratio between the  $I_{2D}/I_G$  of single, double, triple and multi ( $>4$ ) layered graphene sheets are typically greater than 1.6,  $\sim 0.8$ ,  $\sim 0.30$ , and  $\sim 0.07$ , respectively.[36] In case of Fe-*r*GO sample the  $I_{2D}/I_G$  ratio is 0.671, which indicates the presence of triple layer, graphene like domains. The  $I_D/I_G$  peak intensity ratio is a measure of the  $sp^2$  domain size of graphene sheets containing  $sp^3$  and  $sp^2$  bonds and is inversely proportional to the average size of the  $sp^2$  clusters. The  $I_D/I_G$  intensity ratio of the Fe-*r*GO sample is 1.02 which is consistent with previously reported work.[37]

The Raman Spectra of the CNTs that were used in our experiment has D band at  $1358\text{ cm}^{-1}$ . The D band originates due to disorder-induced phonon mode due to finite size crystals and defects. The G band in the Raman Spectra of the CNTs is located at  $1573\text{ cm}^{-1}$ , which corresponds to the  $E_{2g}$  tangential stretching mode of an ordered graphite structure with  $sp^2$  hybridization. The 2D band (also known as the  $G^1$  band) exhibits absorption between  $2680\text{ cm}^{-1}$  and  $2730\text{ cm}^{-1}$ . In our case the 2D band exists at  $2706\text{ cm}^{-1}$ . The 2D band is an indication of the nanotube crystallinity. The stronger the D band greater is the crystallinity.  $I_D/I_G$  band ratio correlates the in-plane crystal domain size and was used to estimate the degree of disorder in graphitic carbon.  $I_D/I_G$  ratio close to zero indicates high

crystallinity, whereas greater than 1 indicates high disorder due to abundant defects in graphitic structure. The CNTs used in the present work have a  $I_D/I_G$  ratio of 0.6, which indicate less structural defects.[38]

The Raman Spectra of Fe-*r*GO/PVDF and CNT/PVDF is shown in Figure 3.7 (a, b) respectively. The  $I_D/I_G$  ratio in Fe-*r*GO/PVDF reduced to 0.92. There is a clear indication of the size enhancement of the  $sp^2$  domain clusters of Fe-*r*GO within the nanocomposite, which is consistent with literature. This indicates the interaction between Fe-*r*GO and PVDF, in which the charge dissimilarity in Fe-*r*GO contributes in attracting some –CH<sub>2</sub>–/–CF<sub>2</sub>– dipoles of PVDF, inducing the polar piezoelectric phases.[16] The  $I_D/I_G$  ratio in CNT/PVDF reduced to 0.55. This indicates reinstatement of greater crystallinity in the CNTs.[39]

### 3.2.4 Electrical Conductivity Measurements



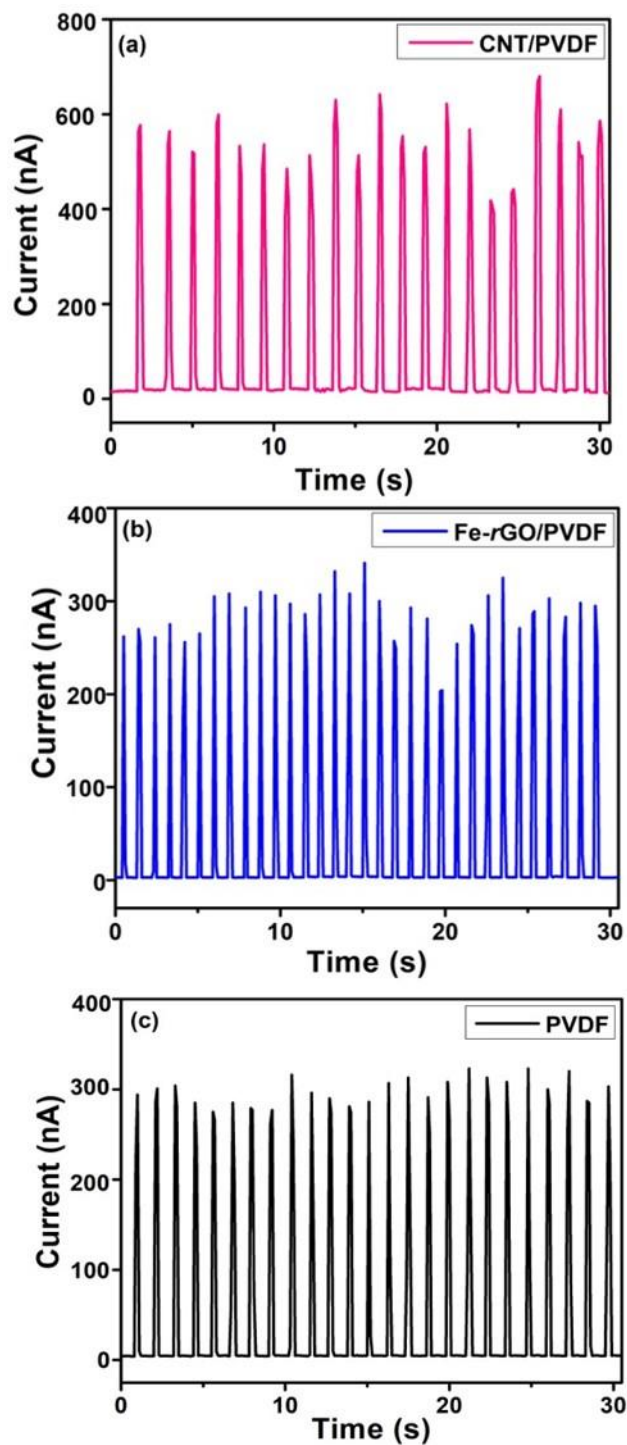
**Figure 3.8** Shows the AC electrical conductivity vs frequency characteristics of (a) CNT/PVDF nanocomposite (b) Fe-*r*GO/PVDF nanocomposite (c) Pure PVDF.

Figure 3.8 (a, b and c) shows the AC electrical conductivity of CNT/PVDF, Fe-*r*GO/PVDF and PVDF nanocomposite films, respectively. The AC electrical conductivity behavior of pure PVDF is linear, which is common for insulating polymers. The electrical conductivity of the Fe-

*r*GO/PVDF nanocomposite is in accordance to the available literature which is closely  $10^{-6}$  S/cm at higher frequencies. The electrical conductivity of the Fe-*r*GO/PVDF nanocomposite film is ten times higher than pure PVDF. The overall conductivity increases due to the presence of *r*GO within the polymer matrix.[40] Also the presence of Fe in Fe-*r*GO increases the overall electrical conductivity. It was reported previously by Akhavan *et al.* that GO sheets originally had conductivity of  $10^{-11}$  S/cm but after reduction with green tea in the presence of Fe the conductivity value increased to  $10^{-6}$  S/cm. The conductivity of *r*GO was found to be  $10^{-9}$  S/cm when it was reduced with green tea alone.[41] The maximum value of the AC electrical conductivity among all the nanocomposites were found to be  $10^{-6}$  S/cm and the reason behind this is the generation of polarization throughout the material and not the movement of electrons.[39] The general observation is that the AC conductivity increases with the addition of CNT and Fe-*r*GO in PVDF.[42] The conductivity increases in CNT/PVDF nanocomposite with increase in frequency but never reaches saturation limit. The conductivity that is reported in literature is of the order of  $10^{-4}$  S/cm for CNT/PVDF nanocomposite for the same amount of CNT used. However, it is found that the conductivity of CNT/PVDF nanocomposite in the present work is  $10^{-8}$  S/cm and nearly  $10^{-6}$  S/cm at 10 Hz and at  $10^7$  Hz, respectively. The decrease in the conductivity is due to the increase in contact resistance among the CNTs. The CNTs gets wet and wrapped by the polymer owing to its high surface energy property, which originates because of the different synthesis conditions.[43] The conductivity of CNT/PVDF nanocomposite is higher than both Fe-*r*GO/PVDF nanocomposite and pure PVDF at lower frequency. The difference diminishes at higher frequency. The difference in conductivity at lower frequencies is due to the interconnected network like structure of CNTs which plays a significant role in improving the conductivity in polymeric systems.[44] The electrical conductivity of dielectric material depends upon critical frequency ( $f_c$ ). The critical frequency ( $f_c$ ) is the frequency till which

the conductivity of polymer nanocomposite remains unchanged, depending upon filler loading. The interfacial polarization effect plays a prominent role below  $f_c$ , due to which the dipoles as well as the induced dipoles have enough time to align themselves in the direction of the applied electric field. This is the reason why the electrical conductivity is frequency independent till the critical frequency ( $f_c$ ). This is the reason why CNT/PVDF nanocomposite, Fe-rGO/PVDF nanocomposite and pure PVDF film shows difference in conductivity levels, at lower frequencies. But when the frequency exceeds the critical frequency ( $f_c$ ), the conductivities become frequency dependent and independent upon the filler material. Absence of polarization effect at higher frequencies is the reason behind this phenomenon. The relaxation time required to orient the dipoles in the direction of the applied electric field decreases with the increase in frequency. Therefore, above critical frequency ( $f_c$ ) the applied electric field tends to reduce the space charge accumulation. Thus, the dispersion of dipoles in the direction of the applied electric field decreases in comparison to the polarization. The conductivity at this point depends upon excitation charged particles and the electron movement along the conductive pathway. Hence the conductivity of all the nanocomposite films are similar at higher frequencies.[39]

### 3.2.5 Electrical Characterizations



**Figure 3.9** Shows the rectified short circuit current generated due to finger tapping from the (a) CNT/PVDF (b) Fe-rGO/PVDF (c) Neat PVDF based device.



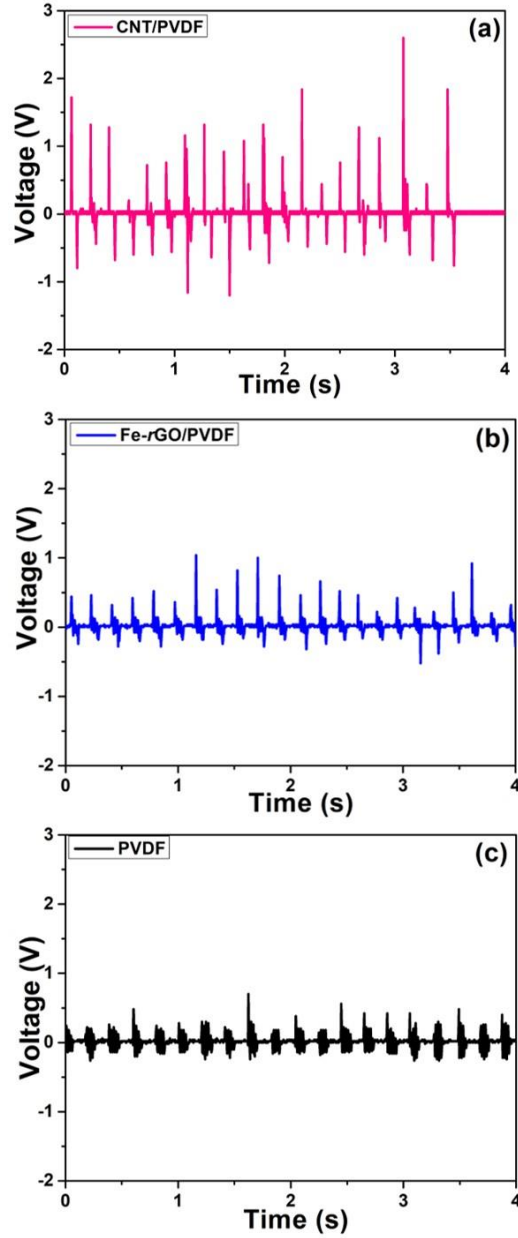


**Figure 3.10** Shows the open circuit voltage generated due to finger excitations from the (a) CNT/PVDF (b) Fe-rGO/PVDF (c) Neat PVDF based device.

The Short Circuit Current generated by the nanocomposite films was measured across the output terminals of a bridge rectifier using Keithley 2401 Sourcemeter. The rectified short circuit output current of the PVDF based energy harvesting devices is shown in Figure 3.9. CNT/PVDF

nanocomposite shows current output as high as 700 nA approximately. Pure PVDF shows current output close to 300 nA, whereas Fe-*r*GO/PVDF based nanocomposite shows output currents little over 300 nA.

The open circuit voltage generated by the nanocomposite films was measured across the electrodes of the piezoelectric nanocomposite films by a digital storage oscilloscope. Figure 3.10 shows the open circuit output voltage response of the PVDF based energy harvesting nanocomposite films. The peak open circuit voltage shown by CNT/PVDF nanocomposite is approximately 2.5 V. The peak open circuit voltage shown by the Fe-*r*GO/PVDF nanocomposite is 1.2 V whereas that for pure PVDF film is 0.6 V. As compared to the pure PVDF sample the CNT/PVDF as well as the Fe-*r*GO/PVDF sample showed higher voltage. The positive and the negative amplitude of the voltage signal originates due to the compression and the relaxation of the piezoelectric nanocomposite, under imparting and releasing of the human finger. An application of external pressure brings changes in the crystal structure of the nanocomposite films. The reason behind the origin of the piezoresponse is to stabilize the deformation in the crystal structure.[16] In a previously published research paper it was mentioned that a composite prepared of CNTs and PVDF combines the conducting property of CNTs and the piezoelectric property of PVDF to give rise to better piezoelectricity in the composite.[45]

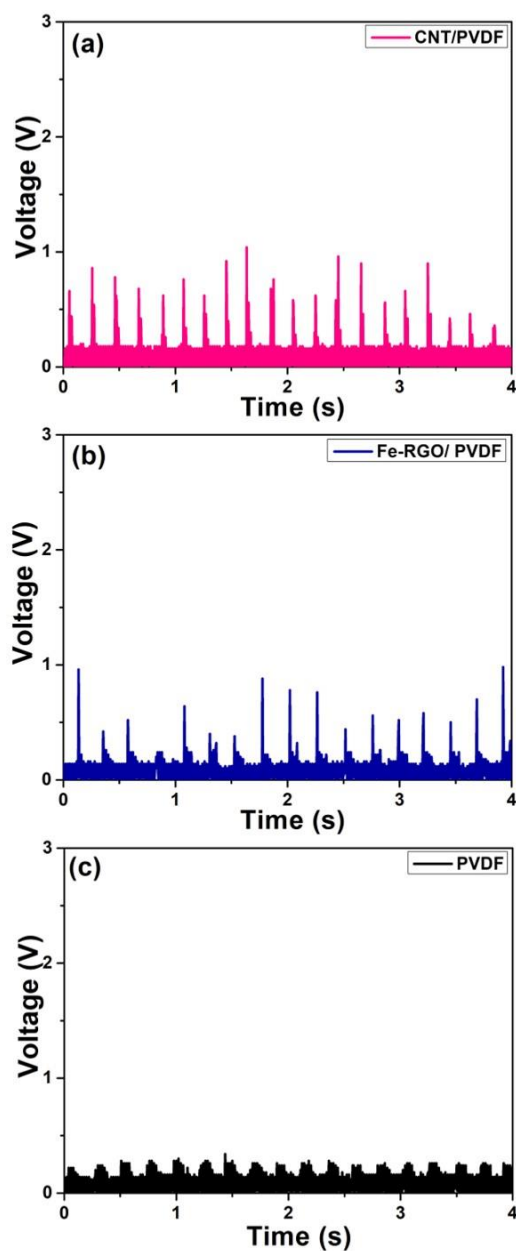


**Figure 3.11** Shows the open circuit rectified voltage generated due to finger excitations from the (a) CNT/PVDF (b) Fe-rGO/PVDF (c) Neat PVDF based device.

The rectified open circuit voltage of the nanocomposite films is shown in Figure 3.11. The CNT/PVDF nanocomposite film shows a peak output voltage of 1.2 V. The rectified open circuit voltage shown by the Fe-rGO/PVDF and pure PVDF films are 0.7 V and 0.3 V respectively. The

rectified output voltages of the PVDF based nanocomposite films drop due to the voltage consumed by the diodes present in the bridge rectifier.[46]

The electrical response is greater in CNT/PVDF based nanocomposite as compared to Fe-*r*GO/PVDF and pure PVDF due to better stabilization of the polar  $\beta$ -phase as well as  $\gamma$ -phase. The charges are transferred to the electrodes through the nanomaterial network throughout the polymer matrix.

In case of Fe-*r*GO/PVDF nanocomposite the formation of the electroactive  $\gamma$ -phase is responsible for the enhanced output electrical current. The mechanism of the formation of  $\gamma$ -phase in the PVDF based nanocomposite is explained subsequently. The  $\pi$ -electrons of *r*GO attract some of the  $-\text{CH}_2-$  dipoles of PVDF (gauche conformation), which is composed of  $-\text{CH}_2-\text{CF}_2-$  chains. Some  $-\text{CH}_2-$  dipoles (trans conformation) are repelled by the Fe/iron oxide particles present within the *r*GO matrix. In the same way, some  $-\text{CF}_2-$  dipoles are attracted (gauche conformation) by the Fe/iron oxide particles and some of the  $-\text{CF}_2-$  dipoles are repelled (trans conformation) by the delocalized  $\pi$ -electrons of the *r*GO, respectively. The several oxygen containing functional groups (like hydroxyl, carbonyl, carboxyl) present in Fe-*r*GO may interact with Fluorine or Hydrogen atoms via hydrogen bonding.[23]

It is interesting to mention here the Fe-*r*GO nanosheets also develop electric potential, when are exposed to mechanical stress. The electric potential which is developed works to further align the PVDF dipoles, in the same direction by stress induced polarization.[47]

The CNTs act as nuclei for the crystallization of PVDF in case of CNT/PVDF nanocomposite. The  $\pi$ -electrons of CNT repel some of the  $-\text{CF}_2-$  dipoles and attract some of the  $-\text{CH}_2-$  dipoles. It is found from Raman Spectroscopy that the CNTs are crystalline and their structural defects reduces within the PVDF nanocomposite. This indicates good interaction among CNTs and dipoles present in the PVDF, resulting in the formation

of piezoelectric polar phases, by the reorientation of the  $-\text{CH}_2-$  and  $-\text{CF}_2-$  dipoles.[45]

After the piezo-potential is produced due to the application of mechanical strain an inductive charge cloud is produced on the upper and lower electrodes. This charge cloud contributes to the flow of electric current in the external circuit.[16]

### 3.2.6 Electric Current Response Stability

Figure 3.12, 3.13 and 3.14 shows the stability of current response for the CNT/PVDF, Fe-*r*GO/PVDF and PVDF nanocomposite films.[48] All the experiments were conducted at room temperature and at normal conditions on a working day in the laboratory. The current was checked for 2000 seconds. Finger excitation was provided to the devices. Magnified current responses before and after the excitation are shown in the figures in inset.

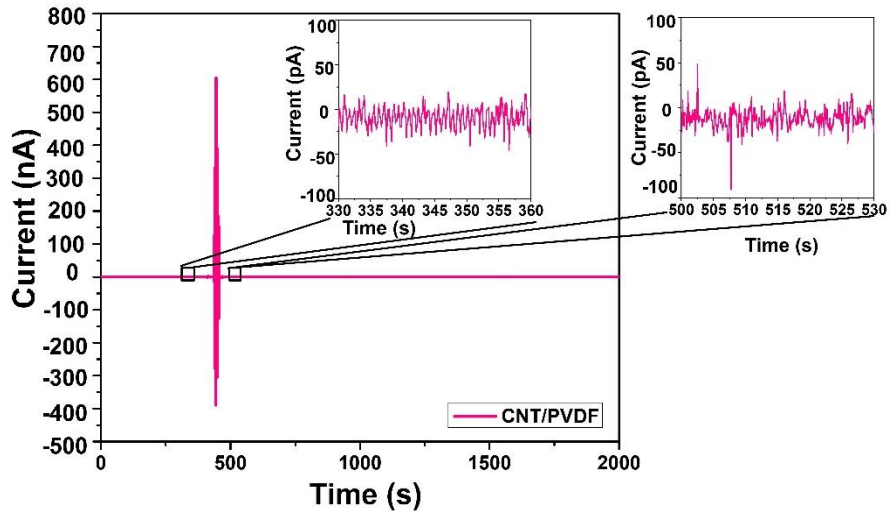


*Figure 3.12 Shows the current response stability for CNT/PVDF nanocomposite film. Inset shows magnified current response.*

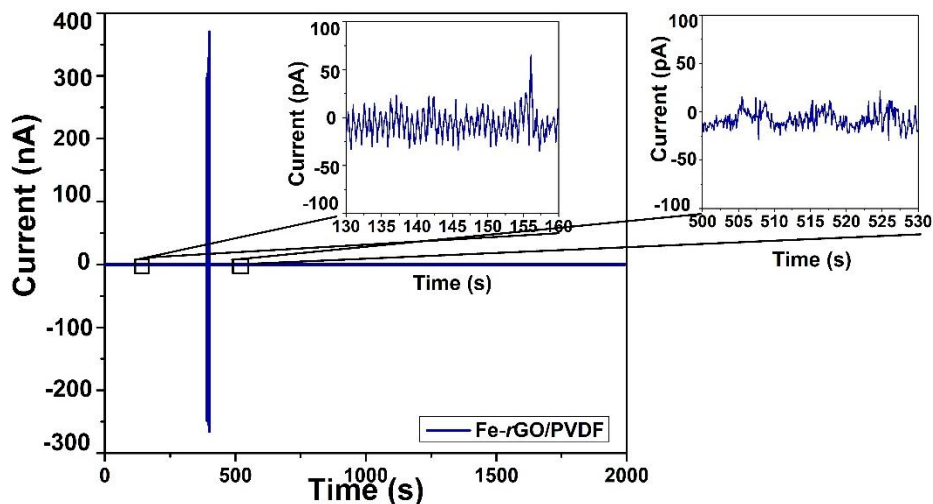


*Figure 3.13 Shows the current response stability for Fe-rGO/PVDF nanocomposite film. Inset shows magnified current response.*

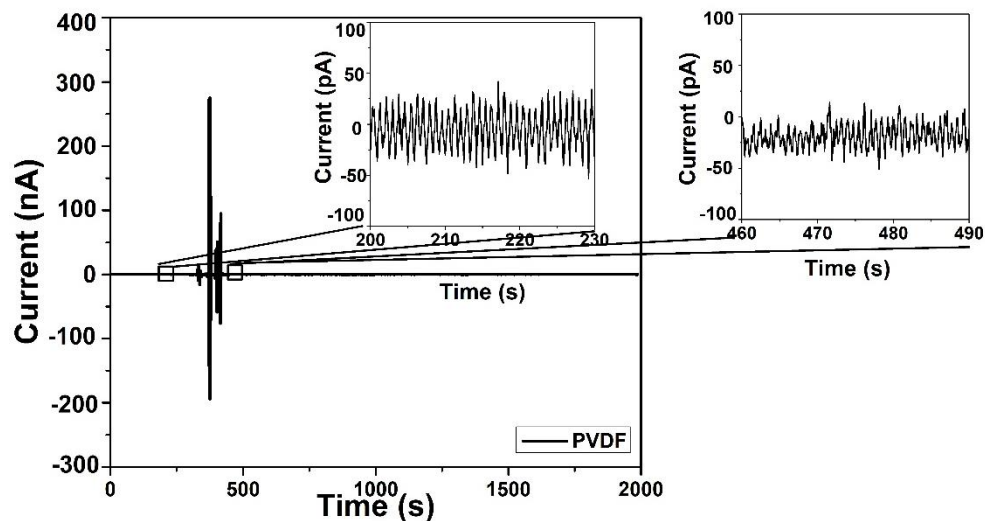


*Figure 3.14 Shows the current response stability for pure PVDF nanocomposite film. Inset shows magnified current response.*

### 3.3 Summary

In this work we have prepared CNT/PVDF and Fe-rGO/PVDF nanocomposite films by following the solution casting method. The nanocomposite films were used to make a mechanical energy harvesting device that could be excited by finger tapping. It is found that the stabilization of polar  $\beta$  and  $\gamma$ -phases in CNT/PVDF and Fe-rGO/PVDF nanocomposites are better when compared to pure PVDF. Among

CNT/PVDF nanocomposite and Fe-rGO/PVDF nanocomposite the polarization was greater in the former. The molecular interactions between the Fe-rGO as well as CNTs with PVDF polymer chains was investigated by Raman spectroscopy. The AC conductivity results confirms that the electrical conductivity of the nanocomposite films increases with the addition of nanofillers in polymer matrix. The addition of nanofiller in the polymer matrix, with the unique device structure provides more displacement to the piezoelectric PVDF film and generates greater electrical response in the output. The approach taken in this work can lay path for possible mechanical energy harvesting applications in the real world.

## References

1. Wang, Z.L. *et al.*, (1989). Piezoelectric Nanogenerators Based on Zinc Oxide Nanowire Arrays. *Science*, 312, 242–247.
2. Wang, X. *et al.*, (2007). Direct-current nanogenerator driven by ultrasonic waves. *Science*, 316, 102–105.
3. Zeng, W. *et al.*, (2013). Highly durable all-fiber nanogenerator for mechanical energy harvesting. *Energy and Environmental Science*, 6(9), 2631–2638.
4. Kawai, H. (2005). The Piezoelectricity of Poly (vinylidene Fluoride). *Japanese Journal of Applied Physics*, 8(7), 975–976.
5. Geim, A.K. *et al.*, (2007). The rise of graphene. *Nature materials*, 6(3), 183–191.
6. Geim, A.K. (2009). Graphene : Status and Prospects. *Science*, 324, 1530–1535.
7. Wu, C. *et al.*, (2012). Hyperbranched-polymer functionalization of graphene sheets for enhanced mechanical and dielectric properties of polyurethane composites. *Journal of Materials Chemistry*, 22(14), 7010–7019.
8. Tong, W. *et al.*, (2014). Novel method for the fabrication of flexible film with oriented arrays of graphene in poly(vinylidene fluoride-co-

- hexafluoropropylene) with low dielectric loss. *Journal of Physical Chemistry C*, 118(20), 10567–10573.
9. Wu, C. *et al.*, (2011). Morphology-controllable graphene-TiO<sub>2</sub> nanorod hybrid nanostructures for polymer composites with high dielectric performance. *Journal of Materials Chemistry*, 21(44), 17729–17736.
  10. Sinha, T.K. *et al.*, (2016). Graphene-Silver-Induced Self-Polarized PVDF-Based Flexible Plasmonic Nanogenerator Toward the Realization for New Class of Self Powered Optical Sensor. *ACS Applied Materials and Interfaces*, 8(24), 14986–14993.
  11. Bhavanasi, V. *et al.*, (2016). Enhanced Piezoelectric Energy Harvesting Performance of Flexible PVDF-TrFE Bilayer Films with Graphene Oxide. *ACS Applied Materials and Interfaces*, 8(1), 521–529.
  12. Ghosh, R. *et al.*, (2016). Reduced Graphene Oxide-Based Piezoelectric Nanogenerator with Water Excitation. *IEEE Transactions on Nanotechnology*, 15(2), 268–273.
  13. Martins, P. *et al.*, (2014). Electroactive phases of poly(vinylidene fluoride): Determination, processing and applications. *Progress in Polymer Science*, 39(4), 683–706.
  14. Alamus, *et al.*, (2012). Evaluation of piezoelectric property of reduced graphene oxide (rGO)–poly(vinylidene fluoride) nanocomposites. *Nanoscale*, 4(22), 7250–7255.
  15. Layek, R.K. *et al.*, (2010). Physical and mechanical properties of poly(methyl methacrylate)-functionalized graphene/poly(vinylidene fluoride) nanocomposites: Piezoelectric  $\beta$  polymorph formation. *Polymer*, 51(24), 5846–5856.
  16. Karan, S.K. *et al.*, (2015). Self-powered flexible Fe-doped RGO/PVDF nanocomposite: An excellent material for a piezoelectric energy harvester. *Nanoscale*, 7(24), 10655–10666.
  17. Lee, J.S. *et al.*, (2008). Crystal structure and ferroelectric properties



- of poly(vinylidene fluoride)-carbon nano tube nanocomposite film. *Molecular Crystals and Liquid Crystals*, 491, 247–254.
18. Iijima, S. (1991). Helical microtubules of graphitic carbon. *Nature*, 354(6348), 56–58.
  19. Baughman, R.H. *et al.*, (2012). Carbon Nanotubes — the Route Toward. *Science*, 787, 787–792.
  20. Zengin, H. *et al.*, (2002). Carbon Nanotube Doped Polyaniline. *Advanced Materials*, 14(20), 1480–1483.
  21. Hummers, W.S. *et al.*, (1958). Preparation of Graphitic Oxide. *J. Am. Chem. Soc.*, 80, 1339.
  22. Ghosh, R. *et al.*, (2013). Chemically reduced graphene oxide for ammonia detection at room temperature. *ACS Applied Materials and Interfaces*, 5(15), 7599–7603.
  23. Fan, Z.J. *et al.*, (2011). Facile synthesis of graphene nanosheets via Fe reduction of exfoliated graphite oxide. *ACS Nano*, 5(1), 191–198.
  24. Mai, H.X. *et al.*, (2005). Shape-selective synthesis and oxygen storage behavior of ceria nanopolyhedra, nanorods, and nanocubes. *Journal of Physical Chemistry B*, 109(51), 24380–24385.
  25. Hu, C. *et al.*, (2016). A Transparent Antipeep Piezoelectric Nanogenerator to Harvest Tapping Energy on Screen. *Small*, 12(10), 1315–1321.
  26. Suyitno, S. *et al.*, (2014). Fabrication and Characterization of Zinc Oxide-Based Electrospun Nanofibers for Mechanical Energy Harvesting. *Journal of Nanotechnology in Engineering and Medicine*, 5(1), 011002-011007.
  27. Zhang, X.S. *et al.*, (2017). Penciling a triboelectric nanogenerator on paper for autonomous power MEMS applications. *Nano Energy*, 33, 393–401.
  28. Jung, W.S. *et al.*, (2015). High Output Piezo/Triboelectric Hybrid Generator. *Scientific Reports*, 5, 1–6.
  29. Aruna, P. *et al.*, (2017). Annealing effects on the electrical properties

- of spin coated poly (3-hexylthiophene) (P3HT) thin films. *Materials Science in Semiconductor Processing*, 61, 39–44.
30. Wang, G. *et al.*, (2009). Synthesis and characterisation of hydrophilic and organophilic graphene nanosheets. *Carbon*, 47(5), 1359–1364.
  31. Adhikary, P. *et al.*, (2015). The co-operative performance of a hydrated salt assisted sponge like P(VDF-HFP) piezoelectric generator: An effective piezoelectric based energy harvester. *Physical Chemistry Chemical Physics*, 17(11), 7275–7281.
  32. Karan, S.K. *et al.*, (2016). An Approach to Design Highly Durable Piezoelectric Nanogenerator Based on Self-Poled PVDF/AlO-rGO Flexible Nanocomposite with High Power Density and Energy Conversion Efficiency. *Advanced Energy Materials*, 6(20), 1–12.
  33. Garain, S. *et al.*, (2015). Self-poled transparent and flexible UV light-emitting cerium complex-PVDF composite: A high-performance nanogenerator. *ACS Applied Materials and Interfaces*, 7(2), 1298–1307.
  34. Adhikary, P. *et al.*, (2016). Flexible hybrid Eu<sup>3+</sup> doped P(VDF-HFP) nanocomposite film possess hypersensitive electronic transitions and piezoelectric throughput. *Journal of Polymer Science, Part B: Polymer Physics*, 54(22), 2335–2345.
  35. Ghosh, S.K. *et al.*, (2015). Self-poled Efficient Flexible “Ferroelectric” Nanogenerator: A New Class of Piezoelectric Energy Harvester. *Energy Technology*, 3(12), 1190–1197.
  36. Akhavan, O. (2015). Bacteriorhodopsin as a superior substitute for hydrazine in chemical reduction of single-layer graphene oxide sheets. *Carbon*, 81(1), 158–166.
  37. Pusty, M. *et al.*, (2016). Synthesis of Partially Reduced Graphene Oxide/Silver Nanocomposite and Its Inhibitive Action on Pathogenic Fungi Grown Under Ambient Conditions. *ChemistrySelect*, 1(14), 4235–4245.
  38. Odedairo, T. *et al.*, (2014). One-pot synthesis of carbon nanotube-

- graphene hybrids via syngas production. *Journal of Materials Chemistry A*, 2(5), 1418–1428.
39. Karan, S.K. *et al.*, (2016). Effect of  $\gamma$ -PVDF on enhanced thermal conductivity and dielectric property of Fe-*r*GO incorporated PVDF based flexible nanocomposite film for efficient thermal management and energy storage applications. *RSC Advances*, 6(44), 37773–37783.
  40. Becerril, H.A. *et al.*, (2008). Evaluation of solution-processed reduced graphene oxide films as transparent conductors. *ACS Nano*, 2(3), 463–70.
  41. Akhavan, O. *et al.*, (2012). Increasing the antioxidant activity of green tea polyphenols in the presence of iron for the reduction of graphene oxide. *Carbon*, 50(8), 3015–3025.
  42. Lopes, A.C. *et al.*, (2013). Dielectric relaxation, ac conductivity and electric modulus in poly(vinylidene fluoride)/NaY zeolite composites. *Solid State Ionics*, 235, 42–50.
  43. Ravikumar, K. *et al.*, (2016). Synergistic effect of polymorphism, substrate conductivity and electric field stimulation towards enhancing muscle cell growth in vitro. *RSC Advances*, 6(13), 10837–10845.
  44. Biswas, S. *et al.*, (2015). Microwave absorbers designed from PVDF/SAN blends containing multiwall carbon nanotubes anchored cobalt ferrite via a pyrene derivative. *Journal of Materials Chemistry A*, 3(23), 12413–12426.
  45. Kim, G.H. *et al.*, (2009). Piezoelectric properties of poly(vinylidene fluoride) and carbon nanotube blends:  $\beta$ -phase development. *Physical Chemistry Chemical Physics*, 11(44), 10506–10512.
  46. Xu, S. *et al.*, (2010). Piezoelectric-nanowire-enabled power source for driving wireless microelectronics. *Nature Communications*, 1(7), 1–5.
  47. Lee, K.Y. *et al.*, (2014). Unidirectional high-power generation via

- stress-induced dipole alignment from ZnSnO<sub>3</sub> nanocubes/polymer hybrid piezoelectric nanogenerator. *Advanced Functional Materials*, 24(1), 37–43.
48. Leberl, D. *et al.*, (2013). High current hybrid single walled carbon nanotube/graphene field emitters. *Journal of Vacuum Science & Technology B, Nanotechnology and Microelectronics: Materials, Processing, Measurement, and Phenomena*, 31(5), 052204.

# CHAPTER 4

---

## Flexible Self-poled *r*GO-Ag/PVDF Nanocomposite Based Piezoelectric Nanogenerator

---

### 4.1 Overview

The crisis due to global warming that originated from the usage of fossil fuels has led to the quest for renewable energy sources such as solar energy, wind energy, hydel energy, nuclear energy. However, they require considerable economic investments as well as distributions and storage infrastructures. Mechanical energy is an ideal alternative which is omnipresent and abundant in the environment that can show the way for self-powered technology to replace traditional batteries which are not mechanically flexible and requires charge replenishment. In the literature mechanical energy harvesting can also be used for generation of other green sources of energy and efficient waste management. In this context Ren *et al.* using mechanical energy harvesting has shown hydrogen production by water splitting,[1] electromagnetic-triboelectric hybrid nanogenerator,[2] self-powering application from waste rubber powder.[3] Formerly several piezoelectric materials like ZnO, BaTiO<sub>3</sub>, PZT, ZnSnO<sub>3</sub>, GaN and BiFeO<sub>3</sub> were used to develop energy harvesting devices.[4-9] Although they show higher efficiency, they are costly, lethal, brittle, and are also unfriendly to nature. Piezoelectric polymers like Poly(vinylidene fluoride) (PVDF) are suitable to overcome these limitations as they are environmentally stable, biocompatible, strongly sensitive to external force, and have high energy conversion efficiency. Piezoelectric polymer develops an electric polarization on the application of mechanical stress, which can harvest mechanical energy from tapping and vibrations present in the ambience.[10, 11] PVDF with its repeating molecular unit ( $-\text{CH}_2-/-\text{CF}_2-$ ) is a ferroelectric polymer which shows the strongest piezoelectric and pyroelectric activity

among the well-known polymers.[12] The electromechanical properties of PVDF depends upon the crystalline structure, chain conformation, dipole orientation within crystalline regions towards the applied processing conditions and post-treatment methods. As discussed in previous chapters PVDF exhibits five different polymorphs viz.  $\alpha$ -phase,  $\beta$ -phase,  $\gamma$ -phase,  $\delta$ -phase and  $\varepsilon$ -phase. Among all the polar phases the  $\beta$ -phase content shows higher piezoelectric, pyroelectric and ferroelectric properties and is more desirable for energy harvesting purposes.[13] Thus it is necessary to enhance the content of the crystalline phases in PVDF which in turn enhances the piezoelectricity so that it could be used to harvest mechanical energy efficiently. However, the conversion of  $\beta$ -phase to  $\alpha$ -phase is associated with an energy barrier.[14] Hence, special techniques are necessary to overcome the energy barrier for the nucleation of a greater fraction of polar  $\beta$ -phase which includes processing techniques like mechanical-stretching and electrical poling at high electric fields, melt crystallization at high pressure or at very high cooling rates, which are costly and are associated with electrical breakdown.[15, 16]

Recently graphene nanosheets owing to its superior electrical, thermal, mechanical and optical properties was reported to be incorporated as a filler in PVDF.[17, 18] However, the poor compatibility between non-polar graphene and polar PVDF prevents the formation of a homogenous composite. Hence, surface functionalization of graphene is necessary for its homogenous dispersion in PVDF. Also, the dielectric loss comes into foray when conducting graphene is incorporated in PVDF. This leads to enhancement in leakage current, which can decrease the lifetime of the composite due to poor heat dissipation factors. To overcome these problems associated with using graphene within the composite, performing oxidative functionalization of graphene to form graphene oxide (GO) in an alternative way. The oxygen containing functional groups in GO interacts with the polymer chains in PVDF and enhances the dispersibility. But the incorporation of GO in PVDF deteriorates the electrical and mechanical

properties of the polymer composite. Hence, an alternative way is to reduce GO to *r*GO, where the later shows partially graphene like properties, with enhanced dispersion in the polymer.[19, 20] It was reported that Fe-*r*GO, Al-*r*GO, Ce<sup>3+</sup>/Graphene were highly effective in enhancing the piezoelectric polar phases in PVDF.[21, 22, 23] The enhancement in the piezoelectric polar phases is related to the electrostatic interactions between the positive and negative charge centers of metal ions and negative charge clouds in *r*GO, respectively. It was reported by Bhavanasi *et al.* that a bilayer film of PVDF-TrFE and graphene oxide exhibits superior energy harvesting performance owing to electrostatic contribution from graphene oxide as compared to a single layer of PVDF-TrFE film.[24] In another interesting research work it was found by Sinha *et al.* that by the incorporation of graphene-silver nanocomposite (GAg) in PVDF an energy conversion efficiency of 15 % and 46.6 % in dark conditions and illuminated conditions, respectively are observed owing to Plasmonic behavior of GAg.[25] Despite the high energy conversion efficiency, the fabrication and study of a wearable/attachable piezoelectric nanogenerator was not attempted by incorporating Ag NPs and *r*GO in PVDF. Ag NPs are simple to synthesize and was previously found to enhance the dielectric properties when formed composite with PVDF.[26] All these reasons made *r*GO-Ag an interesting material to be incorporated in PVDF for mechanical energy harvesting.

In this chapter the fabrication and characterization of a lightweight, flexible, lead free piezoelectric nanogenerator (PENG) is discussed. The PENG discussed in this chapter is an enhanced version as compared to the energy harvester that is discussed in the previous chapters. The enhancement is in terms of the design of the device and in its performance. In this work, we present a *r*GO-Ag/PVDF nanocomposite-based PENG which is synthesized by solution casting process, on which Aluminium tapes are attached that act as electrodes.

Different weight percentages viz. 0.1, 0.5, 1.0, 2.0 weight percentages of  $r$ GO-Ag are added in PVDF separately and five different nanocomposite samples are synthesized. After that the device is encapsulated by Polydimethylsiloxane (PDMS) which makes it environmentally safe, mechanically strong and stable. It is found that similar fabrication techniques for piezoelectric nanogenerators were reported previously.[27, 28] The unrectified as well as rectified electric voltage and current characterizations were measured by exciting the PENG with an external excitation source, subsequently the power density and the energy conversion efficiency of the PENG were also calculated. The PENG could simultaneously light 20 commercial blue light emitting diodes (LEDs). The blue LEDs were arranged to take the shape of the letters IITI- which is an abbreviation of- Indian Institute of Technology Indore. The PENG was provided with hand excitation during the lighting of the LEDs. Also, in this work the bio-mechanical energy harvesting application of the PENG is shown by attaching the PENG to hand and to a footwear. The PENG which is discussed in this chapter can be developed further to use in energy harvesting applications like piezoelectric shoes, floors, walkways, tires, *etc.* that uses vertical compression as the input.

## **4.2 Results and Discussion**

### **4.2.1 Material Synthesis**

Graphite powder was purchased from SD Fine Chemicals Limited, India. Sulphuric Acid ( $H_2SO_4$ ), Sodium Nitrate ( $NaNO_3$ ), Hydrogen Peroxide ( $H_2O_2$ ) and N, N-dimethyl formamide (DMF) were purchased from Merck, India. Potassium Permanganate ( $KMnO_4$ ) was purchased from Rankem, India. Polydimethylsiloxane (PDMS) (Sylgard 184) was purchased from Dow Corning Corporation USA. Conducting Aluminium adhesive tapes were purchased from 3M, USA.



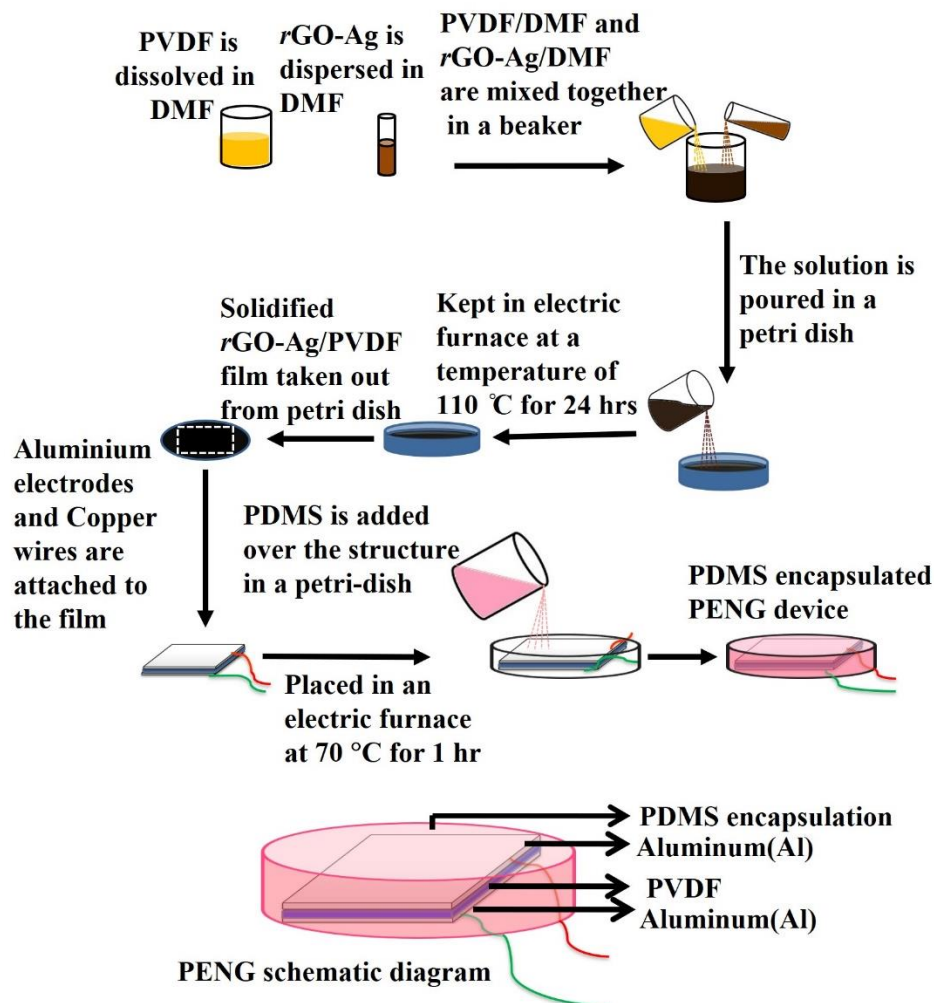


**Figure 4.1** Shows the schematic of the step-wise fabrication of the PENG.

#### 4.2.2 Synthesis of Graphene Oxide

Modified Hummer's method was used for the synthesis of Graphene Oxide.[29, 30] 1g of Graphite Powder, 1g Sodium Nitrate and 50 mL of Sulphuric Acid were stirred together in a round bottom flask in an ice bath for 30 minutes. After that 6g Potassium Permanganate was slowly added to it at 0° C and stirred. After 30 minutes the round bottom flask was transferred to a water bath maintained at 40° C and then stirred. After 1 hour, 100 mL of De-ionized (DI) water was added and the temperature of the water bath was raised to 95° C. After another 30 minutes the solution was diluted by 200 mL DI water. 1 hour later Hydrogen Peroxide was added.

The color of the solution changed from brown to yellow. The final solution was filtered by filter paper. The filtrate was dispersed in water and subsequently, the solution was centrifuged to separate out lighter GO particles. The lighter GO particles are again centrifuged. This time the supernatant was discarded, and the colloidal precipitate was collected and dispersed in DI water. Finally, this solution was ultrasonicated to obtain completely exfoliated graphene oxide.

#### **4.2.3 Synthesis of reduced graphene oxide-silver nanocomposite (*r*GO-Ag)**

To prepare *r*GO-Ag Nanocomposite 1.3 ml of GO suspension (1.35 mg/mL) was added to 98.7 ml of DI water. Within it, 36 mg of Silver Nitrate ( $\text{AgNO}_3$ ), was added and was heated at 95 °C. After 1 hour, 40 mg Sodium Citrate was added, and the solution was heated for another 1 hour. The solution was filtered and was washed by centrifugation method for 3-4 times.[31]

#### **4.2.4 Fabrication of PENG**

The complete steps for the fabrication of the PENG is shown in Figure 5.1. 100 mg PVDF was dissolved in 10 ml DMF. The mixture was stirred with a magnetic stirrer at room temperature. A thick transparent suspension was formed after the PVDF dissolves completely in DMF. 1 mg/ml solution of *r*GO-Ag in DMF was prepared followed by ultrasonication. Then 1 ml of *r*GO-Ag/DMF suspension was added to the PVDF/DMF suspension. After that the mixture was ultrasonicated for 3 hours. Then the mixture was transferred to a petri dish of 10 cm diameter and placed in an electric furnace at 110 °C for 24 hours in order to remove DMF completely.[13] In the similar manner 0.1, 0.5 and 2.0 weight percentage loadings of *r*GO-Ag/PVDF nanocomposite films were synthesized. The *r*GO-Ag/PVDF nanocomposite films were cut into 5.5 × 4 cm dimension pieces. The dimensions of the Aluminium adhesive foil tapes were 5 × 2.6 cm that were pasted to the nanocomposite films. Copper wires were connected between the nanocomposite and the Aluminium foil

tape. For overall encapsulation, the device was placed in a petri-dish within which 10 grams of PDMS (with 10:1 elastomer to curing agent) was poured and placed in an electric furnace at 70°C until the PDMS hardens. The PDMS encapsulation is necessary to protect the PENG from getting damaged by repeated mechanical excitations and to make it water and dustproof.

#### 4.2.5 Material Characterizations of GO and rGO-Ag

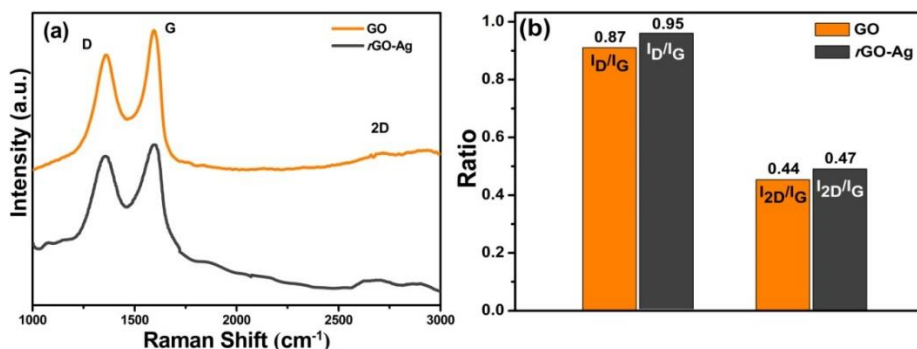


**Figure 4.2** Shows the Raman Spectra of (a) GO and rGO-Ag (b)  $I_D/I_G$  and  $I_{2D}/I_G$  ratio of GO and rGO-Ag.

The Raman spectra of GO and rGO-Ag is shown in Figure 4.2 (a). In case of GO, the D band is located at 1361  $\text{cm}^{-1}$  and is related to the size of the in-plane  $\text{sp}^2$  domains. The G band is located near 1596  $\text{cm}^{-1}$  which originate from the first order scattering of the  $\text{E}_{2g}$  phonons of the  $\text{sp}^2$ -hybridized carbon atoms. The 2D band originates at 2700  $\text{cm}^{-1}$  which is sensitive to the stacking of graphene sheets. The D band of rGO-Ag is located at 1356  $\text{cm}^{-1}$ , the G band is located at 1600  $\text{cm}^{-1}$  and the 2D band is located at 2682  $\text{cm}^{-1}$ . The  $I_D/I_G$  and the  $I_{2D}/I_G$  ratio is shown in Figure 4.2 (b). The  $I_D/I_G$  peak intensity ratio is a measure of the  $\text{sp}^2$  domain size of graphene sheets containing  $\text{sp}^3$  and  $\text{sp}^2$  bonds and is inversely proportional to the average size of the  $\text{sp}^2$  clusters. The  $I_D/I_G$  peak ratio of GO and rGO-Ag is 0.87 and 0.95, respectively. The  $I_D/I_G$  peak ratio in case of rGO-Ag increases, which indicates a reduction in the size of the  $\text{sp}^2$  clusters in the reduction process. The  $I_{2D}/I_G$  peak ratio indicates the number of layers of graphene sheets present. The  $I_{2D}/I_G$  ratio in case of GO and rGO-Ag is 0.44

and 0.47, respectively. It is reported that the ratio between the  $I_{2D}/I_G$  of single, double, triple and multi (>4) layered graphene sheets are typically greater than 1.6, ~0.8, ~0.30, and ~0.07, respectively.[32] This indicates that triple layer graphene sheets are present in both GO and *r*GO-Ag. This result also concludes that during the reduction process of GO to *r*GO-Ag no significant amount of stacking of graphene sheets occurs.

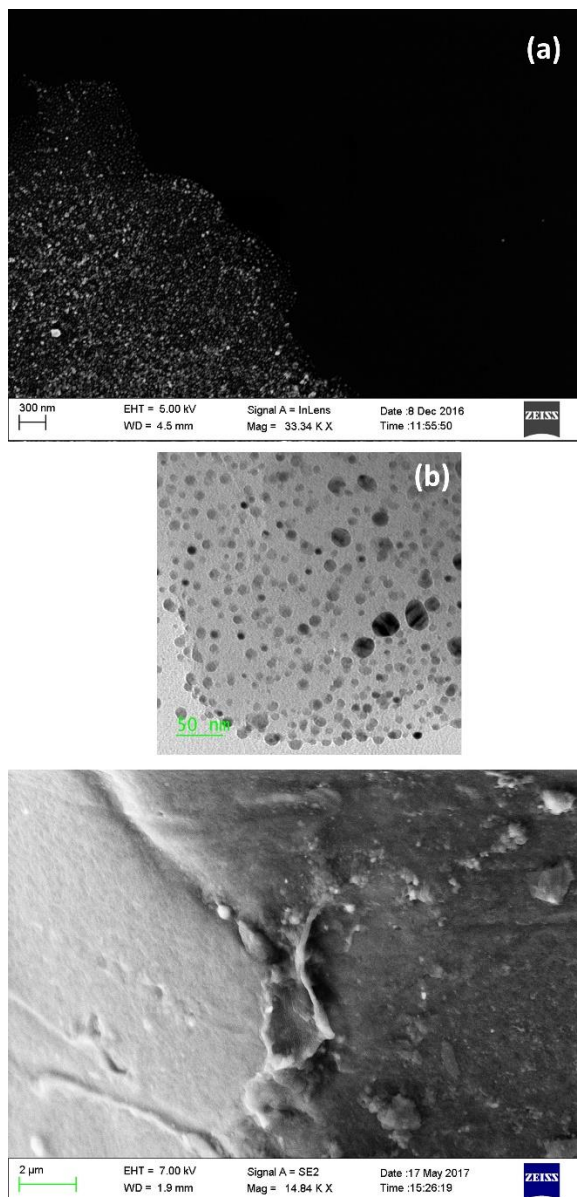


**Figure 4.3** Shows the (a) SEM image (b) TEM image of *r*GO-Ag where Ag nanoparticles are embedded in a thin layer of *r*GO matrix (c) SEM image of the surface morphology of 1.0 *r*GO-Ag/PVDF nanocomposite.

The Field Emission Scanning Electron Microscopy (FE-SEM) image of the *r*GO-Ag nanocomposite is shown in Figure 4.3 (a). In the FE-SEM image *r*GO is present in layers within which silver nanoparticles are evenly dispersed. From the transmission electron microscopy (TEM) image as shown in Figure 4.3 (b) the average particle size of the silver nanoparticles (Ag-NP) can be calculated to be between  $\approx 20$  and  $\approx 30$  nm. The Ag NPs are evenly distributed in the *r*GO matrix and they create conducting paths in the *r*GO matrix. The piezoelectric charges travel towards the electrodes that are attached to the top and the bottom of the nanocomposite and increases the sensitivity of the PENG.

To study the surface morphology, Field Emission-Scanning Electron Microscopy was conducted on the surface of 1.0 *r*GO-Ag/PVDF nanocomposite film. The FE-SEM image as shown in Figure 4.3 (c) shows that the wrinkled and crumpled graphene sheets are completely encapsulated by the PDMS. The encapsulation of the graphene sheets by the polymer visually confirms the bonding interactions between the polymer and the nanofiller.

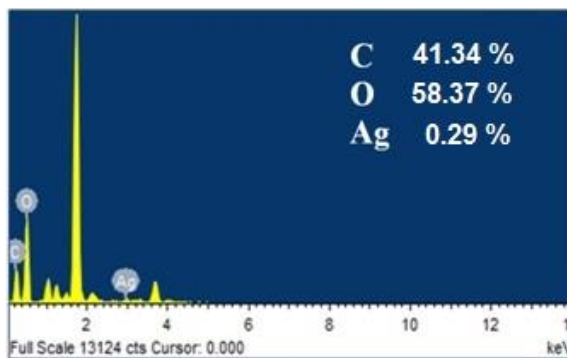


**Figure 4.4** Shows the EDS results which shows the compositional details in atomic percentage of the *r*GO-Ag Nanocomposite.

The EDS results are shown in Figure 4.4. The compositional analysis revealed the atomic percentage of C, O and Ag present in the Nanocomposite. The atomic percentage of Ag is less than 0.3 % in the *r*GO-Ag Nanocomposite. The sharp peak near 2 keV originates due to Si present in the glass substrate.

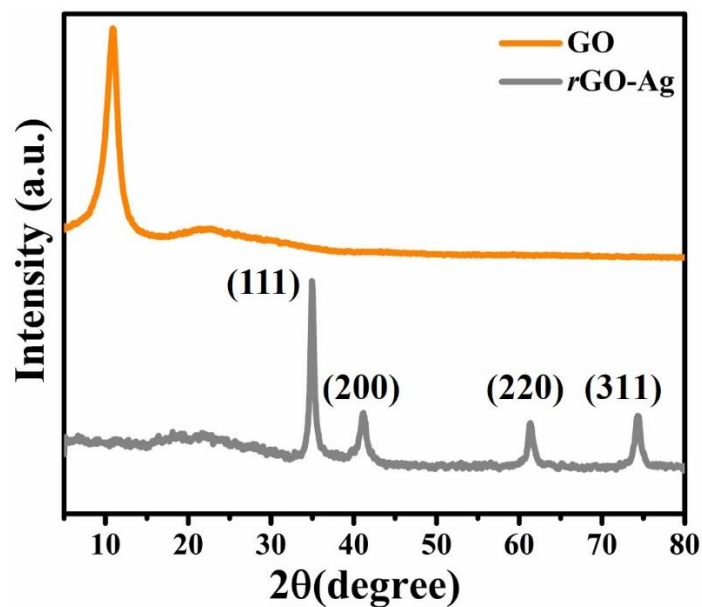


*Figure 4.5 Shows the XRD spectra of GO and rGO-Ag.*

The XRD spectra of rGO-Ag is shown in Figure 4.5 where the presence of a small hump at 25° indicates the exfoliation of Graphene layers from GO to form reduced graphene oxide. The peaks that are present at 38.1°, 44.2°, 64.3°, 77.3° belong to (111), (200), (220), (311) lattice planes of Ag nanoparticles belonging to the face-centred cubic structure.[33]

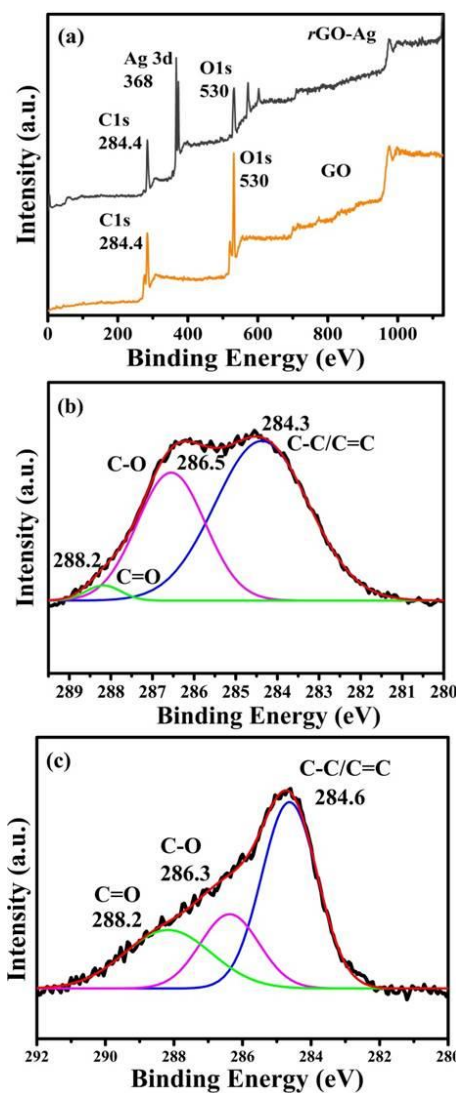


**Figure 4.6** Shows the (a) XPS Survey Spectra of GO and rGO-Ag (b) C1s spectra of GO (c) C1s spectra of rGO-Ag.

The XPS survey spectra of GO and rGO-Ag are shown in Figure 4.6 (a). The peak at 368 eV in the survey spectra of rGO-Ag belongs to Ag, which confirms the presence of metallic Ag in rGO-Ag. Figure 4.6 (b) shows the C1s spectra of GO, where the peaks indicate the presence of C=C, C-O, C=O functional groups present in graphene oxide. Figure 4.6 (c) shows the C1s spectra of rGO-Ag where a reduction in the intensity of the peaks of C-O and C=O is evident, which indicates the reduction of graphene oxide in the process of the formation of rGO-Ag.

#### 4.2.6 Morphological and Structural Characterizations of *rGO-Ag/PVDF* nanocomposite

The deconvoluted XRD spectra of pure PVDF is shown in Figure 4.7 (a). The diffraction peaks at  $17.7^\circ$ ,  $18.2^\circ$  and at  $19.9^\circ$  correspond to (100), (020) and (110) planes of  $\alpha$  crystalline polymorphs of PVDF. Figure 4.7 (b) shows the XRD spectra of 0.1 *rGO-Ag/PVDF* where the  $\alpha$  (020) peak at  $18.2^\circ$  disappears, however, the  $\alpha$  (100) peak at  $17.7^\circ$  and (110) peak at  $19.9^\circ$  appears.[14] The XRD spectra of 0.5 *rGO-Ag/PVDF* is shown in Figure 4.7 (c) where it can be seen that the peaks belonging to the  $\alpha$ -phase disappear, instead peaks at  $18.6^\circ$  and  $20.2^\circ$  appear which belongs to  $\gamma$ (110) and  $\beta$ (200/110) crystalline piezoelectric phases, respectively. This reveals that the addition of 0.5 weight percentage of *rGO-Ag* not only prevents the formation of  $\alpha$  crystalline piezoelectric polymorphs but also favors the formation of polar piezoelectric polymorphs. Figure 4.7 (d) shows the enhancement of the intensities of the peaks belonging to  $\gamma$  (110) and  $\beta$  (200/110), in 1.0 *rGO-Ag/PVDF*. However, the intensities of the peaks belonging to  $\gamma$ (110) at  $18.6^\circ$  and  $\beta$ (200/110) at  $20.2^\circ$  fall a notch below in 2.0 *rGO-Ag* as shown in Figure 4.7 (e). From these observations it can be concluded that *rGO-Ag* is responsible for the nucleation and the stabilization of the polar  $\beta$  and  $\gamma$  piezoelectric polymorphs in PVDF. The enhancement of the  $\gamma$ (110) and  $\beta$ (200/110) peaks is maximum in 1.0 *rGO-Ag*. The reason behind this phenomenon is the interaction between the PVDF polymer chains and *rGO-Ag* in the *rGO-Ag/PVDF* nanocomposite. However, the intensity of the peaks belonging to the piezoelectric polar phases falls in 2.0 *rGO-Ag/PVDF* which may be attributed to the agglomeration of *rGO-Ag* thus leading to the insufficient interaction with PVDF chains. Also, conductive pathways are formed in *rGO-Ag/PVDF* nanocomposite which can also be held as a reason behind the reduction in the nucleation of polar piezoelectric phases. It needs to be mentioned that the advent of the piezoelectric  $\beta$  and  $\gamma$ -phase is purely because of the



presence of *r*GO-Ag in the PVDF. No external exposure to electrical high voltage or mechanical stretching was applied to the *r*GO-Ag/PVDF films. The degree of crystallinity ( $\chi_{C_t}$ ) of the *r*GO-Ag/PVDF nanocomposites was found out from the following equation:

$$\chi_{C_t} = \frac{\sum A_{cr}}{\sum A_{cr} + \sum A_{amr}} \times 100 \% \quad (4.1)$$

where,  $\sum A_{cr}$  and  $\sum A_{amr}$  are obtained by integrating the area under the crystalline and amorphous regions, respectively. The percentage of crystalline regions increases from nearly 9 % in pure PVDF to 46 % in 1.0 *r*GO-Ag/PVDF and falls to 38 % in 2.0 *r*GO-Ag/PVDF. Figure 4.8 shows that the  $\beta$  piezoelectric polymorph contributes to most of the crystalline domains within the *r*GO-Ag/PVDF nanocomposite films. The percentage of highest  $\beta$ -phase presence is found in 1.0 *r*GO-Ag/PVDF which is 38 % where the  $\gamma$ -phase content is only 7%. The calculations of  $\chi_{C_t}$  (total degree of crystallinity),  $\chi_{C_\beta}$  (total degree of beta crystallinity),  $\chi_{C_\gamma}$  (total degree of gamma crystallinity) are provided as equation 4.2, 4.3 and 4.4, respectively.

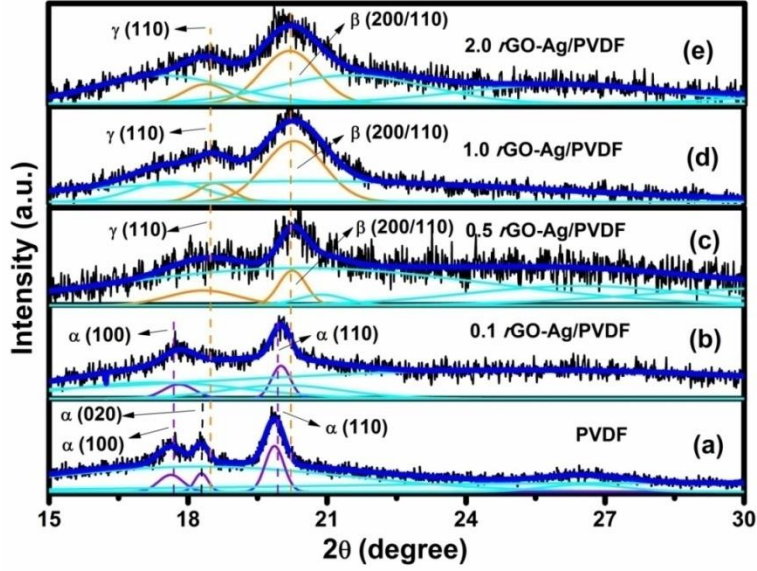


**Figure 4.7** Shows the X-ray diffraction patterns of (a) pure PVDF (b) 0.1 rGO-Ag/PVDF (c) 0.5 rGO-Ag/PVDF (d) 1.0 rGO-Ag/PVDF (e) 2.0 rGO-Ag/PVDF nanocomposite.

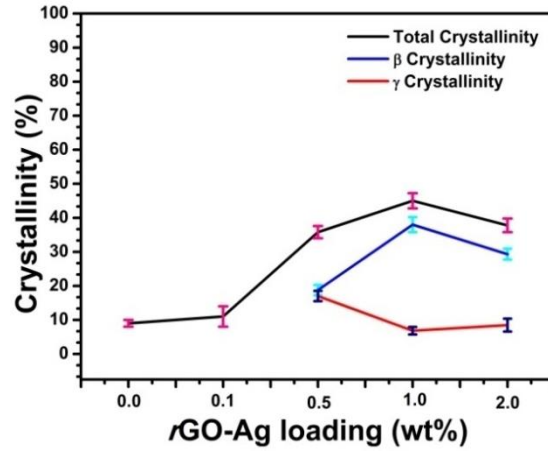


**Figure 4.8** Shows the variation of total crystallinity,  $\beta$  crystallinity, and  $\gamma$  crystallinity in PVDF films with different rGO-Ag loadings.

The total degree of crystallinity was calculated from equation 4.2, where  $\chi_{Ct}$  denotes total degree of crystallinity,  $A_{cr}$  is the integral area of the crystalline peaks and  $A_{amr}$  is the integral area of the amorphous peaks of PVDF.

$$\chi_{Ct} = \frac{\sum A_{cr}}{\sum A_{cr} + \sum A_{amr}} \times 100 \% \quad (4.2)$$

The percentage of  $\beta$ -crystallinity is found from equation 4.3, where  $\chi_{C_\beta}$  is the total  $\beta$ -crystallinity,  $A_\beta$  is the integral area of the  $\beta$  crystalline peaks and  $A_\gamma$  is the integral area of the  $\gamma$  crystalline peaks. Similarly, the  $\gamma$  crystallinity is found from equation 4.4, where  $\chi_{C_\gamma}$  indicates percentage of  $\gamma$ -crystallinity.

$$\chi_{C_\beta} = \chi_{C_t} \times \frac{\Sigma A_\beta}{\Sigma A_\beta + \Sigma A_\gamma} \% \quad (4.3)$$

$$\chi_{C_\gamma} = \chi_{C_t} \times \frac{\Sigma A_\gamma}{\Sigma A_\beta + \Sigma A_\gamma} \% \quad (4.4)$$

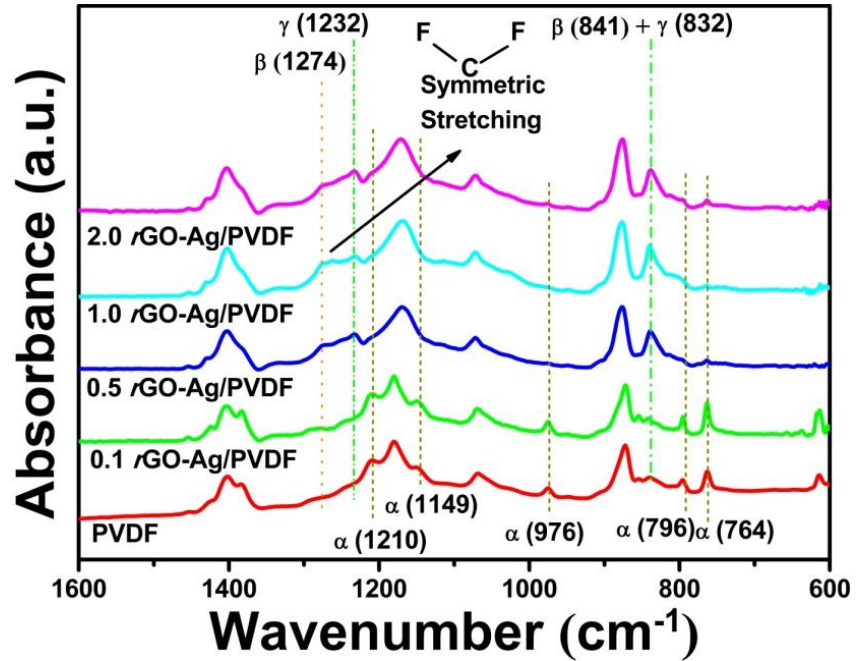


**Figure 4.9** Shows the FT-IR spectra of pure PVDF and *rGO-Ag/PVDF* nanocomposite in the region of 1600–600  $\text{cm}^{-1}$ .

The transformation of phases in the *rGO-Ag/PVDF* nanocomposite is also studied by Infrared (IR) Spectroscopy. Figure 4.9 displays the FT-IR spectra of *rGO-Ag/PVDF* films with different *rGO-Ag* loadings. The common peaks associated with the non-polar  $\alpha$ -phase for pure PVDF are observed at 764, 796, 976, 1149, 1210  $\text{cm}^{-1}$ . The absorption band located at 1274 and at 841  $\text{cm}^{-1}$  belongs to the polar  $\beta$ -phase. In case of  $\gamma$ -phase the corresponding peaks are located at 832, 1232  $\text{cm}^{-1}$ . [22, 34] The

identification of the phase separation between the polar piezoelectric phases is not easy due to the common TTT confirmation which leads to their peak superimposition. The deconvoluted spectrum between 800-900  $\text{cm}^{-1}$  of 1.0 *r*GO-Ag/PVDF is shown in Figure 4.10 (a). The deconvoluted spectrum shows the existence of the  $\gamma$ -phase and  $\beta$ -phase peaks at 832  $\text{cm}^{-1}$  and 841  $\text{cm}^{-1}$ . Figure 4.10 (b) shows the FT-IR spectra between 4000  $\text{cm}^{-1}$  and 2500  $\text{cm}^{-1}$ . The  $\nu_{\text{as}}(-\text{CH}_2-)$  and  $\nu_{\text{s}}(-\text{CH}_2-)$  are two fundamental vibrational bands that are shifted with the increasing amount of *r*GO-Ag. The deconvoluted FT-IR spectra between 4000  $\text{cm}^{-1}$  and 2500  $\text{cm}^{-1}$  of PVDF, 0.1 *r*GO-Ag/PVDF, 0.5 *r*GO-Ag/PVDF, 2.0 *r*GO-Ag/PVDF are shown Figure 4.10 (b) respectively.

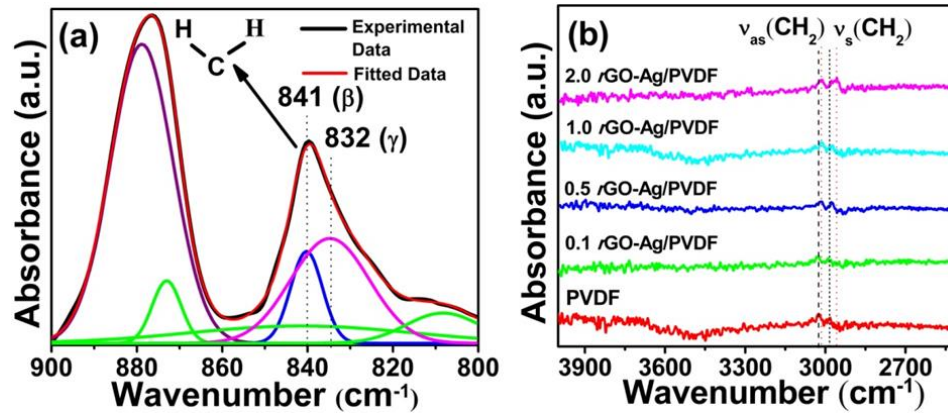


**Figure 4.10** Shows the (a) deconvoluted FT-IR spectra of 1.0 *r*GO-Ag/PVDF nanocomposite film in the region of 900-800  $\text{cm}^{-1}$  (b) FT-IR spectra of all the PVDF films in the region of 4000-2500  $\text{cm}^{-1}$ .

The deconvoluted FT-IR spectra between the 900-800  $\text{cm}^{-1}$  is shown in Figure 4.10 (a) where the peak at 841  $\text{cm}^{-1}$  which originates because of  $-\text{CH}_2-$  wagging vibrations belongs to the  $\beta$ -phase exists beside the 832  $\text{cm}^{-1}$  peak belonging to the  $\gamma$ -phase.

The FTIR spectra between the 4000  $\text{cm}^{-1}$  and 2500  $\text{cm}^{-1}$  is shown in Figure 4.10 (b) where it can be seen that the  $\nu_{\text{as}}(-\text{CH}_2-)$  and  $\nu_{\text{s}}(-\text{CH}_2-)$  which are the two fundamental vibrational bands were shifted to a lower frequency region indicating the presence of interfacial interaction between the surface charge of *r*GO-Ag and  $-\text{CH}_2-/-\text{CF}_2-$  dipoles of the PVDF based

nanocomposite. From these results it is confirmed that *r*GO-Ag plays a vital role in the formation of the  $\gamma$ -phase. The interaction of *r*GO-Ag with the  $-\text{CH}_2-/-\text{CF}_2-$  dipoles is purely electrostatic in nature. The contribution of the electrostatic interaction from the *r*GO-Ag is due to the charges present on the surface of Ag, delocalized  $\pi$  electrons and the oxygen-containing functional groups present on *r*GO. The positively charged Ag nanoparticles present on the *r*GO sheets interact with the  $-\text{CF}_2-$  dipoles of the PVDF segments and in this way contribute towards the nucleation and stabilization of the polar  $\beta$  and  $\gamma$ -phase.

The appearance of the  $\alpha$ -phase peaks are near  $764\text{ cm}^{-1}$ ,  $796\text{ cm}^{-1}$ ,  $976\text{ cm}^{-1}$ ,  $1149\text{ cm}^{-1}$ ,  $1210\text{ cm}^{-1}$ , respectively in 0.1 *r*GO-Ag/PVDF nanocomposite, as shown in Figure 4.9. Due to this reason the  $\gamma$ -phase is not stabilized properly at lower filler concentrations in 0.1 *r*GO-Ag/PVDF. Gradually, as the *r*GO-Ag filler loading increases the peak intensity corresponding to the  $\gamma$ -phase increases. This is reflected in the IR spectra of 0.5 *r*GO-Ag/PVDF. This is a clear indication of the fact that nucleation of the electroactive  $\gamma$ -phase as well as the  $\beta$ -phase takes place by reducing the  $\alpha$ -phase content at the addition of 0.5 weight percent of filler loading in PVDF. It is found that at 1.0 weight percentage addition of *r*GO-Ag in PVDF the stabilization of the polar  $\beta$  and  $\gamma$ -phase becomes more stabilized. It is also found that at 0.5 weight percent loading of *r*GO-Ag the complete suppression of the  $\alpha$ -phase takes place. But in 2.0 *r*GO-Ag/PVDF the  $1274\text{ cm}^{-1}$  characteristic absorption peak of the  $\beta$ -phase diminishes. The  $1070\text{ cm}^{-1}$  peak is linearly dependent on the thickness of the PVDF nanocomposite films and is independent of the formation of piezoelectric polymorphs, hence in the FT-IR analysis the normalization was done about this peak.[13]

$F(\beta, \gamma)$ , which is the relative proportion of both  $\beta$  and  $\gamma$ -phase crystallization was found out to be 70 % in 1.0 *r*GO-Ag/PVDF, where  $F(\beta)$  is 38 % and  $F(\gamma)$  is 32 %. Equation 4.5, 4.6 and 4.7 were used to find out

the value of  $F(\beta, \gamma)$ ,  $F(\beta)$ ,  $F(\gamma)$ , respectively. The variation of the relative proportion obtained from the above calculations are shown in Figure 5.12. The enhancement in the content of the polar electroactive  $\beta$ -phase is the reason behind the enhancement of the output voltage in the 1.0 *rGO*-Ag/PVDF nanocomposite sample. The voltage output recorded in this work is greater than that was reported previously with similar device fabrication techniques.[35, 36]

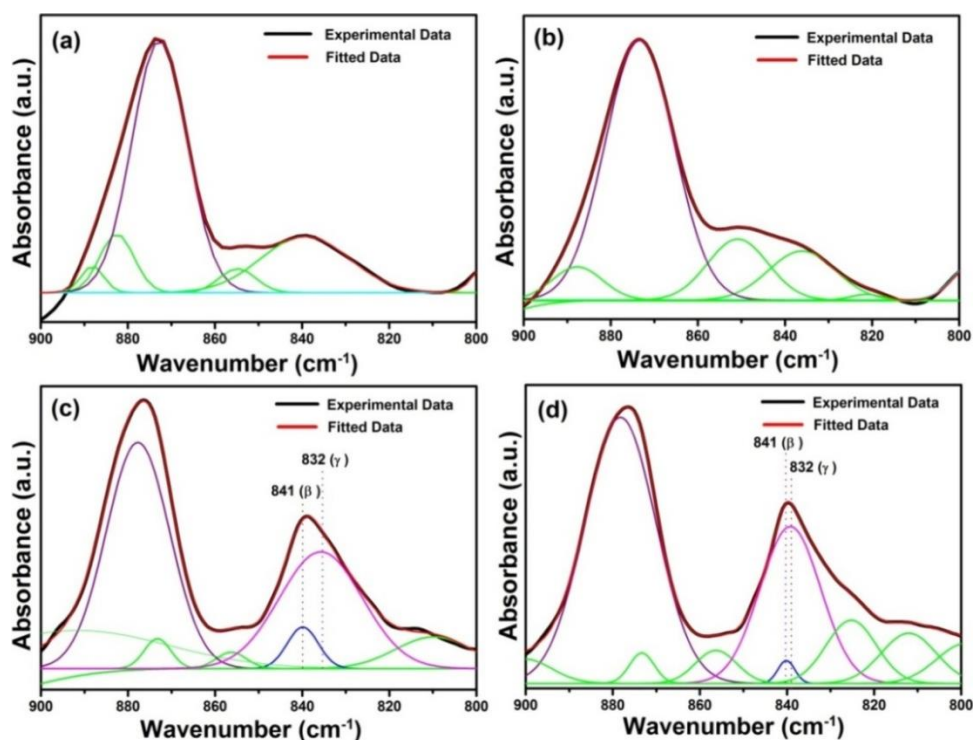


**Figure 4.11** Shows the deconvoluted FT-IR spectra of (a) PVDF (b) 0.1 *rGO*-Ag/PVDF (c) 0.5 *rGO*-Ag/PVDF (d) 2.0 *rGO*-Ag/PVDF.

The deconvoluted FT-IR spectra of PVDF, 0.1 *rGO*-Ag/PVDF, 0.5 *rGO*-Ag/PVDF, 2.0 *rGO*-Ag/PVDF are shown in Figure 4.11 (a-d), respectively. A shift in the deconvoluted peaks corresponding to the  $\beta$  and  $\gamma$ -phase is observed in 0.5 and 2.0 *rGO*-Ag/PVDF, which can be attributed to the change in the interaction of *rGO*-Ag with PVDF chains as the filler loading increases.

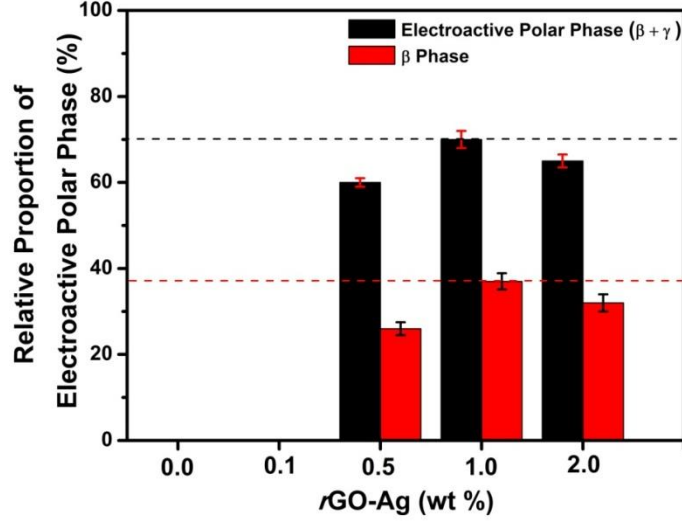


**Figure 4.12** Shows the variation of relative proportion in percentage of combined electroactive polar  $\beta$  and  $\gamma$ -phases (in black) and only  $\beta$ -phases (in red) of PVDF with different rGO-Ag loading by weight percentage.

The relative proportion of polar electroactive phases (both  $\beta$  and  $\gamma$ ) denoted by  $F(\beta, \gamma)$  present in rGO-Ag/PVDF is calculated from the following equation:

$$F(\beta, \gamma) = \frac{A_{(841)}}{(K_{(841)}/K_{(832)})A_{(832)} + A_{(841)}} \quad (4.5)$$

where  $A_{841}$  and  $A_{832}$  is the absorption intensity at  $841 \text{ cm}^{-1}$  and  $832 \text{ cm}^{-1}$  respectively whereas  $K_{841}$  and  $K_{832}$  is the absorption coefficient at  $841 \text{ cm}^{-1}$  and  $832 \text{ cm}^{-1}$ , respectively.

The relative proportion of individual presence of  $\beta$ -phase is denoted by  $F_{\beta}$  and the individual presence of  $\gamma$ -phase is denoted by  $F_{\gamma}$ .

$$F_{\beta} = F(\beta, \gamma) \times \frac{A_{\beta}}{A_{\beta} + A_{\gamma}} \times 100\% \quad (4.6)$$

$$F_{\gamma} = F(\beta, \gamma) \times \frac{A_{\gamma}}{A_{\beta} + A_{\gamma}} \times 100\% \quad (4.7)$$

where  $A_{\gamma}$  and  $A_{\beta}$  are the integrated areas under the  $\gamma$  and  $\beta$  deconvoluted curves.

The  $F(\beta, \gamma)$  was found to be 70% whereas  $F_\beta$  was calculated to be 38 % in case of 1.0  $rGO-Ag/PVDF$  which was highest among all the  $rGO-Ag/PVDF$  nanocomposite loadings, which is shown in Figure 4.12.

$A_{841}$  and  $A_{832}$  are the absorption intensities at  $841\text{ cm}^{-1}$  and  $832\text{ cm}^{-1}$ , respectively.  $K_{841}$  and  $K_{832}$  are the absorption coefficients at the respective wavenumbers.

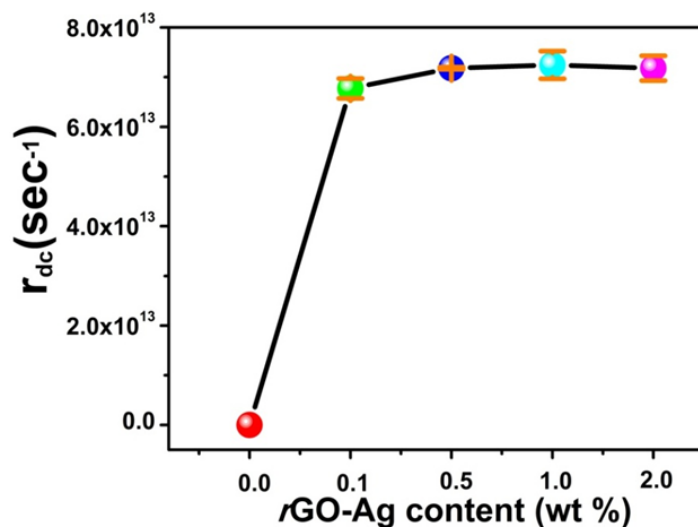


**Figure 4.13** Shows the variation of the damping coefficient with the increase in  $rGO-Ag$  concentration loading.

Figure 4.13 shows the variation of damping coefficient with the rise in the addition of  $rGO-Ag$  concentration. The damping coefficient is an important tool to ascertain the interaction between  $rGO-Ag$  nanosheets and PVDF chains. The asymmetric  $\nu_{as}(-CH_2-)$  and symmetric  $\nu_s(-CH_2-)$  stretching vibration bands of PVDF exists in the region between  $3060$  to  $2940\text{ cm}^{-1}$  do not overlap with other vibrational bands. However, the  $\nu_{as}(-CH_2-)$  and  $\nu_s(-CH_2-)$  vibrational bands shift towards lower wavenumbers. This happens due to the damping oscillations of the  $-CH_2-$  dipoles because of an increase in  $rGO-Ag$  filler concentration, which is shown in Figure 4.14. The electrostatic interactions between the  $-CH_2-$  dipoles and the surface charge of  $rGO-Ag$  enhances the overall mass of the  $-CH_2-$  dipoles of the PVDF. The damping coefficient increases with 1 weight percentage



loading however, it decreases slightly at 2 weight percentage *r*GO-Ag filler loading.

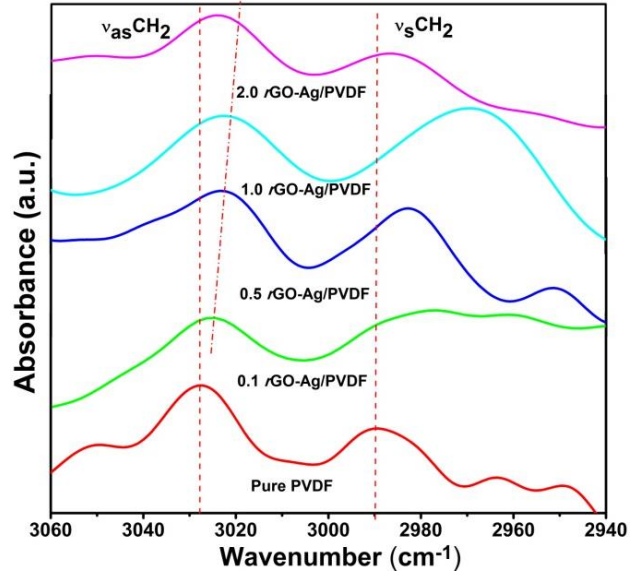


**Figure 4.14** Shows the FT-IR spectra of all the *r*GO-Ag/PVDF based nanocomposites in the region of 3060-2940  $\text{cm}^{-1}$ .

The damping coefficient ( $r_{dc}$ ) is calculated by using the following formula:

$$r_{dc} = 4\pi c (\bar{\nu}_{\text{PVDF}}^2 - \bar{\nu}_{r\text{GO-Ag/PVDF}}^2)^{1/2} \quad (4.8)$$

where  $c$  is the velocity of light,  $\bar{\nu}_{\text{PVDF}}^2$  is the wavenumber of damping free oscillation of the  $-\text{CH}_2-$  group in pure PVDF, whereas  $\bar{\nu}_{r\text{GO-Ag/PVDF}}^2$  is the damping originating from the  $-\text{CH}_2-$  groups in *r*GO-Ag/PVDF nanocomposite.

### Measurement of Dichroic Ratio:

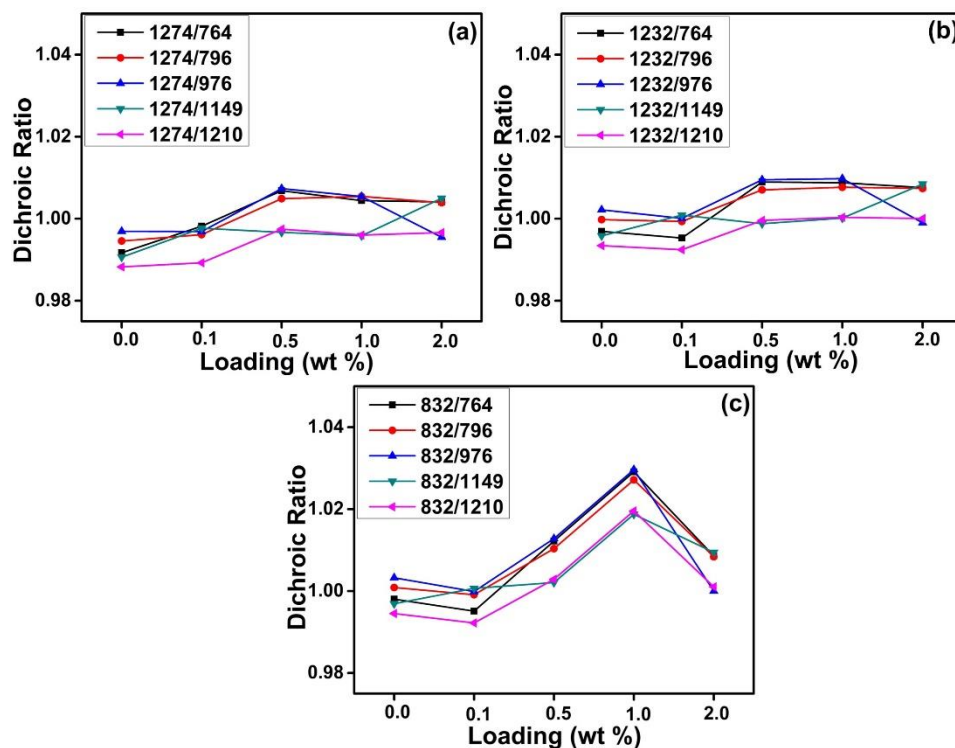


**Figure 4.15** Shows the dichroic ratio of the peak present at (a) 1274  $\text{cm}^{-1}$  belonging to  $\beta$ -phase, (b) 1232  $\text{cm}^{-1}$  belonging to  $\gamma$ -phase (c) 832  $\text{cm}^{-1}$  belonging to  $\gamma$ -phase.

The dichroic ratio is also another means to quantitatively analyze the crystal structures present in the nanocomposite films. The dichroic ratio is obtained by dividing the intensity of crystalline polar phases with the intensities of all the  $\alpha$ -phase peaks present, in the FT-IR spectra, as shown in Figure 4.9. Figure 4.15 (a) shows the dichroic ratio obtained by dividing the intensity of the 1274  $\text{cm}^{-1}$  peak belonging to the crystalline  $\beta$ -phase with that of the intensities of all the  $\alpha$ -phase peaks present at 764, 796, 976, 1149, 1210  $\text{cm}^{-1}$ . Figure 4.15 (b) shows the dichroic ratio obtained by dividing the peak intensities of  $\gamma$ -phase present at 1232  $\text{cm}^{-1}$  with the intensities of all the  $\alpha$ -phase peaks present. Figure 4.15 (c) shows the dichroic ratio obtained between the intensity of the 832  $\text{cm}^{-1}$  peak belonging to polar electroactive phases (contributed by both  $\beta$  and  $\gamma$ -phases), as shown in the peak

deconvolution in Figure 4.10 (a) and intensities of all the  $\alpha$ -phase peaks. The relative amount of the electroactive polar phases increases till 1 weight percentage filler loading. This corroborates that the addition of *r*GO-Ag contributes in inducing the electroactive polar phases in PVDF. However, the dichroic ratio falls at 2 weight percentage of *r*GO-Ag filler loading. These results indicate firmly that the content of *r*GO-Ag contributes to the process of transformation of  $\alpha$ -phase to polar ( $\beta$  and  $\gamma$ ) electroactive phases. It is noteworthy here that in this work the variation of the dichroic ratio is observed without any external mechanical or electrical treatment to the PVDF nanocomposite films.[37]

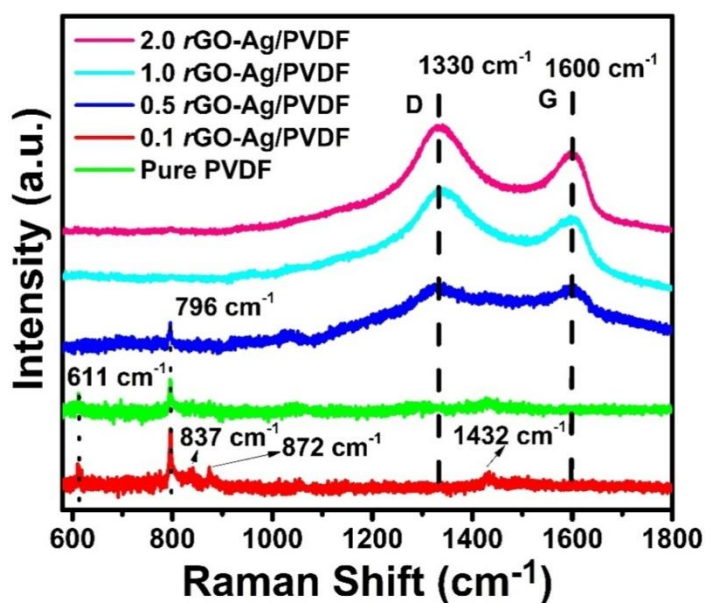


**Figure 4.16** Shows the Raman spectra of pure PVDF and *r*GO-Ag/PVDF nanocomposite in the region of 580–1800  $\text{cm}^{-1}$ .

Figure 4.16 displays the Raman spectra of pure PVDF with prominent peaks at 611 and 796  $\text{cm}^{-1}$ . Both the peaks are attributed to  $\alpha$ -phase or TGT $\bar{\text{G}}$  chain conformation.[38, 39] The peak at 611  $\text{cm}^{-1}$  is attributed to  $\text{CF}_2$  vibrations. The TGT $\bar{\text{G}}$  chain conformation is a trans conformation. The trans conformations are formed due to the induced strain that results because of the swelling in the amorphous regions. Both these peaks are absent in 1.0 *r*GO-Ag/PVDF and 2.0 *r*GO-Ag/PVDF. This

significantly emphasizes the advent of crystalline phases in the PVDF with the high level of incorporation of *r*GO-Ag by weight percentage, in it. The diffused bands present between 1075 and 1095  $\text{cm}^{-1}$  are attributed to  $\alpha$ -phase.[40] The peaks at 837  $\text{cm}^{-1}$ , 872  $\text{cm}^{-1}$  and 1432  $\text{cm}^{-1}$  in pure PVDF is attributed to  $-\text{CH}_2-$  rocking vibrations, CC symmetric stretching and  $\text{CH}_2$  scissoring vibrations respectively. The small peaks at 837  $\text{cm}^{-1}$ , 872  $\text{cm}^{-1}$  and 1432  $\text{cm}^{-1}$  are suppressed in all the *r*GO-Ag/PVDF composites.[41] This indicates the interactions between *r*GO-Ag and PVDF chains. The Raman spectra of *r*GO-Ag becomes prominent in case of 0.5, 1.0 and 2.0 *r*GO-Ag/PVDF composites. The peaks at 1130  $\text{cm}^{-1}$  and 1600  $\text{cm}^{-1}$  are attributed to D and G band of *r*GO. The D band is assigned to disorder in graphitic structure. The D band originates from breathing mode of  $\kappa$ -point photons of  $A_{1g}$  symmetry. The G band is attributed to the in-plane displacement of carbon atoms in hexagonal carbon sheets. The G band arises due to first-order scattering of the  $E_{2g}$  phonon of  $sp^2$  hybridization of carbon atoms.[33]

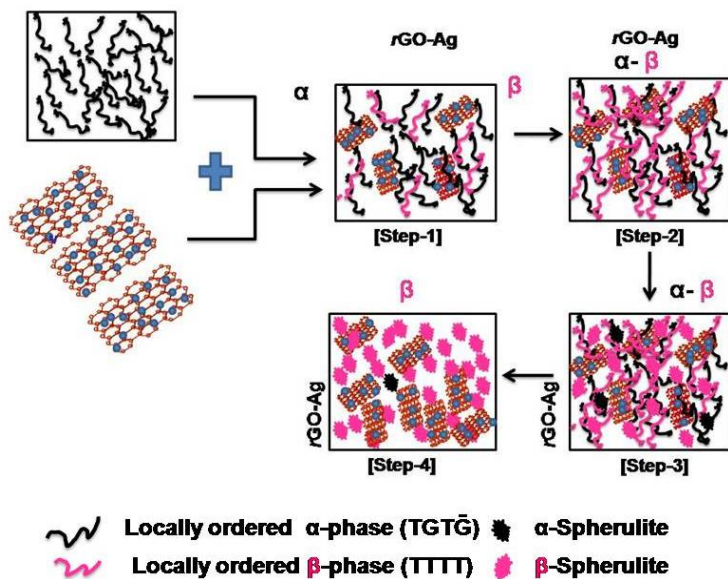


**Figure 4.17** Shows the schematic illustration of the intermediate steps in the formation of the  $\beta$ -phase in *r*GO-Ag-PVDF.

The stepwise formation of the  $\beta$ -phase from the  $\alpha$ -phase is illustrated in Figure 4.17. The transformation occurs in steps. The reason

behind the transformation is the electrostatic interaction between the PVDF polymer chains and *r*GO-Ag fillers. In the first step locally ordered  $\beta$ -phase starts to nucleate from  $\alpha$ -phase which is associated with the simultaneous formation of locally ordered  $\alpha$ -phase. With time a greater number of  $\beta$ -phase crystals start forming from the  $\alpha$ -phase. In the second step the number of  $\beta$ -phase crystals increases. In the third step the aggregation of locally ordered  $\beta$ -phase takes place and spherulite type structures are formed. In the third step the piezoelectric properties are introduced in the nanocomposite. After more time the complete transformation of locally ordered  $\beta$ -phase to spherulite type structures takes place, which marks the end of the final phase.[20, 21]

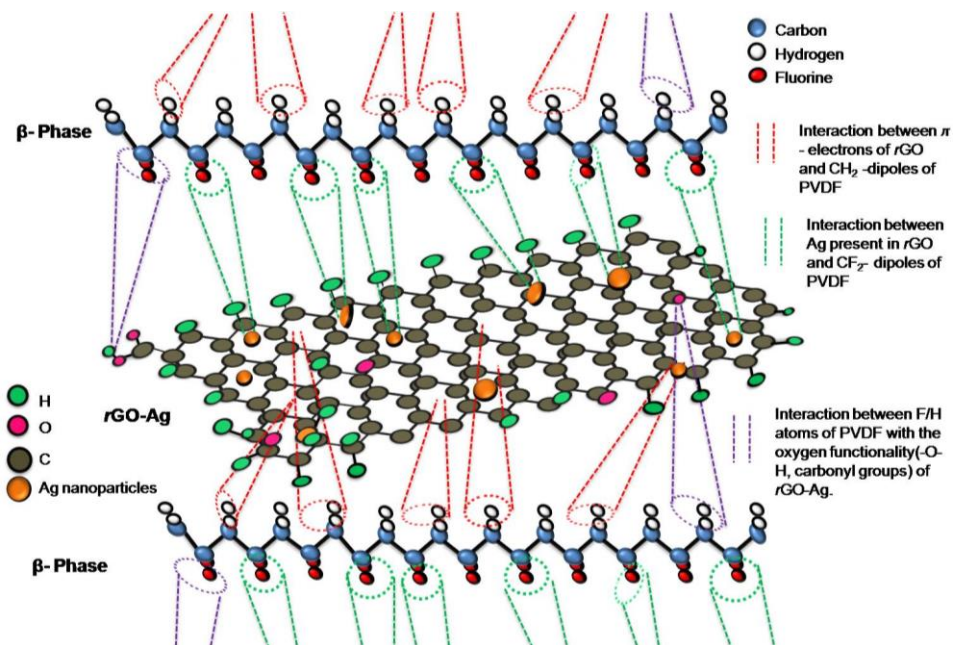


**Figure 4.18** Shows the schematic illustration of the *r*GO-Ag nano-sheets and PVDF molecules. The *r*GO-Ag nano-sheets, interacts with the PVDF chains to form the piezoelectric polar phases.

The schematic illustration of the formation mechanism of the piezoelectric polar phases is shown in Figure 4.18. The  $\pi$ -electrons of the graphene in the *r*GO-Ag are attracted to the  $-\text{CH}_2-$  dipoles of PVDF. In the same way, the  $-\text{CF}_2-$  dipoles of PVDF are repelled by the  $\pi$ -electrons of the

graphene present in the *r*GO-Ag. The positively charged Ag ions are attracted by the  $-\text{CF}_2-$  dipoles of PVDF whereas the Ag ions repel the  $-\text{CH}_2-$  dipoles. The F and H atoms interact with the oxygen-containing functional groups present in the graphene. The formation mechanism of the nucleation of the piezoelectric polar phases in PVDF after the addition of *r*GO-Ag can be explained by the attraction and repulsion between the dipoles present in the PVDF.

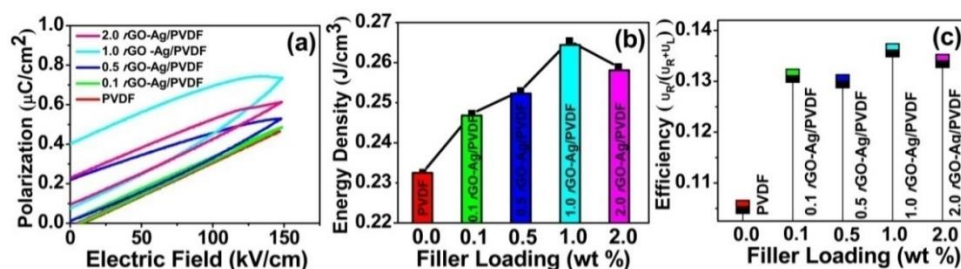


**Figure 4.19** Shows the (a) *P-E* Loop test (b) variation of Energy Density (c) efficiency of the various *r*GO-Ag/PVDF nanocomposite films.

To study ferroelectric properties of the *r*GO-Ag/PVDF nanocomposite films, Polarization-Electric Field (*P-E*) Loop characterization was done which is shown in Figure 4.19 (a). The ferroelectric properties are completely dependent on the electroactive phases of the PVDF polymer. The polymer matrix has ferroelectric domains that are randomly oriented within it. The ferroelectric domains consist of molecular dipoles which contribute directly to the piezoelectricity. The molecular dipoles are formed by the interaction of the filler nanomaterial with the PVDF monomers. The *P-E* hysteresis curve shows the variation of the filler loading. This indicates the fact that *r*GO-Ag leads to the variation of charge contained within the nanocomposite. The charge storage capability of the nanocomposite is indicated by the formation of the loop with a definite area. The loop is formed due to the existence of phase separation between the voltage and charge. The phase separation is a consequence of the energy dissipation of the nanocomposite. The polarization gradually increases with the increase of the applied electric field. This indicates that the molecular dipoles are aligned in the direction

of the applied electric field. A maximum polarization value of  $0.738 \mu\text{C cm}^{-2}$  was obtained in the 1.0 *r*GO-Ag/PVDF nanocomposite film at an applied electric field of  $148 \text{ kV cm}^{-1}$ . The remnant polarization in 1.0 *r*GO-Ag/PVDF nanocomposite film was found to be  $0.160 \mu\text{C cm}^{-2}$ , whereas in pure PVDF the value found was  $0.012 \mu\text{C cm}^{-2}$ . The molecular dipoles which are formed due to the interaction between the PVDF chains and the oxygen containing functional groups accumulates charge on the application of an external electric field. This remnant polarization is due to the charge accumulation of the molecular dipoles.

The released energy density ( $U_R$ ) from the different *r*GO-Ag/PVDF nanocomposites are shown in Figure 4.19 (b). The Maximum released energy density in *r*GO-Ag/PVDF is  $0.26 \text{ J cm}^{-3}$ , whereas in pure PVDF the value is  $0.232 \text{ J cm}^{-3}$ . The released energy density at any electric field is calculated by integrating the area (the shaded region with blue stripes) between the *P-E* loop and the electric field coordinate as shown in Figure 4.20. The energy loss ( $U_L$ ) is calculated by integrating the area enclosed by the *P-E* loop. The total energy density ( $U_T$ ) is found from the algebraic addition of the released energy density and the energy loss density of the *r*GO-Ag/PVDF nanocomposite films which is shown in Figure 4.19 (c). The changes in the polarization properties indicates that the interactions between *r*GO-Ag and PVDF are strong. The high charge retention property of *r*GO-Ag/PVDF nanocomposite makes it a probable candidate for using it as a charge storage material.



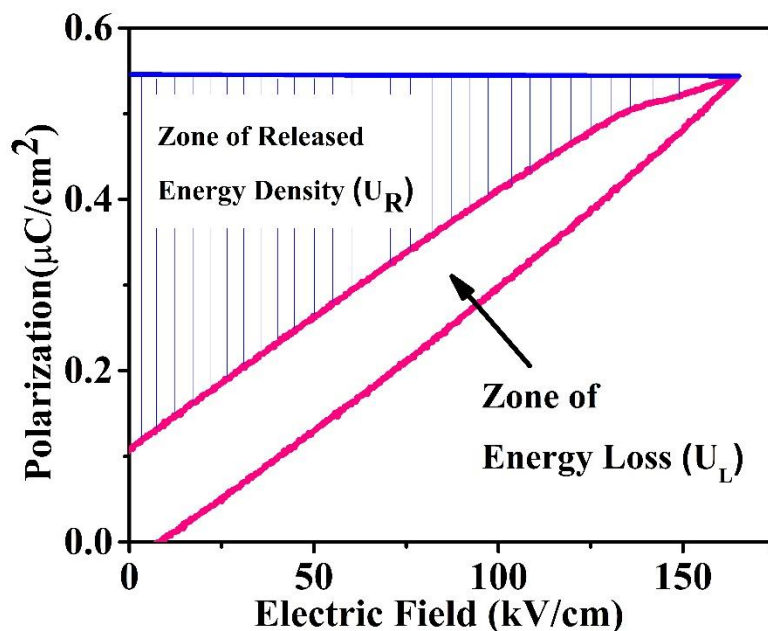


**Figure 4.20** Shows the P-E loop test curve where the shaded area (blue bars) shows the zone of Released Energy Density ( $U_R$ ), area inside the P-E loop shows the zone of Energy Loss ( $U_L$ ).

To calculate the efficiency of the nanocomposites the area under the zone of Released Energy Density ( $U_R$ ) and the area under the zone of Energy Loss is calculated ( $U_L$ ) and the ratio of  $U_R$  to ( $U_R + U_L$ ) is found out.

#### 4.2.7 Electrical Characterizations

To find out the efficacy of the  $rGO$ -Ag/PVDF nanocomposite films to harvest mechanical energy, electrode-composite-electrode (ECE) stack was fabricated where aluminium foil with conducting adhesive was used as an electrode. The ECE stack was completely encapsulated with PDMS layer. Human palm impulse was imparted to all the  $rGO$ -Ag/PVDF nanocomposite films, with different filler loadings. None of the  $rGO$ -Ag/PVDF nanocomposite films were electrically poled. As, the  $rGO$ -Ag/PVDF films showed an enhancement in the formation of the piezoelectric polar phases with the increase in filler loading, hence it was expected that it would also show greater piezo-response. The 1.0  $rGO$ -Ag/PVDF nanocomposite showed an open circuit voltage of 18 V, which is highest among all the nanocomposites that are discussed in this work. The



1.0 *r*GO-Ag/PVDF nanocomposite showed the highest stabilization of the piezoelectric polar crystalline phases and hence the output voltage response from it is also high. The open circuit voltage obtained from the pure PVDF was 0.1 V. The open circuit voltage detected from all the nanocomposites with different filler loadings of *r*GO-Ag is shown in Figure 4.21 (a). The piezoelectric potential is formed due to the instantaneous change in the crystal structure of the PVDF based film on the application of an external pressure. With the increase of the addition of filler material, the piezo-response increases compared to pure PVDF. However, the energy harvesting performance falls in case of 2.0 *r*GO-Ag in PVDF. The decrease in the piezoelectric voltage output at higher filler loading may be due to the presence of leakage of charges in the conducting *r*GO networks within the polymer nanocomposite that is sandwiched between the two electrodes.

The generated open circuit voltage shows a positive and negative half cycle. This is a consequence of the complete cycle of imparting and releasing of human hand impulse on the piezoelectric energy harvesting device. Figure 4.21 (b) indicates that the positive amplitude and the negative amplitude are a consequence of the imparting and releasing of the hand impulse, respectively. The positive half cycle of the generated voltage is greater because it depends on the magnitude of the impulse whereas the negative half cycle depends on the elasticity of the material which brings it back to its original shape.

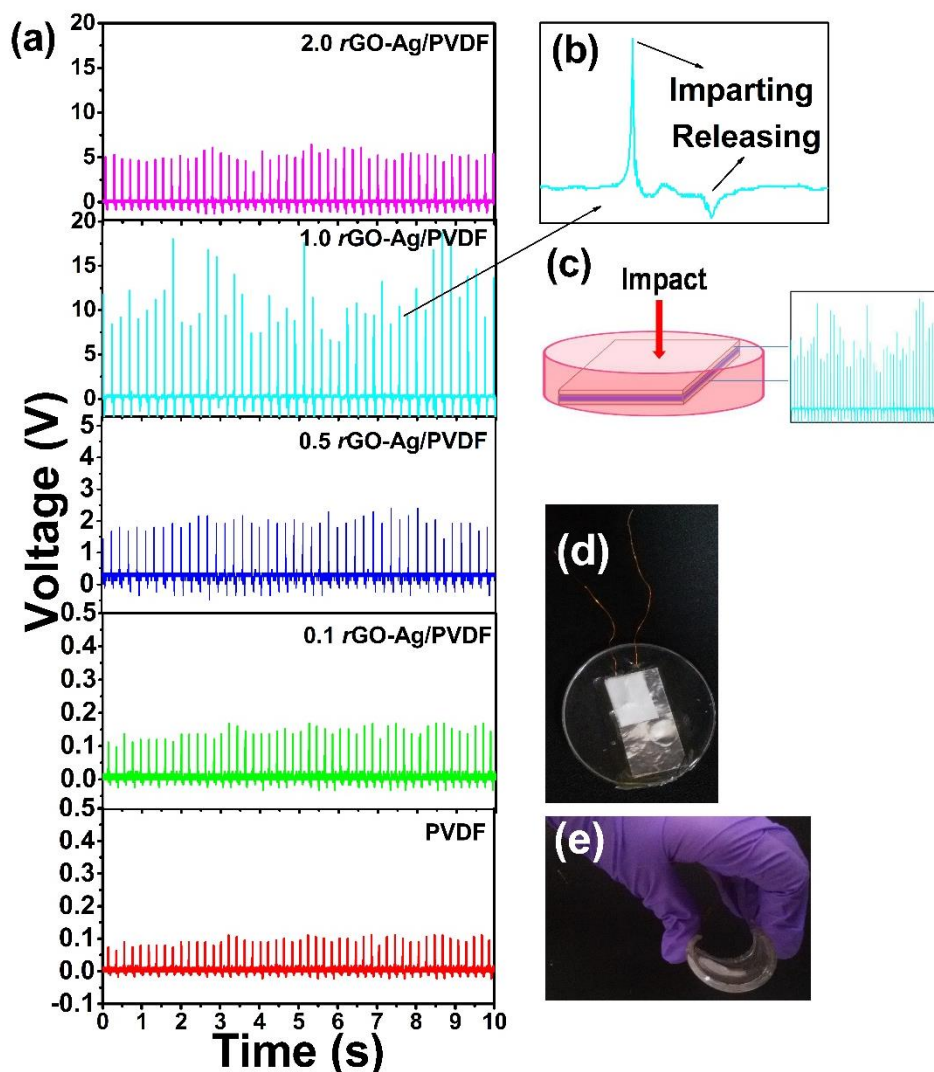


**Figure 4.21** Shows the (a) generated open circuit output voltage that is measured by exciting the 2.0 rGO-Ag/PVDF, 1.0 rGO-Ag/PVDF, 0.5 rGO-Ag/PVDF, 0.1 rGO-Ag/PVDF, PVDF nanocomposite films by hand impulse imparting (b) magnified image of one cycle of voltage response from the nanocomposite after imparting and releasing the impulse (c) schematic diagram of the electrical connections that were used for the measurement of the electrical output using digital storage oscilloscope with hand impulse imparting and relaxation (d) photograph of the PENG that is encapsulated by PDMS (e) flexibility of PENG.

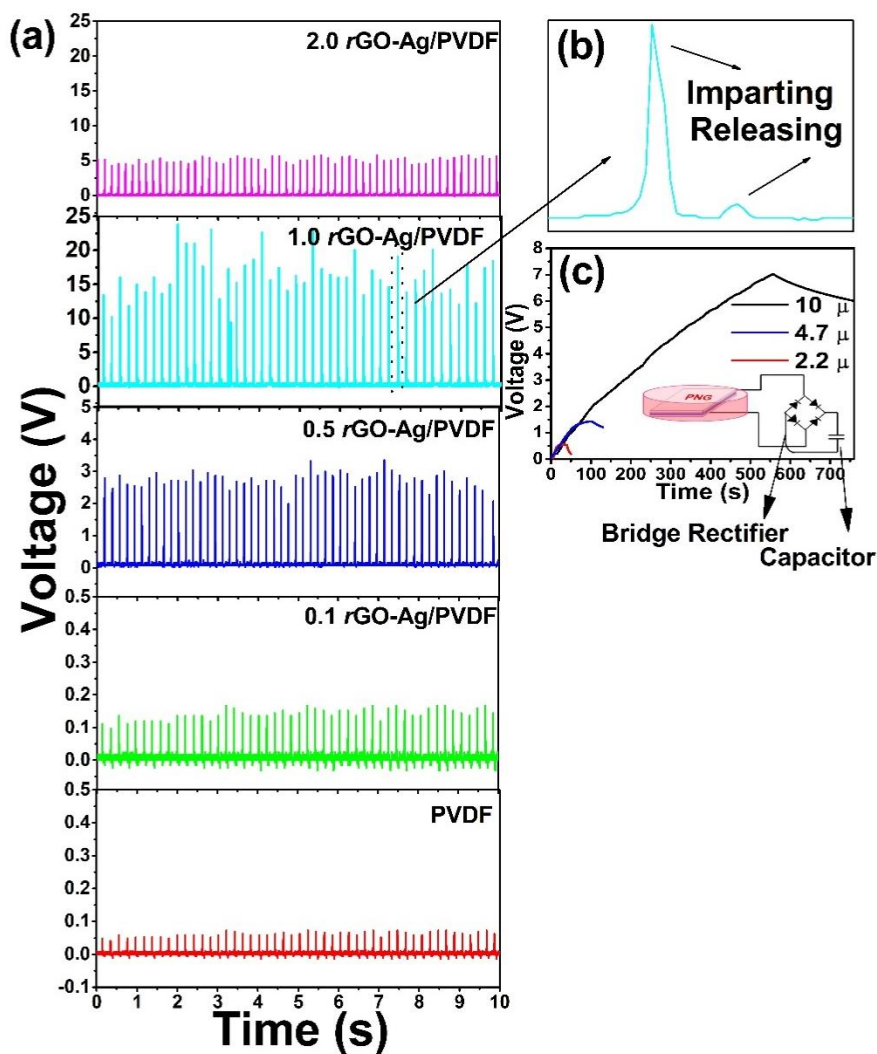


**Figure 4.22** Shows the (a) rectified output voltage that is measured by exciting the 2.0 rGO-Ag/PVDF, 1.0 rGO-Ag/PVDF, 0.5 rGO-Ag/PVDF, 0.1 rGO-Ag/PVDF, PVDF nanocomposite films by human hand impulse imparting (b) magnified image of one cycle of rectified voltage response of the nanocomposite after imparting and releasing the impulse (c) voltage that is accumulated in three capacitors having individual capacitance of 2.2, 4.7 and 10  $\mu\text{f}$ .

Figure 4.22 (a) shows the rectified voltage signal from the rGO-Ag/PVDF based nanocomposite films. A peak rectified output voltage of 24 V was detected from the 1.0 rGO-Ag/PVDF nanocomposite. The output voltage generated from the pure PVDF was close to 0.1 V. A bridge rectifier

was used to rectify the open circuit voltage from the PVDF based energy harvesting device. Rectification leads to the detection of a higher magnitude of voltage because full wave bridge rectifier prevents voltage degradation that arises due to the different resistances present in the piezoelectric nanocomposite films. The rectification process also eliminates self-cancellation of voltages due to polarity mismatch.[42] Figure 4.22 (b) shows the magnified view of a single cycle of the rectified open circuit voltage. The appearance of a small peak at the positive quadrant is a result of the overall rectification of the piezoelectric output signal. The PENG could charge capacitors when connected through a bridge rectifier. This demonstrate the practical applicability of the PENG as a candidate that can recharge batteries. Figure 4.22 (c) shows the capacitor charging performance of the PENG. Three different capacitances of 2.2, 4.7 and 10  $\mu\text{f}$  was connected to the output of a bridge rectifier, under the condition of constant hand impulse imparting on the PENG. The capacitor charging characteristics shows that the voltage rises exponentially and attains a steady state after some time.

Figure 4.23 (a) shows the short-circuit current generated by the PENG upon continuous hand impulse imparting. It was found that the short circuit current increases as the amount of *r*GO-Ag content also increases. In case of the pure PVDF based nanocomposite film the short circuit current reached a value of  $\approx 0.03 \mu\text{A}$ , whereas the maximum current from 1.0 *r*GO-Ag/PVDF nanocomposite reached a value of  $\approx 1.05 \mu\text{A}$ . The short circuit current reduced in case of 2.0 *r*GO-Ag/PVDF. The reduction may be attributed to the presence of the leakage of charges that are present in the conducting graphene material within the PVDF matrix. Figure 4.23 (b) shows the magnified image of a single cycle of the short-circuit current generated by the *r*GO-Ag/PVDF based nanocomposite.

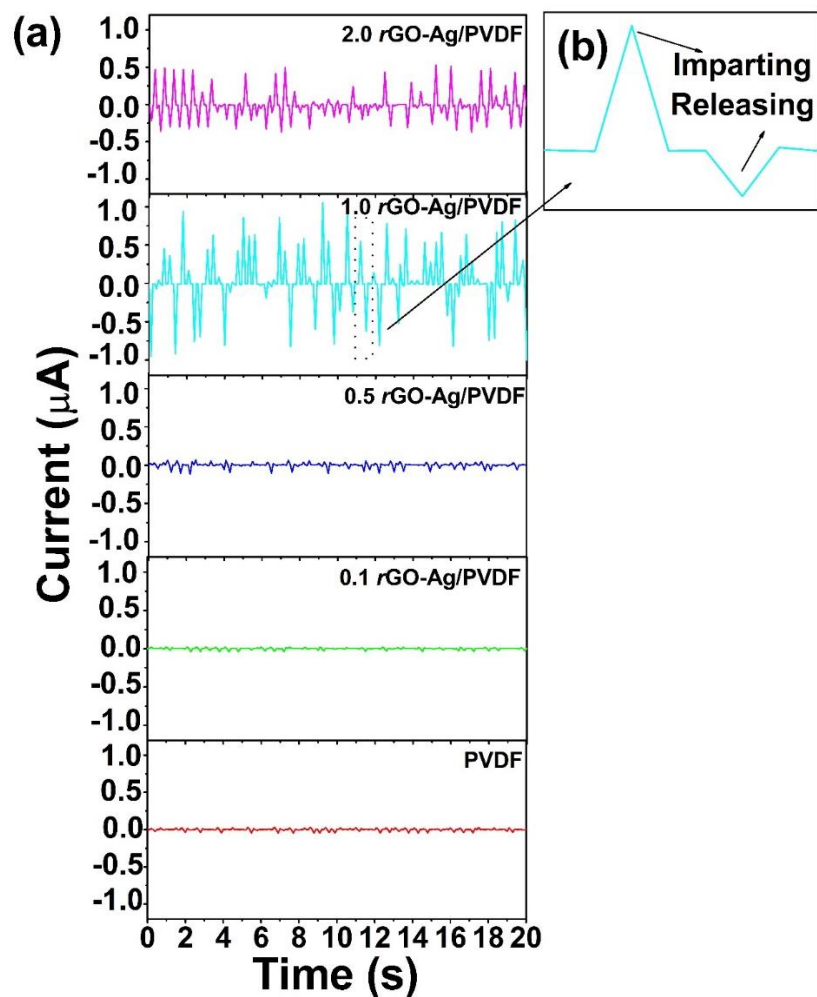


**Figure 4.23** Shows the (a) short-circuit current that is measured by exciting the 2.0 rGO-Ag/PVDF, 1.0 rGO-Ag/PVDF, 0.5 rGO-Ag/PVDF, 0.1 rGO-Ag/PVDF, PVDF nanocomposite films by hand impulse imparting (b) magnified image of one cycle of current response due to human palm impulse imparting and releasing action.

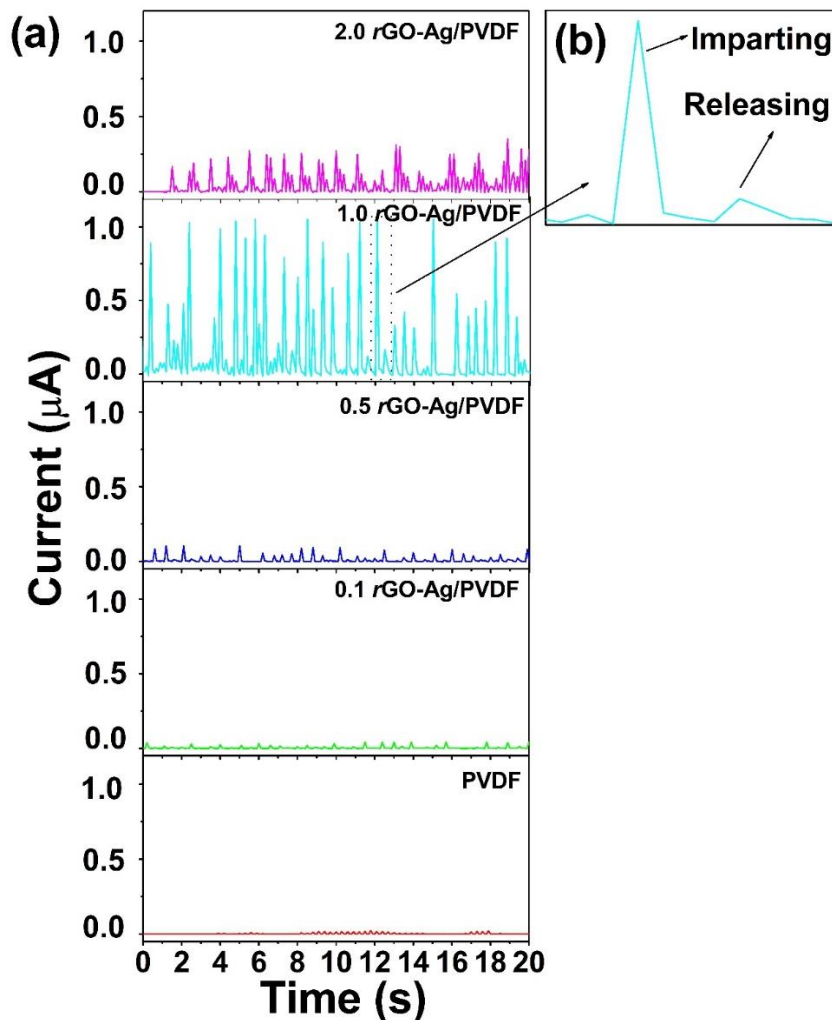


**Figure 4.24** Shows the (a) rectified short-circuit current that is measured by exciting the 2.0 rGO-Ag/PVDF, 1.0 rGO-Ag/PVDF, 0.5 rGO-Ag/PVDF, 0.1 rGO-Ag/PVDF, PVDF nanocomposite by hand impulse imparting (b) magnified image of one cycle of current response due to human palm impulse imparting and releasing action.

Figure 4.24 (a) shows the rectified short-circuit current generated by the different loadings of rGO-Ag/PVDF nanocomposites. The maximum value of the current detected from the 1.0 rGO-Ag/PVDF nanocomposite was found to be  $\sim 1.05 \mu\text{A}$ , whereas the current that was detected from the pure PVDF nanocomposite was  $\sim 0.023 \mu\text{A}$ . From the current characterization it can be concluded that there is an increasing trend of current till 1 percentage weight loading of rGO-Ag, thereafter at 2

percentage weight loading it decreases. The magnified view of a single cycle of the rectified short-circuit current is shown in Figure 4.24(b).

#### 4.2.8 Energy Efficiency Calculation

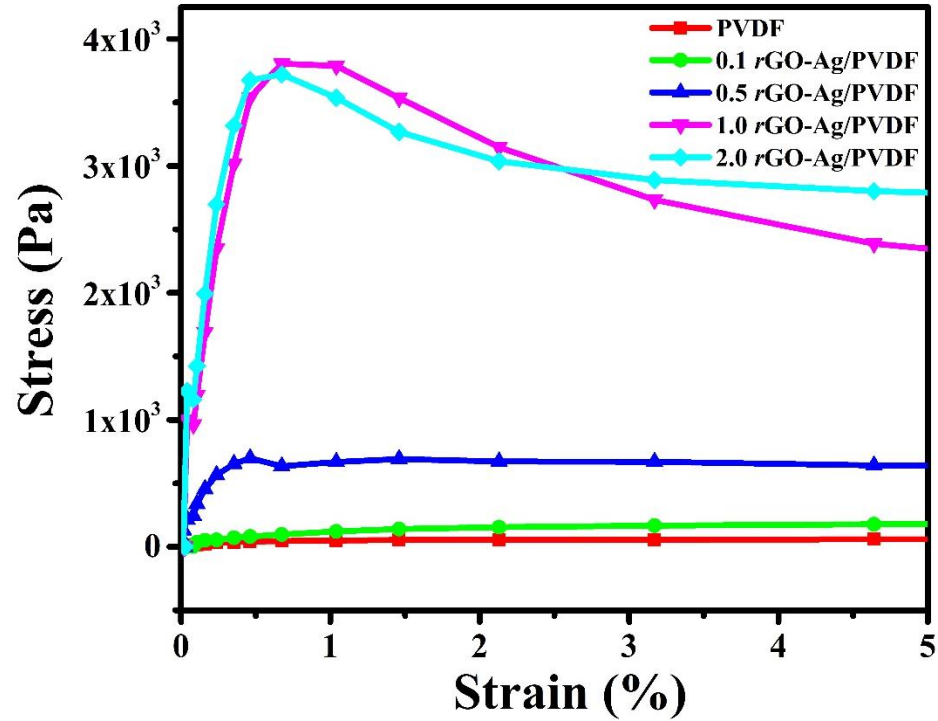


**Figure 4.25** Shows the Stress vs Strain curve of the rGO-Ag/PVDF nanocomposite with different filler loadings.

Figure 4.25 shows the Stress vs Strain curve for all the nanocomposites. The Young's Modulus of the 1.0 rGO-Ag/PVDF nanocomposite is found out to be 7.533 kPa from the Stress vs Strain Curve.

#### Calculation of Imparted Pressure ( $\sigma$ )

The pressure imparted on the PENG is calculated from the following equations:

$$m g h = \frac{1}{2} m v^2 \quad (4.9)$$

$$(F - m g) \Delta t = m v \quad (4.10)$$

$$\sigma = \frac{F}{S} \quad (4.11)$$

Where  $m$  is the mass (the magnitude of mass shown in digital weigh balance by human palm striking which is equal to 0.400 kilograms),  $g = 9.8 \text{ N/kg}$ ,

$h = 0.3 \text{ m}$ ,  $\Delta t = 0.528 \text{ s}$  (which is the average time between two voltage spikes),  $F$  is the force applied on the PENG,  $\sigma$  is the stress applied on the PENG,  $S$  is the surface area of the electrodes.

The force applied on the PENG was found out to be  $\approx 6 \text{ N}$ , and applied stress  $\sigma \approx 4.6 \text{ kPa}$ .

The energy harvesting efficiency of the PENG during capacitor charging is calculated as follows. The input energy ( $W_{in}$ ) provided to the PENG while charging the capacitor during one cycle is given by

$$W_{in} = F \times \Delta l = F \frac{\sigma l}{Y} = 36 \times 10^{-6} \text{ J} \quad (4.12)$$

Where  $F$  is (6 N) which is the applied force on 1.0 rGO-Ag/PVDF based PENG,  $\Delta l$  is the deformation of the PENG when stress  $\sigma$  (4.6 kPa) is applied and  $Y$  is the Young's Modulus (7.533 kPa) of the nanocomposite and the average thickness of the nanocomposite film  $l$  is 0.01 mm.

The total input mechanical energy transfer to the PENG during the capacitor charging is given by

$$E_{in} = \frac{t}{\Delta t} W_{in} = 0.0375 \text{ J} \quad (4.13)$$

where  $t$  is the total time required to charge the capacitor, which is 550 s.  $\Delta t$  is the average time duration between the two consecutive voltage peaks of the imparting pressure cycles, which is 0.528 s.

$$E_{out} = \frac{1}{2} CV^2 = 245 \times 10^{-6} \text{ J} \quad (4.14)$$

The overall energy efficiency ( $\eta$ ) can be found out from the ratio of the electrical energy stored ( $E_{out} = \frac{1}{2} CV^2$ ) in the 10  $\mu\text{f}$  capacitor while charging and the total mechanical energy used ( $E_{in}$ ) to charge the 10  $\mu\text{f}$  capacitor.

$$\eta = \frac{E_{out}}{E_{in}} \times 100 \% = 0.65 \% \quad (4.15)$$



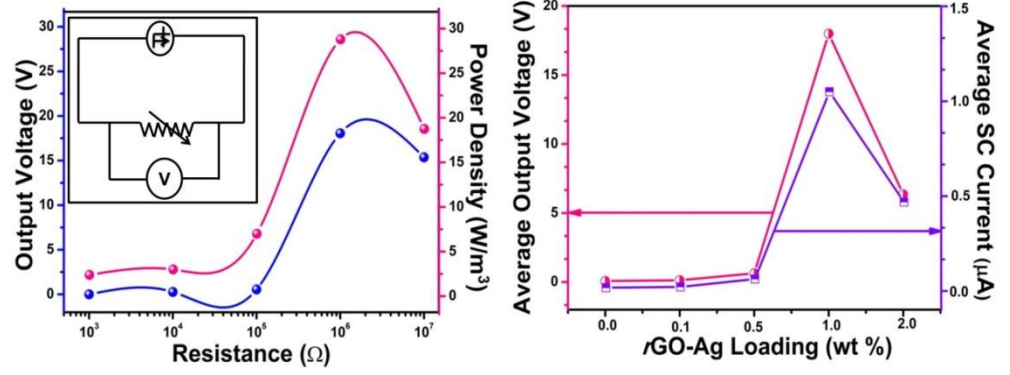


**Figure 4.26** Shows the (a) output voltage generated from 1.0 rGO-Ag/PVDF across the various resistance and the corresponding power density (b) average open circuit voltage and short circuit current generated by the various rGO-Ag/PVDF nanocomposite.

The maximum power transferred by the PENG was found out by connecting various resistances (1k, 10k, 100k, 1M, 10M) across the two terminals of the PENG. The PENG was mechanically excited, and the voltage drop across it was measured, which is shown in Figure 4.26 (a). A maximum voltage of 18 V was detected across 1 MΩ resistance. The maximum power density was found out to be 28 W m<sup>-3</sup>. The reason behind this phenomenon can be attributed to the maximum power transfer theorem according to which maximum external power is drawn from a source of electrical energy with a finite internal resistance when the resistance of the load is equal to the resistance of the source, as seen from the output terminals of the source. The following formula was used to calculate the maximum power density:

$$P = \frac{V \times I}{Volume} = \frac{V^2}{R_L \times Volume} \quad (4.16)$$

The theoretical current can be estimated from

$$I = \sqrt{\frac{P}{R_L}} \quad (4.17)$$

where  $I$  is the current,  $R_L$  is the load resistance,  $P$  is the power across  $R_L$ . The theoretical current was found out to be 28 μA, which is much higher

than the actual peak current value of  $1.05\ \mu\text{A}$ . The reason behind this observation is the fact that the internal resistances present within the nanocomposite consume some of the power.[31] The average output voltage and the average output current from the  $r\text{GO-Ag/PVDF}$  nanocomposite with different weight percentage loading is shown in Figure 4.26 (b).

In Figure 4.27 the schematic illustration of the working mechanism of PENG is shown. When the top of the PENG is excited with hand tapping, due to polarization of the dipoles takes place within the PENG. The polarization of electrical charges is oriented in the vertical direction within the nanocomposite, which is depicted in Figure 4.27 (a). In the same way piezo-potential also develops across the electrodes when fingers of the palm are flexed to which the PENG is affixed, as shown in Figure 4.27 (b). Fewer charges are produced on the nanocomposite with bending action as compared to tapping. The reason behind this is because compression/relaxation force acts only along the axis around which the PENG flexes. This causes a charge imbalance within both the electrodes and to neutralize this effect, charges start flowing through the external circuit. This leads to the flow of piezoelectric current in the external circuit. When the compressive excitation ceases the piezo-potential vanishes and again a charge imbalance is created on the electrodes. In order to neutralize this effect, charges flow through the external circuit but now in the opposite direction.[43] This explains the presence of the positive and negative half cycle in the piezoelectric output response.

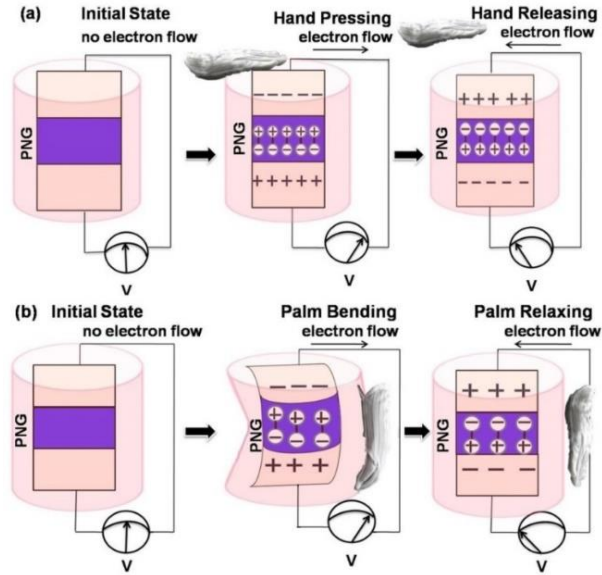


**Figure 4.27** Shows the schematic illustration of the working mechanism of the PENG when excited by (a) human palm tapping (b) bending.

The PENG was attached to human palm on the fingers, to harvest biomechanical energy. The output voltage generated is shown in Figure 4.28 (a) under continuous finger opening and closing action. The PENG was also affixed to a foot wearable flip-flop/slipper and the output voltage was recorded by wearing and simulating foot-stepping/walking action, which is shown in Figure 4.28 (b). Table 4.1 shows that the present work exhibit output performance comparable to that of other piezoelectric nanogenerators.

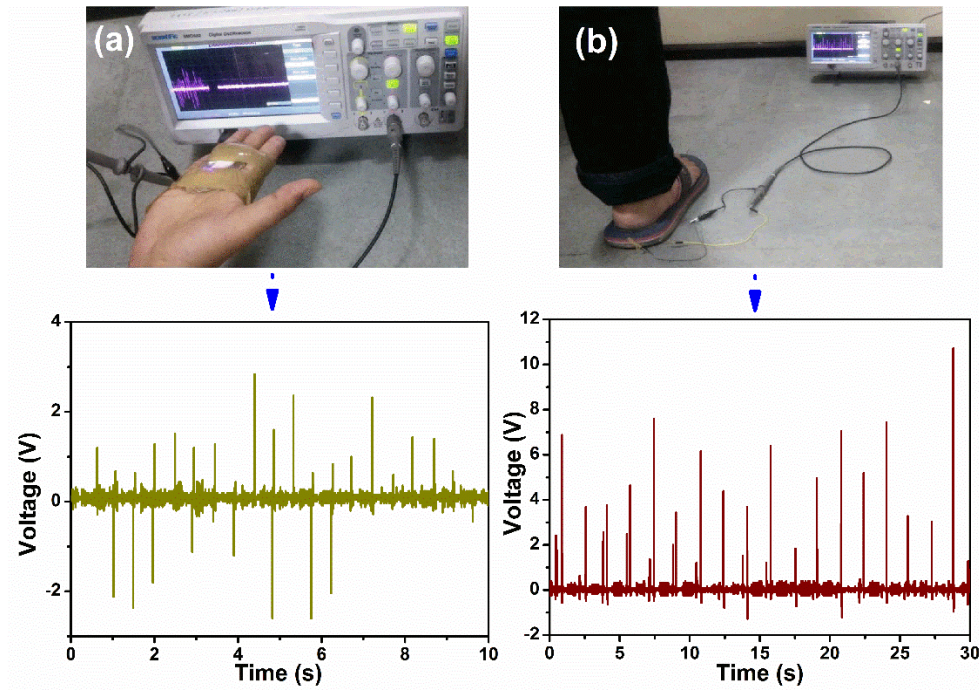


**Figure 4.28** Shows the (a) piezoelectric output voltage generated by the PENG when attached to human fingers under opening and closing motion, in the inset the PENG is shown attached to human fingers on the palm (b) piezoelectric output voltage generated by the PENG when attached to a footwear under footstep excitation conditions, in the inset image of the PENG is shown which is attached to a footwear.

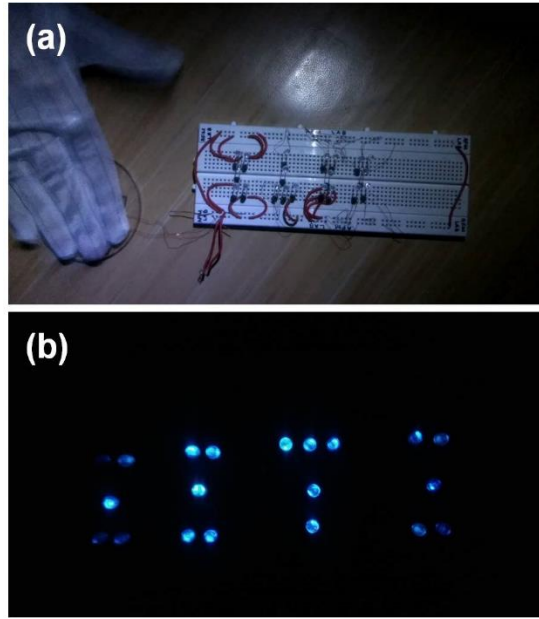


**Figure 4.29** Shows the (a) LEDs that are connected in parallel connection on a bread board before lighting, inset schematic shows the circuit diagram of the arranged LEDs (b) lighting of the LEDs that are arranged to form the letters “IITI”, which is the abbreviation of Indian Institute of Technology Indore, after imparting continuous hand impulse.

The PENG was connected in parallel connection on a breadboard to 20 commercial blue light-emitting diodes (LEDs), without connecting any rectifier in between, which is shown in Figure 4.29 (a). The figure given in the inset shows the circuit diagram of the connections following which the LEDs were connected to the breadboard. Under constant hand impulse imparting action on the PENG, the LEDs start flickering light which is shown in Figure 4.29 (b). This indicates that the PENG showed in this work can be used for the development of clean energy-based lighting solutions for the future.

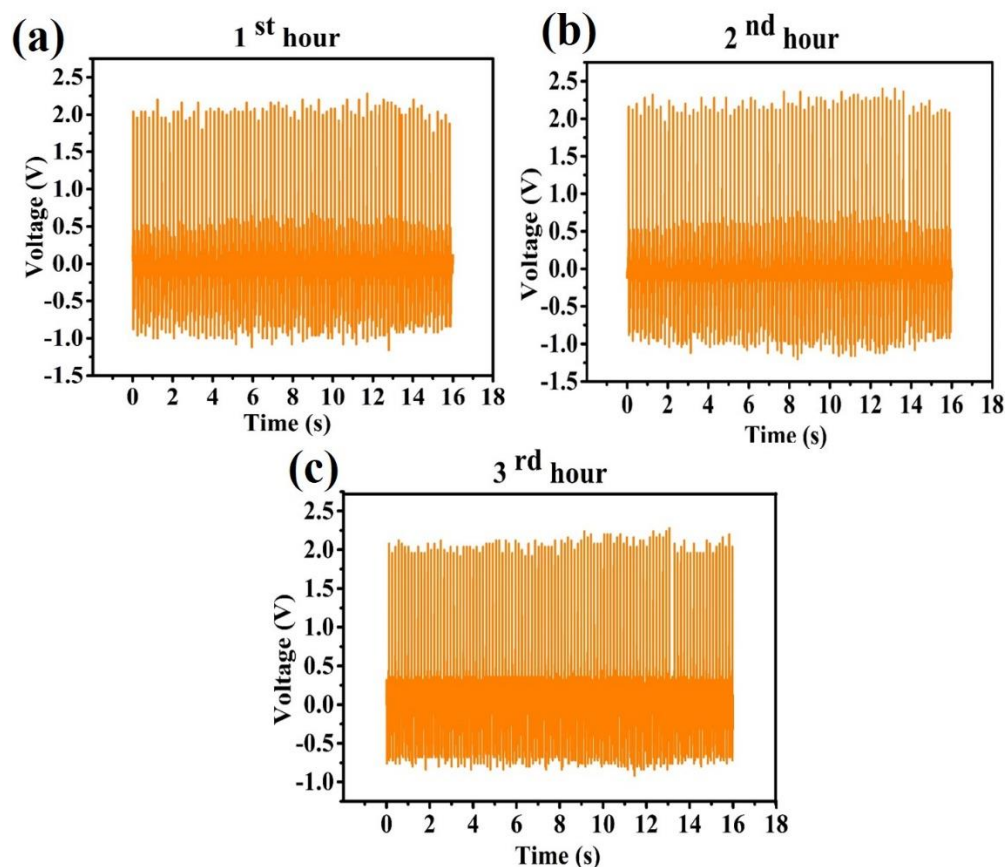


**Figure 4.30** Shows the durability, where the PENG was tested with mechanically operated piezoelectric excitation source consecutively for three hours.

To examine the long-term usage, we tested the PENG with a mechanically operated piezoelectric excitation source consecutively for three hours, which is shown in Figure 4.30. We used the mechanically operated piezoelectric excitation source because it is not possible to provide constant stress imparting and releasing by human hand for hours. The output voltage is less in this case as the magnitude of the stress provided by the mechanically operated excitation source is less compared to human hand impulse. The good durability of the PENG indicates its robust capability for body wearable applications for long-term usage. The good durability of the PENG is attributed to the PDMS encapsulation of the nanocomposite films.

**Table 4.1:** Performance details of previously reported data on energy harvesting devices

Sl. No.	Name of the Piezoelectric Device	Poling Voltage and Duration	Input Source	Voltage	Current /Current Density
1	Cellulose-ZnO[44]	Data Unavailable	Ultrasonic bath	80 mV	1.25 $\mu$ A
2	ZnO NWs/PVDF[45]	100 kV/mm	Linear motor	0.2 V	10 nA/cm <sup>2</sup>
3	Li doped ZnO NW-Polymer Composite[46]	105 kV/cm; 20 h	Bending stage	180 V	50 $\mu$ A
4	BaTiO <sub>3</sub> NPs[47]	100 kV/cm; 20 h	Bending stage	3.2V	350 nA
5	ZnSnO <sub>3</sub> [7]	Not Found	Human finger press	40 V	0.4 $\mu$ A
6	KNbO <sub>3</sub> Nanorod[48]	150 kV; 1h	Linear motor	3.2 V	67.5 nA
7	KNbO <sub>3</sub> Nanowires[49]	5.0 kV/mm; 1 h	Bending tester	10.5 V	1.3 $\mu$ A
8	BaTiO <sub>3</sub> Nanotubes[5]	80 kV/cm; 12 h	Linear motor	5.5 V	350 nA
9	KNN-LTS[50]	2 KV/mm; 24 h	Mechanical tapping	53 V	15 $\mu$ A
10	Native cellulose microfiber[27]	Not Poled	Human hand punching	30 V	500 nA

11	PVDF/AlO- <i>r</i> GO[22]	Not Poled	Human hand punching	36 V	0.8 $\mu$ A
12	BCTZ NPs– polymer composite[51]	1.5 kV: Data Unavailable	Bending stage	15 V	0.8 $\mu$ A
13	PVDF-TrFE Film/Graphene Oxide[24]	30 MV/m, 1 h	Hydraulic/ Mechanical fatigue tester	4.3 V	1.88 $\mu$ A
14	GAg/PVDF[25]	Not Poled	Mechanical stepper machine	100mV	0.1 nA
15	Fe- <i>r</i> GO/PVDF[21]	Not Poled	Human hand punching	5.1 V	0.254 $\mu$ A
16	Fe- <i>r</i> GO/PVDF[20]	Not Poled	Human finger tapping	1.2 V	342 nA
17	CNT/PVDF[20]	Not Poled	Human finger tapping	2.5 V	680 nA
18	<i>r</i> GO-Ag/PVDF (Present Work)	Not Poled	Human hand punching	18 V	1.05 $\mu$ A

### 4.3 Summary

In this work *r*GO-Ag/PVDF based nanocomposite is successfully synthesized through solution casting method. Different weight percent loading of *r*GO-Ag was added to the PVDF. The nanocomposite films were encapsulated by PDMS to fabricate a Piezoelectric Nanogenerator (PENG).



The nucleation and stabilization of piezoelectric polar phases were studied through XRD and FTIR spectroscopy. Instead of the intrinsic non-polar  $\alpha$ -phase that is present in PVDF, the rGO-Ag propagates the nucleation of the crystalline piezoelectric  $\beta$  (majorly) and  $\gamma$ -phases. *P-E* loop test showed the energy storage capability of the nanocomposite films. The PENG showed a peak open circuit voltage of  $\sim 18$  V and a short circuit current of  $\sim 1.05$   $\mu$ A. A peak power density of  $\sim 28$   $\text{Wm}^{-3}$  was shown by the PENG when connected across 1  $\text{M}\Omega$  resistor. The PENG showed an efficiency of 0.65 %. The biomechanical energy harvesting performance of the PENG is shown by attaching it to human palm, followed by continuous finger flexing. Also, to show body/apparel/foot-wear attachable applications of the PENG it was affixed to flip-flop/slippers and output voltage response was recorded with human foot-tapping excitations. The PENG could light 20 commercial blue light-emitting diodes simultaneously under repeated human palm impulse imparting. The PENG could charge a 10  $\mu$ F capacitor to 7 V in  $\sim 550$  s. The PENG showed a good durability and can be used for a prolonged period.

## References

1. Ren, X. *et al.*, (2018). Wind energy harvester based on coaxial rotatory freestanding triboelectric nanogenerators for self-powered water splitting. *Nano Energy*, 50, 562–570.
2. Ren, X. *et al.*, (2017). Magnetic force driven noncontact electromagnetic-triboelectric hybrid nanogenerator for scavenging biomechanical energy. *Nano Energy*, 35, 233–241.
3. Ren, X. *et al.*, (2017). Triboelectric nanogenerators based on fluorinated wasted rubber powder for self-powering application. *ACS Sustainable Chemistry and Engineering*, 5(2), 1957–1964.
4. Saravanakumar, B. *et al.*, (2013). Fabrication of a ZnO nanogenerator for eco-friendly biomechanical energy harvesting. *RSC Advances*, 3(37), 16646–16656.

5. Lin, Z.H. *et al.*, (2012). BaTiO<sub>3</sub> nanotubes-based flexible and transparent nanogenerators. *Journal of Physical Chemistry Letters*, 3(23), 3599–3604.
6. Park, K.I. *et al.*, (2013). Flexible and large-area nanocomposite generators based on lead zirconate titanate particles and carbon nanotubes. *Advanced Energy Materials*, 3(12), 1539–1544.
7. Alam, M.M. *et al.*, (2015). Lead-free ZnSnO<sub>3</sub>/MWCNTs-based self-poled flexible hybrid nanogenerator for piezoelectric power generation. *Nanotechnology*, 26(16), 165403-165408.
8. Huang, C.T. *et al.*, (2010). GaN nanowire arrays for high-output nanogenerators. *Journal of the American Chemical Society*, 132(13), 4766–4771.
9. Ren, X. *et al.*, (2016). Flexible Lead-Free BiFeO<sub>3</sub>/PDMS-Based Nanogenerator as Piezoelectric Energy Harvester. *ACS Applied Materials and Interfaces*, 8(39), 26190–26197.
10. Lee, K.Y. *et al.*, (2015). Transparent flexible stretchable piezoelectric and triboelectric nanogenerators for powering portable electronics. *Nano Energy*, 14, 139–160.
11. Persano, L. *et al.*, (2015). Active polymer nanofibers for photonics, electronics, energy generation and micromechanics. *Progress in Polymer Science*, 43, 48–95.
12. Kepler, R.G. *et al.*, (1992). Ferroelectric polymers. *Advances in Physics*, 41(1), 1–57.
13. Martins, P. *et al.*, (2014). Electroactive phases of poly(vinylidene fluoride): Determination, processing and applications. *Progress in Polymer Science*, 39(4), 683–706.
14. Wang, W. *et al.*, (2010). Effect of electric field on the structure and piezoelectric properties of poly(vinylidene fluoride) studied by density functional theory. *Polymer*, 51(15), 3575–3581.
15. Song, D. *et al.*, (1990). Formation of  $\beta$ -phase microcrystals from the melt of PVF<sub>2</sub>-PMMA blends induced by quenching. *Journal of*

*Materials Science*, 25(1), 57–64.

16. Tao, M. *et al.*, (2013). Effect of solvent power on PVDF membrane polymorphism during phase inversion. *Desalination*, 316, 137–145.
17. Kuilla, T. *et al.*, (2010). Recent advances in graphene based polymer composites. *Progress in Polymer Science*, 35(11), 1350–1375.
18. Pumera, M. (2010). Graphene-based nanomaterials and their electrochemistry. *Chem. Soc. Rev.*, 39, 4146–4157.
19. Wang, D. *et al.*, (2012). Improved dielectric properties of nanocomposites based on poly(vinylidene fluoride) and poly(vinyl alcohol)-functionalized graphene. *ACS Applied Materials and Interfaces*, 4(11), 6273–6279.
20. Pusty, M. *et al.*, (2017). Comparative Study with a Unique Arrangement to Tap Piezoelectric Output to Realize a Self Poled PVDF Based Nanocomposite for Energy Harvesting Applications. *ChemistrySelect*, 2(9), 2774–2782.
21. Karan, S.K. *et al.*, (2015). Self-powered flexible Fe-doped RGO/PVDF nanocomposite: An excellent material for a piezoelectric energy harvester. *Nanoscale*, 7(24), 10655–10666.
22. Karan, S.K. *et al.*, (2016). An Approach to Design Highly Durable Piezoelectric Nanogenerator Based on Self-Poled PVDF/AlO-rGO Flexible Nanocomposite with High Power Density and Energy Conversion Efficiency. *Advanced Energy Materials*, 6(20), 1–12.
23. Garain, S. *et al.*, (2016). Design of in Situ Poled Ce<sup>3+</sup>-Doped Electrospun PVDF/Graphene Composite Nanofibers for Fabrication of Nanopressure Sensor and Ultrasensitive Acoustic Nanogenerator. *ACS Applied Materials and Interfaces*, 8(7), 4532–4540.
24. Bhavanasi, V. *et al.*, (2016). Enhanced Piezoelectric Energy Harvesting Performance of Flexible PVDF-TrFE Bilayer Films with Graphene Oxide. *ACS Applied Materials and Interfaces*, 8(1), 521–529.
25. Sinha, T.K. *et al.*, (2016). Graphene-Silver-Induced Self-Polarized

- PVDF-Based Flexible Plasmonic Nanogenerator Toward the Realization for New Class of Self Powered Optical Sensor. *ACS Applied Materials and Interfaces*, 8(24), 14986–14993.
26. Chen, G. *et al.*, (2016). Nano-KTN@Ag/PVDF composite films with high permittivity and low dielectric loss by introduction of designed KTN/Ag core/shell nanoparticles. *Journal of Materials Chemistry C*, 4(34), 8070–8076.
  27. Alam, M.M. (2016). Native Cellulose Microfiber-Based Hybrid Piezoelectric Generator for Mechanical Energy Harvesting Utility. *ACS Applied Materials and Interfaces*, 8(3), 1555–1558.
  28. Fuh, Y.K., *et al.*, (2015). Hybrid Energy Harvester Consisting of Piezoelectric Fibers with Largely Enhanced 20 V for Wearable and Muscle-Driven Applications. *ACS Applied Materials and Interfaces*, 7(31), 16923–16931.
  29. Ghosh, R. *et al.*, (2013). Chemically reduced graphene oxide for ammonia detection at room temperature. *ACS Applied Materials and Interfaces*, 5(15), 7599–7603.
  30. Ghosh, R. *et al.*, (2016). Reduced Graphene Oxide-Based Piezoelectric Nanogenerator with Water Excitation. *IEEE Transactions on Nanotechnology*, 15(2), 268–273.
  31. Jung, W.S. *et al.*, (2015). High Output Piezo/Triboelectric Hybrid Generator. *Scientific Reports*, 5, 1–6.
  32. Akhavan, O. (2015). Bacteriorhodopsin as a superior substitute for hydrazine in chemical reduction of single-layer graphene oxide sheets. *Carbon*, 81(1), 158–166.
  33. Pusty, M. *et al.*, (2016). Synthesis of Partially Reduced Graphene Oxide/Silver Nanocomposite and Its Inhibitive Action on Pathogenic Fungi Grown Under Ambient Conditions. *ChemistrySelect*, 1(14), 4235–4245.
  34. Kanik, M. *et al.*, (2014). Spontaneous High Piezoelectricity in Poly(vinylidene fluoride) Nanoribbons Produced by Iterative

- Thermal Size Reduction Technique. *ACS Nano*, 8(9), 9311–9323.
35. Li, Y. *et al.*, (2014). Multiple stage crystallization of gamma phase poly(vinylidene fluoride) induced by ion-dipole interaction as revealed by time-resolved FTIR and two-dimensional correlation analysis. *Polymer*, 55(18), 4765–4775.
  36. Xing, C. *et al.*, (2012). Impact of ionic liquid-modified multiwalled carbon nanotubes on the crystallization behavior of poly(vinylidene fluoride). *Journal of Physical Chemistry B*, 116(28), 8312–8320.
  37. Alamusi, *et al.*, (2012). Evaluation of piezoelectric property of reduced graphene oxide (rGO)–poly(vinylidene fluoride) nanocomposites. *Nanoscale*, 4(22), 7250.
  38. Casciola, M. *et al.*, (2008). Polyvinylidene fluoride/zirconium phosphate sulfophenylphosphonate nanocomposite films: Microstructure and mechanical properties. *Journal of Materials Chemistry*, 18(36), 4291–4296.
  39. Elashmawi, I.S. *et al.*, (2015). Raman, morphology and electrical behavior of nanocomposites based on PEO/PVDF with multi-walled carbon nanotubes. *Results in Physics*, 5, 105–110.
  40. Singh, P. *et al.*, (2014). Ferroelectric polymer-ceramic composite thick films for energy storage applications. *AIP Advances*, 4(8), 087117-087128.
  41. Constantino, C.J.L., *et al.*, (2005). Phase transition in poly(vinylidene fluoride) investigated with micro-Raman spectroscopy. *Applied Spectroscopy*, 59(3), 275–279.
  42. Zhang, X.J. *et al.*, (2014). Fabrication of multi-functional PVDF/RGO composites via a simple thermal reduction process and their enhanced electromagnetic wave absorption and dielectric properties. *RSC Advances*, 4(38), 19594–19601.
  43. Ding, R. *et al.*, (2017). High-performance piezoelectric nanogenerators composed of formamidinium lead halide perovskite nanoparticles and poly(vinylidene fluoride). *Nano Energy*, 37, 126–

135.

44. Kumar, A. *et al.*, (2011). Flexible ZnO-cellulose nanocomposite for multisource energy conversion. *Small*, 7(15), 2173–2178.
45. Liao, Q. *et al.*, (2014). Flexible piezoelectric nanogenerators based on a fiber/ZnO nanowires/paper hybrid structure for energy harvesting. *Nano Research*, 7(6), 917–928.
46. Shin, S.H. *et al.*, (2014). Lithium-doped zinc oxide nanowires-polymer composite for high performance flexible piezoelectric nanogenerator. *ACS Nano*, 8(10), 10844–10850.
47. Park, K.I. *et al.*, (2012). Flexible nanocomposite generator made of BaTiO<sub>3</sub> nanoparticles and graphitic carbons. *Advanced Materials*, 24(22), 2999–3004.
48. Jung, J.H. *et al.*, (2012). Lead-free KNbO<sub>3</sub> ferroelectric nanorod based flexible nanogenerators and capacitors. *Nanotechnology*, 23, 375401-375407.
49. Joung, M.R. *et al.*, (2014). Piezoelectric nanogenerators synthesized using KNbO<sub>3</sub> nanowires with various crystal structures. *Journal of Materials Chemistry A*, 2(43), 18547–18553.
50. Xue, Q.T. *et al.*, (2015). A record flexible piezoelectric KNN ultrafine-grained nanopowder-based nanogenerator. *AIP Advances*, 5(1), 1–8.
51. Baek, C. *et al.*, (2016). A flexible energy harvester based on a lead-free and piezoelectric BCTZ nanoparticle-polymer composite. *Nanoscale*, 8(40), 17632–17638.

## **CHAPTER 5**

---

### **Gold Nanoparticle-Cellulose/PDMS Nanocomposite Based Mechanical Energy Harvesting Application**

---

#### **5.1 Overview**

In the previous chapters mechanical energy harvesting based on PVDF is shown in which nanomaterials are incorporated. The addition of nanomaterial is found to have formed polar crystalline phases in PVDF. The formation of the polar crystalline phases has led to the overall enhancement of the piezoelectric output. However, there is another approach that is found in the recent literature towards the development of flexible piezoelectric nanogenerators. Polydimethylsiloxane (PDMS) is a class of polymeric organosilicon compounds that contains siloxane (Si-O-Si) functional groups. PDMS behaves as an ideal substrate and composite matrix because it has unique properties. PDMS is a host polymer for fabricating sensors and actuators because it has low Young modulus, it is biocompatible, optically transparent, cost-effective and has good thermal and chemical stability.[1] Mechanical energy harvesting application can have a broad scale of applicability if the energy harvester can be fabricated in any shape or size depending on the application. Previously it was reported that composite based materials shows good mechanical energy harvesting performance.[1–3] Bones, hairs, collagen fibrils, peptide, cellulose, sugar cane are some of the naturally occurring piezoelectric materials.[4] Cellulose is such a piezoelectric material among them that is obtained abundantly in the nature in its natural form and is eco-friendly and biocompatible. Some of the advantages of cellulose are that it has low density, high mechanical strength, thermal stability and chemical resistance. It is also found that cellulose exhibits both direct and converse piezoelectricity.[5] Cellulose is comprised of both crystallites and amorphous regions of low degree of order.[6,7] It was found that several works were reported previously for energy

harvesting applications using cellulose. Previously, Zheng *et al.* showed energy harvesting using piezoelectric porous nano fibrils of cellulose.[8] Also, the synthesis of cellulose nanofibrils (CNF) follows specialized synthesis techniques which are neither simple nor cost effective.[9] Recently, in an excellent research work it was shown by Alam *et al.* that a piezoelectric generator can be realized by the incorporation of Carbon nanotubes (CNTs) in PDMS matrix.[10] Native cellulose exists in two forms cellulose I and cellulose II. cellulose I is crystalline and has scattered amorphous regions of low degree of order, whereas cellulose II requires further processing techniques to prepare. In this work native cellulose microfibrils is used that is easily available commercially. Also using this approach, the synthesis process remains simple and cost effective. Nanostructures such as ZnS[11], SbSI[12], BaTiO<sub>3</sub>[13], ZnO[14] were reported to be used with cellulose for piezoelectric energy harvesting purpose, but the output voltage was less compared to the results that is obtained in this work. The advantage of incorporating nanostructures in polymer is that due to the high surface to volume ratio a greater deformation of the piezoelectric nanostructures takes place. As a result the output electrical response enhances and the energy conversion efficiency significantly enhances.[15,16] Noble metal nanoparticles are biocompatible and are easy to synthesize. The addition of noble metal nanoparticles were reported previously in synthetic piezoelectric polymers like PVDF.[17] It is well known that incorporation of nanostructured metal oxides in PVDF results in the nucleation and stabilization of polar piezoelectric phases.[18] It is also known that the addition of nano-particles in a polymer nanocomposite leads to an enhancement in the dipole polarization relaxation mechanism.[19] Due to these features gold nanoparticles (Au NPs) are selected as nano-fillers to be incorporated in PDMS along with cellulose to form a nanocomposite. Also, the advantages of working with Au NPs are that they are chemically stable, are easy to synthesize and shows good reproducibility.



In this work native cellulose powder and Au NPs are added in PDMS to form a nanocomposite. It is found that the dielectric constant of Cellulose/PDMS rises as compared to pure PDMS. The dielectric constant of the Au NP-Cellulose/PDMS rises by a very small margin, however it is found that the dielectric loss decreases. Such a material can also be used as a dielectric capacitor. Dielectric capacitors have high power density owing to the very high rate of energy uptake and release. They have very wide applications in hybrid electric vehicles, medical fields, future weapon systems, *etc.*[20] Compared to ceramic based dielectric materials the Au NP-Cellulose/PDMS nanocomposite not only shows excellent flexibility but is also easy to process and can be molded in any shape or size depending on specific applications. Cellulose is an abundantly available natural polymer, which is biodegradable due to which it might be specifically suitable for medical applications. Some of the other advantages of incorporating Au NPs as nano-fillers are that they contribute low filler loading due to which properties like density, flexibility and easy processability of the polymers are not compromised.

In this chapter the fabrication of a piezoelectric mechanical energy harvesting device is demonstrated using the Au NP-Cellulose/PDMS nanocomposite which is named as piezoelectric nanogenerator (PENG). The open circuit voltage from the Au NP-Cellulose/PDMS is greater as compared to Cellulose/PDMS. This enhancement in the piezoelectric signal is attributed to the interaction of cellulose to the large surface area of the Au NPs. The PENG delivered an open circuit voltage of 6V, when periodically excited by a force of 3N generated by a mechanically operated external source. The PENG could charge a 10 $\mu$ F capacitor in 677s. The energy conversion efficiency was estimated to be 1.8%. By direct hand impulse imparting the PENG could light two commercial blue light emitting diodes (LEDs). A touch sensing application of the PENG is also realized.

## 5.2 Results and Discussion

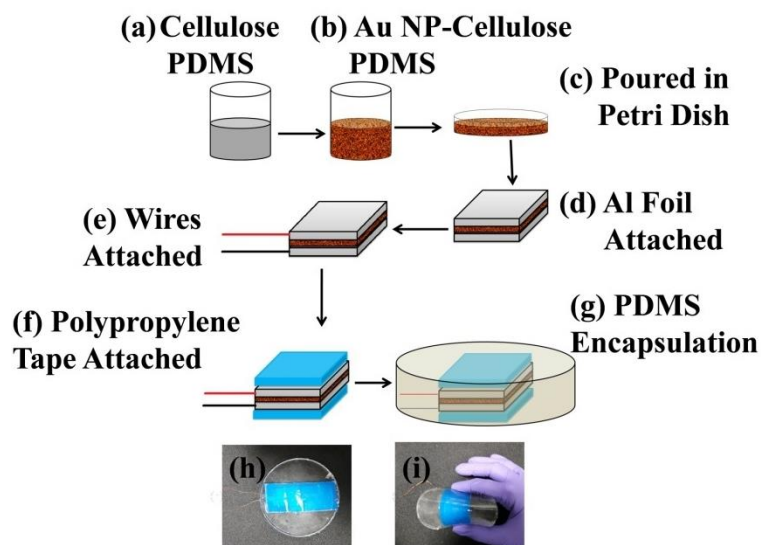


**Figure 5.1.** Shows the schematic diagram of the step-wise fabrication process of the PENG. (a) Cellulose and PDMS were mixed in a beaker (b) Within the mixture of cellulose and PDMS varied quantity of Au NP colloid was added (c) The mixture was poured in a petri dish and was put in an electric furnace for curing (d) After curing the Au NP–Cellulose/PDMS nanocomposite was cut and Aluminium electrode was attached to the top and bottom of the composite (e) After that Polypropylene (PP) tapes were attached on the top to completely cover the Aluminium electrodes (f) Conducting wires were attached to both the surfaces (g) The nanocomposite was encapsulated by PDMS (h) Optical image of the as fabricated PENG (i) Optical image showing the flexibility of the PENG.

### 5.2.1 Synthesis of Au nanoparticle seeds:[21]

To prepare Gold Nanoparticle Seeds, 200 $\mu$ L of 1 M NaOH (Alfa Aesar, India) was added to 100mL of 1mM HAuCl<sub>4</sub>·3H<sub>2</sub>O (Alfa Aesar, India) and the solution was boiled. The solution was stirred with a PTFE coated magnetic stirrer at 300 rpm. After a while, 38.8mM Na<sub>3</sub>Ctr.2H<sub>2</sub>O (Merck, India) was added to the solution quickly. After some time, the colour of the solution turned wine red. Now deionized (DI) water was added to the solution to make it 100ml final volume.

### 5.2.2 Synthesis of Au nanoparticles:

10 mL of seed solution from the previous step was added to a clean beaker, within which 227  $\mu\text{L}$  of 44.7 mM  $\text{HAuCl}_4 \cdot 3\text{H}_2\text{O}$  was added and the solution was boiled under constant stirring at 300rpm. After that 176  $\mu\text{L}$  of 38.8 mM  $\text{Na}_3\text{Cit} \cdot 2\text{H}_2\text{O}$  was added. The reaction process continued for half an hour.

### 5.2.3 Fabrication of Piezoelectric Nanogenerator (PENG):

10g of PDMS (as well as curing agent) was taken in a beaker, within which 500mg of cellulose was added (Loba Chemie, India). After that 2, 20, 200 $\mu\text{L}$  colloid of Gold Nanoparticle was added to the previous mixture. Also, a cellulose and PDMS mixture was prepared, without addition of Gold Nanoparticles for comparison purpose. The mixture was poured in a petri dish and was placed in an electric furnace at a temperature of 70°C, for 1 hour. This step was necessary for the curing/hardening of the PDMS mixture. After the curing process is completed the composites were cut in 3.5  $\times$  8.5 cm dimensions. Aluminium tapes of 3  $\times$  8 cm dimensions with conductive adhesives were attached on top of the as cut composite. Conductive wires were attached to the adhesive of the Aluminium tapes. Then the Aluminium electrodes and the wires were completely covered with Polypropylene tapes. This step was done to eliminate triboelectric effect arising due to direct contact between the Aluminium electrodes and the outer PDMS encapsulation. After this stage the device was placed in a petri dish and was encapsulated by a layer of PDMS to protect the device from mechanical stress, environmental factors like humidity to ultimately increase its longevity. The complete schematic of the fabrication of the PENG is shown in Figure 5.1.

#### 5.2.4 Material Characterizations

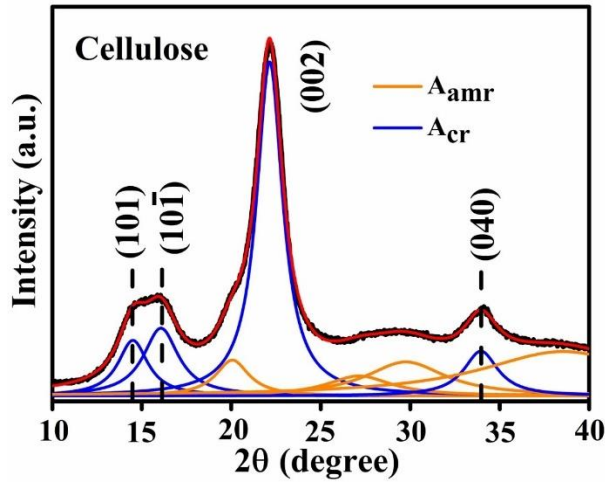


**Figure 5.2.** Shows the XRD spectra of cellulose powder.

The X-ray Diffraction (XRD) Spectra of pure cellulose is shown in Figure 5.2. The XRD spectra of pure cellulose matches with cellulose I. Cellulose I show peaks at  $14.7^\circ$ ,  $16.36^\circ$ ,  $22.38^\circ$  and  $34.28^\circ$  corresponding to (101),  $(10\bar{1})$ , (002) and (040) planes, respectively. The crystallinity shown by pure cellulose is found to be 62.6 %. The degree of crystallinity of the cellulose used is calculated from the following equation: [10]

$$\chi_c = \frac{\sum A_{cr}}{\sum A_{cr} + \sum A_{amr}} \times 100 \% \quad (5.1)$$

where  $\sum A_{cr}$  = total integral area of crystalline peaks,  $\sum A_{amr}$  = total integral area of amorphous halos.

Figure 5.3 (a) shows the field emission-scanning electron microscopy (FE-SEM) image of the cellulose powder, where the cellulose powder is comprised of cellulose microfibrils and some agglomerated microfibrils. The figure in the inset shows the magnified image of one microfibril which has a diameter of roughly 5  $\mu\text{m}$ . Figure 5.3 (b) shows the surface of the Au NP-Cellulose nanocomposite, where the cellulose microfibrils are completely encapsulated by the PDMS. This indicates the formation of a homogenous nanocomposite of Au NPs, cellulose and PDMS.

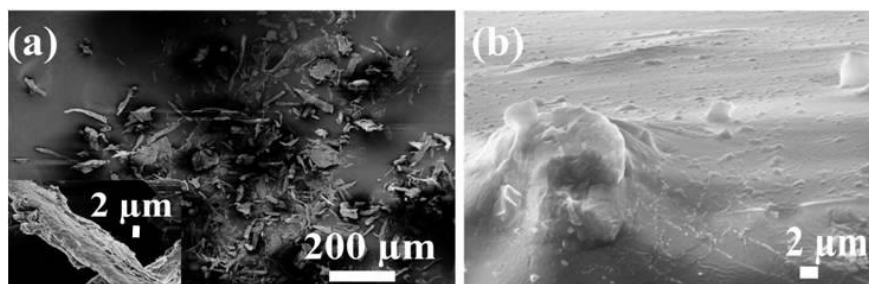


**Figure 5.3.** Shows the FE-SEM image of (a) cellulose microfibrils, the inset shows single microfibrils of cellulose (b) surface of the Au NP-Cellulose nanocomposite, indicating the complete encapsulation of cellulose microfibrils by PDMS.

The particle size of the nanostructures also affects the Surface plasmon resonance (SPR) phenomenon. Au NPs with diameter less than 50 nm absorb light, whereas the Au NPs with larger diameter scatters incident light.[22] The reason behind this phenomenon is that the size of the NPs are considerably smaller than the wavelength of the incident light due to which the distribution of the light and consequently the charges formed due to the polarization, both are uniform. In Au NPs with diameter greater than 50 nm scattering leads to the damping of the motion of the electrons. The relation between the NP size and the full width at half maximum (FWHM),  $\Gamma$  of the SPR band is given by the following equation:[23]

$$\Gamma = a + \frac{b}{R} \quad (5.2)$$

where  $a$  and  $b$  are material constants and  $R$  is the radius of the NP. With the increase in size of the diameter of the NPs, the fraction of electrons close to the surface of the NPs represents a smaller fraction of the total oscillating electrons and hence the total damping is reduced. Thus, the NP size plays an important role in the light dependent polarization of the Au NPs. In this work the size of the Au NPs are less than 50 nm which indicates that the Au NPs are SPR active.

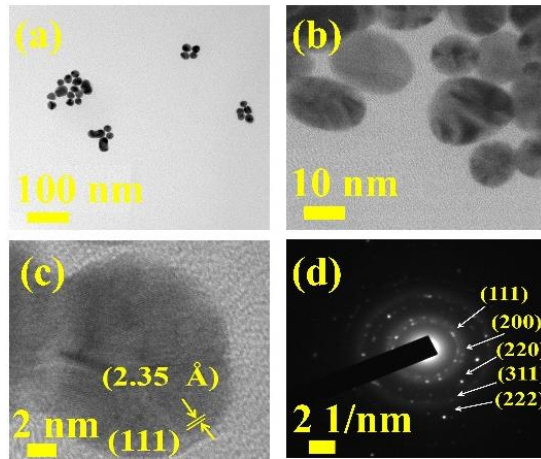


**Figure 5.4.** Shows the (a, b) HRTEM images of Au NPs at two different magnifications (c) lattice fringes (d) SAED pattern corresponding to fcc Au.

The morphological characterization of the synthesized Au NPs were carried out by High resolution- Transmission electron microscopy (HR-TEM). The HR-TEM characterization shows aggregated Au NPs in Figure 5.4 (a,b). The nanoparticles are spherical in shape with an average diameter of  $\sim 15$  nm. The lattice fringes of a single Au NP in the HR-TEM image as shown in Figure 5.4 (c) indicates a  $d$ -spacing of  $2.35\text{\AA}$  corresponding to (111) plane of fcc Au. The SAED pattern as shown in Figure 5.4 (d) shows polycrystalline behaviour of the sample and the pattern can be indexed to fcc phase of metallic Au.[21] The Au NPs were synthesized in this work excluding any surfactant.

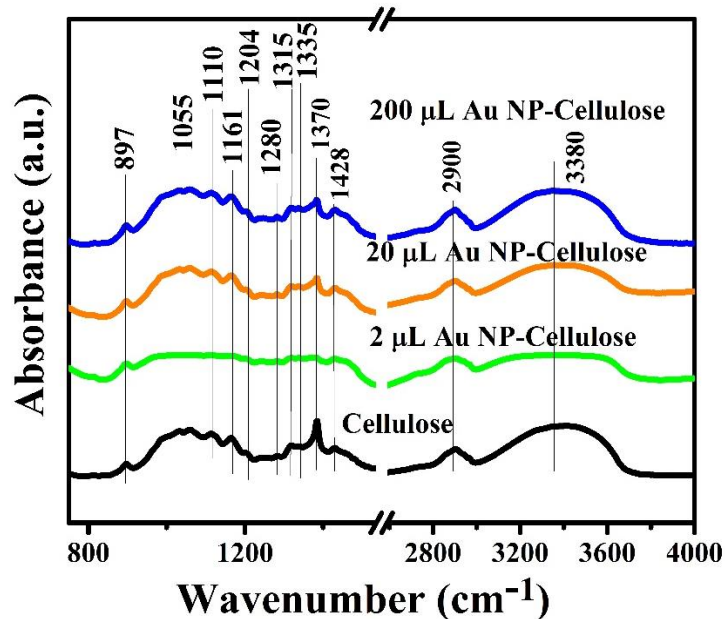


**Figure 5.5.** Shows the ATR-IR Spectra of Pure cellulose powder, 200 $\mu$ L Au NP-Cellulose, 20 $\mu$ L Au NP-Cellulose and 2 $\mu$ L Au NP-Cellulose.

The Infra-red (IR) spectroscopy in Attenuated total reflection (ATR) mode was performed to look out for possible changes in the cellulose structure by the inclusion of Au NPs. The ATR-IR Spectra of Pure cellulose, 2 $\mu$ L Au NP-Cellulose, 20 $\mu$ L Au NP-Cellulose and 200 $\mu$ L Au NP-Cellulose are shown in Figure 5.5 (a). The ATR-IR spectra indicates a reduction in the peak intensity of 1370  $\text{cm}^{-1}$  of cellulose with the addition of 2 $\mu$ L Au NP. The peak at 1370  $\text{cm}^{-1}$  belongs to the COH vibration of cellulose. The peak reduction can be attributed to the formation of hydrogen bonds between the OH functional groups of cellulose and Au NPs, at the expense of the intrinsic COH bonds that were already present in the pure cellulose. However, the same peak is visible with the addition of 20 $\mu$ L Au NP and 200 $\mu$ L Au NP, although it is slightly diminished. This may be attributed to the agglomeration of Au NPs in PDMS matrix. The assignment of the vibrational bands of cellulose I is provided in Table 5.1.

**Table 5.1:** Assignment of vibrational bands of cellulose I determined by IR Spectroscopy in ATR mode

Sl. No.	Wavenumber (cm <sup>-1</sup> )	Band Assignment
1	897	COC asymmetric stretching
2	1055	CO stretching vibrations
3	1110	Asymmetric vibration of glucose ring
4	1161	COC asymmetric vibration
5	1204	COH in-plane at C-6 bending
6	1281	CH and OH vibration
7	1315	COH and HCC vibration
8	1335	OH and CH <sub>2</sub> vibration
9	1370	COH and HCC vibration of cellulose and hemicelluloses
10	1428	CH <sub>2</sub> vibration; HCH and OCH in plane banding; intermolecular hydrogen bond bending
11	2900	CH and CH <sub>2</sub> vibration presence in aliphatic methylene groups
12	3340	Stretching vibrations of CH and OH groups

The Ultra Violet-Visible (UV-Vis) spectra of Au colloid, Pure cellulose, 2μL Au NP-Cellulose, 20μL Au NP-Cellulose and 200μL Au NP-Cellulose are shown in the Figure 5.6. It is observed that there is no absorption in the UV-Vis spectra in the visible region for the microcrystalline pure cellulose sample. However, there is a small amount of absorption in the UV Spectra at wavelengths less than 400 nm. The UV-Vis Spectra of pure Au NPs shows an absorption peak near 520 nm, which is attributed to the SPR bands of the Au NPs. The light is not completely absorbed in the process of promoting the electrons from ground state to the excited state. Some light is absorbed in the process of destructive interference between the excited displacement electrons which are in oscillating state and the light itself. For 200 μL Au NP-Cellulose sample, the SPR band is detected at the same wavelength of 520 nm.



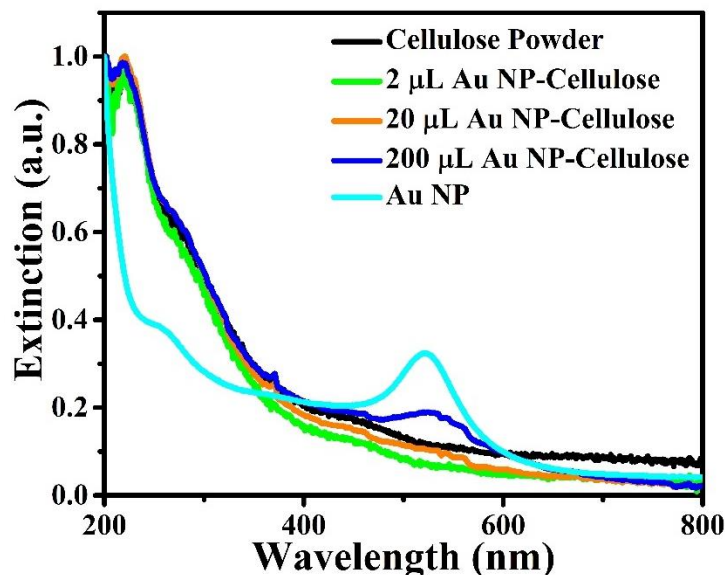


**Figure 5.6.** Shows the UV-Visible spectra of Pure cellulose powder, 2 $\mu$ L Au NP-Cellulose, 20 $\mu$ L Au NP-Cellulose, 200 $\mu$ L Au NP-Cellulose and Au NP.

The SPR band is almost diminished in the 20  $\mu$ L Au NP-Cellulose and 2  $\mu$ L Au NP-Cellulose nanocomposite sample. A gradual peak shift towards higher wave numbers can be observed in the Au colloid, 200 $\mu$ L Au NP-Cellulose and 20 $\mu$ L Au NP-Cellulose samples. The shifting of the peaks to the higher wavenumbers indicate agglomeration of Au NPs.[24]

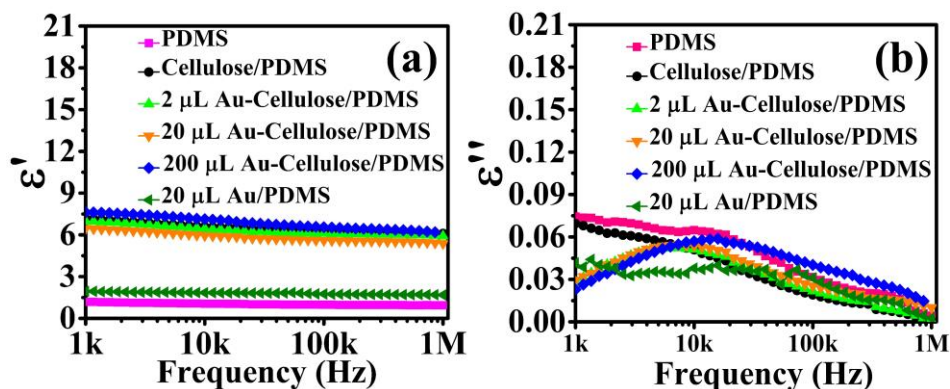


**Figure 5.7.** Shows the (a) Dielectric Constant vs Frequency (b) Dielectric Loss vs Frequency, characteristics of PDMS, Cellulose/PDMS, 2 $\mu$ L Au NP-Cellulose/PDMS, 20 $\mu$ L Au NP-Cellulose/PDMS, 200 $\mu$ L Au NP-Cellulose/PDMS, 20 $\mu$ L-Au/PDMS.

UV-Vis study shows an important observation that the 20  $\mu$ L Au NP-Cellulose and 2  $\mu$ L Au NP-Cellulose nanocomposites are SPR inactive.

This may be attributed to the low concentration of Au NPs within cellulose microfibrils that prevents the UV and visible lights to reach the Au NPs that is present in the nanocomposite.

The dielectric constant of PDMS, Cellulose/PDMS, 2 $\mu$ L Au NP-Cellulose/PDMS, 20 $\mu$ L Au NP-Cellulose/PDMS, 200 $\mu$ L Au NP-Cellulose/PDMS, 20 $\mu$ L Au/PDMS, nanocomposites are shown in Figure 5.7 (a). The dielectric constant of pure PDMS is 1.2 at low frequencies and remains constant over the entire frequency range. The dielectric constant increases after the addition of cellulose in PDMS. The dielectric constant of Cellulose/PDMS is 7.3 and 6.2 at the lowest and the highest frequency value, respectively. The rise in the dielectric constant is due to the presence of cellulose in different orientations due to which the electric field is more effective along the cellulose microfibrils throughout the PDMS matrix.[25] Also the rise in dielectric constant in Cellulose/PDMS may be attributed to the interfacial polarization at the interface between cellulose and PDMS.[26] The 20  $\mu$ L Au NP/PDMS nanocomposite sample have a low dielectric constant of 1.9. This may be attributed to the high electrical conductivity of Au NPs.[27] It was found that the dielectric constant of 200  $\mu$ L Au NP–Cellulose nanocomposite sample is 7.7 which is the highest among all the nanocomposites. The rise in the dielectric constant is attributed to interfacial polarization at the interface between Au NP, cellulose and PDMS. The dielectric constant is high at low frequencies due to the occurrence of interfacial and dipole polarizations occurring at low frequencies.[28] The occurrence of interfacial polarization can be explained by Maxwell–Wagner–Sillars (MWS) effect. According to this effect a significant amount of charge accumulates at the interface of the conducting filler and insulating polymer by surface polarization, which is a consequence of different values of conductivity of the two-different materials that are present. Also, numerous micro/nano capacitors are formed in the nanocomposite due to the presence of Au NPs. It is also observed that the dielectric constant of all the Au NP-Cellulose/PDMS

nanocomposites falls slightly at higher frequencies. This can be attributed to the relaxation behavior of the nanocomposite at higher frequencies. This behavior is believed to be due to the interaction of the Au NPs with cellulose in the PDMS matrix.[29] The dielectric constant of 20 $\mu$ L-Au NP/PDMS is slightly higher than the neat PDMS. This can be attributed to the addition of conducting Au NPs in PDMS matrix, which enhances the space charge polarization and Maxwell-Wagner-Sillars effect.[30]

The dielectric loss of PDMS, Cellulose/PDMS, 2 $\mu$ L Au NP-Cellulose/PDMS, 20 $\mu$ L Au NP-Cellulose/PDMS, 200 $\mu$ L Au NP-Cellulose/PDMS, 20 $\mu$ L-Au/PDMS nanocomposites are shown in Figure 5.7 (b). It is observed that the dielectric loss of pure PDMS, 20 $\mu$ L Au NP/PDMS and Cellulose/PDMS are 0.075, 0.04, and 0.07, respectively. This indicates that in the presence of Au NPs the dielectric loss of PDMS nanocomposite decreases. But due to the addition of cellulose in PDMS the dielectric loss does not decrease. The higher dielectric loss in PDMS and Cellulose/PDMS indicates that the dipoles are more relaxed and hence move more violently under the influence of an external electric field. It is reported that dielectric loss is the proportion of conduction charge transferred to that stored by polarization. This indicates that the low dielectric loss in Au NP-Cellulose/PDMS nanocomposite is suitable for piezoelectric and dielectric applications.[26]

It is observed that the dielectric loss of all the Au NP containing samples increases with frequency but later falls. This can be attributed to the fact that after a certain critical frequency ( $f_c$ ) the dipole oscillations becomes independent of the changing electric fields. Thus the dipole oscillations reduces with the increase in the frequency of the applied electric field above  $f_c$ , simultaneously the dielectric loss also falls.[31] The relaxation time ( $\tau_{rel}$ ) was calculated by using the following relation

$$\tau_{rel} = \frac{1}{f_{min}} \quad (5.3)$$

where  $f_{min}$  is the frequency at the lowest dielectric loss value. The relaxation times for PDMS, Cellulose/PDMS and 2 $\mu$ L Au NP-Cellulose/PDMS were 0.92 $\mu$ s. The relaxation times for 20 $\mu$ L Au NP-Cellulose/PDMS and 20 $\mu$ L-Au NP/PDMS were 0.94 $\mu$ s. The relaxation times for 200 $\mu$ L Au NP-Cellulose/PDMS is 1 $\mu$ s. This indicates that the incorporation of Au NPs makes the dipoles less relaxed. Hence, the dipoles move less violently under the influence of an external electric field in the presence of Au NPs.[32] The dielectric loss is also dependent on the volume fraction of the conductive filler and the density of the polymer matrix. The dielectric loss of all the Au NP-Cellulose/PDMS nanocomposites are less at lower frequencies due to the disruption in the ordered layered structure within the PDMS matrix. This occurs due to the introduction of defects and voids in the nanocomposite owing to the presence of Au NPs.[33] The high dielectric constant and low dielectric loss values make Au NP-Cellulose/PDMS based nanocomposites good energy storage material.

The dielectric polarization in Au NP-Cellulose/PDMS arises due to the stable thermal motion of the different chemical groups present in the nanocomposite. Changes in localized charge density, isomeric transitions, rotation of side groups cannot also be ruled out in the Au NP-Cellulose/PDMS nanocomposite.

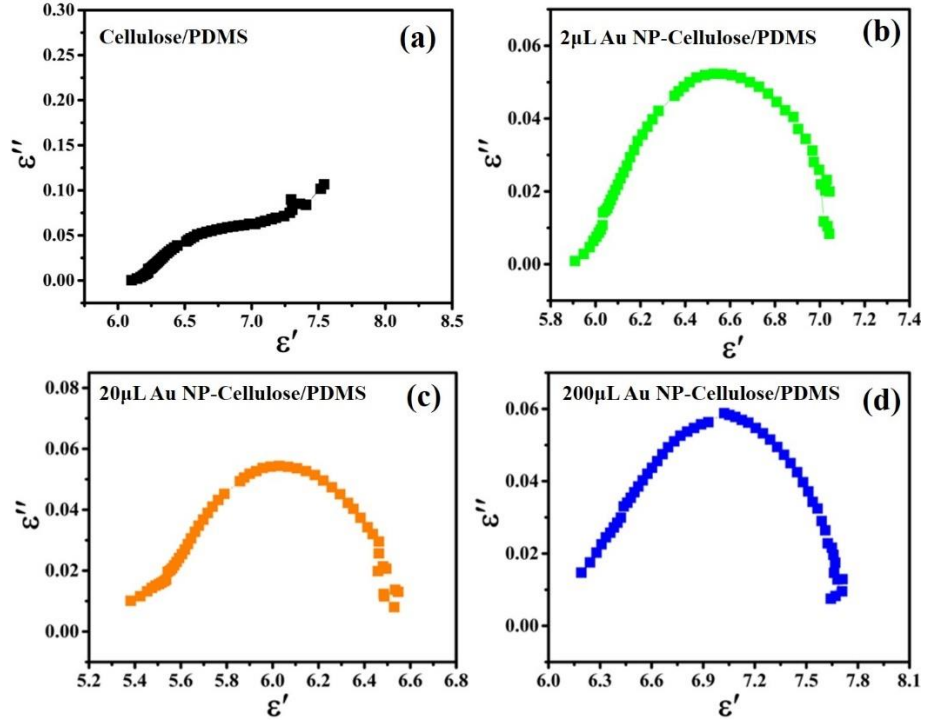


**Figure 5.8.** Shows the  $\epsilon''$  vs  $\epsilon'$  plot of (a) Cellulose/PDMS (b)  $2\mu\text{L}$  Au NP-Cellulose/PDMS (c)  $20\mu\text{L}$  Au NP-Cellulose/PDMS (d)  $200\mu\text{L}$  Au NP-Cellulose/PDMS.

The dispersed spectra in Figure 5.8 (a) corresponding to the  $\epsilon''$  vs  $\epsilon'$  plot of Cellulose/PDMS indicates non-Debye relaxation process. Whereas the semicircular plot corresponding to  $2\mu\text{L}$  Au NP-Cellulose/PDMS,  $20\mu\text{L}$  Au NP-Cellulose/PDMS,  $200\mu\text{L}$  Au NP-Cellulose/PDMS which is also known as the Cole–Cole semicircle is shown in Figure 5.8 (b–d), respectively. To understand the MWS effect, the study of the dipole relaxation mechanism is significant. The Debye relaxation mechanism is caused due to delay in polarization with the application of electric field within a dielectric medium. The number of Cole-Cole semi-circle in any plot is equal to the number of Debye relaxation. The equation for Cole-Cole semicircle is given as:[34]

$$\left(\epsilon' - \frac{\epsilon_s - \epsilon_\infty}{2}\right)^2 + (\epsilon'')^2 = \left(\frac{\epsilon_s - \epsilon_\infty}{2}\right)^2 \quad (5.4)$$

where,  $\epsilon'$  is the dielectric constant,  $\epsilon''$  is the dielectric loss,  $\epsilon_s$  is the static permittivity and  $\epsilon_\infty$  is the relative dielectric permittivity at the high-frequency limit. Thus, one number of Debye relaxation mechanism occur in 2 $\mu$ L Au NP-Cellulose/PDMS and 20 $\mu$ L Au NP-Cellulose/PDMS and 200 $\mu$ L Au NP-Cellulose/PDMS. No Debye relaxation mechanism occur in 200 $\mu$ L Au NP-Cellulose/PDMS and Pure Cellulose/PDMS. The broken Cole-Cole semicircle indicates distributed relaxation times in case of 200 $\mu$ L Au NP-Cellulose/PDMS and Pure Cellulose/PDMS.[35]

### 5.2.5 Electrical Characterizations

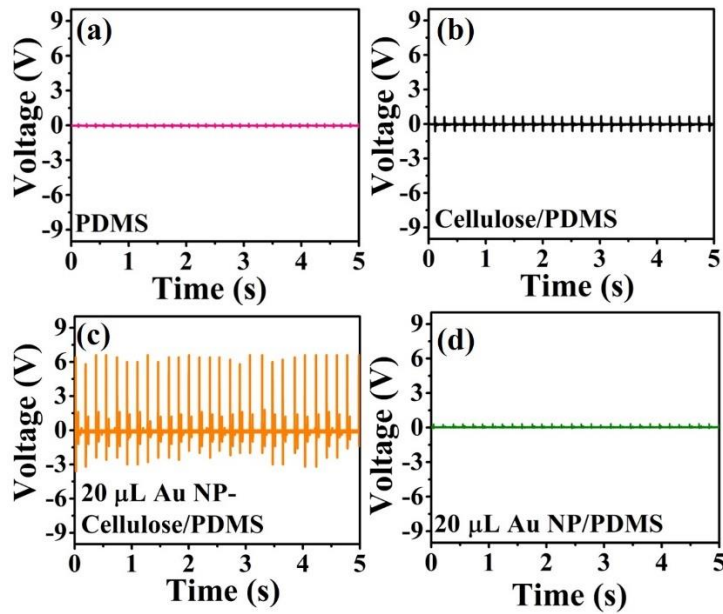


**Figure 5.9** Shows the open circuit voltage of the (a) Pure PDMS (b) Cellulose/PDMS (c) 20  $\mu$ L Au NP-Cellulose/PDMS (d) 20  $\mu$ L-Au/PDMS.

Mechanical energy harvesting device was fabricated from the pure PDMS, Cellulose/PDMS, 20 $\mu$ L Au NP-Cellulose/PDMS and 20 $\mu$ L Au NP/PDMS nanocomposites. The mechanical energy harvesting devices were excited by a self-made mechanically operated external vibration source. The open circuit voltage outputs from all the nanocomposites are shown in Figure 5.9 (a–f). The open circuit voltage generated by pure PDMS is few hundred milli volts. The open circuit voltage generated by Pure Cellulose/PDMS composite is less than 1V, which clearly indicates

that the enhancement of the output voltage is a consequence of the interaction between Au NPs and cellulose. The 20 $\mu$ L Au NP-Cellulose/PDMS showed highest output voltage of nearly 6V among all the nanocomposites. The mechanical energy harvesting performance of 2 $\mu$ L Au NP-Cellulose/PDMS and 200 $\mu$ L Au NP-Cellulose/PDMS were not performed due to their similar dielectric constants and loss values. The open circuit voltage recorded from the 20 $\mu$ L Au NP-Cellulose/PDMS was also less than 1V, which again indicates that the enhancement in the output voltage is not only because of Au nanoparticles or due to water.

The enhancement in the open circuit voltage in the nanocomposite due to the addition of Au NPs was expected as it is reported previously that due to the nanoscale dimensions of the filler material, the interfacial area between the filler and the polymer enhances manifold. Subsequently, dipolar interface layer induced coupling effect takes place, which brings many unexpected excellent macroscopic properties in the nanocomposite like higher polarization, dielectric response, breakdown strength in some cases.[36] However, in this case it is found that the piezoelectric effect enhances due to the possible formation of additional stress induced dipoles within the nanocomposite owing to the hydrogen bonding based interaction between the cellulose and Au NPs as indicated by the IR spectroscopy.

One of the ways to explain the enhanced output voltage is to attribute the presence of large number of additional electrons on the Au NP surface. These electrons engage with a greater number of hydrogen atoms present in the cellulose to form dipoles through electrostatic interactions. These dipoles are aligned in a direction when the nanocomposite is externally excited by a mechanical vibration.

The short circuit current generated from the different nanocomposites due to the excitation generated by a self-made mechanically operated vibration source are shown in Figure 5.10 (a-f). The voltage drops across a 10 M $\Omega$  resistance was measured by a digital storage oscilloscope and from where the current was calculated using ohm's law.

700 nA is the highest output current that is obtained from 20 $\mu$ L Au NP-Cellulose/PDMS. The current output from the 20 $\mu$ L Au NP /PDMS is almost equal to the current output from the pure PDMS. The current output is higher in Cellulose/PDMS as compared to pure PDMS which indicates the piezoelectric activity of cellulose. These results also indicate that the incorporation of Au NPs in Cellulose/PDMS increases the overall current output.

The overall enhancement in the piezoelectric output voltage and current in the Au NP-Cellulose/PDMS can be attributed to the model proposed by Tanaka *et al.*[37] It includes that an enhancement in the dielectric properties is achievable with a properly engineered nanoparticle/polymer multilayered interface. The cellulose microfibrils would behave as a polar inner layer structure, that would isolate the conducting Au NPs, while the PDMS would behave as a robust, physically thick, non-polar insulating layer. Under the application of an external mechanical vibration the polar cellulose microfibrils would charge the surface of the nearby residing Au NPs and in this way contribute to a significant amount of rise in the distribution of the overall piezoelectric polarization throughout the nanocomposite. The PDMS which behaves as the non-polar insulating layer prevents the formation of any conducting paths within the nanocomposite by isolating the Au NPs which are conducting in nature. Due to this reason the dielectric constant remains high throughout and does not reduce in magnitude with the subsequent increase in the concentrations of Au NPs within the nanocomposite.

It is found that the generated output voltages and currents are higher under pressing conditions and lower under releasing conditions. This might be attributed to the elasticity of the PDMS material. The elasticity forces the material to return to its original shape, irrespective of the force that is imparted.[38]



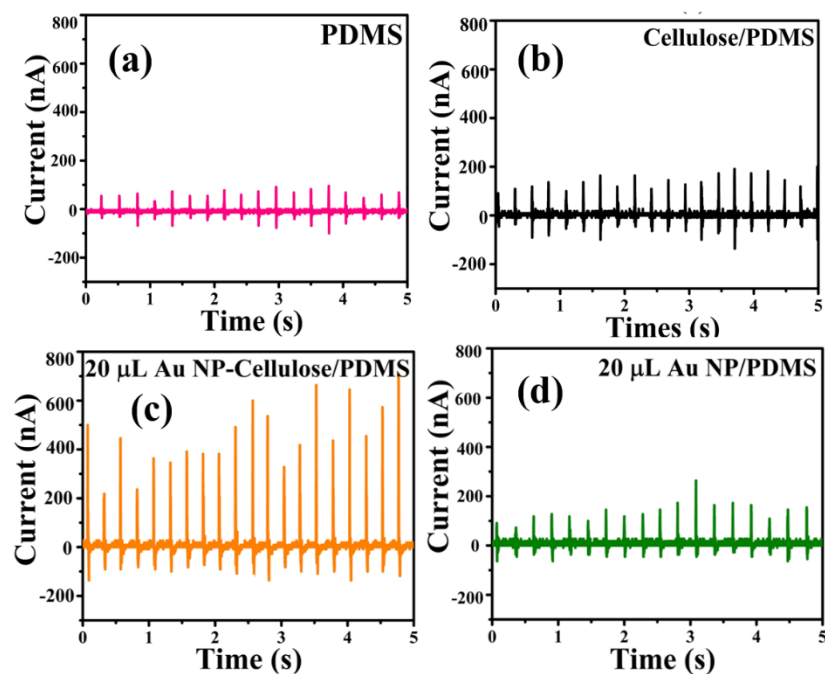


**Figure 5.10.** Shows the short circuit current of the (a) Pure PDMS (b) Cellulose/PDMS (c) 20  $\mu$ L Au NP-Cellulose/PDMS (d) 20  $\mu$ L-Au/PDMS.

### 5.2.6 Piezoresponse Force Microscopy Characterizations

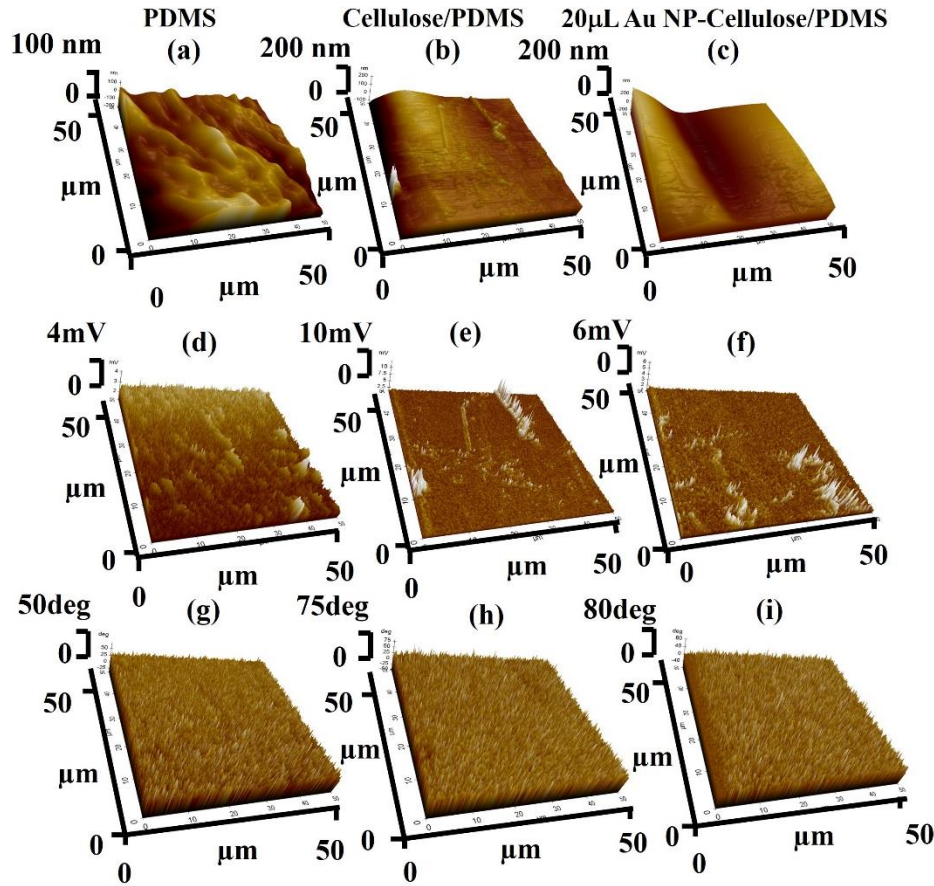


**Figure 5.11.** Shows the 3D PFM (a) height profile (b) amplitude response (c) phase response from the PDMS, Cellulose/PDMS and 20 $\mu$ L Au NP-Cellulose/PDMS nanocomposite samples respectively.

Piezoresponse force microscopy (PFM) is a powerful nanoscale imaging technique which is used to explore the local piezoelectric response. The imaging mechanism of PFM is based on detecting the electromechanical response which is induced by the inverse piezoelectric effect with the help of an atomic force microscopy (AFM) cantilever tip. However, it is well known that PFM characterization is impaired by non-piezoelectric responses like electrostrictive, electrostatic effects that can be present in both contact and non-contact mode of operation.[39] In the present study the PFM was used in the contact mode where the cantilever recorded lateral PFM signals to evaluate the electromechanical responses.

To evaluate the nanoscale electromechanical response from the Au NP-Cellulose based PDMS nanocomposites PFM is performed over  $50 \times 50 \mu\text{m}^2$  area. Figure 5.11 (a–c) shows the PFM 3D height profile of the PDMS, Cellulose/PDMS and 20  $\mu\text{L}$  Au NP-Cellulose/PDMS nanocomposites, respectively. It is seen that PDMS encapsulated cellulose microfibrils are protruding out from the nanocomposite surface in Figure 5.11 (b,c). The PFM amplitude signal is shown in Figure 5.11 (d–f). The voltage signal obtained from PDMS surface is electrostatic or electrostrictive in nature.[40] This can be confirmed by the fact that PDMS is non-piezoelectric material. The electrostatic and electrostrictive effects are dependent on the properties of the material under study.[41] The voltage signal obtained from Cellulose/PDMS and 20  $\mu\text{L}$  Au NP-Cellulose/PDMS nanocomposite is higher than that obtained from pure PDMS. This is because the cellulose present on the surface provides direct piezoelectric response which is a first order electromechanical response in addition to the electrostatic or electrostrictive responses which are higher order response originating from the PDMS. This piezoelectric response from the cellulose that is detected here is a local effect *i.e.* it comes only from the cellulose that is in contact with the PFM cantilever tip. Upon comparing the height profile images and the amplitude images, it can be clearly observed that the voltage spikes in the amplitude images are due to electromechanical responses originating due to the tip interaction with the roughness present on the nanocomposite surface. Thus, it can be concluded that PFM does not provide a complete conclusion towards the effect of Au NPs on the piezoelectric property of cellulose within PDMS matrix in the current study. The PFM phase image which is shown in Figure 5.11 (g–i) indicates several orientations of the domains from which the electromechanical responses originate from the nanocomposite surfaces.[42]

The steady voltage output shows excellent stability and durability of the 20  $\mu\text{L}$  Au NP-Cellulose/PDMS Nanogenerator in Figure 5.12 (a). The nanogenerator is periodically excited and relaxed by an external

electromechanical excitation source. The nanogenerator could charge a 10  $\mu\text{F}$  capacitor to 6.3V in 677s, whereas in the same time, the pure Cellulose/PDMS based nanogenerator could charge a 10 $\mu\text{F}$  capacitor to 1V only, which is shown in Figure 5.12 (b). The nanogenerator could light blue Light Emitting Diodes (LEDs) by continuous hand striking. Figure 5.12 (c) shows the LED in OFF condition and Figure 5.12 (d) shows LED in ON condition, due to continuous human hand impulse imparting. This indicates that the nanogenerator can be used as a probable candidate for future lighting solutions.

Further, we demonstrated a touch sensor application of the PENG. Figure 5.12 (e) shows that the red LED remains turned off when the working electrode area is not touched. Figure 5.12 (f) shows that the red LED is turned on when the working electrode area is touched. The idea was to use the enhanced piezoelectric property of the 20 $\mu\text{L}$  Au NP-Cellulose/PDMS based nanocomposite to light a LED indicator every time the electrode area experiences a finger touch.

The output signal generated by the PENG was amplified by an electronic amplifier circuit which is shown in Figure 5.12 (g). The block diagram of the touch sensor is shown in Figure 5.12 (h). The inputs to the amplifier are connected to the PENG, whereas the outputs of the amplifier are connected to the red LED. Table 5.2 shows the comparison of the efficiency of the recently reported works.

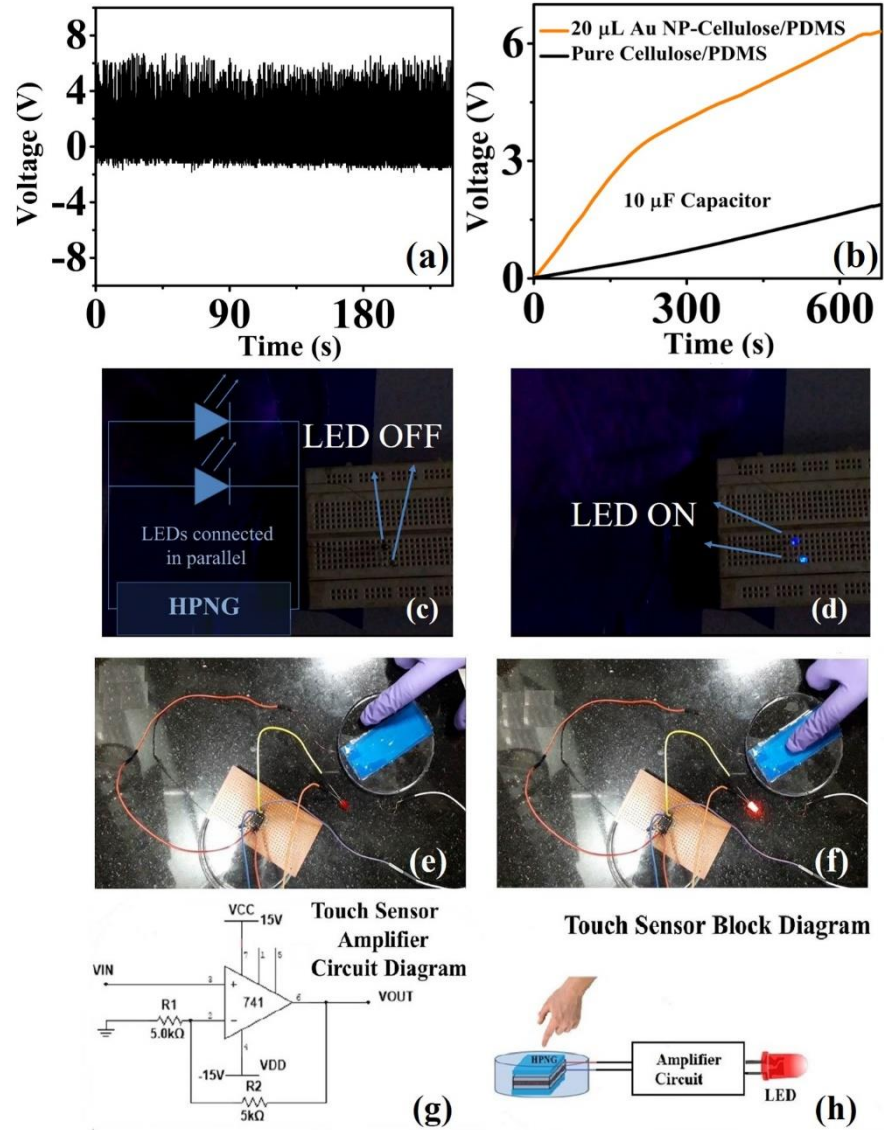


**Figure 5.12.** Shows the (a) stability of the PENG (b) charging of a 10 $\mu$ F capacitor by the PENG fabricated from 20 $\mu$ L Au NP-Cellulose/PDMS and Pure Cellulose/PDMS (c) LED in off condition when PENG is not excited (d) LED in on condition under human palm impact impartment (e) shows the touch sensor application of the Au NP-Cellulose/PDMS Nanogenerator. The LED is switched off when sensor/PENG is touched in the non-sensing area (f) the LED turns on when sensor/PENG is touched in the sensing area (g) amplifier circuit diagram that is used to amplify the harvested current generated by the PENG, to ensure lighting the LED (h) the block diagram of the touch sensor application.

To calculate the power density the PENG was excited while its two terminals were connected across a 2.2 M $\Omega$  resistance. A digital storage oscilloscope was connected across the two terminals of the resistance and a peak output voltage of 6.5 V was recorded. A peak power density of 8.34 mili-W m<sup>-2</sup> was recorded for the PENG using the following equation:

$$P = \frac{V^2}{R \times \text{Area of the electrode}} \quad (5.5)$$

where P is the peak power density, V is the output voltage recorded, R is the value of the resistance.

### 5.2.7 Efficiency Calculation

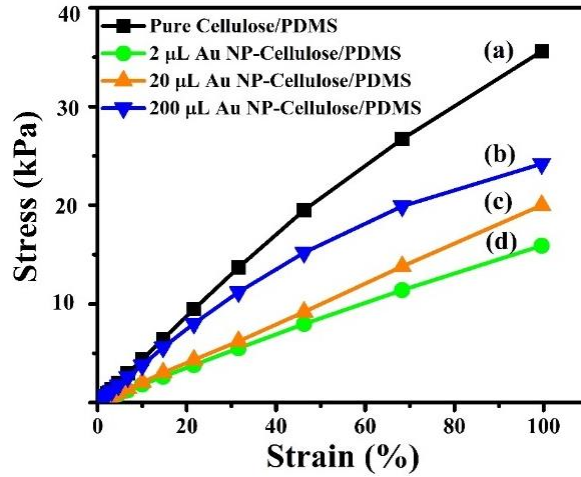


**Figure 5.13.** Shows the Stress vs Strain Curve of (a) Pure Cellulose/PDMS (b) 200 $\mu$ L Au NP-Cellulose/PDMS (c) 20 $\mu$ L Au NP-Cellulose/PDMS (d) 2 $\mu$ L Au NP-Cellulose/PDMS.

The stress vs strain curve of all the nanocomposite samples shows non-linear behavior, as shown in Figure 5.13. This indicates breakage of the network fibres of cellulose, due to bond breaking or fibre pull-out. Twist in the cellulose microfibrils can also be attributed towards this behavior.[35] It can be seen that the non-linearity follows a decreasing trend with the addition of Au NPs, this can be due to the fact that the Au NPs binds with the cellulose and prevents the damage or slippage to the cellulose microfibrils.

The Young's Modulus of the Pure Cellulose/PDMS, 2  $\mu\text{L}$  Au NP-Cellulose/PDMS, 20 $\mu\text{L}$  Au NP-Cellulose/PDMS and 200  $\mu\text{L}$  Au NP-Cellulose/PDMS nanocomposites were found out to be 425 Pa, 326 Pa, 203 Pa, 173 Pa, respectively from the Stress vs Strain curve.

The energy harvesting efficiency of the PENG during capacitor charging is calculated next. The input energy ( $W_{in}$ ) provided to the PENG while charging the capacitor during one cycle is given by:

$$W_{in} = F \times \Delta l = F \frac{\sigma l}{Y} = 2.80 \times 10^{-6} \text{ J} \quad (5.6)$$

where  $F$  is the applied force on the PENG, which is measured externally to be 3 N.  $\Delta l$  is the deformation of the PENG when stress  $\sigma$  is 9.4 kPa and Young's Modulus,  $Y$  is 20.2 kPa and the average thickness of the nanocomposite film  $l$  is 2mm.

The total input mechanical energy transfer to the PENG during the capacitor charging is given by:

$$E_{in} = \frac{t}{\Delta t} W_{in} = 11.02 \times 10^{-3} \text{ J} \quad (5.7)$$

where  $t$  is the total time required to charge the capacitor, which is 677s.  $\Delta t$  is the average time duration between the two consecutive voltage peaks of the imparted pressure cycles by the mechanical excitation generation source, which is 0.172 s.

The electrical energy stored in the capacitor is given by the following equation:

$$E_{out} = \frac{1}{2} CV^2 = 198 \times 10^{-6} \text{ J} \quad (5.8)$$

where  $C$  is the capacitance of the capacitor, which is 10 $\mu\text{F}$ ,  $V$  is the total voltage stored by the capacitor, which is 6.3V.

The overall energy efficiency ( $\eta$ ) is found out from the ratio of the electrical energy stored ( $E_{out} = \frac{1}{2} CV^2$ ) in the 10 $\mu\text{F}$  capacitor while charging and the total mechanical energy used ( $E_{in}$ ) to charge the 10  $\mu\text{F}$  capacitor.

$$\eta = \frac{E_{out}}{E_{in}} \times 100\% = 1.8\% \quad (5.9)$$

The 1.8 % energy conversion efficiency obtained in this work is quite higher than some of the similar recent reported works.

**Table 5.2:** Performance details of previously reported data on energy harvesting devices

Sl. No.	Name of the Piezoelectric Device	Poling Voltage and Duration	Input Source	Voltage	Energy Conversion Efficiency (%)
1	Cellulose-ZnO[43]	Data Unavailable	Ultrasonic bath	80 mV	–
2	ZnO NWs/PVDF[44]	100 kV/mm	Linear motor	0.2 V	–
3	BaTiO <sub>3</sub> NPs[45]	100 kV/cm; 20 h	Bending stage	3.2V	–
4	BaTiO <sub>3</sub> Nanotubes[46]	80 kV/cm; 12 h	Linear motor	5.5 V	–
5	PVDF-TrFE Film/Graphene Oxide[47]	30 MV/m, 1 h	Hydraulic/ Mechanical fatigue tester	4.3 V	–
6	Fe-rGO/PVDF[48]	Not Poled	Human hand punching	5.1 V	–
7	Fe-rGO/PVDF[31]	Not Poled	Human finger tapping	1.2 V	–
8	CNT/PVDF[31]	Not Poled	Human finger tapping	2.5 V	–
9	PVDF/Cellulose [49]	Not Poled	Data Not Available	6.3 V	–
10	ZnO/Cellulose [50]	Not Poled	Smart shaker	908 mV	–
11	rGO-Ag/PVDF[18]	Not Poled	Human hand tapping	18V	0.65
12	ZnSnO <sub>3</sub> [51]	Not Found	Human finger press	40 V	1.17
13	KNbO <sub>3</sub> Nanowires[52]	5.0 kV/mm; 1 h	Bending tester	10.5 V	0.9
14	<b>Au NP-Cellulose/PDMS</b>	<b>Not Poled</b>	<b>Mechanical excitation source</b>	<b>6V</b>	<b>1.8</b>



### 5.3 Summary

In summary in this chapter the mechanical energy harvesting using Au NP-Cellulose/PDMS based flexible nanocomposite is demonstrated. It is found that the incorporation of Au NPs in Cellulose/PDMS shows promising capability to realize efficient mechanical energy harvesting application. It is found in this work that Cellulose/PDMS is a good dielectric material. It is also found that with the incorporation of Au NPs in Cellulose/PDMS there is a decrease in the dielectric loss. It is also observed that the piezoelectric output voltage is enhanced in the Au NP-Cellulose/PDMS nanocomposite. The enhancement in the piezoelectricity is attributed to the overall enhancement in the dielectric property of the nanocomposite. The mechanical energy harvesting device is named as the piezoelectric nanogenerator (PENG). An open circuit voltage of  $\sim 6\text{V}$  is detected from the PENG and a short circuit current of  $\sim 700\text{ nA}$  is detected when excited with a periodic force of  $3\text{N}$ . The PENG could charge a  $10\mu\text{F}$  capacitor to  $6.3\text{V}$  in  $557\text{s}$ . The energy conversion efficiency of the PENG was found to be  $1.8\%$ . The advantages of the PENG device are that poling is not required, which reduces cost and complexity. Also, it shows comparatively better energy conversion efficiency among similar devices of its class as shown in the table. The energy conversion efficiency of the Au NP-Cellulose/PDMS based PENG device is higher than the  $r\text{GO-Ag/PVDF}$  based PENG which was discussed in the previous chapter. The PENG could light two commercial blue LEDs by direct human hand impulse impartment. A touch sensor application with the PENG is also realized.

### References

1. Jeong, C.K. *et al.*, (2014). Large-area and flexible lead-free nanocomposite generator using alkaline niobate particles and metal nanorod filler. *Advanced Functional Materials*, 24(18), 2620–2629.
2. Xue, Q.T. *et al.*, (2015). A record flexible piezoelectric KNN

- ultrafine-grained nanopowder-based nanogenerator. *AIP Advances*, 5(1), 1–8.
3. Alam, M.M. *et al.*, (2015). Lead-free ZnSnO<sub>3</sub>/MWCNTs-based self-poled flexible hybrid nanogenerator for piezoelectric power generation. *Nanotechnology*, 26(16), 165403-165408.
  4. Lee, B.Y. *et al.*, (2012). Virus-based piezoelectric energy generation. *Nature Nanotechnology*, 7(6), 351–356.
  5. Gindl, W. *et al.*, (2010). Converse piezoelectric effect in cellulose I revealed by wide-angle x-ray diffraction. *Biomacromolecules*, 11(5), 1281–1285.
  6. Mahadeva, S.K. *et al.*, (2015). Paper as a platform for sensing applications and other devices: A review. *ACS Applied Materials and Interfaces*, 7(16), 8345–8362.
  7. Qiu, X. *et al.*, (2013). “Smart” materials based on cellulose: A review of the preparations, properties, and applications. *Materials*, 6(3), 738–781.
  8. Zheng, Q. *et al.*, (2016). High-performance flexible piezoelectric nanogenerators consisting of porous cellulose nanofibril (CNF)/poly(dimethylsiloxane) (PDMS) aerogel films. *Nano Energy*, 26, 504–512.
  9. Alexandrescu, L. *et al.*, (2013). Cytotoxicity tests of cellulose nanofibril-based structures. *Cellulose*, 20(4), 1765–1775.
  10. Alam, M.M. *et al.* (2016). Native Cellulose Microfiber-Based Hybrid Piezoelectric Generator for Mechanical Energy Harvesting Utility. *ACS Applied Materials and Interfaces*, 8(3), 1555–1558.
  11. Sultana, A. *et al.*, (2018). ZnS-paper based flexible piezoelectric nanogenerator. *AIP Conference Proceedings*, 1942, 120018-120022.
  12. Toroń, B. *et al.*, (2018). Novel piezoelectric paper based on SbSI nanowires. *Cellulose*, 25(1), 7–15.
  13. Zhang, G. *et al.*, (2015). Novel piezoelectric paper-based flexible nanogenerators composed of BaTiO<sub>3</sub> nanoparticles and bacterial

- cellulose. *Advanced Science*, 3(2), 1–7.
14. Kim, K.H. *et al.*, (2011). Paper-based piezoelectric nanogenerators with high thermal stability. *Small*, 7(18), 2577–2580.
  15. Ghosh, R. *et al.*, (2016). Reduced Graphene Oxide-Based Piezoelectric Nanogenerator with Water Excitation. *IEEE Trans. Nanotechnol.*, 15(2), 268–273.
  16. Agrawal, R. *et al.*, (2011). Giant piezoelectric size effects in zinc oxide and gallium nitride nanowires. A first principles investigation. *Nano Letters*, 11(2), 786–790.
  17. Sinha, T. K. *et al.*, (2016). Graphene-Silver-Induced Self-Polarized PVDF-Based Flexible Plasmonic Nanogenerator Toward the Realization for New Class of Self Powered Optical Sensor. *ACS Applied Materials and Interfaces*, 8(24), 14986–14993.
  18. Pusty, M. *et al.*, (2019). A flexible self-poled piezoelectric nanogenerator based on a *r*GO-Ag/PVDF nanocomposite. *New Journal of Chemistry*, 43(1), 284–294.
  19. Dang, Z.M. *et al.*, (2007). Significantly enhanced low-frequency dielectric permittivity in the BaTiO<sub>3</sub>/poly(vinylidene fluoride) nanocomposite. *Applied Physics Letters*, 90(1), 2005–2008.
  20. Dang, Z.M. *et al.*, (2013). Flexible nanodielectric materials with high permittivity for power energy storage. *Advanced Materials*, 25(44), 6334–6365.
  21. Leng, W. *et al.*, (2015). Room temperature seed mediated growth of gold nanoparticles: mechanistic investigations and life cycle assesment. *Environmental Science: Nano*, 2(5), 440–453.
  22. Garcia, M.A. (2011). Corrigendum: Surface plasmons in metallic nanoparticles: Fundamentals and applications. *J. Phys. D: Appl. Phys.*, 44, 283001-283022.
  23. Noguez, C. (2007). Surface plasmons on metal nanoparticles: The influence of shape and physical environment. *Journal of Physical Chemistry C*, 111(10), 3606–3619.

24. Wu, X. *et al.*, (2014). Green synthesis and formation mechanism of cellulose nanocrystal-supported gold nanoparticles with enhanced catalytic performance. *Environmental Science: Nano*, 1(1), 71–79.
25. Yan, J. *et al.*, (2016). High Performance Flexible Piezoelectric Nanogenerators based on BaTiO<sub>3</sub> Nanofibers in Different Alignment Modes. *ACS Applied Materials and Interfaces*, 8(24), 15700–15709.
26. Carponcin, D. *et al.*, (2014). Electrical and piezoelectric behavior of polyamide/PZT/CNT multifunctional nanocomposites. *Advanced Engineering Materials*, 16(8), 1018–1025.
27. Schmid, G. *et al.*, (2005). Gold nanoparticles: Assembly and electrical properties in 1-3 dimensions. *Chemical Communications*, 6, 697–710.
28. Zhang, L. *et al.*, (2015). Highly improved electro-actuation of dielectric elastomers by molecular grafting of azobenzenes to silicon rubber. *Journal of Materials Chemistry C*, 3(19), 4883–4889.
29. Karan, S. K. *et al.*, (2016). Effect of  $\gamma$ -PVDF on enhanced thermal conductivity and dielectric property of Fe-rGO incorporated PVDF based flexible nanocomposite film for efficient thermal management and energy storage applications. *RSC Advances*, 6(44), 37773–37783.
30. Zhang, C. *et al.*, (2016). Enhanced dielectric properties of poly(vinylidene fluoride) composites filled with nano iron oxide-deposited barium titanate hybrid particles. *Scientific Reports*, 6, 4–12.
31. Pusty, M. *et al.*, (2017). Comparative Study with a Unique Arrangement to Tap Piezoelectric Output to Realize a Self Poled PVDF Based Nanocomposite for Energy Harvesting Applications. *ChemistrySelect*, 2(9), 2774–2782.
32. Cisneros López. E.O, *et al.*, (2015). Effect of Agave Fiber Surface Treatment on the Properties of Polyethylene Composites Produced by Dry-Blending and Compression Molding. *Polymer composites*,

- 38(1), 96–104.
33. Song, S. *et al.*, (2016). Bioinspired Graphene Oxide/Polymer Nanocomposite Paper with High Strength, Toughness, and Dielectric Constant. *ACS Applied Materials and Interfaces*, 8(45), 31264–31272.
  34. Yu, H. *et al.*, (2012). Graphene/polyaniline nanorod arrays: Synthesis and excellent electromagnetic absorption properties. *Journal of Materials Chemistry*, 22(40), 21679–21685.
  35. Saini, D.R. *et al.*, (1984). Dynamic mechanical properties of highly loaded ferrite-filled thermoplastic elastomer. *Journal of Applied Polymer Science*, 29(12), 4123–4143.
  36. Tanaka, T. *et al.*, (2004). Polymer nanocomposites as dielectrics and electrical insulation- perspectives for processing technologies, material characterization and future applications. *IEEE Transactions on Dielectrics and Electrical Insulation*, 11(5), 763–784.
  37. Tanaka, T. *et al.*, (2005). Proposal of a multi-core model for polymer nanocomposite dielectrics. *IEEE Transactions on Dielectrics and Electrical Insulation*, 12(4), 669–681.
  38. Karan, S.K. *et al.*, (2016). An Approach to Design Highly Durable Piezoelectric Nanogenerator Based on Self-Poled PVDF/AlO-rGO Flexible Nanocomposite with High Power Density and Energy Conversion Efficiency. *Advanced Energy Materials*, 6(20), 1–12.
  39. Espinosa, H.D. *et al.*, (2012). A review of mechanical and electromechanical properties of piezoelectric nanowires. *Advanced Materials*, 24(34), 4656–4675.
  40. Newnham, R.E. *et al.*, (1997). Electrostriction: Nonlinear electromechanical coupling in solid dielectrics. *Journal of Physical Chemistry B*, 101(48), 10141–10150.
  41. Eliseev, E.A. *et al.*, (2014). Electrostrictive and electrostatic responses in contact mode voltage modulated scanning probe microscopies. *Applied Physics Letters*, 104(23), 1–6.

42. Ferri, A. *et al.*, (2019). Local Electrical Characterization of PVDF Textile Filament. *Fibers and Polymers*, 20(7), 1333–1339.
43. Kumar, A. *et al.*, (2011). Flexible ZnO-cellulose nanocomposite for multisource energy conversion. *Small*, 7(15), 2173–2178.
44. Liao, Q. *et al.*, (2014). Flexible piezoelectric nanogenerators based on a fiber/ZnO nanowires/paper hybrid structure for energy harvesting. *Nano Research*, 7(6), 917–928.
45. Park, K.II, *et al.*, (2012). Flexible nanocomposite generator made of BaTiO<sub>3</sub> nanoparticles and graphitic carbons. *Advanced Materials*, 24(22), 2999–3004.
46. Lin, Z.H. *et al.*, (2012). BaTiO<sub>3</sub> nanotubes-based flexible and transparent nanogenerators. *Journal of Physical Chemistry Letters*, 3(23), 3599–3604.
47. Bhavanasi, V. *et al.*, (2016). Enhanced Piezoelectric Energy Harvesting Performance of Flexible PVDF-TrFE Bilayer Films with Graphene Oxide. *ACS Applied Materials and Interfaces*, 8(1), 521–529.
48. Karan, S.K. *et al.*, (2015). Self-powered flexible Fe-doped RGO/PVDF nanocomposite: An excellent material for a piezoelectric energy harvester. *Nanoscale*, 7(24), 10655–10666.
49. Fashandi, H. *et al.*, (2016). Morphological changes towards enhancing piezoelectric properties of PVDF electrical generators using cellulose nanocrystals. *Cellulose*, 23(6), 3625–3637.
50. Mun, S. *et al.*, (2016). Enhanced electromechanical behavior of cellulose film by zinc oxide nanocoating and its vibration energy harvesting. *Acta Materialia*, 114, 1–6.
51. Alam, M.M. *et al.*, (2015). Lead-free ZnSnO<sub>3</sub>/MWCNTs-based self-powered flexible hybrid nanogenerator for piezoelectric power generation. *Nanotechnology*, 26(16), 165403–165408.
52. Joung, M.R. *et al.*, (2014). Piezoelectric nanogenerators synthesized using KNbO<sub>3</sub> nanowires with various crystal structures. *Journal of*

*Materials Chemistry A*, 2(43), 18547–18553.





## CHAPTER 6

---

### Inhibitive Action of Partially Reduced Graphene Oxide/Silver Nanocomposite on Pathogenic Fungi

---

#### 6.1 Overview

In the previous chapter the term “nanomaterial” was introduced which was followed by their synthesis methods and characterization techniques. In this chapter the synthesis details, characterizations and applications of reduced graphene oxide-silver nanocomposite is discussed.

Graphene as well as its compounds show some interesting properties with respect to their interaction with microbes. Recent studies have suggested that Graphene Oxide (GO) also shows antibacterial properties.[1, 2] It was reported that GO and *rGO* papers show antibacterial properties, are biocompatible as well.[3] It was also found that under anaerobic conditions when graphene oxide interacts with *E.coli* bacteria, it forms reduced graphene oxide. It was reported that graphene oxide can be reduced by bacteria which also shows antibacterial properties.[4] Also, it is interesting to note that graphene oxide can inactivate *E.coli* bacteria in the presence of melatonin, which can be reactivated after the removal of the graphene sheets.[5] Photo catalytically reduced graphene oxide can increase the antibacterial activity of  $\text{TiO}_2$  many times when irradiated under solar radiation.[6]

The evolution of GO as a bactericide is a welcome proposition, keeping in view the resistance of microbes towards antibiotics. Also, the broad spectrum antibacterial properties of Silver is widely known.[7, 8] The cell membrane of bacteria can get damaged due to  $\text{Ag}^+$  ions, leading to cell death.[9, 10] Copper is underuse from ancient times as a bactericide. Recently the antibacterial property of Cu nanoparticles embedded on silica thin films were reported.[11] In another interesting work the interaction of

Copper nanoflakes with *E.coli* bacteria were reported. In the same work the nanoflakes got chemically reduced in the presence of the bacteria, resulting in the death of the bacteria. The Copper nanoflakes behaved as bacterial sensor.[12] ZnO and TiO<sub>2</sub> materials in the form of nanoparticles (NPs) were reported to have anti-microbial properties.[13-15] Ag NPs were tested in rats for therapeutic usage as antimicrobial agent and were found safe to be used.[16] The effectiveness of Silver against antibiotic resistant microbes is already reported.[17, 18] The availability of higher number atoms on the surface of the Ag NPs, makes them interact with microbes and studies have confirmed that as size of the NPs increase, its effectiveness against microbes decrease.[19, 20] It is also reported that shape of the Ag NPs also impacts its antimicrobial property.[21] The effectiveness of the Ag NPs were also found to be dose dependent.[22] Ag NPs were also reported to be in application for water decontamination as a first step towards industrial application. However, it is necessary to disperse the NPs as solution to prevent their aggregation for bactericidal applications and for their separation to remove them after treatment.[23] The Ag NPs requires mechanical support that can hold them in suspension for effective action. It was reported previously that Ag NPs can be held on SiO<sub>2</sub> matrix as well as on TiO<sub>2</sub> matrix, which is also biocompatible.[24, 25] It was reported in another work that Ag was coated on carbon nanotubes (CNT) on pyrolytic carbon substrate and its bactericidal properties were studied.[26] However the usage of CNT as a replacement for antibiotic is not feasible due to the associated cost, ease of functionalization and cytotoxicity associated with human cells.[27] Graphene oxide is an ideal replacement of CNT in such circumstances. The layered structure of GO nanosheets provides enough surface area to load NPs on them.[28] Also it has good water dispersion property. It can be functionalized with ease and shows biocompatibility.[29] Based on these results previously significant works were carried out to see the antimicrobial effect of rGO-Ag. Previously the species specific anti-microbial activity of GO/rGO-Ag nanocomposite were widely

reported.[30-38] Experiments have also highlighted the synergistic effect on the enhancement of bactericidal effect of GO-Ag Nanocomposite.[39] Although, previously synthesis, characterization and antibacterial property of *rGO-Ag NC* were studied in detail.[40] It was found that, no significant studies were done to see the effect of the nanocomposite on microbes belonging to the kingdom fungi. In the current study we have based to check the effect of the *rGO-Ag* nanocomposite on pathogenic fungi belonging to phylum *Zygomycota*. The phylum *Zygomycota* is subdivided into two categories *Trichomyces* and *Zygomycetes*. The *Zygomycetes* are classified as those that cause disease known as Zygomycosis in human beings by the inhalation of spores. It has been found to cause upper and lower respiratory tract diseases in rabbits. *Zygomycetes* present in fermented milk or dried breads have been reported to cause gastrointestinal diseases. According to research, humans with low immune strength are at a greater risk of developing Zygomycosis. Chronic use of steroids leads to susceptibility in developing Zygomycosis. Burn patients are also at a greater risk to develop disease induced by *Zygomycetes*. Even these microbes have the potential to damage the central nervous system once they infect a human being.[40] In this work we have synthesized reduced graphene oxide- Silver Nanocomposite (*rGO-Ag NC*) and studied its antifungal effect.

## **6.2 Results and Discussion**

### **6.2.1 Synthesis of GO**

Graphene Oxide was prepared by modified Hummer's method, which is explained subsequently:[41, 42] At first 1g of Graphite Powder, 1g Sodium Nitrate and 50 mL of Sulphuric Acid were stirred together in a round bottom flask in ice bath for 30 minutes. After that 6g Potassium Permanganate was slowly added to it at 0° C and stirred. 30 minutes later the round bottom flask was transferred to water bath maintained at 40°C and stirred. After 1 hour, 100 mL of De-ionized (DI) water was added and the temperature of the water bath was raised to 95° C. After another 30

minutes the solution was diluted by 200 mL DI water. 1 hour later Hydrogen Peroxide was added. The colour of the solution changes from brown to yellow. The final solution was filtered by filter paper. The filtrate was dispersed in water and subsequently the solution was centrifuged to separate out lighter GO particles. The lighter GO particles are again centrifuged. This time the supernatant was discarded, and the colloidal precipitate was collected and dispersed in DI water. Finally, this solution was ultrasonicated to obtain completely exfoliated graphene oxide.

### **6.2.2 Synthesis of *r*GO-Ag Nanocomposite**

To prepare *r*GO-Ag Nanocomposite 1.3 ml of GO suspension (1.35 mg/ mL) was added to 98.7 ml of DI water. Within it 36 mg of Silver Nitrate ( $\text{AgNO}_3$ ), was added and was heated at 95 °C. Later after 1 hour, 40 mg Sodium Citrate was added, and the solution was heated for another 1 hour. The solution was filtered and was washed by centrifugation method for 2-3 times.

### **6.2.3 Instruments used for Material Characterizations and Electrical Characterizations**

The morphological characterization was done by XRD (Bruker D8 Advance X-ray diffractometer) with  $\text{Cu-K}_\alpha$  radiation ( $\lambda = 1.54 \text{ \AA}$ ), Field emission scanning electron microscope (Supra 55 Zeiss), High Resolution Transmission Electron Microscopy (JEOL, JEM – 2100), Raman Spectroscopy (Labram-HR 800 spectrometer) equipped with excitation radiation at wavelength of 488 nm from an Argon ion laser at a spectral resolution of about  $1 \text{ cm}^{-1}$ , UV-Visible spectroscopy (Agilent Cary-60 UV-vis), FT-IR (Bruker Tensor 27 spectrophotometer), X-ray photoelectron spectroscopy (Oxford Omicron ESCA with monochromatic Al radiation as an excitation source  $\lambda = 1486.7 \text{ eV}$ ).

### **6.2.4 Material Characterizations**

The FE-SEM image of graphene oxide is shown in Figure 6.1, which is synthesized by Hummers' method. The image shows clear layered structure

which are interlinked with each other, which clearly indicates the formation of Few Layer Graphene (FLG) by the chemical intercalation and exfoliation of natural Graphite. Figure 6.1 (b) shows the presence of Ag Nanoparticles densely populated on partially reduced GO flakes, which indicates the formation of *r*GO-Ag Nanocomposite. The *r*GO sheets are layered structure and are folded, crumbled and corrugated which conforms with available literature.[43, 44] The Ag Nanoparticles are uneven in shape but are overall spherical in dimension and their diameter varies in the range of 50-80 nm. The Silver Nanoparticles are dispersed on the *r*GO sheets. Energy dispersive X-ray spectroscopy (EDS) was carried out to ensure the composition of *r*GO-Ag Nanocomposite. The EDS results are shown in Figure 6.2. The compositional analysis revealed the atomic percentage of C, O and Ag present in the Nanocomposite. The atomic percentage of Ag is less than 0.3 % in the *r*GO-Ag Nanocomposite. The sharp peak near 2 keV originates due to Si present in glass substrate.

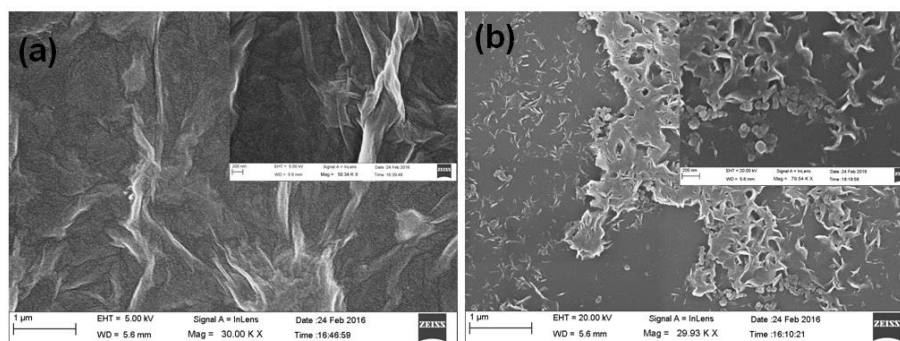


**Figure 6.1** Shows the SEM image of (a) GO which is wrinkled and crumbled and is prepared by modified Hummer's method; inset shows magnified image of the same (b) *r*GO-Ag Nanocomposite, where the Ag NPs are embedded on the surface of the wrinkled and crumbled *r*GO flakes; inset shows magnified image of Silver Nanoparticles.

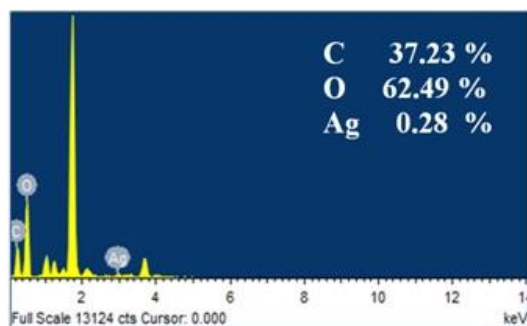


**Figure 6.2** Shows the EDS results which indicate the compositional details in atomic percentage of the rGO-Ag Nanocomposite.

Figure 6.3 (a) Shows High Resolution Transmission Electron Microscopy (HRTEM) image of the rGO-Ag Nanocomposite, where Ag Nanoparticles are seen lying embedded in the rGO matrix. The rGO layer is almost invisible which indicates the presence of monolayer graphene. Figure 6.3 (b) shows the HRTEM image of an individual Silver Nanoparticle. From the lattice fringes the  $d$ -spacing is calculated to be 2.32 Å, which indicates the presence of (111) plane of Ag. The presence of sharp (111) peak of Ag is also confirmed from the XRD results.

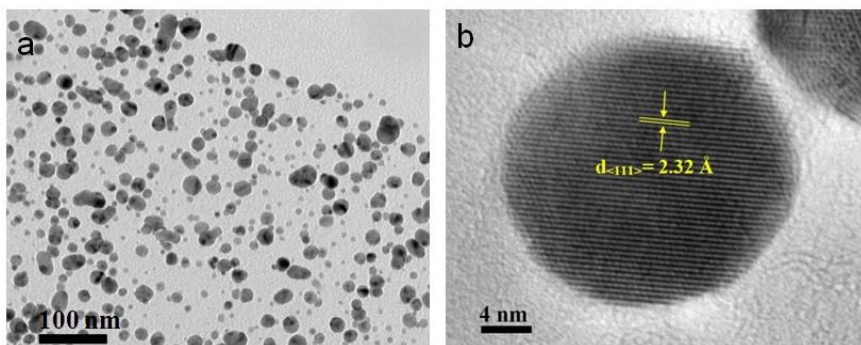


**Figure 6.3** Shows the (a) HRTEM image of rGO-Ag Nanocomposite (b) the lattice fringes of individual Ag Nanoparticle on rGO sheet.

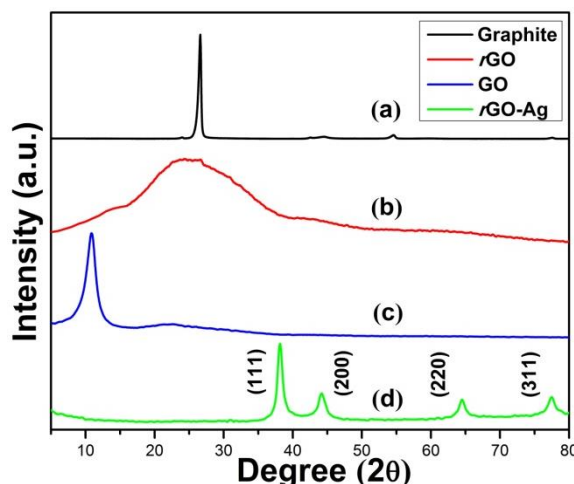


**Figure 6.4** Shows the XRD Spectra of (a) Graphite (b) rGO (c) GO (d) rGO-Ag Nanocomposite.

In Figure 6.4 (a) the XRD spectra of pure Graphite is shown. The (002) diffraction peak is present at  $26.6^\circ$  which corresponds to  $3.35 \text{ \AA}$  interlayer spacing.[45] This signifies the crystalline nature of pristine Graphite. The XRD spectra of reduced graphene oxide is shown in Figure 6.4 (b) which shows a wide peak at  $25^\circ$ , corresponding to an interlayer distance of  $3.36 \text{ \AA}$ . [46] After performing the chemical oxidation of pure Graphite following Hummer's Method the peak shifts to  $11.2^\circ$  indicating complete oxidation of Graphite into graphene oxide with an interlayer distance of  $8.60 \text{ \AA}$  as shown in Figure 6.4 (c). [47] The rGO-Ag Nanocomposite shows peaks at  $38.1^\circ$ ,  $44.2^\circ$ ,  $64.3^\circ$ ,  $77.3^\circ$  which corresponds to (111), (200), (220), (311) lattice planes respectively of the Ag Nanoparticles owing to its face centered cubic structure which is shown in Figure 6.4 (d). [48, 49] The characteristic flat peak of rGO that is present in the XRD pattern of rGO-Ag Nanocomposite is suppressed, due to the high intensity Ag peaks present.

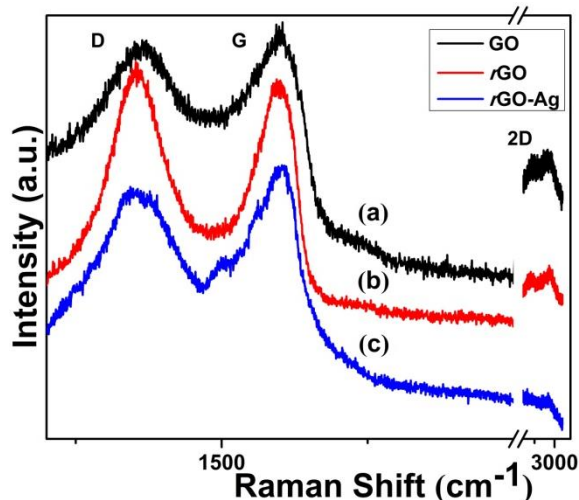


**Figure 6.5** Shows the Raman Spectrum of (a) GO (b) rGO (c) rGO-Ag Nanocomposite.

Figure 6.5 shows the Raman Spectra of GO, rGO and rGO-Ag Nanocomposite. In the Raman spectrum it can be seen that the pristine graphite nature is absent that is confirmed by the presence of multiple peaks, which indicates the exfoliation of graphite.[50] The D band intensity is related to the size of the in-plane  $sp^2$  domains. The D band provides information towards the defects or partial disorders present in the graphitic domains. A strong D band indicates formation of more  $sp^2$  domains and also confirms the presence of lattice distortions of graphene basal planes.[51] The relative intensity ratio of both peaks ( $I_D/I_G$ ) is a measure of disorder degree and is inversely proportional to the average size of the  $sp^2$  clusters.  $I_D/I_G$  intensity ratio for rGO is larger than that for GO (0.949 for GO and 1.04 for rGO), which indicates loss of graphitic structures.[52] The increased  $I_D/I_G$  ratio in rGO indicates establishment of graphene domains by the reduction of graphene oxide, but the domains were of lesser size compared to preceding graphite phase. The intensity of G band increased in rGO-Ag nanocomposite compared to rGO. This can be attributed to Surface Enhanced Raman Scattering (SERS) effect originating from the Ag nanoparticles embedded on reduced graphene oxide surface.[53] The 2D band is an indicator of the stacking of the nano sheets of GO. The peak for G and 2D exists at  $1604\text{ cm}^{-1}$  and  $2897\text{ cm}^{-1}$ , respectively. However, in case



of the *r*GO-Ag NC the G peak has shifted to a lower wavenumber of 1600  $\text{cm}^{-1}$  and the 2D peak shifted to a higher wavenumber 2920  $\text{cm}^{-1}$ . The shift of the G and 2D band in the *r*GO-Ag NC is of the order of 4  $\text{cm}^{-1}$  to lower wavenumber and 23  $\text{cm}^{-1}$  to higher wavenumber, respectively. This indicates the formation of multilayer Graphene like sheets while the formation of *r*GO-Ag NC. Similarly, for *r*GO the G band is shifted to a lower wavenumber of 1594  $\text{cm}^{-1}$  and 2D band is shifted to a higher wavenumber of 2933  $\text{cm}^{-1}$ , as compared to the as synthesized GO, which indicates the formation of multilayer graphene sheets. If the intensity ratio of 2D peak and G peak ( $I_{2D}/I_G$ ) are greater than 1.6, ~0.8, ~0.30, ~0.07 then this indicates the presence of single, double, triple and multi (greater than 4) layer graphene sheets respectively. The  $I_{2D}/I_G$  values of GO, *r*GO, *r*GO-Ag NC are 0.686, 0.483, 0.16, respectively. It indicates the presence of double layer GO, triple layer *r*GO and greater than 4 layered graphene nanosheets.[54]

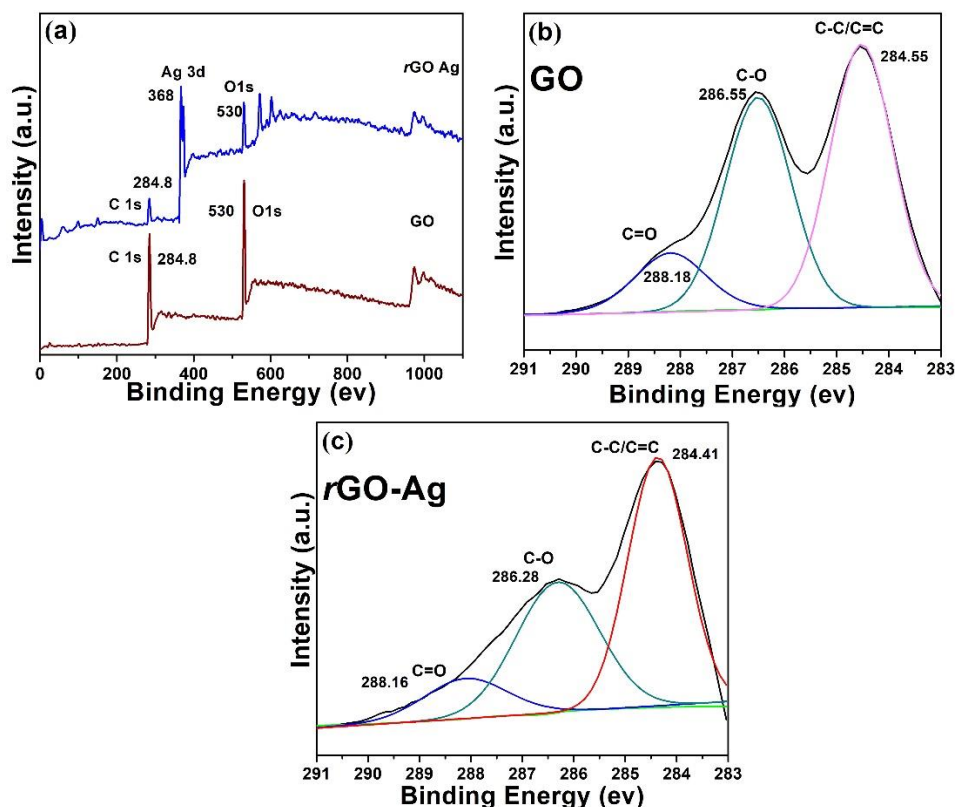


**Figure 6.6** Shows the (a) XPS Survey Spectra which indicates the various elements present in GO and rGO-Ag NC (b) C1s Peak Deconvolution of GO (c) C1s peak Deconvolution of rGO-Ag Nanocomposite.

The XPS survey spectra of GO is shown in Figure 6.6 (a) where the peaks for carbon and oxygen are present, whereas in the rGO-Ag nanocomposite apart from carbon and oxygen the presence of silver is also found. This proves the presence of metallic silver within graphene oxide. Figure 6.6 (b, c) shows the C1s peak deconvolution of GO and rGO-Ag NC, respectively. Figure 6.6 (b) shows the deconvoluted peaks which indicates the presence of C-O and C=O functional groups in graphene oxide. It is worth noting that the peaks corresponding to C-O and C=O of rGO-Ag nanocomposite as shown in Figure 6.6 (c) have reduced, though not vanished. This indicates that the nanocomposite is made up of partially reduced graphene oxide. As shown in Figure 6.6 (b, c) the peaks near the 284 eV of Binding Energy confirms the presence of bonds between carbon atoms of conjugated honey-comb lattice. This indicates the presence of  $sp^2$

hybridized carbon structures present in GO as well as in the *r*GO-Ag nanocomposite.[55, 56]

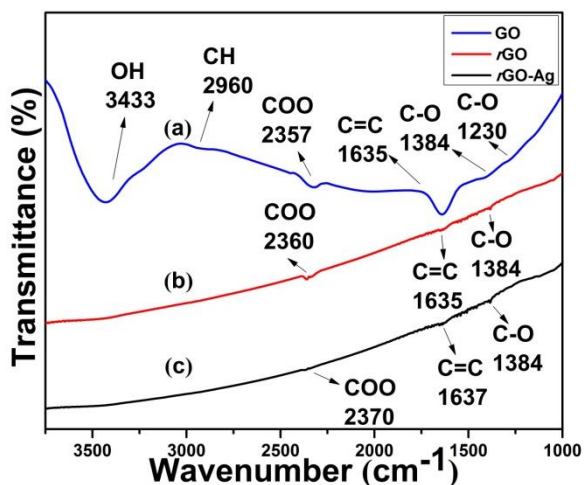


**Figure 6.7** Shows the FTIR Spectra of (a) GO (b) *r*GO (c) *r*GO-Ag nanocomposite.

Figure 6.7 (a) shows the FTIR Spectra of GO where the peaks at  $3433\text{ cm}^{-1}$ ,  $2960\text{ cm}^{-1}$ ,  $2357\text{ cm}^{-1}$ ,  $1635\text{ cm}^{-1}$ , corresponds to O–H, C–H, COO, C=C functional groups, respectively. The peaks at  $1384\text{ cm}^{-1}$  and  $1230\text{ cm}^{-1}$  corresponds to the presence of carboxy and epoxy functional groups (C–O). The FTIR spectra of reduced graphene oxide is shown in Figure 6.7 (b). It shows that the carboxy and epoxy functional groups are absent. It is found that the peak at  $1627\text{ cm}^{-1}$  which belongs to C=C has reduced in intensity indicating the disruption of  $\text{sp}^2$  hybridization of carbon atoms, resulting due to the heat treatment. The peak at  $3433\text{ cm}^{-1}$  has also reduced drastically which can be attributed to the removal of O–H functional groups because of the heat treatment. The FTIR spectra of *r*GO-Ag nanocomposite as shown in Figure 6.7 (c) shows the absence of OH peak at  $3433\text{ cm}^{-1}$ , slight decrease in the peak for COO at  $2370\text{ cm}^{-1}$ , decrease in peak intensity of carboxy at  $1384\text{ cm}^{-1}$  and decrease in the peak corresponding to epoxy at  $1230\text{ cm}^{-1}$ . The change observed in the shape of the peak corresponding to COO group located at  $2370\text{ cm}^{-1}$ , maybe because of the interaction of Silver Nanoparticles with the functional groups present in the Graphene by chemical bonds or by ionic interactions.[57, 58]

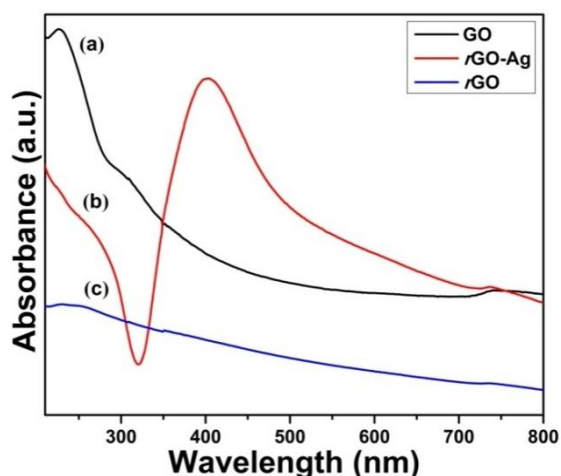


**Figure 6.8** Shows the UV-Vis Spectra of (a) GO (b) rGO-Ag nanocomposite (c) rGO.

Figure 6.8 (a) shows the UV-Vis spectra of graphene oxide. The spectra corresponding to GO conforms to that available in literature by showing the existence of a strong band at 226 nm and a shoulder at 308 nm. The origin of the 226 nm absorption band belongs to the  $\pi$ - $\pi^*$  transitions of aromatic C=C bond. The 308 nm shoulder band corresponds to  $n$ - $\pi^*$  of C=O bond.[59] The spectrum of rGO-Ag in Figure 6.8 (b) shows the characteristics of both GO as well as Ag. In the spectrum a strong plasma absorption band at 404 nm is visible, which corresponds to Ag Nanoparticles and also a peak for rGO at 262 nm, originating from  $\pi$ - $\pi^*$  transitions of aromatic C=C bond is also found.[60, 61] It also indicates the concomitant reduction of Ag ions to Ag Nanoparticles and GO to partially reduced GO, within the process of rGO-Ag nanocomposite synthesis, which is also suggested in literature.[62] The UV-Visible spectra of reduced graphene oxide is shown in Figure 3.8 (c). Here the peak due to  $\pi$ - $\pi^*$  transitions of aromatic C=C bond have shifted to 253 nm, which indicates removal of functional groups from the surface of GO.[63]

### 6.2.5 Silver Ion Release Test

Silver ion release test was performed to study the silver ions releasing from the rGO-Ag nanocomposite. Figure 6.9 shows the amount of silver ions released as a function of elapsing days in HNO<sub>3</sub> solution. It was

found that the silver ions were released with increasing trend of rate till day three and after that rate of silver ion release decreased. The fast rate of silver ion release at the beginning stage may be attributed to easy water diffusion into the surface of graphene flakes where the silver nanoparticles are loaded. The rate of silver ion release reduced after day three which may be attributed to slow diffusion of water within the interstitial graphene layers.[13,15]

#### **6.2.6 Experimental Details of Silver Ion Release Test**

1 mg of *rGO-Ag NC* was dissolved in 50 ml of 0.1 M  $\text{HNO}_3$ . After that a three-electrode electrochemical setup was used to conduct anodic stripping voltammetry. A stainless-steel strip was used as the working electrode. A graphite strip was used as counter electrode. A saturated calomel electrode was used as the counter electrode. The solution was stirred at 120 rpm. Chronoamperometry was carried out to deposit dissolved silver from the solution to the stainless-steel working electrode for 1000 s by applying a constant potential of  $-0.5$  V. Later linear sweep voltammetry (LSV) was used to strip the deposited silver from the stainless-steel electrode by applying a potential window of  $0-0.8$  V. The height of the peak current from the LSV was recorded for each day. Also, concentration vs current plot was obtained by running the same process using different known concentrations of  $\text{AgNO}_3$  in 0.1 M  $\text{HNO}_3$ . The later plot was used to calibrate and obtain silver ion release concentration ( $\mu\text{M/ml}$ ) vs time (days) for the former experiment.[64]

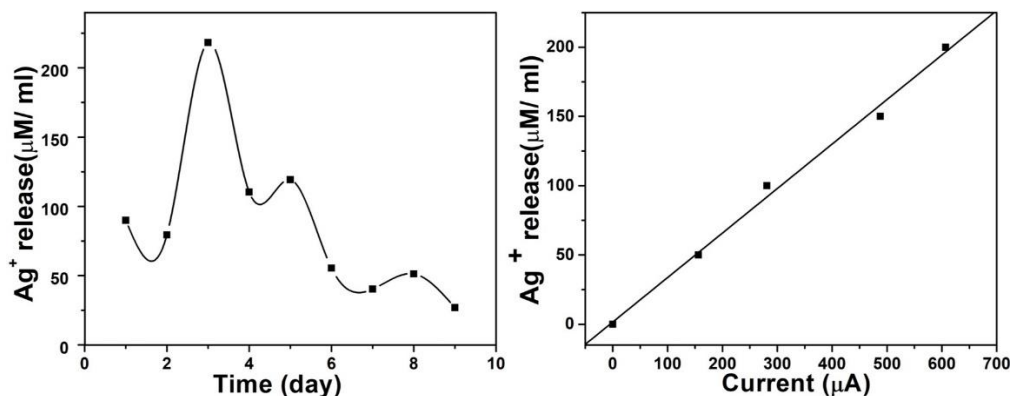


**Figure 6.9** Shows the (a) Silver ion release test results of rGO-Ag NC (b) standard curve of silver ions for calibration of the ion current.

### 6.3 Antifungal Application of rGO-Ag

#### 6.3.1 Preparation of Agar Medium

The Luria Bertani (LB) Agar medium was prepared to test the anti-microbial activity of the rGO-Ag, by mixing 3 g NaCl, 3 g Tryptone, 1.5 g Yeast Extract, 4.5 g Agar Agar Powder in 300 mL of De-ionized Water. After that the mixture was autoclaved for 90 minutes in a Borosil reagent bottle. The melted LB Agar was poured in sterilized Petri Dishes of 10 cm diameter and was left to solidify in sterile environment. All the chemicals were purchased from HiMedia laboratories, India. To incubate the microbes, the petri dish was exposed to open environment for 5 minutes and was then placed in an incubator with temperature set at 30° C. After two days of incubation, growths of fungal as well as bacterial colonies were seen. The fungal colonies were separated out from the first growth medium and were transferred to a secondary plate having the same medium.

Several, 2 mm × 2 mm region of Agar material along with fungal colonies were dug out from the secondary plate and were incubated in various control agents viz. Water, antibiotic doxycycline, partially reduced graphene oxide-silver nanocomposite, graphene oxide, reduced graphene oxide and silver nanoparticles (all in aqueous medium) for 60 minutes each. Then they were transferred to Petri dishes to see the effect of the control medium on the

fungus colonies. The final sets of Petri Dishes were kept for incubation at 30° C for two days.

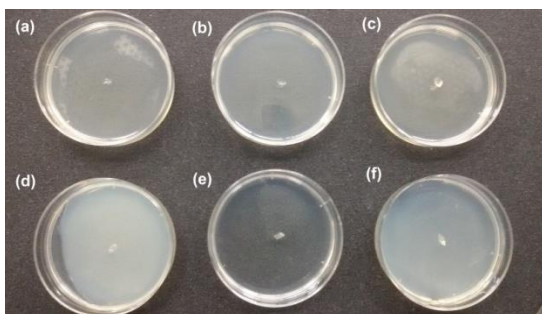


**Figure 6.10** Shows the optical Images of Luria Bertani Agar Petri Plates just after exposure to fungus. Fungus incubated with (a) Water (b) Antibiotic Doxycycline (c) rGO-Ag nanocomposite (d) GO (e) rGO (f) Ag nanoparticles.

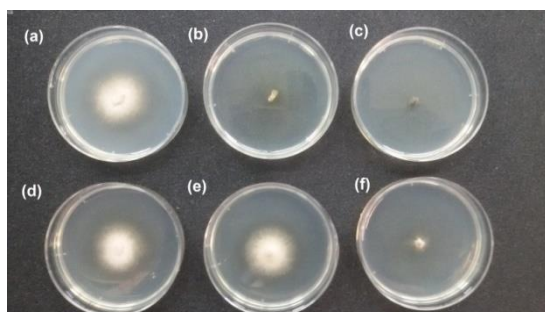
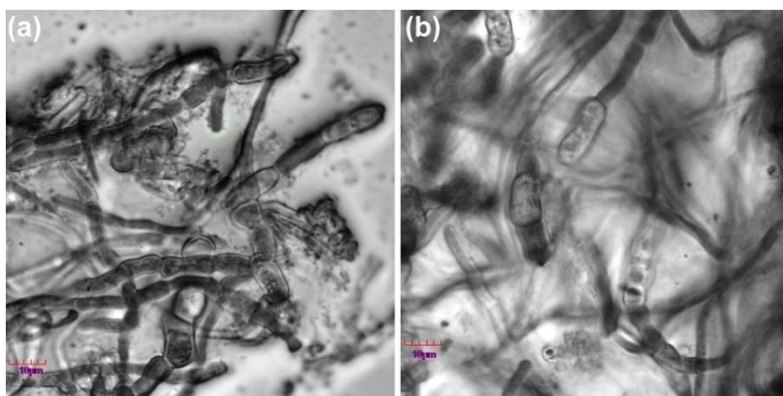


**Figure 6.11** Shows the optical Images of Luria Bertani Agar Petri Plates, showing fungal growth profile after 3 days of incubation. Fungus incubated with (a) Water (b) Antibiotic Doxycycline (c) rGO-Ag nanocomposite (d) GO (e) rGO (f) Ag nanoparticles.

Figure 6.10 shows Petri Plates containing Luria Bertani (LB) Agar medium, with second cell lines placed at the center. The second cell lines were incubated with different control agents for 60 minutes. Figure 6.11 shows the image of Fungal Specimen that were incubated in (a) Water, (b) Antibiotic Doxycycline, (c) rGO-Ag nanocomposite, (d) GO, (e) rGO, (f) Ag NP. All the nanomaterials were used as water dispersion. Observations on day two shows no microbial growth on antibiotic treated specimen in Figure 6.11 (b). Also Figure 6.11 (c) shows almost no fungal growth on the specimen treated with rGO-Ag nanocomposite. This indicates the

antifungal property of the partially reduced graphene oxide-silver nanocomposite. Heavy fungal growth is seen in Figure 6.11 (a, d, e) in which water, GO and *r*GO treated specimens were added respectively. Figure 6.11 (f) shows less fungal growth to the sample treated with Ag nanoparticles. From Figure 6.11 (d, e, f) it is seen that GO, *r*GO and Ag NP, respectively does not inhibit fungal growth individually, but *r*GO-Ag nanocomposite inhibits fungal growth, as shown in Figure 6.11 (c). This shows the synergistic effect of *r*GO and Ag NPs as an antifungal agent.

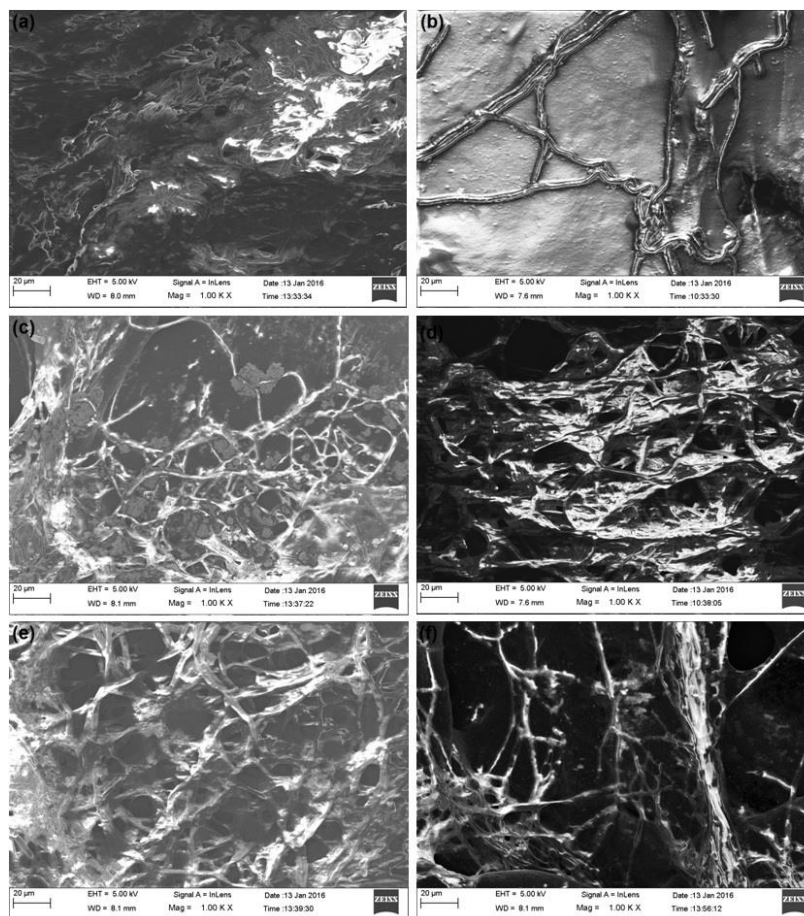
### 6.3.2 FE-SEM Image of Fungal microbes



**Figure 6.12** Shows the optical microscopy of fungal colonies (a) indicating Hyphae like structures (b) Sporangium like structures.

Figure 6.12 (a, b) shows the optical microscopy images of the microbes. In Figure 6.12 (a) Fungal Hyphae like structures are visible whereas Sporangium and Sporangium like structures are visible in Figure 6.12 (b).

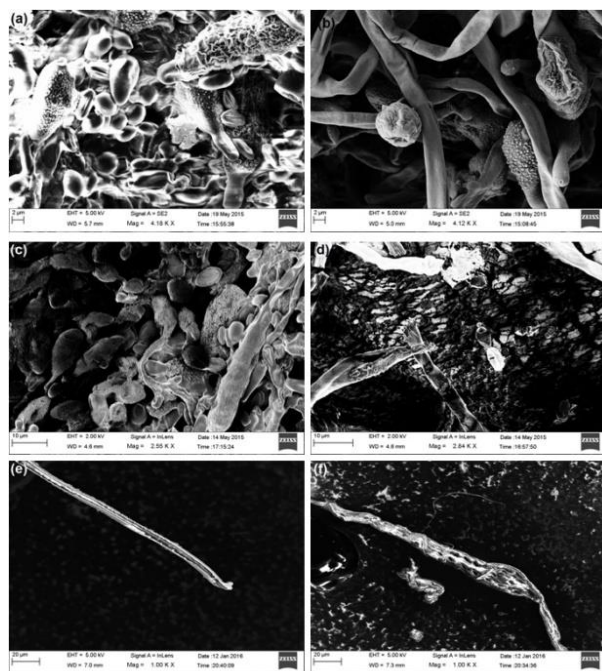




**Figure 6.13** Shows the SEM image of microbial cell culture where the fungal colonies are treated with (a) Water (b) Antibiotic Doxycycline (c) *rGO-Ag Nanocomposite* (d) GO (e) *rGO* (f) Ag NPs.

The images of fungal colonies treated with water are shown in Figure 6.13 (a). The images of fungal colonies after treatment with Antibiotic Doxycycline is shown in Figure 6.13 (b). Figure 6.13 (c) shows fungal colonies treated with *rGO-Ag* nanocomposite. It can be observed that the particles of the nanocomposite have formed agglomerations on the fungal cells. This can be confirmed with the SEM images of the microbes that are treated with graphene oxide, which also conforms to that available in the literature. The SEM image of the microbes treated with GO as shown in Figure 6.13 (d) show less GO agglomeration as compared to *rGO* treated fungal cells, as shown in Figure 6.13 (e). The reason behind this may be the presence of large agglomerated particles of reduced graphene oxide.[2] The

image of fungal colonies after treatment with Ag NPs is shown in Figure 6.13 (f).



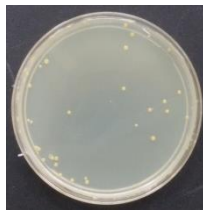
**Figure 6.14** Shows the SEM image of microbial cell culture where it is found that (a), (c), (e) cell membrane intact before treatment (b), (d), (f) cell membrane damaged after treatment with rGO-Ag nanocomposite.

Figure 6.14 (a) shows the SEM image of microbial cell membrane for normal growth conditions without any treatment. Figure 6.14 (b) shows ruptured and wrinkled cell membranes of the cells which were treated with rGO-Ag nanocomposite. This is a visual confirmation of the anti-microbial effect of rGO-Ag -nanocomposite. From the SEM images as shown in Figure 6.14 (d), the rGO-Ag nanocomposite treated microbes show damaged cell membranes, in comparison to untreated microbes as shown in Figure 6.14 (c). Figure 6.14 (e) shows untreated fungal hyphae, whereas Figure 6.14 (f) shows highly damaged fungal cell wall after treatment with rGO-Ag Nanocomposite.

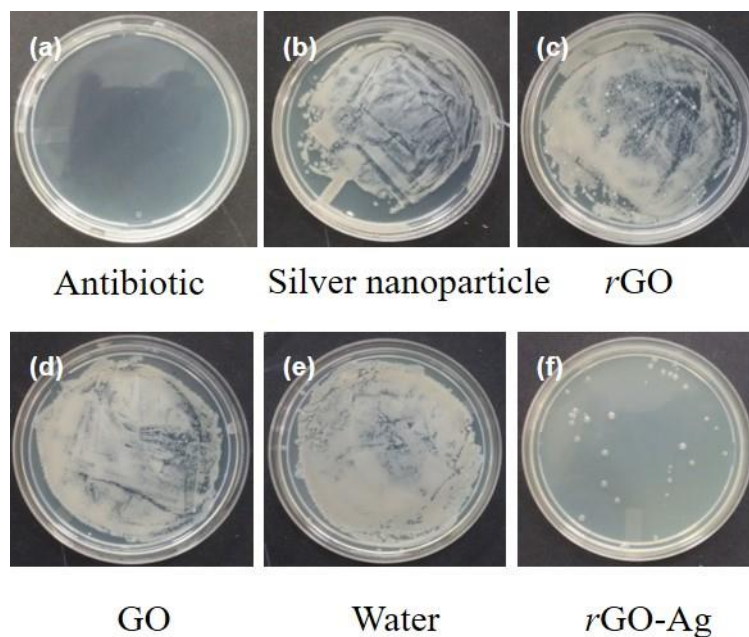
### 6.3.3 Plate Count Method to Ascertain Antifungal Activity

Plate count method was employed to find out the anti-microbial activity of the nanomaterials. The number of viable cells in the Agar plate

treated with *rGO*-Ag nanocomposite was found to be 2040 cell/ ml, after 2 days of treatment in the nanocomposite. No visible colonies were seen on the plate which was incubated with antibiotic Doxycycline. However, all other plates which were treated with Ag NP, *rGO*, GO and water were fully covered up with uncountable number of bacterial colonies. This demonstrates the highly potent antibacterial activity of the *rGO*-Ag NC.



**Figure 6.15** Shows LB Agar plate on which bacteria were grown by blowing air from mouth after 1 day of incubation.



**Figure 6.16** Shows LB Agar plates containing bacteria grown by blowing air from mouth after 1 day of incubation, where the Agar Plates are treated with (a) Antibiotic Doxycycline (b) Silver Nanoparticles (c) *rGO* (d) GO (e) Water (f) *rGO*-Ag NC.

To carry out the quantitative study of the antimicrobial property of the *rGO*-Ag NC, a sterile Agar plate was exposed to human saliva. Figure

6.15 shows the bacterial growth on the LB Agar Plate after 1 day of incubation. A single bacterial colony was taken and was incubated in 5 ml Lysogeny Broth for 1 day. After that 200  $\mu\text{L}$  of sample from the broth was collected and was diluted to 1200  $\mu\text{L}$  of final volume. Within this 1200  $\mu\text{L}$  of sample, 1 mg of the desired nanomaterial was added. This solution was kept incubating for two days, for all the different nanomaterials.

Then 100  $\mu\text{L}$  of sample from the previously incubated solution was taken and was diluted 10 times, which was further added on the Agar Plate and was spread by a sterile spreader, until the Agar surface dried up. The plates were kept for incubation for 1 day. The optical images of the plates are shown in Figure 3.16.[65]

#### **6.3.4 Synergistic effect of *rGO*-Ag**

The effect of cell membrane damage may be attributed to the anti-microbial effect of *rGO*-Ag Nanocomposite. Recent studies have indicated that the reasons behind the damage of the microbial cell membranes are oxidative stress and physical piercing.[3] It can be seen in the SEM image of GO which is shown in Figure 6.1 (a) that the edges of the GO flakes synthesized in the current work are not as sharp. Due to the above-mentioned reason the damage to the microbial cell membrane due to physical piercing in the current work, maybe ruled out. Toxicity induced by metal ions as reported in previous studies is also another reason for cell membrane destruction. However as discussed previously it may not be the sole reason for the death of the microbes.[66] This can be supported by the image shown in Figure 6.11 (f), which shows less inhibited microbial growths in the presence of Ag NPs alone, whereas *rGO*-Ag nanocomposite showed complete microbial growth inhibition as shown in Figure 6.11 (c). From this the synergistic effect of *rGO* and Ag nanoparticles as a bactericidal agent can be confirmed as reported previously.[39] Also similar type of synergistic effect is shown by vertically aligned MWCNTs with open tips having Ag NPs penetrated within.[67] The reason behind the synergistic effect of GO and Ag as reported previously is that, the large

surface area of GO provides oxygen containing functional groups to Ag nanoparticles, which reduces them to Ag ions. Recently it was shown that in a nanocomposite of graphene and metal, graphene can accept electrons.[68] By this the possibility arises where graphene oxide can accept electrons from silver nanoparticles to form silver ions, which indicates the enhancement of the anti-microbial efficacy of the nanocomposite. From previous reports it was found that Silver nanoparticles residing on graphene sheets can give away electron to form ions in some circumstances.[69] The Ag ions can show toxic effects by inhibiting the respiratory enzymes within the bacteria. This creates reactive oxygen species in the cells, which causes damage to the cell membrane and finally leads to the cell death.[20, 39]

## 6.4 Summary

In this work *r*GO-Ag nanocomposite was prepared and its anti-microbial effect was studied. It was found that fungus belonging to phylum *Zygomycota*, which can be fatal to human life is susceptible to *r*GO-Ag NC. Fungal colonies were incubated on Luria Bertani Agar medium. Characterizations were carried out on GO, *r*GO and *r*GO-Ag nanocomposites to study their structural morphology and to find out their effect on microbial growth. SEM imagery of microbes helped in the identification of Fungi and showed damaged cell membranes after treatment with *r*GO-Ag nanocomposite. To find out the cause of anti-microbial effect of *r*GO-Ag nanocomposite, the process of mechanical piercing was ruled out. The cytotoxic effect of Ag NPs was also discussed. As a probable mechanism to explain the antimicrobial effect of *r*GO-Ag nanocomposite, the synergistic effect of partially reduced graphene oxide and Ag are discussed and is held responsible for the generation of reactive oxygen species within the microbes that leads to destruction of cell membrane and subsequently leads to microbial cell death.

## References

1. Akhavan, O. *et al.*, (2010). Toxicity of graphene and graphene oxide nanowalls against bacteria. *ACS Nano*, 4(10), 5731–5736.
2. Liu, S. *et al.*, (2011). Antibacterial activity of graphite, graphite oxide, graphene oxide, and reduced graphene oxide: Membrane and oxidative stress. *ACS Nano*, 5(9), 6971–6980.
3. Hu, W. *et al.*, (2010). Graphene-based antibacterial paper. *ACS Nano*, 4(7), 4317–4323.
4. Akhavan, O. *et al.*, (2012). Escherichia coli bacteria reduce graphene oxide to bactericidal graphene in a self-limiting manner. *Carbon*, 50(5), 1853–1860.
5. Akhavan, O. *et al.*, (2011). Wrapping bacteria by graphene nanosheets for isolation from environment, reactivation by sonication, and inactivation by near-infrared irradiation. *Journal of Physical Chemistry B*, 115(19), 6279–6288.
6. Akhavan, O. *et al.*, (2009). Photocatalytic reduction of graphene oxide nanosheets on TiO<sub>2</sub> thin film for photoinactivation of bacteria in solar light irradiation. *Journal of Physical Chemistry C*, 113(47), 20214–20220.
7. Dunn, K. *et al.*, (2004). The role of Acticoat<sup>TM</sup> with nanocrystalline silver in the management of burns. *Burns*, 30 Suppl. 1, S1-S9.
8. Thomas, S. *et al.*, (2014). A comparison of the antimicrobial effects of four silver-containing dressings on three organisms. *Journal of Wound Care*, 12(3), 101–107.
9. Percival, S.L. *et al.*, (2005). Bacterial resistance to silver in wound care. *Journal of Hospital Infection*, 60(1), 1–7.
10. Yuranova, T. *et al.*, (2003). Antibacterial textiles prepared by RF-plasma and vacuum-UV mediated deposition of silver. *Journal of Photochemistry and Photobiology A: Chemistry*, 161(1), 27–34.
11. Akhavan, O. *et al.*, (2010). Cu and CuO nanoparticles immobilized by silica thin films as antibacterial materials and photocatalysts.

*Surface and Coatings Technology*, 205(1), 219–223.

12. Akhavan, O. *et al.*, (2011). Copper oxide nanoflakes as highly sensitive and fast response self-sterilizing biosensors. *Journal of Materials Chemistry*, 21(34), 12935–12940.
13. Raghupathi, K.R. *et al.*, (2011). Size-dependent bacterial growth inhibition and mechanism of antibacterial activity of zinc oxide nanoparticles. *Langmuir*, 27(7), 4020–4028.
14. Zhang, H. *et al.*, (2009). Potent Antibacterial Activities of AgTiO<sub>2</sub> Nanocomposite Powders Synthesized by a One-Pot Sol-Gel Method. *Environ. Sci. Technol.* 2(852), 2905–2910.
15. Dastjerdi, R. *et al.*, (2010). A review on the application of inorganic nano-structured materials in the modification of textiles : Focus on anti-microbial properties. *Colloids and Surfaces B: Biointerfaces*, 79(1), 5–18.
16. Jain, J. *et al.*, (2009). Silver Nanoparticles in Therapeutics : Development of an Antimicrobial Gel Formulation for Topical Use. *Molecular Pharmaceutics*, 6(5), 1388-1401.
17. Jones, S.A. *et al.*, (2004). Controlling wound bioburden with a novel silver- containing Hydrofiber dressing. *Wound Repair and Regeneration*, 12(3) 288–294.
18. Kim, J.S. *et al.*, (2007). Antimicrobial effects of silver nanoparticles. *Nanomedicine: Nanotechnology, Biology and Medicine*, 3(1), 95–101
19. Jones, C.M. *et al.*, (2010). A review of the antibacterial effects of silver nanomaterials and potential implications for human health and the environment. *Journal of Nanoparticle Research*, 12(5), 1531–1551.
20. Martinez-Castanon G.A. *et al.*, (2008). Synthesis and antibacterial activity of silver nanoparticles with different sizes. *Journal of Nanoparticle Research*, 10(8), 1343–1348.
21. Pal, S. *et al.*, (2007). Does the Antibacterial Activity of Silver

- Nanoparticles Depend on the Shape of the Nanoparticle ? A Study of the Gram-Negative Bacterium *Escherichia coli*. *Appl. Environ. Microbiol.*, 73(6), 1712–1720.
22. Shrivastava, S. *et al.*, (2007). Characterization of enhanced antibacterial effects of novel silver nanoparticles. *Nanotechnology*, 18, 225103-225111.
  23. Bao, Q. (2011). Synthesis and characterization of silver nanoparticle and graphene oxide nanosheet composites as a bactericidal agent for water disinfection. *Journal of Colloid and Interface Science*, 360, 463–470.
  24. Akhavan, O. *et al.*, (2009). Bactericidal effects of Ag nanoparticles immobilized on surface of SiO<sub>2</sub> thin film with high concentration. *Current Applied Physics*, 9(6), 1381–1385.
  25. Akhavan, O. (2009). Lasting antibacterial activities of Ag–TiO<sub>2</sub>/Ag/a-TiO<sub>2</sub> nanocomposite thin film photocatalysts under solar light irradiation. *Journal of Colloid And Interface Science*, 336(1), 117–124.
  26. Liu, T. *et al.*, (2007). A study on bactericidal properties of Ag coated carbon nanotubes. *Journal of Colloid and Interface Science*, 264, 282–286.
  27. Kumarathasan, P. *et al.*, (2014). Cytotoxicity of carbon nanotube variants: A comparative in vitro exposure study with A549 epithelial and J774 macrophage cells. *Surface & Coatings Technology*, 5390, 1–14.
  28. Das, M.R. *et al.*, (2011). Colloids and Surfaces B : Biointerfaces Synthesis of silver nanoparticles in an aqueous suspension of graphene oxide sheets and its antimicrobial activity. *Colloids and Surfaces B: Biointerfaces*, 83(1), 16–22.
  29. Chen, H. *et al.*, (2008). Mechanically Strong, Electrically Conductive, and Biocompatible Graphene Paper. *Advanced Materials*, 20(18), 3557–3561.



30. Chook, S.W. *et al.*, (2012). Antibacterial performance of Ag nanoparticles and AgGO nanocomposites prepared via rapid microwave-assisted synthesis method. *Nanoscale Research Letters*, 7(1), 541.
31. Liu, L. *et al.*, (2011). Facile synthesis of monodispersed silver nanoparticles on graphene oxide sheets with enhanced antibacterial activity. *New Journal of Chemistry*, 35, 1418–1423.
32. Ma, J. *et al.*, (2011). Preparation, characterization and antibacterial properties of silver-modified graphene oxide. *Journal of Materials Chemistry*, 21(10), 3350–3352.
33. Pasricha, R. *et al.*, (2009). A Facile and Novel Synthesis of Ag–Graphene-Based Nanocomposites. *Small*, 5(20), 2253–2259.
34. Shen, J. *et al.*, (2010). Facile Synthesis and Application of Ag–Chemically Converted Graphene Nanocomposite. *Nano Research*, 3(5), 339–349.
35. Lu, J. *et al.*, (2009). One-Pot Synthesis of Fluorescent Carbon Graphene by the Exfoliation of Graphite in Ionic Liquids. *ACS Nano*, 3(8), 2367–2375.
36. Tang, X. *et al.*, (2011). Growth of silver nanocrystals on graphene by simultaneous reduction of graphene oxide and silver ions with a rapid and efficient one-step approach. *Chem. Comm.*, 47, 3084–3086.
37. Wang, X. *et al.*, (2012). Green controllable synthesis of silver nanomaterials on graphene oxide sheets via spontaneous reduction. *RSC Advances*, 2, 3816–3822.
38. Xu, W.P. *et al.*, (2011). Facile synthesis of silver@graphene oxide nanocomposites and their enhanced antibacterial properties. *Journal of Materials Chemistry*, 21(12), 4593–4597.
39. Tang, J. *et al.*, (2013). Graphene Oxide–Silver Nanocomposite As a Highly Effective Antibacterial Agent with Species-Specific Mechanisms. *ACS Appl. Mater. Interfaces*, 2013, 5, 9, 3867–3874.
40. Ribes, J.A. *et al.*, (2000). Zygomycetes in Human Disease. *Clin*

- Microbiol Rev.*, 13(2), 236–301.
41. Hummers, W.S. *et al.*, (1958). Preparation of Graphitic Oxide. *Journal of the American Chemical Society*, 80(6), 1339.
  42. Ghosh, R. *et al.*, (2013). Chemically reduced graphene oxide for ammonia detection at room temperature. *ACS Applied Materials and Interfaces*, 5(15), 7599–7603.
  43. Liu, X. *et al.*, (2014). A facile molten-salt route to graphene synthesis. *Small*, 10(1), 193–200.
  44. Ji, J. *et al.*, (2011). Sulfonated graphene as water-tolerant solid acid catalyst. *Chem. Sci.*, 2, 484–487.
  45. Cui, P. *et al.*, (2011). One-pot reduction of graphene oxide at subzero temperatures. *Chem. Commun.*, 47(45), 12370–12372.
  46. Krishna, R. *et al.*, (2015). Improved Reduction of Graphene Oxide. *Materials Today: Proceedings*, 2(1), 423–430.
  47. Hsiao, M.C. *et al.*, (2013). Thermally conductive and electrically insulating epoxy nanocomposites with thermally reduced graphene oxide-silica hybrid nanosheets. *Nanoscale*, 5, 5863–5871.
  48. Dar, R.A. *et al.*, (2014). Green synthesis of a silver nanoparticle–graphene oxide composite and its application for As(III) detection. *RSC Advances*, 4(28), 14432–14440.
  49. Roy, I. *et al.*, (2015). Physical and electrochemical characterization of reduced graphene oxide/silver nanocomposites synthesized by adopting a green approach. *RSC Adv.*, 5(32), 25357–25364.
  50. Hassan, H.M.A. *et al.*, (2009). Microwave synthesis of graphene sheets supporting metal nanocrystals in aqueous and organic media. *Journal of Materials Chemistry*, 19(23), 3832–3837.
  51. Marcano, D.C. *et al.*, (2010). Improved Synthesis of Graphene Oxide. *ACS Nano*, 4(8), 4806–4814.
  52. Sobon, G. *et al.*, (2012). Graphene Oxide vs Reduced Graphene Oxide as saturable absorbers for Er-doped passively mode-locked fiber laser. *Optics Express*, 20(17), 2460–2465.

53. Hsu, K. *et al.*, (2014). Green synthesis and synergistic catalytic effect of Ag / reduced graphene oxide nanocomposite. *Nanoscale Res. Lett.*, 9(1), 484.
54. Akhavan, O. (2015). Bacteriorhodopsin as a superior substitute for hydrazine in chemical reduction of single-layer graphene oxide sheets. *Carbon*, 81(1), 158–166.
55. Shao, W. *et al.*, (2015). Preparation, Characterization, and Antibacterial Activity of Silver Nanoparticle-Decorated Graphene Oxide Nanocomposite. *ACS Appl. Mater. Interfaces*, 7, 12, 6966–6973.
56. Er, E. *et al.*, (2014). An efficient way to reduce graphene oxide by water elimination using phosphoric acid. *RSC Advances*, 4(55), 29173–29179.
57. Hui, K.S. *et al.*, (2014). Green synthesis of dimension-controlled silver nanoparticle-graphene oxide with in situ ultrasonication. *Acta Materialia*, 64, 326–332.
58. Weber, C.F. (2014). Hormones and Antibiotics in Nature: A Laboratory Module Designed to Broaden Undergraduate Perspectives on Typically Human-Centered Topics. *Journal of Microbiology & Biology Education*, 15(2), 277–286.
59. Soroush, A. *et al.*, (2015). Surface modification of thin film composite forward osmosis membrane by silver-decorated graphene-oxide nanosheets. *Environmental Science: Nano*, 2(4), 395–405.
60. Huang, J. *et al.*, (2013). Tracking the intracellular drug release from graphene oxide using surface-enhanced Raman spectroscopy. *Nanoscale*, 5, 10591–10598.
61. Wu, T. *et al.*, (2011). Surface plasmon resonance-induced visible light photocatalytic reduction of graphene oxide: Using Ag nanoparticles as a plasmonic photocatalyst. *Nanoscale*, 3(5), 2142–2144.
62. Zhang, Z. *et al.*, (2011). Sodium citrate: A universal reducing agent

- for reduction/decoration of graphene oxide with Au nanoparticles. *Nano Research*, 4(6), 599–611.
63. Yang, S. *et al.*, (2012). A facile green strategy for rapid reduction of graphene oxide by metallic zinc. *RSC Advances*, 2(23), 8827–8832.
  64. Kumar, R. *et al.*, (2005). Silver ion release from antimicrobial polyamide/silver composites. *Biomaterials*, 26(14), 2081–2088.
  65. Tang, J. *et al.*, (2013). Graphene oxide-silver nanocomposite as a highly effective antibacterial agent with species-specific mechanisms. *ACS Applied Materials and Interfaces*, 5(9), 3867–3874.
  66. Kang, S. *et al.*, (2007). Single-walled carbon nanotubes exhibit strong antimicrobial activity. *Langmuir*, 23(17), 8670–8673.
  67. Akhavan, O. *et al.*, (2011). Silver nanoparticles within vertically aligned multi-wall carbon nanotubes with open tips for antibacterial purposes. *Journal of Materials Chemistry*, 21(2), 387–393.
  68. Akhavan, O. *et al.*, (2012). Adverse effects of graphene incorporated in TiO<sub>2</sub> photocatalyst on minuscule animals under solar light irradiation. *Journal of Materials Chemistry*, 22(43), 23260–23266.
  69. Tang, X.Z. *et al.*, (2015). Improved chemical stability of silver by selective distribution of silver particles on reduced graphene oxide nanosheets. *RSC Advances*, 5(61), 49257–49262.

## Conclusion and Future Scopes

---

### 7.1 Thesis Summary

This thesis is based on the synthesis, characterization and applications of graphene oxide (GO), metal oxide, reduced graphene oxide-metal oxide nanocomposite, reduced graphene oxide-metal oxide/polymer nanocomposite, Au NPs, Au NP-Cellulose/PDMS nanocomposite. The synthesis of GO is carried out in this work following modified Hummer's method. Using material characterization techniques like XRD, SEM, HR-TEM, FTIR, UV-Vis, Raman Spectroscopy the synthesis of good quality GO is confirmed then using this synthesis of Fe-*r*GO was carried out.

The fossil fuels are towards the verge of getting extinguished and the quest is on for finding a suitable alternative to fossil fuels. The conventional energy systems are heavily dependent on the fossil fuels. This is increasing the volume of CO<sub>2</sub> in the atmosphere, which will have a heavy impact on the ecosystem where we live. The present energy systems in the world are based on distributed grids, however the energy systems of the future are predicted to be based on smart grids or grid free systems that might be powered by nanogenerators. In this dissertation PVDF based nanogenerator was fabricated where the piezoelectric output is realized by incorporating *r*GO-metal oxide-based nanomaterials. Fe-*r*GO, CNT and *r*GO-Ag were incorporated in PVDF separately. It was found that polar piezoelectric phases induced due to their additions. Fe-*r*GO and CNT were used to fabricate a piezoelectric PVDF film and its energy harvesting ability was confirmed by incorporating a unique device structure. Following the trend to incorporate graphene oxide-metal oxide nanoparticles in PVDF, *r*GO-Ag was incorporated in PVDF to fabricate an energy harvesting device. The *r*GO-Ag/PVDF based mechanical energy harvesting device could directly light LEDs and could charge capacitor. The bio-mechanical energy

harvesting performance of the as fabricated device was also demonstrated. Also, an Au NP-Cellulose/PDMS nanocomposite based piezoelectric-plasmonic hybrid nanogenerator fabrication was demonstrated successfully. It is found that volume specific addition of Au NPs enhances the overall piezoelectric output. It is concluded that the enhancement in the dielectric property contributes to the enhanced piezoelectricity voltage output from the Au NP-Cellulose/PDMS nanocomposite.

Also, in this work the anti-fungal activity of GO, *r*GO, Ag NPs and *r*GO-Ag are individually tested. It was found that the *r*GO-Ag shows potent anti-fungal activity as compared to GO, *r*GO and Ag NP individually. This is attributed to the synergistic effect of *r*GO and Ag NPs. The GO sheets contain oxygen containing functional groups which reduce the Ag NPs residing on them to Ag ions thereby enhancing their anti-microbial efficacy. The Ag ions shows toxic effects within the microbial cell by inducing reactive oxygen species, thereby killing the microbial cell. The antifungal application and the energy harvesting application research that are shown here in this work are important pertaining to the problems faced by the modern world. The menace of antibiotic resistance is a threat to the mankind and if not handled properly lethal diseases can swipe the entire population.

The chapter wise summary of this dissertation is as follows:

1. The first chapter introduces the concept of nanomaterials. The concept of nanogenerator is introduced in terms of nanomaterials. The different types of nanogenerators are explained viz. piezoelectric and triboelectric. The advantages of piezoelectric nanogenerator (PENG) and triboelectric nanogenerator (TENG) are discussed.
2. The second chapter is about the synthesis and various characterization techniques. The classification of the different types of nanomaterials are discussed, which is followed by discussion of properties of nanomaterials. Different types of nanomaterial synthesis techniques are also discussed,

which is followed by discussion on nanomaterial-polymer nanocomposite synthesis. Material characterization techniques are discussed after that.

3. The third chapter is about synthesis of Fe-*r*GO/PVDF and CNT/PVDF nanocomposite and its application for mechanical energy harvesting using a unique device structure. The device is excited by finger tapping vibrations. The output voltage was detected by digital storage oscilloscope. AC electrical conductivity measurements were carried out on the nanocomposites, which indicated that the presence of CNT and Fe-*r*GO increase the electrical conductivity in the polymer by creating conducting paths within the polymer matrix.

4. In the fourth chapter *r*GO-Ag/PVDF based PENG is synthesized and a mechanical energy harvesting device is fabricated with it. It was found that the addition of *r*GO-Ag increases the piezoelectric property of PVDF through electrostatic interactions. Its mechanical energy harvesting capability is tested by charging capacitors, lighting LEDs and by showing biomechanical applications. The PENG showed a moderate efficiency value of 0.65 %.

5. In the fifth chapter Au NP-Cellulose/PDMS nanocomposite is synthesized and its mechanical energy harvesting application is realized. It was found that compared to pure PDMS, the dielectric constant of Cellulose/PDMS increases. It is also found that when Au NPs are included in the nanocomposite the dielectric loss decreases. The dielectric constant increases due to the combined interaction of conducting Au NPs, piezoelectric cellulose and insulating PDMS within the nanocomposite. The dielectric loss decreases due to the addition of Au NPs which increases the overall bulk of the dipoles, due to which it becomes less responsive to change in the external electric field. The presence of Au NPs in the Cellulose/PDMS matrix leads to the increase in the overall piezoelectric dipoles throughout the nanocomposite. The PENG could light up LEDs, charge capacitors. A touch sensor application is realized. It showed an efficiency value of 1.8 %.

6. In the sixth chapter the synthesis and characterization and antifungal activity of *r*GO-Ag is discussed. The menace of antibiotic resistance is discussed, and *r*GO-Ag is projected as an alternative to the menace of antibiotic resistance. The synergistic effects of *r*GO and Ag towards the antifungal activity are explained in the process.

## **7.2 Future scope**

This doctoral study is based upon PVDF, which is a synthetic piezoelectric polymer. PVDF is selected because it provides opportunity for the development of a flexible energy harvesting device. This opens the possibility to explore some naturally found piezoelectric materials like cellulose, animal bones, spider webs.

The future scope of this work is towards the development of piezoelectric energy harvesting with new device structure. The efficiency enhancement will also remain an important target towards achieving a better energy harvesting device. The nanogenerators that are fabricated in this dissertation are capable of directly lighting LEDs, charging capacitors. However, the general need of the nanogenerators is to power handheld electronic devices and not just lighting LEDs. This requires an enhancement in the instantaneous power density. The addition of piezoelectric nanomaterials in PVDF can be a possible field of research where the individual and combined roles of the piezoelectric nanomaterials and the polymers can be studied. It is expected that the combined role of the piezoelectric nanomaterials and PVDF polymer will enhance the piezoelectric output.

Triboelectric nanogenerators which were mentioned earlier are another class of nanogenerators whose working mechanisms are based upon triboelectric effect and electrostatic effect. It not only has high efficiency but also follows an easy working mechanism, which can be run from different sources and different conditions. The major sources of harvesting mechanical energy using triboelectric nanogenerators are running water, textile, body movement.



Piezoelectric and triboelectric hybrid nanogenerators are another type of mechanical energy harvester that uses both, a piezoelectric layer as well as another layer that is made up of a material which shows triboelectric effect. As expected, the hybrid nanogenerators show a high output power density due to the combined effect of the triboelectric as well as piezoelectric effects.

To enhance the efficiency of the energy harvesting devices other nanomaterials that are not explored in this dissertation like Perovskite materials, new and yet to be explored 2D materials like Borophene *etc.*

